MONITORING 3D VIBRATIONS IN STRUCTURES USING HIGH RESOLUTION BLURRED IMAGERY

by

David M.J. McCarthy

School of Civil and Building Engineering
Loughborough University

A Doctoral Thesis

Submitted in partial fulfilment of the requirements
for the award of
Doctor of Philosophy
of Loughborough University

September 2015

Abstract

Keywords: *Vibration, Deformation, Motion-blur, Structural Health Monitoring, Close Range Photogrammetry, Engineering*

This thesis describes the development of a measurement system for monitoring dynamic tests of civil engineering structures using long-exposure motion blurred images, named LEMBI monitoring. Photogrammetry has in the past been used to monitor the static properties of laboratory samples and full-scale structures using multiple image sensors. Detecting vibrations during dynamic structural tests conventionally depends on high-speed cameras, often resulting in lower image resolutions and reduced accuracy.

To overcome this limitation, the novel and radically different approach presented in this thesis has been established to take measurements from blurred images in long-exposure photos. The motion of the structure is captured in an individual motion-blurred image, alleviating the dependence on imaging speed. A bespoke algorithm is devised to determine the motion amplitude and direction of each measurement point.

Utilising photogrammetric techniques, a model structure's motion with respect to different excitations is captured and its vibration envelope recreated in 3D, using the methodology developed in this thesis. The approach is tested and used to identify changes in the model's vibration response, which in turn can be related to the presence of damage or any other structural modification. The approach is also demonstrated by recording the vibration envelope of larger case studies in 2D, which includes a full-scale bridge structure, confirming the relevance of the proposed measurement approach to real civil engineering case studies.

This thesis then assesses the accuracy of the measurement approach in controlled motion tests. Considerations in the design of a survey using the LEMBI approach are discussed and limitations are described. The implications of the newly developed monitoring approach to structural testing are reviewed.

Acknowledgements

The completion of this research project would have been impossible without the support of many people, some of whom I wish to express my thanks to here.

First, I wish to take the opportunity to express my gratitude to my supervisors, Jim Chandler and Alessandro Palmeri for their persistent motivation, guidance, support and patience, and for always making time to be available. Their discussions, knowledge and insight were critical to the progress of this work.

Thanks to Nick Rodgers for the care and technical support of the specialist instruments. Thanks to Mike Smeeton and Neil Parks for their support in the laboratory, particularity during the early stages of this project. Thanks to Polytech Inc. for their generous loan of the RSV instrument.

My deepest gratitude goes to my family, and especially my fiancé Vicci, for their love and support throughout my life, without which this dissertation would have been so much more difficult. Thanks to Vicci also for her time spent locating and visiting suitable test structures, and for jumping on bridges.

Special thanks to Till, Rene and Chris for their assistance carrying out demonstrations on the Wilford bridge, on a cold and snowy day. Thanks to Vangelis for his assistance in the laboratory with the shake table and models.

My time at work was always made more enjoyable by my Research Hub peers and friends, including Till, Vicki, Edgar, Özlem, Eleonora, Henry, Vicky, Tom, Kate, Jon, Cristina, Paula, Lynda, Richard, Eleonora, Louise and many others. Their friendship at and after work made for an enjoyable and memorable time in Loughborough.

Thanks to the Loughborough University Graduate School for funding this project.

Contents

List of Figures

List of Tables

Nomenclature

Abbreviations and acronyms

CCD	Charge-coupled device
COMAC	Coordinate Modal Assurance Criterion
CRF	camera response function
CSV	comma separated values
DFT	Discrete Fourier transform
DIC	Digital image correlation
DOF	depth of field
DSPI	Digital Speckle-Pattern Interferometry
DST	descrete Fourier transform
EO	exterior orientation
EXIF	exchangeable image file format
FE	Finite Element
GAP	General Adjustment Program
GNSS	Global navigation satellite system
IO	interior orientation
LDV	Laser Doppler Vibrometer
LEMBI	long exposure motion blurred image
LSM	Least squares matching
MAC	Modal Assurance Criterion
MP	Megapixels
ND	neutral density

PIP	Pixel intensity profiles
PSF	point spread function
RTS	Robotic Total Station
TIFF	Tagged image file format
TLS	Terrestrial Laser Scanner
TS	Total Station
VC	vertical circle
WCB	Whole Circle Bearing

Symbols

α, β	PSF generation constants
$*$	discrete image convolution
$\overline{A}$, $\overline{B}$	mean pixel intensity value
$a_{0...2}$, $b_{0...2}$, $c_{1..2}$	planar geometric transform parameters
A_{ij}, B_{ij}	image 'window'
$\mathbf{B}$	blurred image
$\mathbf{L}$	sharp image
Δu	measured distance
$\Delta x'$, $\Delta y'$	error correction
$\mathcal{F}$	Fourier transform
K_1, K_2	radial distortion parameters
L	motion polar distance
m, n	image 'window' dimensions
m_b	image-scale number
$\mathbf{N}$	sensor noise
$\mathbf{K}$	point spread function
P_1, P_2	tangential distortion parameters
r	motion polar angle
r	rotational parameters

T	harmonic motion period
t	exposure time
u	image motion
v	velocity
X, Y	image coordinates (planar transforms)
x, y	object coordinates (planar transforms)
X, Y, Z	object space coordinates (collinearity equations)
x', y'	image coordinates
x'_0, y'_0	principle point offset
X_P, Y_P	principle point

Chapter 1

Introduction

Civil engineering structures are key components of modern infrastructure, and exist throughout the world. Continual innovation in structures and engineered materials combined with the need to minimise costs creates a desire to develop materials and methods that can be used with greater efficiency. This requires detailed testing before construction and a need for more advanced and detailed monitoring strategies. Existing structures may also be part of continuous health monitoring programmes to protect against failures resulting from undetected deterioration.

Structural testing analysis techniques include those that examine static properties of the structure, and those that analysis dynamic properties. In a static test, classically, gradually increasing loads are applied to the structure under test whilst its performance is monitored. Depending on this outcome, the structure is then deemed safe for its intended function. However, this approach may be inconvenient as it requires test weights to be manoeuvred on to the structure, which often requires that it be taken out of service. Tests utilising dynamic techniques use much lower loads and can reveal more than static techniques. Although the analysis of measured data remains complex, there is a distinct trend to use dynamic testing in structural engineering (Kasinos *et al.*, 2014).

Various sensors and instrumentation are available to the responsible engineer to aid assessment. Photogrammetry has demonstrated its potential as a monitoring tool for structural health monitoring, allowing simultaneous non-contact measurement of multiple monitoring points. The approach can be comparatively cheap, using off-the-shelf equipment, and is effective at both large and small scales. Normally, a conventional method is

adopted where absolute coordinates are measured at discrete 'epochs', each captured at an appropriate frame rate. The literature review carried out as part of this research has identified key limitations of such an approach when it comes to higher sampling rates, and how a compromise exists between the rate of image acquisition, necessary to detect faster vibrations, and image resolution, necessary for accurate spatial measurement.

In this thesis, an alternative approach has been developed using the inherent advantage of acquiring long exposure motion blurred images, in which the whole motion of an object is captured in a single frame. The long exposure motion blurred image measurement ("LEMBI" measurement) permits the use of higher image resolutions for more accurate measurement of the vibration envelope. Significantly, it is frequency independent, allowing vibration envelope measurement of fast vibration without dependence on imaging speed.

1.1 Aim and Objectives

The overall aim of this research project is

> *To develop novel image processing approaches for monitoring testing of structural elements using dynamic techniques.*

This aim is separated into five objectives:

> *Objective 1. Compose a literature review to assess current and particularly image based methods used for measuring deformations in structural testing, including both conventional and non-contact approaches.*

To gain the understanding of existing monitoring systems in use for structural testing, a thorough literature review has been carried out. This review covers contact and non-contact sensors and evaluate both. The review includes established and well understood approaches in addition to the most recent developments in modern instruments.

With the aim of developing a measurement method exploiting motion-blurred images, an understanding of image processing techniques is required, including algorithms already in use in photogrammetry as well as developments from computer science. A review of the mathematical models already common in photogrammetry is also included.

Objective 2. Develop algorithms for measuring blur in long-exposure images captured during dynamic structural tests and design a method of incorporating these into routine structural testing.

The long exposure imaging strategy differs from that currently in use, as it inevitably creates images that cannot be processed automatically using existing photogrammetric software. Bespoke image registration and measurement algorithms are therefore required. These have been developed in the MathWorks Matlab software package. Not only should the algorithms derive measurements describing deformation from long-exposure images, but are incorporated into a workflow suitable for routine structural testing. Such an algorithm would be designed initially to permit two dimensional planar monitoring in a user selectable plane.

Objective 3. Test the accuracy of such an image based system against conventional instrumentation.

As with any measurement system, an assessment of the accuracy is important to understand the capabilities and limitations of the approach. An experiment has been defined to determine the achievable accuracy of the approach by comparing image-based measurements with those made using conventional instrumentation known to be more accurate.

Objective 4. Investigate potential of measuring deformation in three spatial dimensions using multiple camera locations and digital photogrammetry.

Having successfully achieved two dimensional monitoring in objective 2, the technique is extended to include full 3D monitoring. How off-the-shelf photogrammetric algorithms could be used directly, or how the solution required a bespoke algorithm has been considered, and bespoke algorithms were written where required. An appropriate workflow has been designed also.

Objective 5. Assess the scalability of image-based monitoring techniques for real structures using a series of case studies.

To demonstrate the approach is practicable for monitoring of real-life civil engineering structures, a case study on a larger structure outside the laboratory was sought. This case study demonstrates the effectiveness of the approach at smaller scales and identified practical considerations concerning monitoring of real structures.

1.2 Contribution to Knowledge

The "contribution to knowledge" of this research is to demonstrate and assess a new approach for measurement of harmonic vibrations in civil engineering structures using long-exposure motion blurred images. The demonstrated approach is radically different to conventional photogrammetric techniques, producing data in a different format, emphasising the accurate measurement of the vibration envelope over absolute position-time history. The limited measurable frequencies is alleviated with the frequency invariant approach.

A workflow has been designed from image capture to generating results. A new image measurement algorithm was required to determine image coordinates and displacements, and for the additional steps for coordinate matching for 3D measurement. The vibration measurement technique is demonstrated by monitoring deformation using several case studies, providing information that is both cheaper and richer than is possible with conventional contact sensors.

1.3 Thesis Structure

This thesis follows the logical progression of the measurement approach's development, testing and assessment, and comprises the following five chapters:

Literature review This chapter contains a review of existing literature in the field. This reveals an opportunity to develop and assess the new approach for dynamic testing.

Methodology After initially discussing the instruments available to this research project, this chapter details the development of the working long-exposure motion blurred image

(LEMBI) measurement solution. A number of image measurement strategies are trialled, before deciding on the solution considered most effective. Algorithm development is detailed, and key algorithms are included in Appendix C. The accuracy of these measurements are discussed here as part of the algorithm development.

Case studies This chapter demonstrates the applicability and scalability of the created approach with three case studies: the laboratory shake table demonstration represents a large scale test in a controlled environment; a larger vertical timber section demonstrated increasing scale in 2D and 3D monitoring; and a full scale a suspension bridge demonstrates a full small-scale structure. The results of these case studies are presented.

Discussion The results from the previous chapter are evaluated, and considerations identified whilst carrying out monitoring of the case studies are discussed. These considerations are expanded to describe the limitations of long exposure images for structural monitoring, as well as advantages that exist over other methods. Comparisons with other measurement approaches are made, and the implication to wider structural testing discussed.

Conclusion The final chapter summarises the findings in this thesis, and assesses whether the initial aim and objectives of this research project have been fulfilled. Recommendations are made for potential future work, particularly focussing upon improvements to the measurement approach. A range of potential other applications of the method are identified also.

Chapter 2

Literature Review

The purpose of this literature review is to examine prior work conducted in the field of structural testing and assess how image processing techniques can be applied. Knowledge is pooled from structural testing of civil engineering structures, photogrammetry and image deblurring. Current techniques for structural testing are introduced and a distinction is made between static and dynamic test techniques. A range of monitoring sensors will be examined and advantages of image processing methods for full-field measurement highlighted. Deblurring techniques for measuring the apparent blur in images of moving objects are then introduced. The review then examines in greater detail the particular techniques and considerations of the approach and introduces some algorithms used in the processing of digital images.

2.1 Structural testing

Structural testing is used to evaluate the performance of structural members, both in-situ and in the laboratory environment. Structural testing may be carried out to test the relation between analytical models and their structural behaviour. For example, the development of new, more efficient building materials or those made from recycled materials requires experimental verification. Typically, loads are applied to test specimens of different sizes and their performance monitored as the load increases to a prescribed limit (or in the case of destructive tests, their ultimate capacity). New materials may respond differently, demanding more advanced monitoring systems to record complex

deformation patterns.

The integrity of existing structures may wish to be tested also. During construction, installed elements may be tested for proof of their performance. The structure may be overloaded above its intended working load and based on its performance, deemed safe for its intended use. The record of the test serves as evidence of the structural integrity. Knowledge of the performance of installed structural elements could be used to influence the design of other building elements (Moss and Matthews, 1995). A structure may also be tested if, for example, a change of use of a building is desired, to verify its integrity following a potentially damaging event, or to verify the quality of repair work.

2.1.1 Structural Health Monitoring

Structural health monitoring (SHM) is a growing area of research involving long-term monitoring projects for existing structures. The destructive test methods used in a laboratory are generally unsuitable for existing structures and non-destructive test techniques are used instead. Existing structures may be tested to detect damage occurring due to long-term material deterioration or a consequence of fatigue caused by cyclic loading. Routine testing is used to achieve an early indication of structural degradation so that improvements may be made in good time. Usually, permanent gauges are fitted and data is either continuously collected or is collected at regular intervals. The measured data are checked against calculated limits which, if exceeded, prompt further more-extensive examination (Brownjohn, 2011).

2.1.2 Static testing techniques

It is common to monitor the displacement of a beam element using a gauge fitted at the beam's mid-span, at the point of maximum deflection. Where additional measurements are required, possibly to assess the deformed shape of the beam, the number of gauges will be increased and often arranged at equal spacing or positioned under load locations. The real-time monitoring of displacement gives an indication of how the test is progressing, and a graph of displacement against increasing load shows how the test element performed.

Strain gauges may be used to monitor the localised deformations of materials. In the case of concrete, measuring crack widths and locations gives an indication of the performance of the paste-aggregate bond or, where they are used, additives designed to control crack formation (Benning *et al.*, 2004). When monitoring strains in concrete, strain gauges connected to a data-logger are frequently used to measure crack widths. Strain gauges provide limited information, being able to measure in the one location where they are fitted. Gauges could be concentrated in areas expected to fail, however, while the formation of cracks is predictable in general, it is difficult to predict the exact location where a crack will occur.

Static testing of real structures may be considered inconvenient if it is to be carried out on a regular basis (Moss and Matthews, 1995). Applying increasing load to a real structure may involve transporting numbers of heavy weights to site. For some applications, large tanks may be placed on a structure and have water pumped in or out to more easily control the amount of load. It is usually necessary to take a structure out of service for the test to take place.

2.1.3 Dynamic testing techniques

Dynamic testing usually involves a structure vibrating either naturally by wind or traffic loading, or artificially by exciters. The 'vibration response' of the structure is then recorded for analysis. In principle, dynamic testing can be extremely powerful as a monitoring tool, as a structure's natural frequencies measured at one point will be sensitive to changes in any part of the structure.

Practical testing of in-service structures with dynamic techniques is usually less invasive than testing using static techniques. Much lower loads are required and smaller deformations are experienced, so testing may be carried out while the structure is in service. Analysis of data collected during dynamic testing is, however, more complicated than using static techniques so specialised expertise is required. Interpreting data is complicated and it is particularly challending to locate and quantify damage (Brownjohn, 2011).

2.1.3.1 Natural frequencies

The vibration response of a structure, as measured in a discrete location, is the superposition of harmonic functions tuned to the structure's natural frequencies. Natural frequencies of a structure can be found by applying the discrete Fourier transform to the vibration response recorded in the time domain. The Fourier transform can establish the amount of energy associated with the harmonic vibrations superimposed in the vibration response. Natural frequencies are sensitive to mass and stiffness and a measured change in a natural frequency would usually indicate a change in stiffness, probably due to some structural change (Hassiotis and Jeong, 1993).

Modal shapes Natural frequencies alone can determine the existence of cracks or other forms of damage but not the location where they have occurred (Pandey *et al.*, 1991). More advanced algorithms utilise modal shapes derived from the vibration response measured at several locations on the structures. Modal shapes measured at different time intervals can be compared using the Modal Assurance Criterion (MAC) and Coordinate Modal Assurance Criterion (COMAC) coefficients, that will indicate a structural change if they vary from unity (Pandey *et al.*, 1991). The response modal shapes may be compared with finite element (FE) models of predicted situations to attempt to locate and quantify damage. However, the accuracy of a FE model is dependent on the fine selection of parameters, to which modal shapes are highly sensitive.

Since techniques utilising modal shapes require the vibration response of several sensors at different points on a structure, a higher number of sensors provides the most accurate results as larger interpolation is otherwise necessary (Carden and Fanning, 2004; Dilena and Morassi, 2011). FE models attempt to replicate structural changes in simulated locations to identify the damage, but note the accuracy considerations of using FE models suggested above. The more advanced 'modal curvature technique' introduced by Pandey *et al.* (1991) uses relative changes to identify and locate cracks in a structure rather than comparing to multiple FE models of possible situations. This method was improved on by Al-Ghalib *et al.* (2011) who proposed the 'curvature difference ratio'.

Fan and Qiao (2011) and Morassi *et al.* (2007) discuss determining natural frequencies from known details about a structure as a 'forward problem'. The usual aim of structural

health monitoring is the reverse of this: to learn about the structure from its natural frequencies. Fan and Qiao explain how the problem is 'ill-posed' and remark that cracks in different locations with different severity can yield similar data. This 'inverse' problem has a non-unique solution and for a solution to be found a certain amount of engineering judgement is required (Morassi and Tonon, 2008).

Comparative studies of damage detection score techniques on their ability to identify the presence of, the location of, and the extent of structural damage (Hassiotis and Jeong, 1993; Farrar and Jauregui, 1998; Abdel Wahab and Roeck, 1999; Alvandi and Cremona, 2006; Fan and Qiao, 2011). They usually report that, given different data sets, no one technique can be applied universally. The most successful demonstrations have been using simulated data from FE models rather than on real structures, where the level of environmental load noise is a significant challenge (Brownjohn, 2011). Environmental noise can change natural frequencies by between 5-10%, which inevitably hides frequency shifts of less than 5% (Carden and Fanning, 2004). Newer techniques attempt to filter out environmental effects and claim to allow detection of frequency shifts of 1% (De Roeck *et al.*, 2000), however, a prior lengthy study of environmental effects is required. Reoccurring reports are that lower modes are less susceptible to minor structural changes than higher modes but those higher modes in turn are more susceptible to identifying false positives. For large structural changes, location is not predicted as closely, though light damage is more difficult to detect at all (Hassiotis and Jeong, 1993).

2.1.3.2 Nyquist sampling theorem

Unlike in static testing, where the main sensor selection criteria is the measurement accuracy, dynamic testing also requires the sensors sampling rate (or sensing frequency) to be considered. Sensors designed for dynamic measurement, such as accelerometers, have relatively very high sampling rates (the most advanced instrumentation reaching in the order of megahertz; Polytech Ltd., 2014b) whereas the 'alternative' non-contact sensors that offer other advantages have lower sampling rates in the order of tens of hertz.

The Nyquist sampling theorem dictates the possible vibration frequencies that are detectable in relation to the sampling frequency of the sensor. It has applications within radio telecommunications and signal processing as well as monitoring of structural vibra-

tions. The Nyquist sampling criteria states that in order to detect frequencies of b Hz, the data must be sampled at a rate of at least $2b$ Hz (Lovse *et al.*, 1995; Morlier *et al.*, 2007). Roberts *et al.* (2004) found bridges in Switzerland had natural frequencies of up to 50 Hz, though most exhibited frequencies of less than 10 Hz for highway bridges and 20 Hz for rail bridges. Nickitopoulou *et al.* (2006) considered typical natural frequencies of existing major tower structures to be less than 0.5 Hz.

2.2 Sensors

When selecting sensors for monitoring schemes, the cost of the sensors is often a major factor. Contact sensors typically measure at a single point only. Optical non-contact sensors are more expensive but can monitor many points from a single instrument location. If a long-term structural health monitoring scheme is planned for a structure, contact sensors may be retrofitted after construction, though this will take time. Sensors may also be embedded or cast in situ to a structure during construction, but engineers should plan for some sensors to be possibly damaged.

Sensors may measure acceleration, velocity or displacement. Depending on how the data will be used, records can usually be transferred between these domains by integration and differentiation (though additional considerations when double integrating data from accelerometers are discussed in section 2.2.1.3).

In the following, sensors that are currently available for a monitoring scheme are introduced and their advantages when used for static and dynamic testing techniques are identified.

2.2.1 Contact gauges

2.2.1.1 Contact displacement gauges

Dial gauges are a simple and traditional mechanical device that measure displacements in one direction (see figure 2.1a). Dial gauges designed for structural testing are inexpensive, with typical accuracies of ± 0.01 mm (Lee and Shinozuka, 2006b; Ronnholm *et al.*, 2009). Electronic gauges linked to a digital data logging device are more widely used today (see

figure 2.1b). These electronic gauges are convenient because they allow measurements to be continuously recorded from all gauges, allowing displacement history to be analysed later.

The gauge body is fixed in position such that a central plunger is in contact with the structural element under investigation, and moves as the latter deflects. They can be fixed in any orientation, though are typically limited to only measuring displacements in one direction (Lee and Shinozuka, 2006b). They must be fastened to some stationary reference such as a platform which usually has to be close to the structure. Where the beam is highly elevated they can be located at ground level in contact with weights suspended from the beam under test (Bungey *et al.*, 2006). Gauges are available with a variety of displacement ranges and a typical gauge has a deflection range of about 50-100 mm. Although the gauge can be repositioned if deflections exceed its displacement range, this is generally undesirable.

Bungey *et al.* (2006) states that traditional dial gauges remain of value as they provide the engineer with a quick indication of the rate of deflection and are often used in combination with electronic displacement gauges. The engineer's appreciation of the rate of increase in deflection is important to assess how the test is progressing. For in situ testing, it is important to monitor for any indication of plastic deformations as the test progresses, which would require the test to be stopped and loads removed.

2.2.1.2 Foil strain gauge

Foil strain gauges are used to measure material strain, the dimensionless unit of deformation per unit length. The gauges are made of a thin layer of foil onto which coils of an electronic resister are fixed with adhesive (see figure 2.1c). The foil gauge is fixed to the test element which, as it deforms, stretches the foil changing its resistivity which is measured and from which strains can be derived. Strains up to 3% at a precision of 0.01% can typically be measured (Omega Engineering, 2011).

Foil strain gauges have a limited range and if exceeded, the gauge will almost certainly be destroyed. When used for long-term monitoring, strain gauges can be susceptible to changes in temperature, humidity and ageing (British Standards Institution, 1986). It is not normally possible to reuse foil strain gauges.

(a) Dial gauge

(b) LVDT

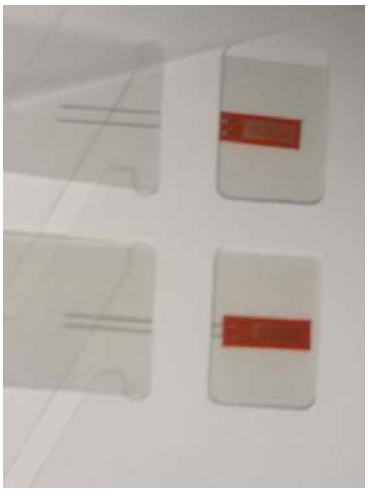

(c) Foil Strain Gauges

(d) Robotic Total Station

(e) Accelerometer

(f) Terrestrial Laser Scanner

(g) Laser Doppler Vibrometer

(h) Laser Tracker Systems (Leica Geosystems, 2015)

Figure 2.1: A selection of sensors used for monitoring structures

2.2.1.3 Accelerometers

Accelerometers are widely used for dynamic testing and less expensive than some of the more advanced instruments discussed later. They are small and relatively lightweight, so add negligible loading to a structure once fitted (see figure 2.1e). However, they measure at a single point only and require individual calibration, installation and associated cabling infrastructure. Battista *et al.* (2011) noted how problems with cabling infrastructure resulted in loss of power to the accelerometers, causing weeks of missing data.

Accelerometers produce an acceleration history at a point and can, in principal, be transferred to the velocity and displacement domains by integration and double integration, respectively. However, this is an indirect measure of displacement and susceptible to 'drift', called accelerometer bias or zero offset (Roberts *et al.*, 2004; Lee and Shinozuka, 2006b). The process is not completely automated as it requires filter selection, baseline correction and use of judgement where anomalies exist (Chang and Xiao, 2010; Yi *et al.*, 2010a).

The output of the accelerometer is simply two electrical contacts. A separate data logging system (usually comprising of a PC with specialised input hardware or signal amplifier) is required to record the actual acceleration signal. Each accelerometer is provided with a calibration certificate which relates the recorded accelerometer contact voltage to the actual acceleration. The specific data logging hardware in use is significant to the system's accuracy.

2.2.2 Non-contact sensors

The methods described above are simple and direct, however, whilst being widely used they require good access to the test element which is not always possible, for example, when testing bridge or ceiling beams. Non-contact sensors offer measurement where traditional sensors cannot. This may be because the measuring point itself is inaccessible, or a stable reference needed to measure displacements cannot be installed.

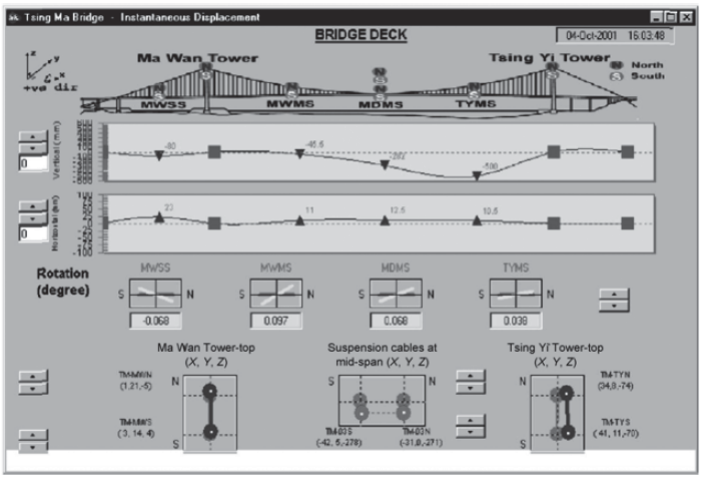

Figure 2.2: Screen display of instantaneous displacement of Tsing Ma Bridge (Yi *et al.*, 2010b).

2.2.2.1 GNSS

Global Navigation Satellite Systems (GNSS) make it possible to determine 3D coordinates of remote location using satellite signals. They are particularly useful in remote locations without a traditional surveying control framework. The space element of the American Department of Defence GPS system consists of 24 satellites, each continuously transmits the current time as well as its current position (Kijewski-Correa *et al.*, 2006). The 'errors' between signal arrival times can be used to calculate the receiver's position. For accurate monitoring applications, two receivers are used; a stationary base station receiver located at a known position off the structure, and a roving receiver at the measuring point.

GPS has been demonstrated for non-contact long-term monitoring of bridges (Nakamura, 2000; Roberts *et al.*, 2006; Yi *et al.*, 2010b) and demonstrated potential for monitoring displacements where a close stable reference is not available. Processing of GPS data can be highly automated, unlike accelerometers for which a certain amount of user input is required. This makes it particularly suitable for integration in to an automated structure monitoring system, as demonstrated by Yi *et al.* (2010b) (figure 2.2).

The GPS roving receiver does not require line of sight with the base station, though it is dependent on a clear sky view. Single obstructions could make GPS positioning impossible (Meng *et al.*, 2004). GPS derives absolute position estimates from which relative displacements are determined(Chang and Xiao, 2010). Errors do not normally accumulate and data does not suffer the 'drift' in displacement found in the double integration

of accelerometer data (section 2.2.1.3). This makes GPS suitable for measuring static displacements and 'quasi-static' behaviour such as wind-induced or thermal movements of a bridge (Lovse *et al.*, 1995; Nakamura, 2000; Nickitopoulou *et al.*, 2006).

An important consideration is the high cost of GPS systems, though the hardware is reliable. Attainable accuracies are theoretically 5–10 mm horizontal and 10–20 mm vertical, although accuracy varies as satellites come in and out of view (Lovse *et al.*, 1995; Nakamura, 2000; Meng *et al.*, 2004; Roberts *et al.*, 2004, 2006; Chan *et al.*, 2006; Kijewski-Correa *et al.*, 2006; Nickitopoulou *et al.*, 2006; Yi *et al.*, 2010a,b; Moschas and Stiros, 2011). It is suggested that using pseudolites—additional terrestrial transmitters that transmit GPS-like signals—can improve accuracy (Meng *et al.*, 2004).

There are many sources of error in the GPS system. Most of them are mitigated by locating the base receiver close to the roving receiver (Lovse *et al.*, 1995; Nickitopoulou *et al.*, 2006; Yi *et al.*, 2010b) but multipath remains the greatest source of error. Chokering ground-plate antennas are favourably used for their capability of minimising multipath but despite hardware improvements, accuracy can be variable. Multipath error remains greatest near reservoirs, metal piers and cables, and suspension bridges (Nickitopoulou *et al.*, 2006) which, unfortunately, are likely subjects for structural health monitoring.

GPS antennas have been combined with accelerometer to use the benefits of both sensors (Roberts *et al.*, 2004; Meng *et al.*, 2007; Moschas and Stiros, 2011). The absolute measure of displacement from the GPS sensor is used to correct for accelerometer bias, while the highly sensitive accelerometer detects vibration too small to be detected by GPS. The most recent systems also make use of more signals provided by the Russian GLONASS system, and once complete the European GALILEO system (provision of inital service in 2016, with completion due in 2020; European Commission, 2015).

2.2.2.2 Robotic Total Station

Total stations are well known measurement instruments capable of optically measuring over long distances to visible accuracies. A Robotic Total Station (RTS) system aids its operator in its usual operation by tracking the movements of a hand-held reflector (figure 2.1d). Three dimensional coordinates of the moving reflector can be measured from distances of up to 500 m with an accuracy of 3-5 mm. Only a single target can be

Figure 2.3: Robotic total station at Tamar Bridge (Battista *et al.*, 2011).

measured at a time with a few seconds needed to systematically orientate the telescope towards each target. Given the high cost of these instruments, consideration must be given to how they will be kept secure and protected from poor weather. Figure 2.3 shows how an instrument has been used as part of a monitoring system on the Tamar suspension bridge (Battista *et al.*, 2011).

Reviews of RTS for measuring dynamic vibration suggest some difficulties (Psimoulis and Stiros, 2008; Chang and Qunge, 2009). In the few tests conducted first modal frequencies are identified where they are less than 3-4 Hz and have amplitudes of at least 5 mm. However, remarks are made about the instruments ability to keep track of high amplitude vibrations (> 3 cm) and although sampling rates of 20 Hz are claimed by the manufacturer, only 6-7 Hz has been achieved in published tests (Psimoulis and Stiros, 2008). Chang and Qunge (2009) noted that the target moving during single measurements may cause distance and angular measurement to not correspond exactly, as well as inaccuracy in the distance measurement itself.

2.2.2.3 Terrestrial Laser Scanner

The Terrestrial Laser Scanner (TLS) combines reflectorless electronic distance measurement with precise positioning motorised mirrors (figure 2.1f). The TLS systematically scans a user-defined area and produces a massive number of three dimensional coordinates in a 'point cloud' (the latest TLS hardware can record 1 million points per second; Leica Geosystems, 2014). This instrument is not light dependent, no object targets, surface

texture, insitu sensors, or cabling infrastructure are required and inaccessible surfaces can be measured provided they are visible (Park *et al.*, 2007). Monitoring can be conducted from maximum distances of 350 m (Park *et al.*, 2007) to 6000 m (3D Laser Mapping, 2011) depending on the instrument selected.

Although the accuracy of a single observation is only about 5–10 mm, when a surface is fitted to a point cloud of a plane, higher accuracy can be achieved (Park *et al.*, 2007; González-Aguilera *et al.*, 2008). González-Aguilera *et al.* (2008) notes a shortfall of using the TLS is that although deformation can be found by comparing surfaces fitted to the data, actual measurement points cannot be repeated exactly. However, a more recent product by 3D Laser Mapping (3D Laser Mapping, 2011) which combines a laser scanner with DSLR camera together with specialist software (figure 2.4) is designed for monitoring slopes and rock walls from a permanent vantage point and claims repeatability of the point grid as a key advantage. Problems may also occur measuring smooth shiny or dark surfaces that do not reflect light diffusely. Data is processed automatically and detection of a displacement activates an alarm.

When used to monitor displacements in static testing, measurement has been noted to have taken a 'surprisingly' long time (Ronnholm *et al.*, 2009), and would normally be impractical for deformation monitoring. Although the instruments are capable of higher speeds with lower accuracy, the time to measure a structure is currently too slow to be used for monitoring structural dynamics in their typical configuration (Ronnholm *et al.*, 2009). Recent developments have, however, shown dynamic response information to be acquired from wind turbine blade segments by utilising the scanner's rapid distance measurement (Grosse-Schwiep *et al.*, 2014).

2.2.2.4 Laser Tracker Systems

Similarities exist between laser tracker systems (LTS) and total stations, in that both comprise optical targeting and distance measuring systems upon two angle encoders. LTS emphasises high positional measurement accuracy over measurement range. Measurement accuracy is of the order of tens of microns, but this accuracy is only achieved with a reasonably short target distance (2—3 m). Maximum measurement range is in the order of 160 m when used in combination with the largest reflectors (Hexagon Metrology, 2014).

Figure 2.4: 3D Laser Mapping VZ-400 Terrestrial Laser Scanner (3D Laser Mapping, 2011)

Like other optical measurement approaches, line-of-sight is necessary, and temporary obstructions or poor weather will cause temporary loss of data. The use of a reflector is necessary, and the device only monitors one reflector at a time. However, the very high measurement accuracy could allow detection of higher modal shapes than other less sensitive non-contact sensors. Unlike the LDV, the LTS also measures in three dimensions, allowing detection of vibrations multiple directions.

2.2.2.5 Laser Doppler Vibrometer

The laser Doppler vibrometer (LDV) is commonly used in the vibration community for dynamic testing (figure 2.1g) (Helfrick *et al.*, 2011). A laser light source is directed at any point on the surface of a test object. Vibration of the surface will cause the reflected light to undergo a shift in frequency (a Doppler shift), that will correlate to the surface velocity (Nassif *et al.*, 2005). An interferometric technique is used to compare the reflected wavelength with the original emitted laser wavelength to find velocity and the measured velocity can be integrated or differentiated to find displacement or acceleration, respectively. Lovse *et al.* (1995) stated that LDVs are typically capable of measuring at 2 kHz and 1 µm. The sampling rate of current hardware is 100 kHz, measuring to the order of nanometres (Sunny Instruments Singapore, 2009; Metrolaser Inc., 2011; Direct Industry, 2011). To measure multiple points the instrument must be set up repeatedly unless one of the more advanced instruments introduced below is used.

Scanning LDV The improved scanning LDV (SLDV) is an LDV with motorised direction control that moves systematically between pre-programmed points. Measurement is only made at one point at a time and the instrument takes time to traverse a whole structure. For long duration measurements of multiple points, vibration must remain constant (Lovse *et al.*, 1995). Fast Scan SLDV (FS-SLDV) speeds up monitoring by optimising the pause time at each point depending on the number of response cycles needed to obtain a good measurement.

Continuous Scanning LDV The continuous scanning LDV (CS-LDV) is a more advanced machine that sweeps the measuring beam over the area of interest whilst simultaneously taking measurements (Stanbridge *et al.*, 2004; Helfrick *et al.*, 2011). These machines allow full-field measurement of a surface with high accuracy and at a high sampling frequency. The current CS-LDV hardware is confined to laboratory experiments and Lee and Shinozuka (2006a) warn that the high laser intensity that would be required to measure over the typical distances used in monitoring of real civil engineering structures could be dangerous to the human eye.

2.2.2.6 Interferometry techniques

Interferometry uses interference patterns, often of either the visible or microwave part of the spectrum, to measure relative movements of objects. Digital Speckle-Pattern Interferometry (DSPI) techniques make use of optical laser systems containing CCD arrays to carry out measurement using interferometry. Figure 2.5 shows the arrangement of optical components in a measuring system.

An object displacement would result in a phase-shift in the back-scattered electromagnetic waves (Stanbridge *et al.*, 2004). The reflected light is superimposed with the source light. Depending on the phase of the two light waves, they will either reinforce each other, or cancel out (Hariharan, 2006). Interference fringes are produced and changes in the fringe pattern may be perceived as an out-of-plane displacement of the surface (Schmidt *et al.*, 2003). Because interferometry is a full-field measurement technique, rather than only measuring in discrete locations on an object, it allows visualisation of strain gradients and identification of 'hot spots' (Schmidt *et al.*, 2003).

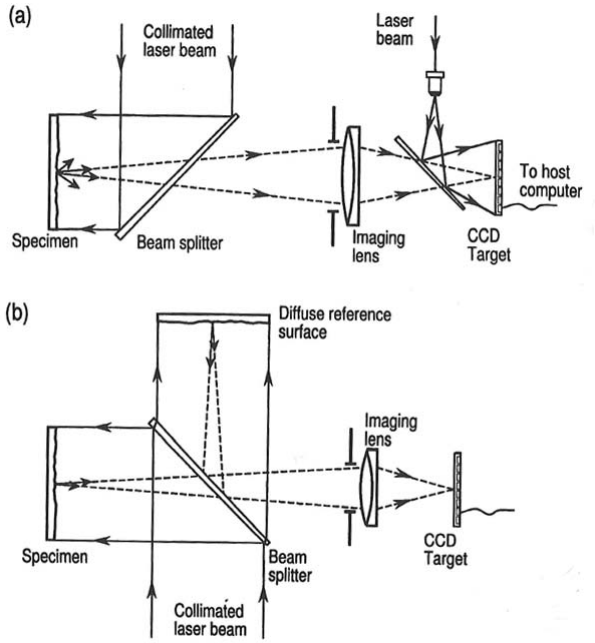

Figure 2.5: Two commonly used ESPI arrangements which are sensitive to out-of-plane displacements (Rastogi, 2001).

Gentile (2009) demonstrates the use of microwave interferometry for remote monitoring of reflectors fitted to suspension bridge stay cables. The technique has high measurement accuracy with a high sampling frequency, potentially allowing many natural frequencies to be measured. The recorded data is only one dimensional, so although simultaneous monitoring of more than one target is possible, each target's response is only distinguishable if they are separated in range.

Moiré photography is a similar technique whereby fringes are produced by two superimposed patterns. A specific pattern must be applied to the test subject prior to tests, which normally limits this type of monitoring to laboratory tests. To produce the interference fringes, either one pattern recorded in an initial image is superimposed with images for each later epoch, or the pattern is created in the camera itself (Kearney and Forno, 1989). Tests by Forno (1988) demonstrated how the techniques could be applied to full-scale structures, but covering a whole structure with a pattern presented practical difficulties and was considered less convenient than individual targets.

2.2.2.7 Photogrammetry and Image Processing

Moss and Matthews (1995) introduce photogrammetry's traditional use for aerial surveys

and note its ability to measure 3D coordinates. Relief can be detected by small apparent differences in images of the same area taken from different positions. A classical configuration is for 'stereopairs' to be acquired and measured, traditionally in a stereoplotter, or today using computer software.

Terrestrial photogrammetry allows measurements of civil engineering structures to be made by a camera located off the structure and no stable reference is needed. The technique is scalable: that is, the same technique is applied to large-scale laboratory experiments as well as to full-scale real structures. Photogrammetry has been frequently judged suitable for monitoring structural tests by measuring a structure before loads are applied and then comparing to subsequent measurement 'epochs' to find deformations (Scott, 1978; Cooper and Robson, 1990; Moss and Matthews, 1995; Robins *et al.*, 2001; Whiteman *et al.*, 2002; Albert *et al.*, 2002; Yoneyama *et al.*, 2005; Ronnholm *et al.*, 2009; Leitch, 2010).

Scott (1978) demonstrated how photogrammetry would allow a very high number of measurement points to be recorded within a relatively short time. Digital image processing nowadays allows these images to be processed within seconds. The high number of targets makes possible recording of complex deformations that would otherwise require a high number of ordinary sensors or other more expensive equipment. Cooper and Robson (1990) did not consider this a truly non-contact technique for the need of having to apply targets, however, it does offer the similar benefit of not requiring a stable reference immediately adjacent.

As well as observing target positions, the photos of the structure themselves are of archival value (Baldwin, 2011). They may be used later to extract additional data which, at the time of acquisition had not been considered important. This attribute makes photogrammetry particularly suitable when it is uncertain exactly what data is required (Luhmann *et al.*, 2006).

The hardware required for photogrammetry is less expensive than that used by GPS monitoring systems or laser doppler vibrometer (Helfrick *et al.*, 2011), though Moss and Matthews (1995) remarks that a high level of expertise is required and specialist equipment is preferred. Although acquisition time is relatively fast, a main disadvantage is the time delay for processing images. Traditional sensors provide a desirable real-time

reading. For image processing, an advanced system would be required for real-time monitoring. Without such a system, results will not be available until the data is processed, often after leaving the site.

While the most accurate measurement work still requires targets to be fixed to structures, digital image correlation (DIC) makes possible measurement of structures without targets fitted, provided their surface has sufficient texture (section 2.3.4). Not needing to place physical targets reduces the preparation and on-site time of monitoring and allows very densely distributed measuring points that would be impractical if individually targeted (Schmidt *et al.*, 2003; Yoneyama *et al.*, 2005; Warren *et al.*, 2011).

This section has considered the range of available sensors for monitoring vibrations in structures, including those that make direct contact with the test structure and those non-contact sensors which monitor remotely. Differences were identified not only in the measurement accuracy attainable for each sensor, but also in the measurement sampling frequency, and the domain in which measurements are made. Table 2.1 summarises the properties of the sensors identified in this section. In most cases, because sensors are available in different configurations for specific tasks, the listed properties are an example of the typical properties of a sensing system that could be employed for monitoring of civil engineering structures.

2.3 Image Processing in Structural testing

A particular advantage of an image processing approach when used for structural testing is that it is non-contact. This means that a stable reference immediately adjacent to test subjects is not required. This was demonstrated in several of the tests cited above where fitting displacement gauges would be difficult, or would otherwise require the use of scaffolding to create a stable base. This section describes the ways that image processing and photogrammetry have been combined and applied specifically for structural testing.

Photogrammetry offers three dimensional measurement where most other sensors measure in one dimension (Cooper and Robson, 1990; Moss and Matthews, 1995). Capturing photographs is a relatively fast and simple, and a very large number of measurements are possible within a single image, limited only by the resolution of the image and, if used,

Sensor	Measurement Quantity	Maximum Measurement Accuracy (mm)	Maximum Sampling Frequency (Hz)	Maximum Sensing Range	Measurement Domain
Contact displacement gauges	Individual	100 µm	50 Hz–20 kHz	⋆	Distance
Strain gauges	Individual	0.1 µe	50 kHz	⋆	Strain
Accelerometers	Individual	0.001 g	10 kHz	⋆	Acceleration
GNSS	Individual	50 mm	10 Hz	†	3D position
Robotic Total Station	Sequential	5 mm	5–10 Hz	500 m	3D position
Terrestrial Laser Scanner	Many	5 mm	50 kHz	300 m	3D position
(Scanning) Laser Doppler Vibrometer	Individual (Many)	5 µm/s	20 kHz	30 m	Velocity
Interferometry	Many	0.5 mm	10 Hz	30 m	Distance
Photogrammetry	Many	0.5 mm	10 Hz	30 m	2D/3D position

⋆ Contact gauges must be in contact with the measurement location, but range to data logging hardward is limited by power and data transfer infrastructure.
† GNSS systems do not have a limiting sensing range, but for accurate work a base station is usually located within 100 m.

Table 2.1: Summary of identified sensor properties. Listed properties are examples of those of likely sensors used for monitoring civil engineering structures.

size of targets (Scott, 1978). This makes possible monitoring of complex deformations without a very high number of traditional contact sensors.

Many demonstrations of the approach use the traditional approach of artificial targets (see section 2.4.2.1). Other newer approaches make use of DIC. The latter method is possible where the structure has sufficient texture, and fixing of targets is not necessary. Image processing considerations of DIC are discussed further in section 2.3.4.

2.3.1 Displacement measurement

Target displacements can be found by calculating the difference between coordinates of the same measuring point at different moments in time, and then scaled to an actual measure of displacement.

Case studies have shown photogrammetric monitoring of example structures such as beams, trusses, bridges and geotechnical samples. Typical tests have examined the static response by monitoring the deflection of photogrammetric targets as increasing load is applied to the sample. Demonstrations also give laboratory-scale examples of monitoring complex deformation in beam load tests as well as measuring the width of small scale hairline cracks in concrete (Albert *et al.*, 2002; Ronnholm *et al.*, 2009; Uhl *et al.*, 2011; Yilmazturk and Kulur, 2012; Valença *et al.*, 2012; Tasci, 2013; Adhikari *et al.*, 2013). Maas and Hampel (2006) give examples of large scale monitoring of complex structures such as buildings, bridges and reservoir dams. Most of these case studies have utilised photogrammetric concepts used elsewhere and have demonstrated the strengths of the approach, as well as documenting some of the operational difficulties that were encountered. Some have also demonstrated successful 3D monitoring. Some case studies appear less well founded on photogrammetric theory, but nevertheless show successful monitoring at a decreased accuracy.

2.3.1.1 Omitting lens distortion for localised deformation monitoring

A lens model is normally required for accurate photogrammetric work in order to correct for distortions created by the lens. This correction may be optional under the correct conditions when only localised relative object deformations are required, rather than

absolute position accuracy. For any given target, lens distortion will almost certainly be present, but a small change in coordinate (as is usually the case for structural engineering testing) is affected by almost the same distortion effect, as the ray path will pass though the same part of the lens. For small localised deformations the lens distortion effect can be safely ignored as the error will effectively cancel out.

This assumption may not hold true during 3D monitoring even though deformation may as small. Lacking the necessary lens model may affect the target's determined coordinates which would subsequently effect how image-space coordinates are transformed into object-space coordinates. If this were to be attempted, the theory would have to be tested.

2.3.2 Strain measurement and automatic crack detection

By comparing the measured displacements, of neighbouring targets, it is possible to find strain, the unitless measure of a material's extension divided by the undeformed distance between the measuring points. This has been demonstrated by Robins *et al.* (2001); Benning *et al.* (2003, 2004); Lange and Benning (2006); Hampel and Maas (2009) and Valença *et al.* (2012). The high number of possible monitoring points allows one sensor to monitor the whole field of strains, and measurement of larger strains than traditional gauges allow. Where targets are applied to a structure, a fixed gauge length between pairs of marks or targets is used. Knowledge of achievable accuracies is then even more important. Whilst displacements are typically in the order of millimetres, the relative displacement of points in close vicinity is often much smaller, approaching the accuracy limits of the measurement system.

In concrete testing, samples marked with a regular grid of circular targets was developed by Benning *et al.* (2004) for tracing the line of individual cracks automatically. The crack numbers, start locations and directions of propagation were measured to give an indication of structural performance and allow an estimation of the concrete-reinforcement interface quality to be made (Benning *et al.*, 2004). Hampel and Maas (2009) noted that for this approach, although crack width is measured precisely, the position of the crack cannot be located exactly. Only the two targets between which the crack occurs are

indicated and where multiple cracks occur between two targets, the technique will only measure the accumulated crack widths. Other shortfalls of a targeted approach, such as preparation time were noted also (Benning *et al.*, 2003). Jahanshahi and Masri (2013) propose an approach using image thresholding to identify and trace the path of cracks before then using correlation on image patches either side of the crack to measure crack widths. The approach is demonstrated on images of simulated cracks of known width.

The density and spacing of measurement points is, therefore, crucial. This use of digital image correlation (section 2.3.4) is of relevance here, since a good speckle pattern is suitable for many densely distributed measuring points, approaching 'full-field' deformation monitoring (Hampel and Maas, 2009; Jerabek *et al.*, 2010; Orr *et al.*, 2012).

2.3.3 Considerations

The scalability of image processing means measurements of large structures are possible to sub-millimetre accuracy, while the accuracy of measuring small scale laboratory tests is in the order of microns. Before prescribing photogrammetry as a monitoring method the achievable accuracy in a particular experiment must be understood. The accuracy of a system is dependent on a range of factors, including: camera focal length, object distance, sensor resolution and target size as well as the specific algorithms using in processing.

3D measurements are possible using the photogrammetric techniques discussed in section 2.4.4.1 and multiple cameras. If it is known a priori that only planar deformations are expected, only a single camera is necessary. Although photogrammetry is frequently used to create three dimensional models from multiple images, Cooper (1984) emphasises the use of a single camera in obtaining higher-accuracy measurements in close-range applications. However, in this arrangement, any out-of-plane displacements will result in a scaling error (Jerabek *et al.*, 2010). Requiring only one camera obviously reduces cost, but also by not requiring the additional hardware for camera shutter synchronisation. Minimal time to process the images also improves increasing the feasibility of real-time monitoring.

The attainable accuracies in image processing are potentially higher than other non-contact measurement techniques and given occasions on which image processing is used

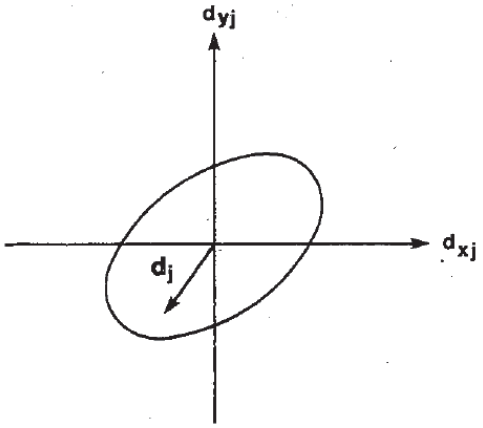

Figure 2.6: The 95% confidence point displacement ellipse and an (insignificant) displacement vector $\mathbf{d}_j$ (Cooper, 1987).

and the nature of the data, there is often not a 'check' available to confirm the image processing measurements. Images captured of the same object that has not moved will not always give an identical measurement due to random errors. An analysis of the repeatability of target coordinates has been suggested as a method of assessing random errors (Shortis *et al.*, 2001; Jurjo *et al.*, 2010). However, this type of assessment will not be directly assessing accuracy as Luhmann *et al.* (2006) warns that to determine true accuracy, errors can only be calculated by comparing these measurements with those established by a more accurate method.

An understanding of the accuracy and precision of a monitoring system is important to differentiate between these random errors and actual object deformations. Cooper (1987) explains that before displacements can be confidently claimed, a statistical analysis of the accuracy of the monitoring system must be carried out. The size of random errors are best described by an error ellipse, which normally represents a 95% confidence interval, and if a deformation pierces the edge of the ellipse, a significant deformation can be claimed with 95% confidence (figure 2.6).

2.3.4 Digital Image Correlation

Measurement in images is not limited to discretely marked targets. Where objects in images have sufficient texture, points can be tracked using feature-based matching, a technique that has become commonly referred to as Digital Image Correlation (DIC). The

image processing considerations are discussed later in section 2.4.2.6. Yoneyama *et al.* (2005) compared the technique when using a speckle pattern and the unpainted concrete face of the beam and found measurement of displacements, to the order of millimetres, effective in both cases. Using DIC to measure unprepared surfaces and without fixing targets may significantly reduce the on-site preparation time and effort.

The DIC technique has been used for dynamic monitoring of structures. Morlier *et al.* (2007) used DIC to monitor a pedestrian footbridge and was able to estimate first and second mode shapes despite a very low sensor resolution. Three natural frequencies were found in another small lab test by Helfrick *et al.* (2011). As with other non-contact techniques, data can be produced for a whole visible surface, which can be of more use than a few discrete points.

DIC was used by an National Physical Laboratory team (Baldwin, 2011) to make initial assessments of damage to the Hastings Pier caused by a fire in 2010. Rather than using a single high resolution camera, many pictures were captured and collaged together to create a single 1.4 gigapixel image. The identified application of this technique was a quick and cheap way to identify areas of the structure that needed further investigation. Apparent changes was found in the one part of the substructure noted to have been where the fire was at its fiercest.

A disadvantage is the considerable computer processing required (Tao and Xia, 2005; Helfrick *et al.*, 2011). The limits of accuracy are also more complicated than a targeted technique, since it is dependent on the quality of the localised texture. Initial subsets can be selected based on texture quality to improve the accuracy of individual points, but this could result in an uneven distribution of monitoring points (Jerabek *et al.*, 2010). Alternatively, later analysis may be simplified by specifying a regular grid of initial subsets, so that every measurement point is regularly spaced, although the likelihood of an incorrect measurement from a poorly-textured subset is increased.

A comparative study of sensors for remote monitoring of structures has been made by Lee *et al.* (2006); Helfrick *et al.* (2011). Helfrick *et al.* (2011) commented that DIC could be a practical approach for vibration monitoring, but that the frequency response may not be high enough for some applications. It was also noted that the technique is better suited to single frequency excitation. The techniques and computing processes involved

are discussed further in section 2.4.1.3.

2.3.5 Dynamic Monitoring

As introduced in section 2.1.3, there is a current trend towards dynamic measurement techniques. Many practical tests have been conducted and monitored using cameras, both in the laboratory environment and of existing structures. Many tests used consumer camcorders, while others used the more specialised machine-vision sensors. There are several tests using only a single sensor to measure plane deformations. These appear to be satisfactory when data is processed using the Fourier transform to find natural frequencies (Lee *et al.*, 2006; Chang, 2007; Choi *et al.*, 2011). More recent publications use multiple cameras and photogrammetric techniques for 3D measurement (Kalpoe *et al.*, 2011).

The principle of comparing images taken at different 'epochs' remains the same, but the time between epochs is reduced by increasing the rate of image acquisition to many image frames per second. Dynamic monitoring using image processing is limited by a compromise between sensor resolution and the number of frames per second that can be recorded (illustrated in figure 2.7). The choice of sensor is the most important decision of all system parameters (Castellini and Tomasini, 2004), as the number of frames per second will limit the frequency of vibrations that can be detected (section 2.1.3.2) and a sensor resolution too low will fail to detect low amplitude vibration. Very high resolution sensors can measure many targets over a whole structure, but often record at below 10 Hz. Other sensors can record at up to 1 MHz but small images sizes mean they can only measure single, or a very limited number of targets within close proximity of each other (Albert *et al.*, 2002). Current hardware is capable of capturing 4 MP images at 500 Hz (Intergrated Design Tools, 2015), which for a 1 m tall sample structure lab test could allow measurement to 0.05 mm (at 0.1 px accuracy), but a change in object scale also influences accuracy (to about 2.5 mm for a 50 m span bridge). Olaszek (1999) considered that, for most civil engineering structures, the first natural frequency does not exceed 5 Hz, therefore considered a 25 Hz video rate to be sufficient. This would, however, limit the higher natural frequencies that could be detected which, as discussed in section

Figure 2.7: Sensor selection requires a compromise between image and temporal resolutions

2.1.3.1, are more sensitive to structural changes.

Olaszek (1999) discusses how a low sampling frequency, although higher than the Nyquist frequency, can create errors when linearly interpolating between momentary measurements. A continuous and smooth character of bridge dynamic effects was assumed and spline interpolation used to fit a continuous curve that passes through all measured points (figure 2.8). Olaszek considered that using spline interpolation is this way could reduce the dynamic error by a factor of approximately 10.

In most tests using video camcorders, which typically have a maximum resolution of 1280×720 pixels, telephoto lenses which 'zoom-in' to the single point can be used to obtain the necessary accuracy. However, the advantage of an image capturing many monitoring points is then lost as just one relatively small area on the structure fills the whole frame. This also prevents including control points in the image, used elsewhere to provide a correction for any small camera movements or vibration, or defining an external coordinate system. Tests have been successful demonstrated without control points, but it is acknowledged that an ignored error could have occurred (Olaszek, 1999; Wahbeh *et al.*, 2003; Lee and Shinozuka, 2006b; Lee *et al.*, 2006; Chang, 2007; Chang and

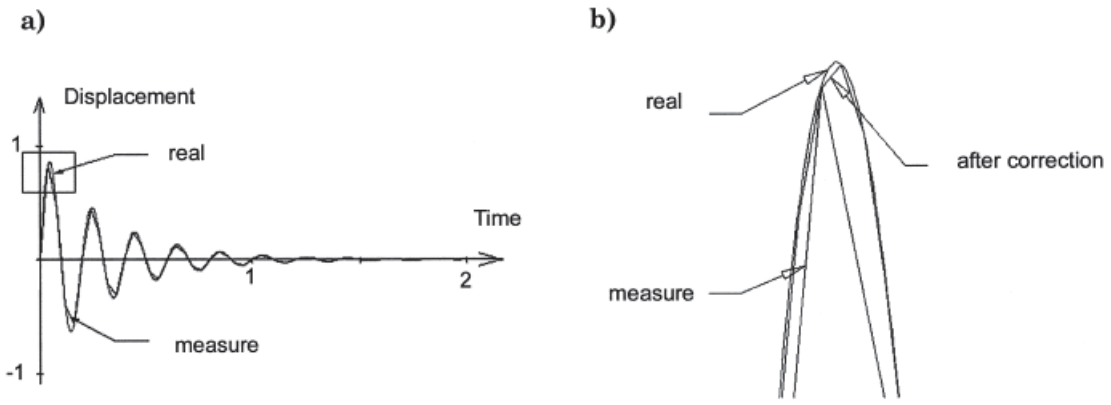

Figure 2.8: Reducing dynamic error: (a) the damped sinusoidal transient graph and its sampling part, (b) close up of area marked in (a) (Olaszek, 1999).

Xiao, 2010; Park *et al.*, 2010; Choi *et al.*, 2011) and that the error is probably significant (Olaszek, 1999). Olaszek (1999) considers control points necessary and that the accuracy of the system is highly dependent on their arrangement.

2.4 Image Processing Techniques

If image-based monitoring is available or prescribed as part of a structural monitoring system, preparation is necessary to determine exactly how monitoring will be carried out. The usability, accuracy and success of the system is dependent on the type of sensor and how they and the targets are used, as well as the particular algorithms used for processing. This section discusses the techniques and considerations of processing images digitally are presented.

2.4.1 Hardware selection

2.4.1.1 Cameras

Although some improvements in sub-pixel measurement of images are possible using more advanced processing algorithms, the choice of image sensor will have a significant influence on accuracy. For 3D measurement a system for accurately synchronising the shutters of the multiple cameras must be used. For real-time monitoring a system to transfer data from the camera to the computer, process and analyse it in real-time is necessary also.

Metric cameras, traditionally used for aerial surveys, were manufactured to low tolerances to minimise distortions and were specifically designed for photogrammetric work. These cameras were embedded with fiducial marks, marks which are projected on to the image border that would identify the principal point in the image and assist the photogrammetrist in taking measurements by using the marks as an origin (Wolf and Dewitt, 2000). Semi-metric cameras were not built to the same stringent specifications as metric cameras but contained a reseau grid to detect and correct for film deformations. These semi-metric cameras traditionally used in close-range photogrammetry have been made obsolete by digital photography (Luhmann *et al.*, 2006). Film deformation errors are eliminated, and because the sensor has rigid and well-defined edges, a Cartesian coordinate system is usually chosen with its origin in the upper left corner of the image instead of the centre (Wolf and Dewitt, 2000).

Consumer-grade cameras provide significant cost savings and have demonstrated their potential for photogrammetric work (Ogleby *et al.*, 1999; Wackrow and Chandler, 2007). Thomas and Cantré (2009) also consider that consumer-grade cameras can be used and can give accuracies suitable for deformation measurement when used with the right software. Basic compact cameras have been used for photogrammetric purposes where there are sufficient known points in an image to carry out self-calibration (Chandler *et al.*, 2005). However, this method is supported by a large number of automatically selected tie-points, something that cannot be relied upon when the subject in the image is moving as would be expected in a structural test.

2.4.1.2 Lens Calibration

Lenses not designed for photogrammetric work may not be manufactured to the accuracy necessary to avoid distortions. However, while distortions are often worse in cheap low-quality lenses, they are normally predictable and can be modelled (Luhmann *et al.*, 2006).

Radial distortion can typically reach greater than 100 µm at image edges (Luhmann *et al.*, 2006), but can be corrected using a polynomial function. Tangential distortion is much smaller than radial distortion and needs to be corrected for more accurate photogrammetric work. Another distortion found in digital cameras is affinity or shear distortion, occurring where pixels in the form of a parallelogram rather than square. The

parameters needed to calculate corrections for these systematic errors are normally established by camera calibration, after which accuracies of at least 1:5000 can normally be achieved (Cronk and Fraser, 2006).

Calibration would traditionally be carried out by photographing a regular grid pattern, but self-calibration techniques now allow this to be completed by taking multiple photographs of the same object (Luhmann *et al.*, 2006). Calibration would normally need to be carried out after any change in the lens system (focal length or focus) (Shortis *et al.*, 2001). Fixed focal length lenses are often used for terrestrial photogrammetry work for this reason. Software tools are now freely available to automate the calibration process, such as the Matlab Calibration Toolbox (Bouguet, 2010).

Whilst correction for lens distortions are necessary to determine accurate absolute positions, a simplified solution where lens correction is omitted may be used for localised deformation monitoring under the right circumstances (section 2.3.1).

2.4.1.3 Computer processing time

High image resolution and number of frames per second can create a very large quantity of data. It is also highly desirable for a sensor to monitor a structural test in real-time, to keep the engineer informed of how the test is progressing. Real-time monitoring using imagery is limited by the time delay in processing of images before quantitative results can be generated (Scott, 1978; Cooper and Robson, 1990; Lee and Shinozuka, 2006b; Lee *et al.*, 2006; Choi *et al.*, 2011). Current digital systems allow processing within seconds. Though computer processing hardware improves rapidly towards real time measurement, demands continuously become higher as researchers use sensors with higher resolution and desire better measurement accuracy (Lee *et al.*, 2006). It is currently possible to monitor tests in real time but only at a reduced image resolution with an associated loss in accuracy.

2.4.2 Image registration methods

A challenge in image processing is the development of algorithms to understand and interpret real objects in images. The problems encountered in 'computer vision' or 'vision

metrology' and the difficulties in object identification compared to humans are discussed by Mikhail (2001). Usually in photogrammetric work, algorithms intend to distinguish, identify and measure artificial targets from the background. However, it is likely that any kind of object or shape can appear in an image in practical situations, unless very carefully framed, and a computer algorithm can easily identify false positives.

Semi-automated approaches identify regions in an image matching set parameters, with input from a human operator. It is necessary for an operator to confirm that the automatically identified points are correct or modify the selection by adding or removing points. Alternatively, the operator could manually tell the computer to focus in the location of each point and then allow the computer algorithm to carry out the final identification.

2.4.2.1 Artificial Targeting

Adding artificial targets to objects in images is advantageous because they provide identifiable points, accuracy improvements and potential for fully automatic point identification (Luhmann *et al.*, 2006). From a detection point of view, El-Hakim (1996) prescribes requirements for targets, to improve object detection later in the process. Targets should be:

- well defined, so that there is a high probability of being identified;
- consistent in and compatible with all expected viewing angles;
- rare enough, so as to be recognisable against other shapes in an image (El-Hakim, 1996).

Plane circular targets are frequently used because of their symmetry, for being rotation and scale invariant (Luhmann *et al.*, 2006) and for ease of finding their centroid mathematically (section 2.4.2.5). Their size is chosen based on image scale and a diameter of at least 10 pixels is normally chosen (Shortis *et al.*, 1995; Robins *et al.*, 2001; Mikhail, 2001; Shortis *et al.*, 2003). In general, larger targets should improve accuracy but there is little improvement when targets are so large that the centre of the target is represented as a large cluster of constant intensity pixels (Shortis *et al.*, 1994).

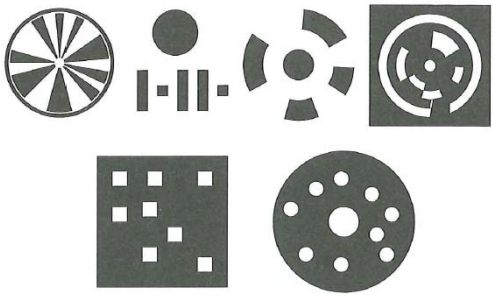

Figure 2.9: A selection of coded targets (Luhmann *et al.*, 2006)

2.4.2.2 Coded targets

The mathematical transformations that establish the camera's exterior orientation in a known object coordinate system (section 2.4.3) require control points within the image to be matched to coordinates in the object space. After target coordinates are identified from images they must be matched to their object space coordinates, either manually by the operator or preferably automatically by the computer algorithm. Coded targets are normally used for this purpose (Fraser, 1997).

The actual coordinate is identified by an ordinary circular target in the centre of the target pattern. The target is then normally identified by either, one or more broken concentric circles around the central point, or an arrangement of other standard targets in the vicinity of the target, examples of which are shown in figure 2.9 (Fraser, 1997; Luhmann *et al.*, 2006; Li and Liu, 2010).

2.4.2.3 Target material

The material used to create targets should be the most suitable for their application with consideration to orientation of cameras, lighting, target durability and method of fixing to the object. Compared to traditional instrumentation, adhesive targets are very durable, as they are normally only subject to surface dirt which can be wiped clean. Sufficient contrast can often be achieved using paper targets providing they are a sensibly chosen colour contrasting with the background, and the target is appropriately lit.

Retroreflective targets are frequently used for their exceptional visibility, although they are more expensive. These targets are made from reflective sheeting that is either covered with a black mask to provide the desired pattern, or cut out of the sheet material

(Luhmann *et al.*, 2006). Ring-flashes are often used around the lens to provide even illumination to the targets. Retro-reflective targets in combination with high intensity flashes can produce quasi-binary images whereby mostly only the desired targets are recorded before any image processing is carried out (Qiqiang and Xin, 2009). Cooper and Robson (1990) reported that using retro-reflective targets in combination with a ring flash was particularly effective in producing high-contrast images when photographing a bridge from distances of 5–10 m, but also noted the importance of dry targets to get effective reflections. Fitting retro-reflective targets should be limited to when it is known that they will be effectively lit, as Ronnholm *et al.* (2009) found that using these targets without a circular flash resulted in poor contrast.

Wahbeh *et al.* (2003) used an arrangement of LEDs on a black backing to create a high visibility target. This 'active' target was demonstrated on a full-scale structure that was monitored from a distance of over 200 m. For their short demonstration the target was battery powered, but for long-term monitoring a power supply would be needed.

2.4.2.4 Image segmentation

El-Hakim (1996) explains and compares methods of segmentation, whereby targets are separated from the background. The simplest and most commonly used algorithm is 'thresholding', whereby grey values above a certain threshold are identified as target objects. Where targets have grey values distinctly different to the background, a single threshold value can be used which can be set manually or, for better automation, by statistical considerations (Mikhail, 2001). A more advanced technique is to use local thresholds in different areas of the image. In order to improve identification, the image can be enhanced by methods including contrast and edge enhancement.

Edge detection algorithms identify distinct changes in pixel intensity in an image. A square 'window' traverses the image and where a high gradient of grey values is found within the window, that pixel in the image is marked as a potential edge pixel. There are different algorithms that can be used to identify these edges; the simpler algorithms are more susceptible to image noise, whilst the more complex algorithms often give better results, although no one algorithm can be applied universally.

Region extraction methods divide the image into discrete areas and identify properties

such as shape, centroid and brightness. Neighbouring pixels with similar grey values are matched to each other to form regions. Region extraction algorithms can be highly complex, even allowing targets that are very poorly defined in unoptimised images to be identified. Targets are usually well-defined and a thresholding algorithm followed by a simple region extraction algorithm is normally sufficient. Because every application is different, parameters will still often need to be set on a trial-and-error basis (El-Hakim, 1996; Srinivasan and Shobha, 2008).

Once potential regions have been identified, targets can be distinguished from other erroneous shapes in the image by their type and shape, a process known as 'blob testing' (Shortis et al., 1994). The operator would manually set criteria such as target size, obliqueness (a ratio of width to height) or circularity (by comparing its area to its perimeter). Regions within these set limits are then accepted as the desired targets.

2.4.2.5 Coordinate measurement

Once targets are located and the individual pixels representing the target identified, a number of different algorithms can be used to calculate the actual centroid coordinate. Centroiding algorithms are identified and compared by Shortis *et al.* (1994).

'Binary centroid' is a simple algorithm that calculates the target's centre of gravity but makes no use of pixel grey values (Shortis *et al.*, 1995). Accuracy is significantly improved by using a weighted centroid algorithm that makes use of pixel grey values. An extension of this algorithm is to square the grey values, which has been shown to slightly improve accuracy by giving more influence to the higher-intensity pixels of the target than the low intensity pixels at its periphery (Shortis *et al.*, 1995). An alternative technique is to fit an ellipse to identified target edge pixels. Although circular targets are very often used, they will appear elliptical in images because of perspective effects. Centroiding and ellipse fitting techniques allows measurement to an accuracy of 0.1-0.03 pixels to be achieved (Luhmann, 2011).

The most accurate technique is to use least squares matching (LSM) to find the best match of a circular target pattern to the image. LSM techniques can achieve a precision of 0.05-0.01 pixels (Luhmann, 2011).

2.4.2.6 Feature-based matching

As introduced in section 2.3.4, rather than measuring circular targets, it is possible to measure the apparent movement of small 'patches' of an object's image where the object has sufficient texture. This can reduce set-up time since installation of individual targets at each monitoring point are not necessary. Processing of images can also be highly automated.

Monitoring 'patches' are selected in the first image, either in a regular grid defined by the operator, or by focusing upon well defined patches that provide good texture (Jerabek *et al.*, 2010). Using only well-defined patches has the benefit of more confidence in the accuracy of measured displacements. However, the irregular spacing of data points could make later processing more difficult or require undesirable interpolation. Defining a regular grid of monitoring patches resolves this difficulty, however, Morlier *et al.* (2007) noted that in tests on a pedestrian footbridge, no motion could be detected in several zones of the image taken, due to inadequate light resulting in poor contrast in some areas.

A 'moving window' technique is used to compare each of the selected patches in the first image with possible positions in the subsequent images. A correlation statistic is then calculated for each 'window' position and the location with the greatest correlation statistic is accepted as the new position of that monitoring point. The normalised cross correlation coefficient, given in equation 2.1 (Wolf and Dewitt, 2000), is often used;

$$c = \frac{\sum_{i=1}^{m}\sum_{j=1}^{n}\left[(A_{ij}-\bar{A})(B_{ij}-\bar{B})\right]}{\sqrt{\left[\sum_{i=1}^{m}\sum_{j=1}^{n}(A_{ij}-\bar{A})^2\right]\left[\sum_{i=1}^{m}\sum_{j=1}^{n}(B_{ij}-\bar{B})^2\right]}} \tag{2.1}$$

where A_{ij} and B_{ij} are the two image 'windows' to be compared, of size $m \times n$. $\overline{A}$ and $\overline{B}$ are the mean pixel intensity of the image windows A and B. This formula provides a measure of how well the grey values match between patches of the first and subsequent images.

While using DIC for monitoring strain in polymers, Jerabek *et al.* (2010) noted that the most important parameter affecting accuracy is the spacing of the subsets, as this is equivalent to a gauge length. The selection of subset size has to be based on operator's

experience and judgement.

2.4.3 Image Geometry - 2D

As introduced in section 2.3, if it is known a priori that deformations will be restricted to a single plane, only a single camera is necessary. Where any out-of-plane deformations may occur it is necessary to use multiple cameras for 3D measurements, as better discussed in section 2.4.4. The methods used to calculate real-space coordinates from points measured in a single image follow here.

2.4.3.1 Single planar measurement and transformations

The image registration methods discussed above allow measurement of coordinates in an image. In order to calculate real coordinates of an object, a scale must be given to images to transform measurements from the image plane, measured in pixels, to an object plane, measured in units of length. Object scale is related to the object distance, camera focal length and camera sensor dimensions.

In practice, a camera can rarely be arranged perfectly such that a simple scale factor can be applied. Yoneyama *et al.* (2005) used a shift lens to optically distort an oblique angle image to appear as if captured normal to the object. A more convenient method may be to use mathematic models to transform coordinates measured in the image to real-space object coordinates, taking into account the effect of perspective. These mathematical models relate the 2D pixel coordinate system (usually measured in pixels) to a 2D planar real-word measurements (often measured in millimetres). This is usually necessary as the more tangible object space coordinate system usually provides the desired measurements. Parameters defining the relationship between the camera's orientation and objects are necessary. Whilst this can be measured externally, it is usually more convenient for the parameters to be established by arranging 'control points' to appear within images and separately measuring their coordinates. Luhmann *et al.* (2006) provides further discussion on plane transformations.

Plane affine transformation Figure 2.10(a) shows how the affine transformation allows a plane to rotate and translate. It also has an additional parameter for shearing

and for scaling in both axes, which allows 'stretch' in the transformed coordinates. The transformation equations show that six parameters must be determined:

$$\begin{aligned} X &= a_0 + a_1 x + a_2 y \\ Y &= b_0 + b_1 x + b_2 y \end{aligned} \tag{2.2}$$

where x and y are object coordinates (in object space units such as millimetres) and X and Y are image coordinates (in pixels); $a_{0...2}$ and $b_{0...2}$ are the six transformation parameters for translation, scaling and shearing in both axes.

Robins *et al.* (2001) used a simple affine transformation while measuring target displacements in images of a concrete beam. However, this transformation is only suitable if the optical axis can be perfectly aligned perpendicular to the object plane, otherwise this transformation will yield incorrect results by insufficiently modelling perspective effects.

Projective transformation In the projective transformation, rays of light that pass from one plane to another pass through a single point: the equivalent of the focal centre of a camera (figure 2.10(b)). This transformation model is can be used for single images as it correctly models perspective effects (Luhmann *et al.*, 2006).

$$\begin{aligned} X &= \frac{a_0 + a_1 x + a_2 y}{1 + c_1 c + c_2 y} \\ Y &= \frac{b_0 + b_1 x + b_2 y}{1 + c_1 c + c_2 y} \end{aligned} \tag{2.3}$$

where X and Y are image coordinates, and x and y are object space coordinates. $a_{0..2}$, $b_{0..2}$, c and $c_{1..2}$ are constant transformation parameters.

These equations may be solved when at least four control points are included in the image to calculate the necessary parameters. Using more than four points create a more robust measurement network by adding redundancy and may increase accuracy (Moss and Matthews, 1995), but the simultaneous equations would then need to be solved by adjustment (Luhmann *et al.*, 2006).

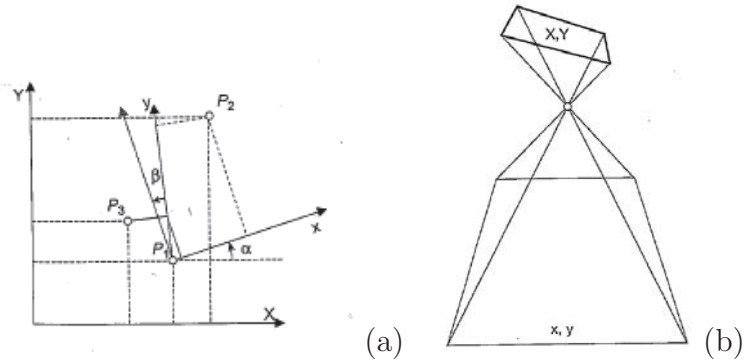

Figure 2.10: Representation of the a) affine and b) projective transformations (Luhmann *et al.*, 2006).

The transformation parameters are found by relating the known real coordinates of these control points with their image coordinates measured during image registration. This is usually done using the coded targets described in section 2.4.2.2. The calculated transformation parameters can then be used to relate coordinates measured in the image space to real world coordinates.

2.4.4 Image Geometry - 3D

2.4.4.1 3D measurement using the collinearity equations

The collinearity equations (equation 2.4) are the fundamental equations used for photogrammetric measurement. They are built from the assumption that light travels in a perfectly straight line from an object point, through the perspective centre of the camera and is projected on to the image plane.

These equations are used in least square adjustment to determine 3D positions for observed objects:

$$\begin{aligned} x' &= x'_0 + z' \frac{r_{11}(X - X_0) + r_{21}(Y - Y_0) + r_{31}(Z - Z_0)}{r_{13}(X - X_0) + r_{23}(Y - Y_0) + r_{33}(Z - Z_0)} + \Delta x' \\ y' &= y'_0 + z' \frac{r_{12}(X - X_0) + r_{22}(Y - Y_0) + r_{32}(Z - Z_0)}{r_{13}(X - X_0) + r_{23}(Y - Y_0) + r_{33}(Z - Z_0)} + \Delta y' \end{aligned} \tag{2.4}$$

where x' and y' are the image coordinates corresponding to the point defined by the object space coordinates X, Y and Z; X_0, Y_0 and Z_0 are the coordinates of the perspective

centre, whilst z' is the camera focal length and r is the matrix defining the rotational parameters; x'_0 and y'_0 represent the offset of the principle point; $\Delta x'$ and $\Delta y'$ are error corrections where necessary.

A bundle adjustment will solve all variables where there is no unique solution, creating a 'best-fit' by minimising residual errors and the method of least squares (Luhmann *et al.*, 2006).

2.4.4.2 Monocular 3D measurement

3D measurement using a single camera has been demonstrated by Chang and Xiao (2010). A specific target patterns with several identifiable points was used and measured changes in target size were interpreted as a change in object distance. In this experiment, cameras were oblique to the target motion. These tests demonstrate proof-of-concept, but because motion in the direction of the principal axis was not isolated from other motion, out-of-plane measurement accuracy cannot be considered proven.

2.4.5 Motion blurred images

Sharp images are almost always desired for the most accurate photogrammetric work. In some circumstances, images unavoidably become blurred by motion. The creation of motion blurred images is a well studied topic in computer science, usually to attempt to restore degraded images to a more usable appearance. Kraus (1993) provides a discussion on sources of loss of sharpness in images and comments on the systems that cause these effects. Image blur caused by motion can be described by equation 2.5 (Kraus, 1993). In particular, Kraus discusses how changes in image motion are related to pixel intensity distributions in the resultant image (figure 2.11).

$$u_{th} = \frac{10^3 \cdot v \cdot t}{3.6 \cdot m_b} \tag{2.5}$$

where v is the velocity (km/h), $u =$ image motion (mm), t is the exposure time (s) and m_b is the image-scale number. Kraus (1993) notes how 'forward motion compensation' in aerial cameras can compensate for uniform motion using this model.

A prevailing research area in image processing is the restoration of blurred images.

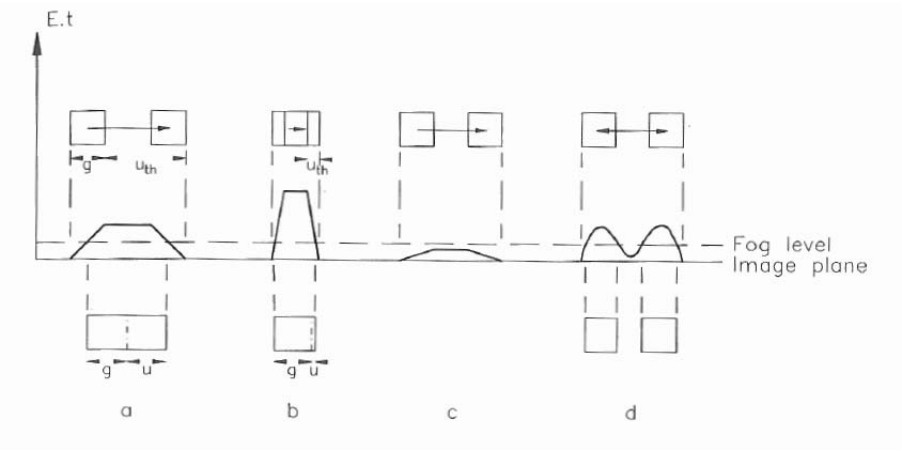

Figure 2.11: Image change as a result of image motion (Kraus, 1993)

Although some image enhancement algorithms can improve the appearance of images by sharpening blurred lines, image restoration is more advanced and uses knowledge of the movements of the camera or object to describe the motion that blurred the image (Banham and Katsaggelos, 1997). Image deblurring is popular because it is often desirable to improve poorly captured images in amateur, professional and scientific photography (Chen *et al.*, 1996; Banham and Katsaggelos, 1997; Ben-Ezra and Nayar, 2004; Arashloo and Ahmadyfard, 2007; Sorel and Flusser, 2008). Most of these approaches first involve estimating the motion that caused the image to become blurred (section 2.4.5.2). Often the success of the final deconvolution relies on the closeness of the estimated motion, and so a reliable estimation of the motion that originally degraded the image is crucial.

Other algorithms for measuring moving objects examine localised image gradients to identify blurred edges. One such example is measuring the movement of fast moving balls in sport science (Boracchi *et al.*, 2007; Dai and Wu, 2008; Caglioti and Giusti, 2009). It has also been demonstrated for measuring other moving objects (Li *et al.*, 2007; Wang *et al.*, 2007; Lin *et al.*, 2008) and even for spacecraft navigation (Xiaojuan and Xinlong, 2011) (figure 2.12). These algorithms are typically designed for a specific purpose and recognise only the circular or linear structures they are originally intended for.

2.4.5.1 The 2-D Discrete Fourier Transform

The 2-D Discrete Fourier transform (DFT) is one fast way of obtaining estimating blur in images (Solomon and Brekon, 2011). In a similar manner to how the 1-D DFT represents

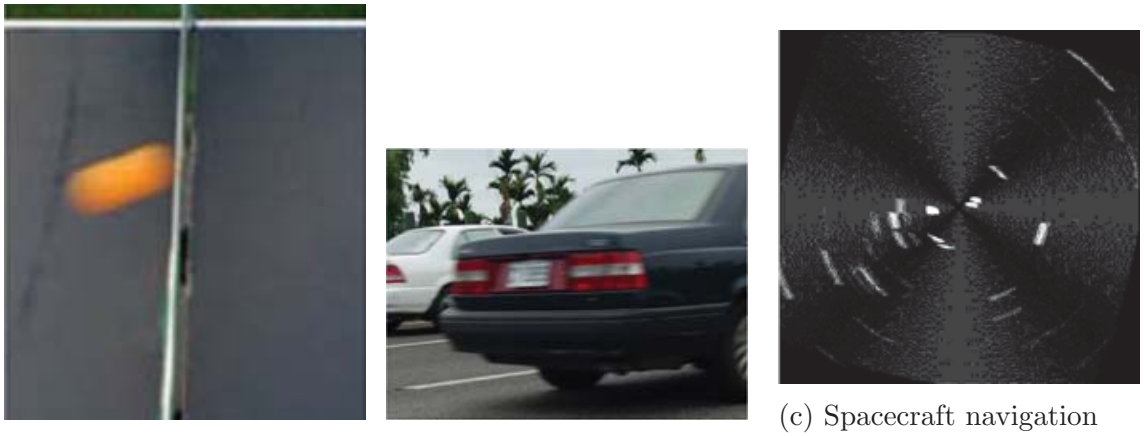

(a) Moving sports balls (Caglioti and Giusti, 2009)

(b) Vehicle speed detection (Lin *et al.*, 2008)

(c) Spacecraft navigation (Xiaojuan and Xinlong, 2011)

Figure 2.12: Examples of other motion blur measurement applications

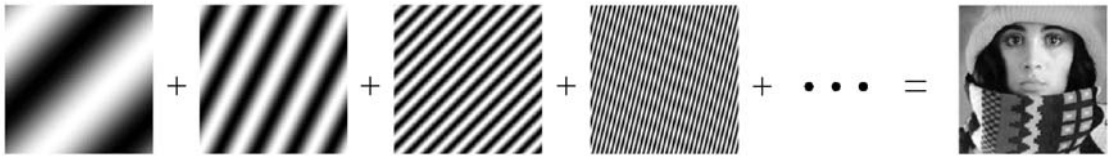

Figure 2.13: A combination of 2-D harmonic functions can synthesize an arbitrary spatial function (Solomon and Brekon, 2011).

periodic 1-D signals as a combination of sine and cosine functions, the 2-D DFT finds periodic functions that can be combined to synthesise the original image (figure 2.13) (Solomon and Brekon, 2011). Brayer (1997) provides an introduction to frequency domain images. Note that the definition of frequency differs here slightly from that used when analysing time domain vibration response, explained in section 3.2.2.1.

Some image processing problems are simplified by applying the DFT to an image and representing the image in the frequency domain. At first appearances, the frequency domain image can appear unintelligible, but images can contain distinctive features. For example, sharp edges or repeating patterns exhibit distinctive frequency in the frequency domain image. For blurred images, the frequency domain image exhibits fringes that will indicate the orientation and magnitude of the motion (Li *et al.*, 2007; figure 2.14).

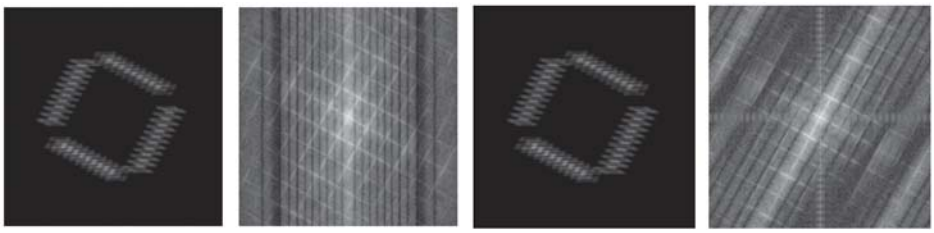

Figure 2.14: Examples of blurred images in the frequency domain (Li *et al.*, 2007).

Figure 2.15: Samples of generated point spread functions describing linear and other non-linear motion. These figures were created using the procedure desribed by Fergus *et al.* (2006) from motion blurred images taken in the lab.

2.4.5.2 The Point Spread Function and Image Deconvolution

The way in which an image has been blurred can be conveniently described in the point spread function (PSF), examples of which are given in figure 2.15. Whilst the earlier introduced equation 2.5 will estimate linear motion with a simple distance measurement, the PSF can describe both simple and complicated blurs caused by motion and other optical degradation. Equation 2.6 is frequently used to model image degradation with a PSF (Fergus *et al.*, 2006).

$$\mathbf{B} = \mathbf{K} * \mathbf{L} + \mathbf{N} \tag{2.6}$$

where $\mathbf{L}$ is the sharp input image which is transformed by $\mathbf{K}$, the point spread function; $\mathbf{B}$ is the output blurred image; $\mathbf{N}$ represents sensor noise at each pixel; $*$ is used to denote discrete image convolution.

This model is adopted or adapted by many as the fundamental assumption for space-invariant blur (Banham and Katsaggelos, 1997; Fergus *et al.*, 2006; Li *et al.*, 2007; Lin *et al.*, 2008; Dai and Wu, 2008; Sorel and Flusser, 2008). The PSF can be convolved with an image to artificially degrade it. PSFs can contain simple linear blur, as well as linear sinusoidal motion and the shape of more complicated non-linear motion. It can be seen from the examples in figure 2.15 that, although not stored numerically, the PSF

contains information which visibly describes the motion, which could be measured with an appropriate algorithm. Any PSF, however, is discretised into pixels, so the potential for sub-pixel measurement may be limited, and thus the precision of estimated motion amplitudes may have a lower bound of one pixel. It can also be seen in the third example of a resolved PSF that is imperfect, and the resolved motion path is discontinuous whilst it can be assumed that motion of real objects is not.

To improve the appearance of motion blurred images, deblurring algorithms take a blurred image together with its estimated PSF to produce an unblurred image. The Weiner-Helstrom filter is one regularly used restoration algorithm (Solomon and Brekon, 2011) and the effectiveness of this and many other algorithms is mostly dependent on the quality of the estimated PSF.

Many authors proposed competing algorithms for estimating PSFs of blurred images (Chen *et al.*, 1996; Banham and Katsaggelos, 1997; Ben-Ezra and Nayar, 2004; Li *et al.*, 2007; Dai and Wu, 2008; Sorel and Flusser, 2008; Dai and Wu, 2009; Chakrabarti *et al.*, 2010; Trouve and Champagnat, 2011; Hirsch *et al.*, 2011; Xie *et al.*, 2011; Paramanand and Rajagopalan, 2012). The PSF can be estimated using other sharp images of an object but of a lower resolution, or the more complex algorithms are capable of 'blind estimation' without any additional images or sensors. These algorithms examine whole images and look for particular blur features. Other sensors such as inertial sensors may be used to estimate the PSF (Joshi *et al.*, 2010). 'Multi-channel' deblurring refers to using more than one blurred image that are blurred in different ways but in combination may be restored (Sorel and Flusser, 2008). The most recent deblurring algorithms are capable of estimating 'space variant' motion blur by modelling the movement of a camera to account for different PSFs in different areas of an image (Sorel and Flusser, 2008).

2.4.5.3 Camera Response Functions

Differences found between motion blurred and simulated images during tests (section 3.2.2.3) were attributed to the camera's non-linear response functions, which relates input light intensity to recorded pixel value. Figure 2.16 gives an example of a camera response for a Nikon D80. Chang and Reid (1996); Debevec and Malik (1997) and Kim *et al.* (2012) describe how, in order to improve the appearance of images for viewing, the intensity of

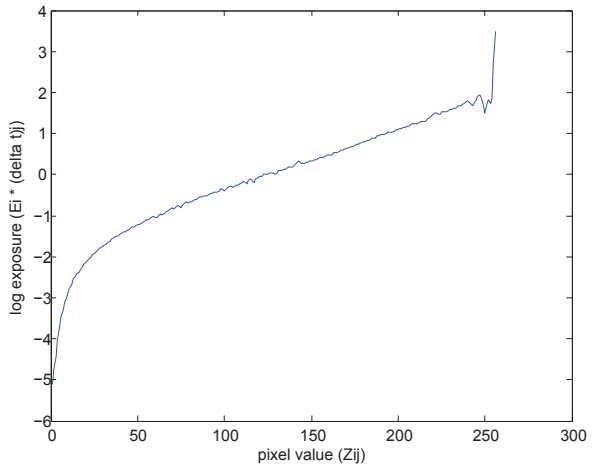

Figure 2.16: Example camera response function for a Nikon D80 camera, estimated from images captured within the School (office environment) using the solution by Debevec and Malik (1997).

colours in an image usually has a logarithmic relationship with the light energy that entered the lens, not only in digital sensors but also in film chemistry. This function has also been attributed to the ringing artefacts often seen in images restored by the Richardson-Lucy and Weiner deconvolution algorithms (Kim *et al.*, 2012). In particular, Debevec and Malik (1997) proposed an elegant solution to finding the camera response function from a sequence of images captured with different shutter speeds, and provided their Matlab code in their paper.

2.4.5.4 Measuring the motion blur of circular targets and objects

The application of measuring speed and trajectory of sports balls, and measuring movements of stars in astronomy, are similar in that they both involve examining circular blurred objects. Blurred circles are typically measured by identifying points around the blur edge or on other distinct parts of the blur path (figure 2.17; Boracchi *et al.*, 2007). These methods examine localised areas of images for particular patterns. Dai and Wu (2008) show the difficulties in measuring particular points on the borders of blurs where the edge appears as a gradient rather than a sharp edge. Some algorithms make assumptions of constant velocity whereas newer algorithms can account for non-uniform motion.

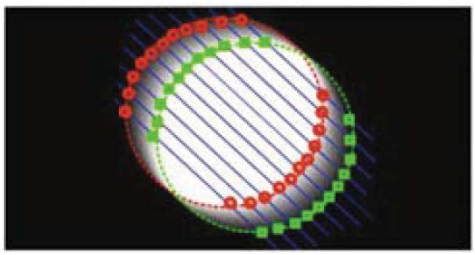

Figure 2.17: Intensity profiles along directions approximately parallel to the blur direction in the image have similar characteristics (Boracchi *et al.*, 2007).

2.5 Summary

This literature review has pooled knowledge for three subject areas: structural testing of civil engineering structures, photogrammetry, and image deblurring. Structural tests are routinely carried out in a laboratory environment. Routine 'structural health monitoring' is also regularly carried out on civil engineering structures to assess their structural integrity as well as to predict and plan for future structural work. There are distinct differences between static testing and dynamic testing. Static testing involves slowly applying loads to a test element and measuring its deformation. Dynamic testing is a more complicated technique whereby vibrations of much lower load act on the structure and its vibration response is measured. An analysis of the vibration response can identify changes in a test element's stiffness. As methods of carrying out dynamic testing improve for civil engineering structures, this approach is emerging as a more convenient method of carrying out regular testing.

Non-contact measuring instruments offer advantages over traditional contacting instrumentation such as remote monitoring of a very high number of measuring points. Optical image-based methods for measuring discrete marked targets in static testing are well documented, whilst image-based monitoring of dynamic tests and digital image correlation are more recently developing areas. The selection of sensor is an important factor in the accuracy of any image-based monitoring scheme. Current sensor hardware requires a compromise between spatial and imaging speed to be made.

Image deblurring techniques allow photographs that are blurred by a moving camera or of moving objects to be improved post-capture. The most effective methods first estimate the camera or object's motion before deblurring the image. The following chap-

ter discusses a methodology for using localised image blur measurement techniques for determining the vibration response in dynamic structural tests.

Chapter 3

Methodology

The existing methods for monitoring dynamic tests described in the literature review have been effective within the constraints for which they are described. However, they suggest that an alternative method is necessary in order to alleviate the inherent compromise that exists when selecting sensors for monitoring of dynamic structures. Instead of capturing vibrations using very high speed imaging, a high-resolution long-exposure photograph could be used, in which the localised object image becomes motion blurred (figure 3.1). A specialised image registration algorithm would be necessary to make measurements from such a motion blurred image. This chapter discusses the development of an algorithm for monitoring vibrations in structures using such long-exposure blurred imagery, some of which is presented here.

The first section identifies and describes the attributes of the imaging hardware and other monitoring instrumentation used in the course of this research project (section 3.1.1). Following this, a number of currently existing algorithms for photogrammetry measurement of sharp images, as well as some other algorithms applicable to blurred images are described, recreated and the effectiveness of each tested (section 3.2). After evaluating a number of these image processing approaches, a combination of the most effective was developed into a working solution for measuring vibration in blurred images (section 3.3). This algorithm is described in detail, and the accuracy of the measurements is verified.

After the development of the algorithm for processing of individual images, the approach was extended to include 3D monitoring capabilities. Technical challenges in addi-

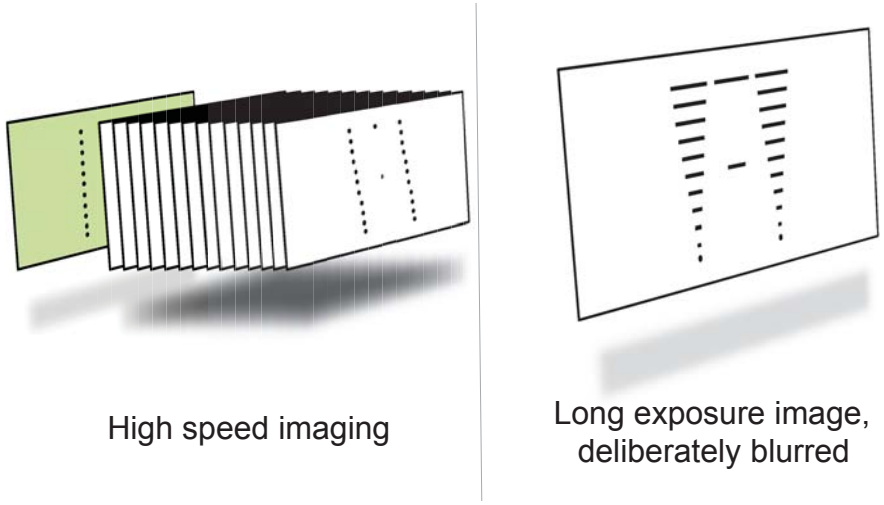

Figure 3.1: An illustration of the proposed LEMBI measurement approach

tion to those normally encountered in 3D photogrammetry are discussed, existing partly because of individual targets having two coordinates in each image. A solution to these additional challenges is presented.

3.1 Equipment and instrumentation

3.1.1 Camera hardware

The cameras used for this project included a pair of Nikon D80 cameras (Figure 3.2a) and a Nikon D7000. The lenses available for these cameras included a pair of 24 mm fixed focal length lenses. A range of other fixed focal length lenses between 24 mm and 85 mm were available, as well as zoom lenses (although the zoom lenses are not favoured). All lenses and cameras share the 'Nikon F' mount, and are all interchangeable. Key properties of both cameras are given in table 3.1.

For simultaneous activation of the two camera's shutters, a double external trigger that connects to two cameras had been constructed by a lab technician (Figure 3.2b). Pressing the button activates a relay that closes the trigger circuit for both cameras simultaneously. For convenient activation of the double external trigger, it can also be activated by an external signal from other lab equipment. This was convenient for tests using the shaker table (introduced in section 3.1.3) where long sequences of images were taken automatically, and the timing of the camera trigger synchronised with other data logging

Table 3.1: DSLR camera properties

	Nikon D80	Nikon D7000
Effective pixels	10.2 MP	16 MP
Image size	3872 x 2592 px	4928 x 3264 px
Sensor	23.6 x 15.8 mm CCD sensor	23.6 x 15.7 mm CMOS sensor

(a) Nikon D80 camera (b) Double external trigger

Figure 3.2: The Nikon DSLR cameras and double external trigger

hardware. Switching the external trigger to 'External Sync' enables the internal relay to be activated by an external power source through a 3.5 mm jack port. The consumer grade cameras were supplied with automatic setting of most parameters activated by default, several of which had to be manually controlled in the course of the following tests to capture appropriate images and to maintain synchronisation (appendix E). During monitoring, precautions were taken to ensure no camera movement (section 3.3).

3.1.2 Camera calibration field

Calibration of camera lens systems is normally necessary for the most accurate photogrammetric work. Except for in the cases of localised displacement measurement only (section 2.3.1.1), the camera's lens system must be modelled to account for systematic errors caused by lens distortions (section 2.4.1.2). The cameras internal components, including the sensor geometry, the focal length and parameters describing lens distortion

and collectively described as the camera's interior orientation (IO).

As discussed in the literature review (section 2.4.1.2) specialist cameras manufactured to small tolerances can be used to reduce distortion by the lens system. Alternatively, less expensive hardware can be used, provided that lens distortion is taken into account. Since the distortions caused by these lenses are generally predictable and can be modelled with a small number of parameters, this method can deliver significant cost savings whilst still providing high accuracy.

The automated camera calibration provided by the PhotoModeler software package (EOS Systems Inc., 2013) is a fast and convenient method for determining calibration parameters from a series of images of sheets or coded targets, and this software has been used in the research. The guidance from EOS Systems suggests laying calibration sheets on the floor, and moving around them with the camera. However, this is an inflexible solution as the range of suitable lenses and focal length is restricted. If a lens was desired to be focused to infinity, then carrying out lens calibration on a 1.5 m tripod will likely mean the calibration image sequence suffers from out-of-focus blur, and the calibration process might not be accurate.

A camera calibration target field was designed and assembled on a wall in the laboratories of the School of Civil and Building Engineering. This field was designed to be suitable for calibrating cameras for a large range of applications. Images can be acquired from a maximum object distance of 5 m, at which distance it was found that targets remained in focus when lenses were focused at infinity. At this distance, the largest targets at 12 mm diameter are visible in the image, and with a 24 mm lens would represent approximately 9.5 pixels in the image space, a suitable target size. When either a longer focal length or shorter focus distance is desired, a smaller area of the calibration field will be visible in images, and smaller targets will be then visible at these scales, the smallest targets being 2 mm. Intermediate 6 mm targets were also included in the test field design. The test field geometry was designed as shown in the diagram in figure 3.3.

The targets were printed on sheets of A3 paper which were used to decorate a 5.0 x 3.3 m wall with 190 coded targets. Rather than using PhotoModeler's 'Print Calibration Sheets' function, the standard 'Create Coded Targets' was chosen, because in this mode the centres of the targets could be marked with small crosses. The sheets were then

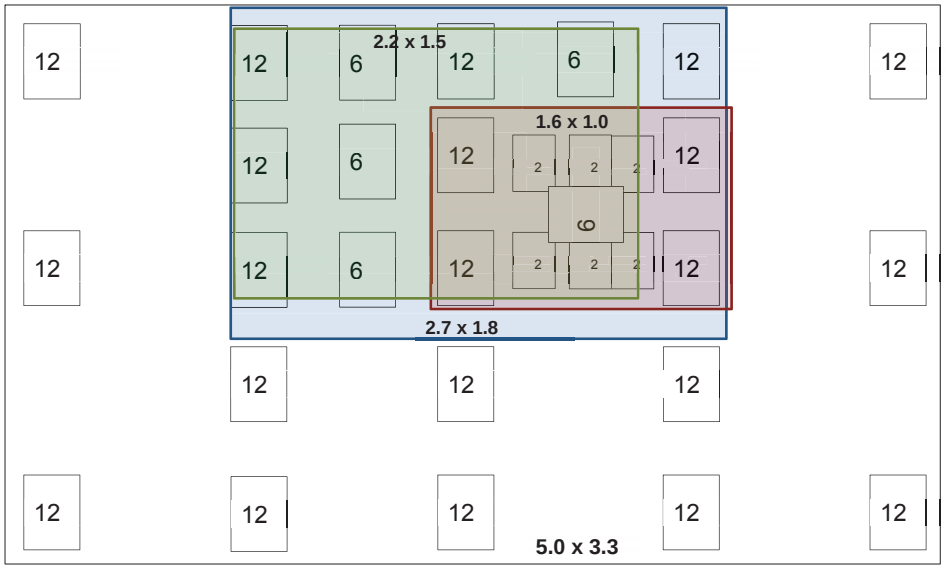

Figure 3.3: The design of the camera calibration field, showing three different sizes of targets

arranged on a spare wall using wallpaper paste (figure 3.4).

Although not necessary for calibration, coordinates for the first and fifth target on every large size sheet (approximately 22% of all the targets) of the targets were measured using a total station, making observations from three locations. It was for this that the centre of the coded targets needed to be marked. The readings were then put into an adjustment in the StarNet software (MicroSurvey, 2011). This set of coordinates can then be used to validate of the calibration results achieved in PhotoModeler.

Whilst this range is suitable for many applications, it does not provide targets suitable for macro images at a very large scale. In these instances it is anticipated that calibration targets could be printed on a single sheet of typical office-sized paper, so a dedicated calibration field would be unessential for these tasks.

Whenever a lens calibration was required, a series of images of the calibration field were taken using the sensor and lens combination. Images were arranged following PhotoModler's recommended guidelines, which recommends 12 convergent images distributed around four sides in different orientations. PhotoModler's, multi-sheet automatic calibration was used and calibration parameters X_P, Y_P, K_1, K_2, P_1 and P_2 were determined. If PhotoModeler alerted about the focal length, the EXIF data approximation of focal length was used, since the resultant focal length determined by Photomodeler's self-calibration

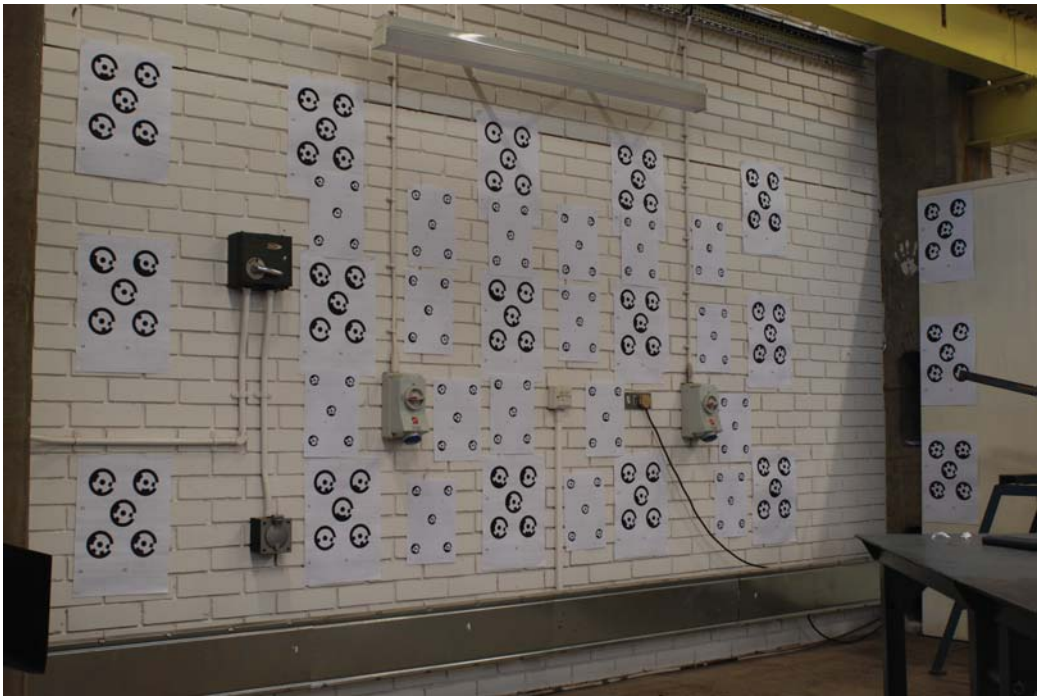

Figure 3.4: The completed camera calibration field

in this mode was closer to the specification focal length of the lens. The 'Photomodeler's best estimate' method resolved a focal length which was significantly less than the lens specification, and the resultant other distortion parameters were significantly different to those determined in combination with a near-specification focal length (although it is possible that the different parameters is this model are still effective).

3.1.3 Shake table

Images exhibiting strictly controlled motion blur, created in laboratory conditions were desired to examine the appearance of motion blurred images with varying amounts of blur. Tests were devised using a structural dynamics shake table (figure 3.5), which allowed exact control of motion in a fixed direction. The table can be programmed with a certain motion, by creating an input waveform. The input signal relates to the force applied to the moving armature, which is proportional to its acceleration. The moving table bed is horizontal, and test models and targets were rigidly screwed to the table surface. Cameras could then mounted on a tripod opposite the targets.

The shake table used is an APS 400 'Electro seis' with the horizontal table kit (fig-

ure 3.5). The APS 145 signal amplifier is used to provide the necessary power to the table. The signal amplifier input is a single channel DC signal, provided through a NI CompactDAQ system (figure 3.6). A custom Matlab script running on a PC controls the output signal of the CompactDAQ. The table bed has dimensions of 356 x 356 mm, provided with a 50 x 50 mm grid of threaded holes into which machine screws can be inserted. The maximum stroke of the table is 157 mm. This instrument was of particular value because it could be used to generate known displacements to an object, which could be compared to estimates derived from an image based solution. A range of other monitoring equipment was available also.

3.1.4 Monitoring equipment

A range of monitoring instruments were available in the dynamic structures laboratory. These included gauges to connect to the accelerometer and voltage signal input connectors of the CompactDAQ system modules. Accelerometers were available for monitoring the movement of test objects, including triaxial accelerometers (described in more detail in section 2.2.1.3). A laser displacement gauge was also fitted to the table to monitor the table's actual position. Since the range of the table is beyond the maximum range of the laser, an angle section fitted to the back of the table is inclined, so that the output signal from the laser is linearly proportional to the table position. The table's displacements could also be found using an accelerometer and subsequently double integrating the accelerometer data, but this approach is subject to drift as discussed further in section 2.2.1.3. The laser displacement gauge provides more accurate absolute position measurement, so is favoured when making comparisons. The amplifier's output monitor signal was also returned to the CompactDAQ's voltage input to monitor the status of the amplifier.

The accelerometers are individually calibrated by the manufacturer, and each has a calibration constant in mm s^{-2} V^{-1}, which must be assigned to the data input channel to get the correct measurement. The laser gauge is not formally calibrated, since its output depends on the exact inclination of the angled section at the rear of the table, but it outputs a linearly increasing signal with respect to the table position. The increase in

Figure 3.5: APS 400 shake table

Figure 3.6: Shake table control system (NI CompactDAQ and APS 125 signal amplifier)

output signal per distance travelled by the armature is determined and used to calculate the table's absolute position at any time.

These monitoring instruments were used to provide independent external reference measurements for testing the proposed measurement system. The laser displacement gauge was used to monitor a structure's input force, and the accelerometers were used, either to also measure the motion of the table or to measure the response anywhere on the model structures.

3.2 Current Target Measurement and Image Registration methods

The literature review identified some existing approaches to measuring or estimating motion in motion-blurred images, some of which used artificial targets, and some of which detection motion in natural scenes. To test the effectiveness of these approaches and assess their suitability for monitoring of structural vibrations, experiments were conducted using controlled motion-blurred images created with the shake table, with the aim of selecting or devising an approach suitable for the application.

As well as making qualitative observations of each approach by comparing the appearance of results on-screen, and comparing how reliable each measurement is, the accuracy of measurements made with each method was assessed by comparing the image-derived measurements with those recorded by the other sensors fitted to the shake table.

3.2.1 2D image geometry

To allow each comparison between image-derived measurements and reference sensors, it was necessary to transform image-derived measurements into object-space in units of millimetres. Where deformations are expected to be planar, relatively simple transform calculations can be used to transfer image-space measurements in units of pixels to the object-space in units of millimetres. A discussion of planar transforms is given in section 2.4.3, and the projective transform was deemed most suitable, because of its tolerance to the perspective effect of the imaging plane not being exactly coplanar with the object plane. Two wooden stands were positioned on either side of the object, with three 'RAD' coded control targets on each, which allow for automatic identification and measurement by PhotoModeler (EOS Systems Inc., 2013). The wooden stands and control points should be arranged such that all points are coplanar. This was achieved by a careful visual alignment of all control points, and ensuring that all monitoring points are also aligned to the desired measuring plane. For convenient positioning when monitoring larger model structures, a BSW 5/8" nut was fixed to the base of these stands, to allow the stands to be mounted onto standard surveying instrument tripods.

The projective transformation requires both image coordinates and object-space coordinates for each control point to determine the transformation parameters. Although a Matlab algorithm for the recognition and measurement of RAD coded targets was developed, the algorithm could not recreate the accuracy achieved by the PhotoModeler software. Indeed, while the Matlab routine reliably recognised target codes, the target measurement algorithm was based on a weighted centroid algorithm, rather than the least squares matching approach used by PhotoModeler, which is known to be more accurate (Luhmann, 2011). PhotoModeler Scanner was used to automatically determine the image coordinates for coded targets, and the derived image coordinates were exported to a CSV file.

Real-world object-space coordinates for each control point were determined by measuring the control points with a Leica TCR405 total station (TS) in reflectorless mode. Whole circle bearing (WCB), horizontal and vertical distances were noted down. Although 3D coordinates were determined using these measurements, 2D planar coordinates were required.

The vertical distances measured by the total station were used to represent the vertical (y-axis) plane-space coordinates (with a simple constant added to bring the readings within a convenient range of positive numbers). More calculations are necessary to determine horizontal (x-axis) plane-space coordinates from the TS measurements. The measured WCB and horizontal distances were entered into a spreadsheet and X and Y horizontal coordinates calculated in an arbitrary coordinate system. On this occasion, a MS Excel was used as it allowed measurements to be conveniently entered, contained an easy-to-use regression function and provides a simple output which is easily passed to other Matlab routines. The parameters of a straight regression line (slope and intercept) fit to these coordinates was calculated using MS Excel's 'linest' function. Regression statistics are also displayed in the spreadsheet to check the fit, and a plot in the spreadsheet provides a visual check. The plot also aides identification of any gross errors in measurements.

Given the regression line parameters (slope and intercept), a local coordinate system was then defined by rotating the object-space coordinate by the angle that the regression line makes with the vertical axis. A 2D rotation matrix was used for this transforma-

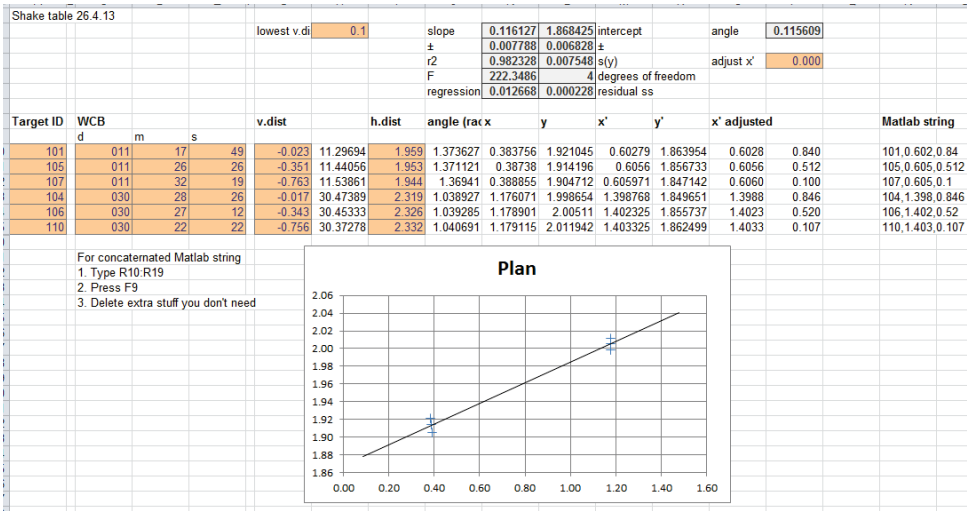

Shake table 26.4.13

				lowest v.di	0.1	slope	0.116127	1.868425	intercept		angle	0.115609	
						±	0.007788	0.006828	±				
						r2	0.982328	0.007548	s(y)		adjust x'	0.000	
						F	222.3486	4	degrees of freedom				
						regression	0.012668	0.000228	residual ss				

Target ID	WCB d	m	s	v.dist		h.dist	angle (rac	x	y	x'	y'	x' adjusted		Matlab string
101	011	17	49	-0.023	11.29694	1.959	1.373627	0.383756	1.921045	0.60279	1.863954	0.6028	0.840	101,0.602,0.84
105	011	26	26	-0.351	11.44056	1.953	1.371121	0.38738	1.914196	0.6056	1.856733	0.6056	0.512	105,0.605,0.512
107	011	32	19	-0.763	11.53861	1.944	1.36941	0.388855	1.904712	0.605971	1.847142	0.6060	0.100	107,0.605,0.1
104	030	28	26	-0.017	30.47389	2.319	1.038927	1.176071	1.998654	1.398768	1.849651	1.3988	0.846	104,1.398,0.846
106	030	27	12	-0.343	30.45333	2.326	1.039285	1.178901	2.00511	1.402325	1.855737	1.4023	0.520	106,1.402,0.52
110	030	22	22	-0.756	30.37278	2.332	1.040691	1.179115	2.011942	1.403325	1.862499	1.4033	0.107	110,1.403,0.107

For concaternated Matlab string
1. Type R10:R19
2. Press F9
3. Delete extra stuff you don't need

Figure 3.7: The spreadsheet used to calculate planar control coordinates from a total station survey

tion (equation 3.1) and the x coordinate used to represent the place-space horizontal coordinate.

$$\begin{pmatrix} x_1 \\ y_1 \end{pmatrix} \begin{pmatrix} \cos\theta & -\sin\theta \\ \sin\theta & \cos\theta \end{pmatrix} = \begin{pmatrix} x_0 \\ y_0 \end{pmatrix} \tag{3.1}$$

These object-plane space coordinates were stored as another CSV file. To determine the parameters of the projective transformation, Matlab's 'cp2tform' function was called with a list of image-space coordinates with their corresponding plane-space object coordinates. The output is the projective transformation parameters which were then used to transform image coordinates into object-space coordinates using Matlab's 'tformfwd' function. Both of these function are from the family of geometric transformation functions in Matlab's Image Processing Toolbox.

As discussed in section 2.4.1.2, a lens model can be safely excluded from the processing chain when calculating localised deformation. The systematic errors incurred by not using a camera model, whilst may be significant for absolute coordinate determination, will be minimal when determining local differences.

3.2.2 Natural texture approaches

There are many examples identified in the literature (Ben-Ezra and Nayar, 2004; Fergus *et al.*, 2006; Arashloo and Ahmadyfard, 2007; Dai and Wu, 2008; Sorel and Flusser, 2008) for determining the motion causing blur in images of ordinary scenes, typically as a result of the camera moving during acquisition, or capturing fast moving objects such as at sporting events. The images used are generally ordinary scenes rather than structured images containing artificial targets, and their aim is mainly to improve the aesthetics of poorly captured photographs. In particular, the problem is usually created by a moving camera which blurs the whole image, instead of localised blur caused by a moving object in part of the image. If a solution using natural texture approaches was used, images would not require marked targets and a similar arrangement to DIC would be possible. Not only would set-up time be reduced, but measurement would approach full-field, provided the object has suitable surface texture.

The suitability of some of these earlier published measurement methods was tested by recreating the methods described in their publications, which follows in this section. Some of these approaches produce a point spread function (PSF), which can contain information about motion direction, extent, distribution and even describe non-linear motion (section 2.4.5.2).

3.2.2.1 Frequency domain

The possibility of transforming images from the spatial to frequency domain was introduced in the literature review (2.4.5.1). The term 'frequency' is classically used to describe the Fourier's counterpart of time. In this subsection, the term is used to describe the power spectrum of a spatial domain (pixels), rather than a time domain. Frequency is usually defined as an inverse of time, but here it is an inverse of pixels.

Frequency domain analysis can simplify image processing problems, including that of motion blur. By passing images through a 2D discrete Fourier transform (DFT), images can be expressed as a series of periodic functions (section 2.4.5.1). Analysing frequency domain images is suggested as an approach to determining the motion path causing motion blur by Li *et al.* (2007). Li *et al.* show how the spectrum image exhibits dark

Figure 3.8: This image of 'Lena' has become a standard test for image processing algorithms

'ripples' perpendicular to the vibration direction, which can then be measured.

Fringe Detection The approach demonstrated by Li *et al.* was tested, by collecting motion blurred images and examining the frequency-domain spectral intensity function to detect fringes. Several sample images were captured, some of outdoor scenes taken with a hand-held camera and others were of images of moving photogrammetric targets, and also some sample images downloaded from the internet. Although the approach was successful with a low resolution 'Lena' image (figure 3.8), it was mostly unsuccessful using the images of sample targets, with the spectral intensity function appearing unintelligible. This is possibly due to the increased noise in higher resolution images, or the remaining high frequency components of 'structured' motion-blurred images rather than those of scenes.

Function Division According to the convolution theorem (Solomon and Brekon, 2011), the Fourier transform of images created in the spatial domain by the convolution of a sharp image with a point spread function (PSF), is equal to the frequency-domain image created by matrix multiplication of their transforms in the frequency domain, that is (Solomon and Brekon, 2011):

$$\mathcal{F}\{f(x,y) * h(x,y)\} = F(k_x, k_y)H(k_x, k_y) \tag{3.2}$$

where $*$ denotes discrete image convolution. Here, as explained in section 2.4.5.1, the use of the term 'frequency' differs from that where frequency is the inverse of the time

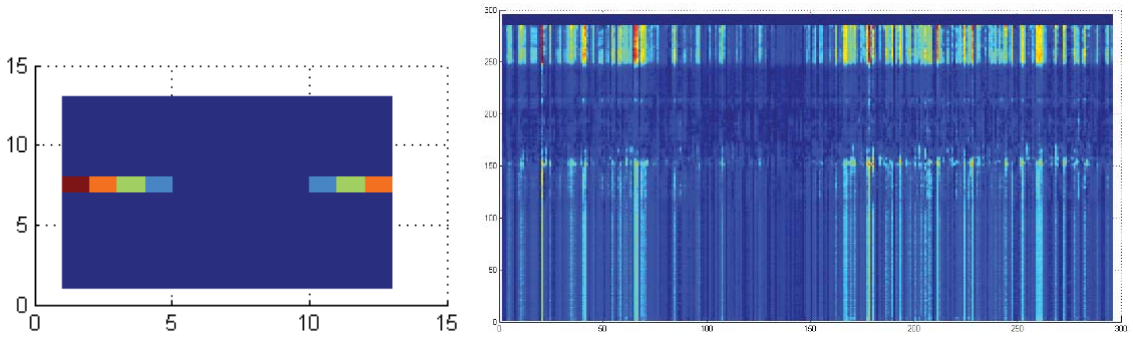

(a) (b)

Figure 3.9: (a) the simulation PSF, (b) the resultant PSF

domain.

If a blurred image is created this way in the frequency domain, the spatial domain image can be retrieved via the inverse DFT. It was suggested that, given a sharp and blurred image of the same scene, the PSF could be retrieved in the frequency domain. A blurred image, $\mathbf{B}$, was created with a sharp image, $\mathbf{S}$, and a PSF (figure 3.9a). It was hoped that the original PSF could be recovered with the equation:

$$\text{PSF} = \mathcal{F}^{-1}\left(\frac{\mathcal{F}(\mathbf{B})}{\mathcal{F}(\mathbf{S})}\right) \tag{3.3}$$

Although this approach provides a theoretical solution, tests revealed that it is impracticable. It would appear that this is a poorly conditioned problem, since the frequency domain Fourier transform is not a unique solution, it is only a very close approximation. Although the resultant PSF from dividing is technically correct, it does not resemble a PSF which can be measured. In fact, convolving the resultant PSF with the sharp images does produce an apparently similar motion-blurred image. A further practical limitation is also that the Fourier transform slows down for larger images, and maybe unacceptably slow for larger image patches.

3.2.2.2 Blind deconvolution algorithms

As identified in the literature review (section 2.4.5.2), in the field of computer science there are competing algorithms for 'blind deconvolution' of blurred images: i.e. taking a blurred image and restoring it without any other information. Published demonstrations

used ordinary unstructured scenes that are 'deblurred'. Since the problem is usually that the camera is moving and the object is stationary, many algorithms estimate the motion with a smaller patch of the main image and assume the motion is spatially invariant for restoring the rest of the image. This assumption probably holds true when all objects in the image are very far from, or approximately at the same distance from the camera. Most algorithms use an iterative approach that takes a considerable time to process. Notable examples of blind deconvolution include that by Fergus *et al.* (2006), who make their Matlab routine available to use. Their routine was utilised, implemented and tested on a range of motion blurred images.

Like the previous approach, because these images are of ordinary scenes, using these algorithms to measure motion would not necessitate attaching targets to images with sufficient texture. Monitoring could be made to a grid, approaching full-field measurement. These blind deconvolution algorithms are also frequently capable of identifying PSFs for non-linear motion.

Samples of PSFs recovered from sample images were provided in figure 2.15. Unfortunately, these blind deconvolution algorithms were very slow and take several minutes to compute PSFs for small patches within images. Poor estimates of PSFs, that are not very representative of the motion that caused the blur are common, and where they occur there is not a quality check to identify them. The capability for sub-pixel measurement may also be limited. These limitations may be solvable when de-blurring poorly captured scenes, for which this algorithm was intended, where it is possible to identify and limit processing to the image patches most likely to be successful. For structural testing it is necessary to prescribe the image patches relating the points of interest on the structure, and the approach is less likely to succeed.

3.2.2.3 Image Correlation

Blind deconvolution algorithms discussed above are capable of identifing the PSF that creates motion-blurred images without assuming a certain motion direction or shape. When these published algorithms are tested the demonstrate that estimation of PSFs is complex and difficult to achieve, particularly when there is no 'a priori' knowledge of the motion.

Figure 3.10: Samples of generated point spread functions describing harmonic motion.

The problem was simplified by restricting the motion direction, and so making a one-dimensional problem. By assuming the vibration to be one-dimensional, sinusoidal and (initially) in a fixed direction, the resultant PSFs become limited and the problem can be reduced to solving one unknown (the motion amplitude). It was decided to develop an algorithm that solves this more simple challenge initially, before adding the additional complexity of orientation later.

Matlab has a function included in the Image Processing Toolbox for creating motion blur PSFs, 'fspecial'. This single function can create different filters such as edge detection filters, but also a motion blur filter. The desired length and angle are input to the function, and the output is a point spread function describing constant velocity motion. Unfortunately, motion caused by constant velocity is not always a valid assumption (Kraus, 1993).

For a more accurate representation of a PSF for structural vibrations, which are generaly harmonic (section 2.1.3.1), a bespoke function was created for generating PSFs of sinusoidal motion (figure 3.10). A 2D ordinary sinusoidal curve can be created, with a period of half the motion distance, the function is limited to the range from one half of to negative half of the desired distance, and is zero beyond this range. This continuous function can then be discretised into a matrix (padded with zeros). The initial PSF generating function initially provided integer displacements of integer values, and was later extended to create PSFs for subpixel displacements (figure 3.23). The PSF generation algorithm is further developed in section 3.3.1.

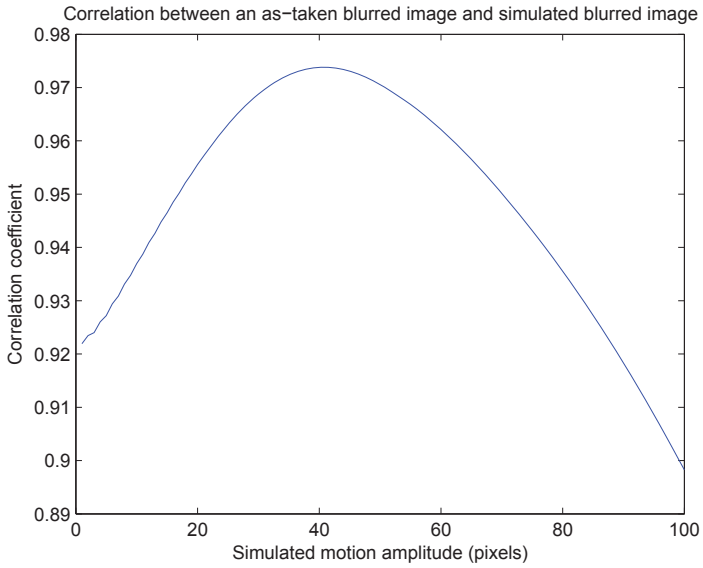

Figure 3.11: Image correlation results show a clear trend

Such an approach could theoretically work in images of natural texture. However, to work successfully, the texture would have to have sufficient 'boldness' to not be so severely degraded that it is lost when blurred, and ideally not have a repeating pattern. For this reason, it was elected to restrict use to well defined targets (at least initially). This approach could be used to validate the earlier blind deconvolution method, or to improve its accuracy.

An iterative method using image correlation between as-taken motion-blurred images and artifically created motion-blurred images was designed. After making a first estimate of the motion direction and distance, a PSF would be generated that described this motion. This PSF would be used to create an artificial motion-blurred image by convolving the sharp image taken while the object was stationary with the PSF. A correlation statistic was calculated to compare the artificial motion-blurred image with the actual as-taken motion-blurred image. The motion parameters that were used to create the PSF would be iterated until the motion parameters related to the highest simulated image correlation statistic can be identified. After initial development and testing, this approach appeared successful, and a trend in image correlation statistics clearly shows an identifiable 'peak' (figure 3.11).

Unfortunately, the generated image with the highest correlation statistic was created using slightly greater motion amplitude than was known to have actually caused the

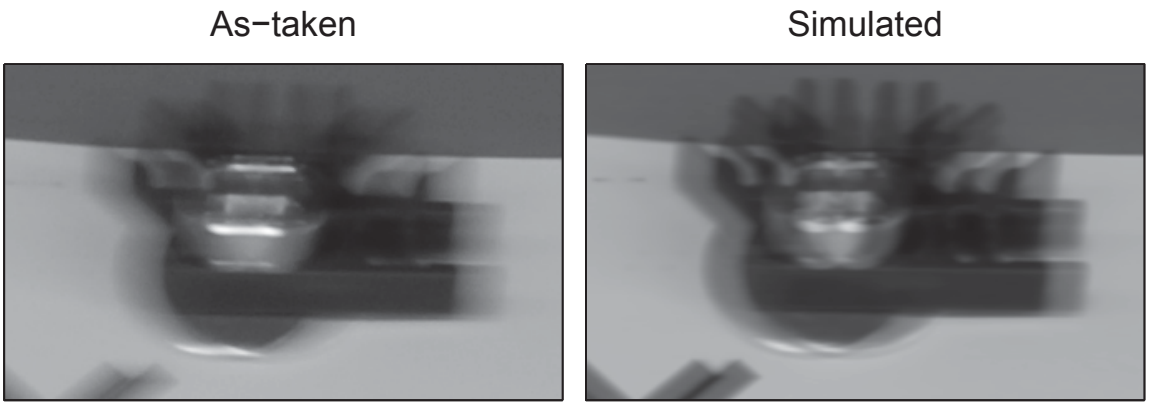

Figure 3.12: Although very similar, pixel intensities with the gradient area were darker in the simulated image.

motion blur. A systematic error appeared to exist. On closer inspection, although very similar, pixel intensities within the gradient area were darker in the simulated image. The highest correlation statistic was not where the image motion matched (figure 3.12) and it was thought this is because where gradient areas appear darker, they produce a higher correlation statistic when aligned with a gradient area nearer to a dark (or in the figure, an 'always occluded') part of the image. It was recognised that since PSFs must sum to unity, the overall intensity of the PSF could not be incorrect. The difference in PSF was instead attributed to non-linear camera response functions.

Several assumptions were made in generating the simulated image: including that the pixel intensities were assumed to be a value linearly proportional to the amount of time that a picture occupies that image pixel. It was also assumed that the pixel intensity is proportional to the light intensity at each sensor pixel in the real as-taken image, however, other filters are applied before the final pixel value is recorded. On the D80 camera a physical filter exists on the sensor array, as well as any other filters attached to the lens, and software filters are applied by the camera before an image is recorded. This somewhat invalidates the assumption that a blurred image is the product of a sharp unblurred image with an OTF, since the the final pixel value is not linearly related to the time the object spent in that position.

A camera response function (CRF) describes how the intensity of light reaching a sensor pixel is related to the final pixel value. To improve image aesthetics, the two are

not proportional and are, in fact, related logarithmically (Grossberg and Nayar, 2004), which more closely mimics human perception of varying light intensity (figure 2.16).

The CRF for the Nikon D80 with the appropriate exposure settings was determined using the approach described by Debevec and Malik (1997) (figure 2.16). A look-up table relating light intensities (on an arbitrary scale but assumed proportional to radiance) to pixel values was essentially created. The look-up table was used to create a light-intensity spectrum image, by replacing pixel values with their light intensity equivalent. Image measurement using the iterative image correlation was repeated to see if the new light intensity spectrum image improved the accuracy of the result. Unfortunately, only a small increase in accuracy was observed. The anticipated improvement in accuracy may not have been realised because of another systematic effect that created the error.

Whilst the presence of a systematic error caused by a non-linear CRF is supported by literature (Grossberg and Nayar, 2004; Debevec and Malik, 1997), attempts to correct for it were unsuccessful. Whilst the presence of the error is assumed, its affect on accuracy remains untested and the main cause for the observed error in the correlation image registration approach may be another unanticipated error.

One effect of the CRF which could be permanent is that if the function is applied before the recorded higher-bit value of the pixel is reduced to within the 256 value range, this would introduce an almost cyclic systematic effect. This could not be reversed by inverting the CRF.

This systematic error was later solved in the proposed solution by comparing edge features of artificial targets. Whilst the pixel intensity values of the gradient within the motion blurred path is affected, the position of the edge features of artificial targets was not (section 3.3).

Whilst consideration of these natural texture measurement approaches has demonstrated and evaluated possible measurement algorithms, a number of measurement difficulties were encountered. Investigation diverted to those approaches requiring artificial targets, as it was anticipated that the greater control over the image would permit greater accuracy and reliability.

3.2.3 Artificial targeting approaches

The addition of artificial targets for object points is common in photogrammetry. Using a target of known appearance allows object points to be more easily identified and coded targets allow automatic labelling. Depending on the approach, natural features of interest may need be identified manually in images. The centroiding accuracies of circular targets also approach 0.01 px in ideal conditions (Luhmann, 2011). Natural features typically do not have identifiable points, but must be 'matched' between images taken at different epochs, or from different camera stations. Accuracies are lower, and the change of appearance can cause lower accuracy in measurement which requires testing and further examination.

To examine the appearance of motion-blurred images, targets were printed on paper and stuck on to the shake table (section 3.1.3). Images of the targets were taken whilst the table was in motion. With the aim of determining an approach for measuring motion blur, different combinations of targets and corresponding target registration algorithms were sampled. Although circular targets are common in photogrammetry, they will not necessarily be the most suitable target for measurement of motion blur. Their apparent effectiveness for creating predictable images was judged (figure 3.13). This section reports on the judged effectiveness of each approach.

Figure 3.13: The selection of artificial targets tested on the shake table

3.2.3.1 Cross targets

Black cross targets on a white background were subjected to one-dimensional sinusoidal motion to test how this target type appeared in motion blurred images. The resultant motion-blurred image showed two faint crosses linked by a fainter smear. Luhmann *et al.* (2006) noted how the ring operator can be used to mark the centre of cross targets.

An algorithm adapted from the ring operator for marking these cross targets was developed and could also successfully mark the two ends of the cross' motion (figure 3.14).

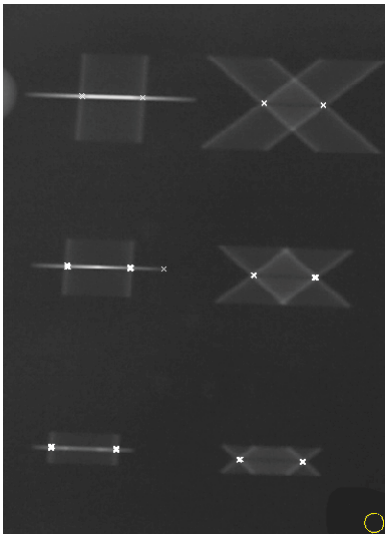

Figure 3.14: Centres of cross targets identified

This algorithm used a moving circle to traverse the image capturing a profiles of pixel intensities on the circle's circumference at each position. The circle would move progressively from location to location whilst the algorithm attempted to identify four 'peaks' in the pixel intensities. Once identified, alternate peaks could be joined by two intersecting lines, their intersection marking the estimated centre of the apparent 'cross' image. The algorithm was iterative, the circle moving closer to the centre of the cross target with each iteration.

The lines of the cross were identified by only a small number of pixel intensity values. For the larger blurs, the target became rapidly indistinguishable. To make the cross bolder, crosses with broader strokes were used and these were identifiable more easily, but the accuracy of marking the centre was reduced. Cross centres also became difficult to distinguish when the motion was not sinusoidal.

Although each extent of the blur was measured at the centre of the cross, the measurement approach does not associate pairs of measured points belonging to a single target with each other. If more than one target existed in an image, it would be possible to incorrectly link marked points. Although corresponding points are likely to be relatively close to each other, relying on proximity alone could be unreliable (figure 3.15). This test identified the need for a target recognition algorithm capable of measuring multiple points of interest on a single physical target that are associated, rather than measuring different points of interest on the target independently.

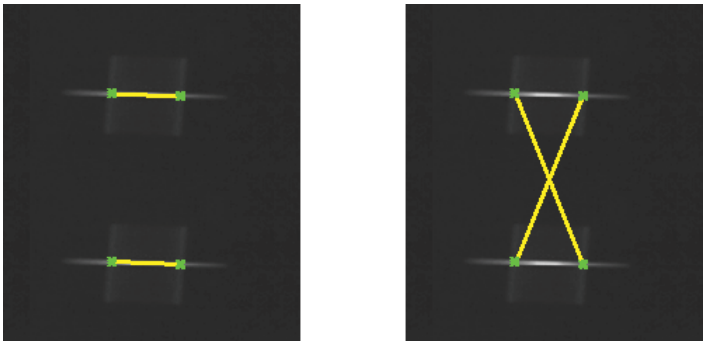

Figure 3.15: Pairs of marks are not associated hence it is possible to incorrectly link marks where targets are near each other.

3.2.3.2 Circular targets

Circular targets are regularly used in photogrammetric work for marking control points and other object points of interest. Advantages include that they are easily identifiable, rotation invariant and can be accurately measured. Circular targets were included on the test sheet on the shake table and their appearance in images was also examined.

The appearance of motion-blurred circular targets was found to conform to two patterns, depending on the amplitude of the vibration in relation to the target diameter (figure 3.16). In the first case, where vibration amplitude is smaller than target diameter, a region of the image is always occupied by the black target, and pixels in this region take a value the same as the black of the un-blurred target. Two approximate crescent regions are generated on either side of the central dark region, arising from exposure to both the black target and the white target border during the time the shutter is open. Pixels receive a value related approximately to the amount of time they exposed to white or black, but as discussed later in section 3.2.2.3, post-processing steps are apparent which make this relationship not linearly proportional.

The use of circular targets is also similar to past approaches for monitoring tests using static (Benning *et al.*, 2004; Albert *et al.*, 2002; Valença *et al.*, 2012; Yilmazturk and Kulur, 2012; Thomas and Cantré, 2009; Maas, 1998) and dynamic (Choi *et al.*, 2011; Lee and Shinozuka, 2006a) techniques, and is familiar to photogrammetrists. The arrangement of circular targets for monitoring would also be suitable for the deformation monitoring approaches demonstrated in these papers.

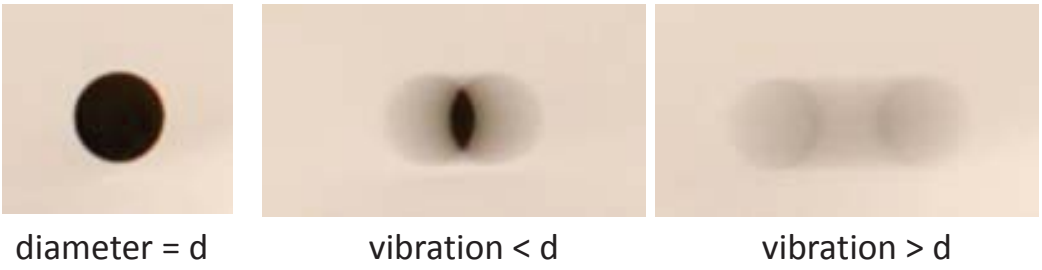

Figure 3.16: Motion blurred circular targets where motion is smaller and larger than target diameter. The motion-blurred images correspond with figure 2.11(b) and (d) by Kraus (1993).

3.2.3.3 Image correlation of circular targets

Whilst circular targets were tested extensively on the shake table, the effectiveness of the earlier tested image correlation approach with circular targets were considered further. To develop a procedure to estimate the displacements, simulated images of blurred circular targets at different motion amplitudes were created and compared with the as-taken motion-blurred image. Sinusoidal PSFs of different motion amplitude were defined as in previous testing (section 3.2.2.3) and then convolved with an image captured with no motion using Matlab's 'imfilter' function.

It was noticed that the position of the table at rest was different to the centre of the mid-point of the table's motion. This factor had not been previously appreciated with less structured images being considered. Rather than computing one correlation statistic for each test motion amplitude, it was necessary to calculate cross-correlation coefficients to locate where the mid-point of the table's motion matched the sinusoidal image, and the highest coefficient was accepted. The correlation coefficient for each tested amplitude was, therefore, calculated using Matlab's 'normxcorr2' cross correlation function, with the maximum value accepted.

As shown in figure 3.17, the simulated and as-taken images are broadly similar. A peak in the correlation statistics could be identified, and at first it was thought that would represent the correctly identified motion, but as previously a similar systematic error remained.

It is also noted that whilst images can be correlated and the highest correlation

Figure 3.17: (a) As-taken and (b) simulated image of a motion blurred circular target

accepted, the correlation coefficient does not indicate the direction to improve the result whilst iterating displacements. Many iterations are therefore necessary before a solution is found. If the approach was extended to also consider direction, the number of iterations would increase exponentially.

3.2.3.4 Edge Detection

Differences in absolute pixel intensities between as-taken and simulated images exist, restricting the use of correlation methods alone. An alternative approach was required and comparing detected edges was tested, as it was observed that although absolute pixel values may differ, edges of gradients in blurred circular targets did coincide. Instead of iterating to achieve the highest image correlation statistic, iterating to achieve the same detected edges was proposed.

Circular targets were again used, although it is likely that if successful, it is possible that this approach would be suitable for other targets. Chang and Xiao (2010) used edge detection for measurement of a specific chequered target.

A range of edge detection algorithms are available, and each has its own set of advantages and disadvantages. None can be applied universally to all cases, so a range of the default edge detection algorithms in Matlab's build in 'edge' function ('Sobel', 'Prewitt', 'Roberts', 'Log' and 'Canny') were applied to images of blurred circular targets, and outputs compared. Figure 3.18 shows that the Log operator appears to effectively identify the edge at the extreme periphery of the blurred target subject to motion approximately equal to the targets diameter. However, when the target was subjected to a smaller amount of motion the same edge is not identified (figure 3.19). The edge detection

algorithms also showed changing effectiveness under different lighting conditions.

These images were then compared to simulated images of the same motion within the same edge detection algorithm applied. Matching images were found to not be susceptible to the systematic error encountered earlier (section 3.2.2.3). Although not suffering this error, the approach alone can only achieve pixel level accuracy, since the detected edges are restricted to pixel level resolution.

3.2.3.5 Pixel Intensity Profiles

Edge detection methods did not appear to introduce a systematic offset error, yet had poor precision. Boracchi *et al.* (2007) discuss an image processing approach for measuring the velocity of sports balls (which appear as motion-blurred circles) from its motion blurred image. This approach was tested for this application. The approach establishes a series of intensity profiles of pixels through a motion-blurred circle. Changes in gradient are then identified as features within the blurred circle. Points are then marked around certain features of motion-blurred circular targets, and finally, ellipses are fit to compatible points for each end of the motion.

A simple thresholding filter was first applied to the image of the target so that the target can be identified. Instead of using Otsu's method to choose a threshold between distinct pixel intensity differences (The MathWorks Inc., 2014a), a higher threshold is selected to ensure that the whole target region is detected (figure 3.20). Some simple measurements about the target geometry were made, such as the orientation and length of the major and minor axes. This information provides a rough estimate of the size and orientation of the motion, and the pixel intensity profile lines are then arranged, with the appropriate length, orientation and spacing.

The intensity profiles are extracted in turn. The intensity profile line was sampled using bilinear interpolation and represented by a vector. The line was sampled 200 times, since this was adequate to pick up sufficient detail about the changes in gradient. Pixel intensity profiles (PIP) took one of two forms, depending on whether the motion is less or greater than the diameter of the target, and both cases are shown in figure 3.21. Changes in gradient were identified in the PIP, and the respective coordinates of the gradient changes in the image determined.

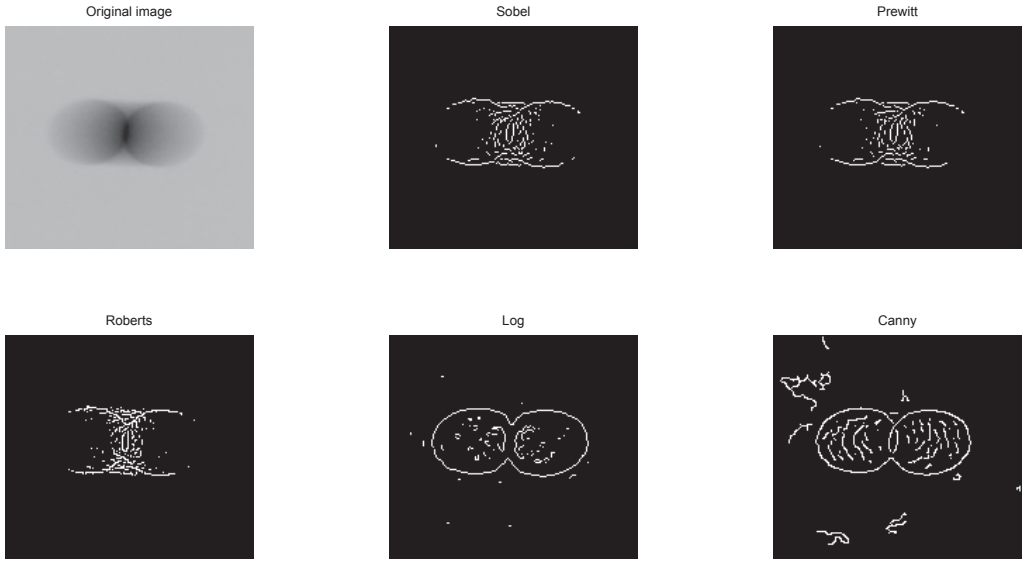

Figure 3.18: Various edge detection algorithms on a motion-blurred circular target (motion approximately equal to target diameter

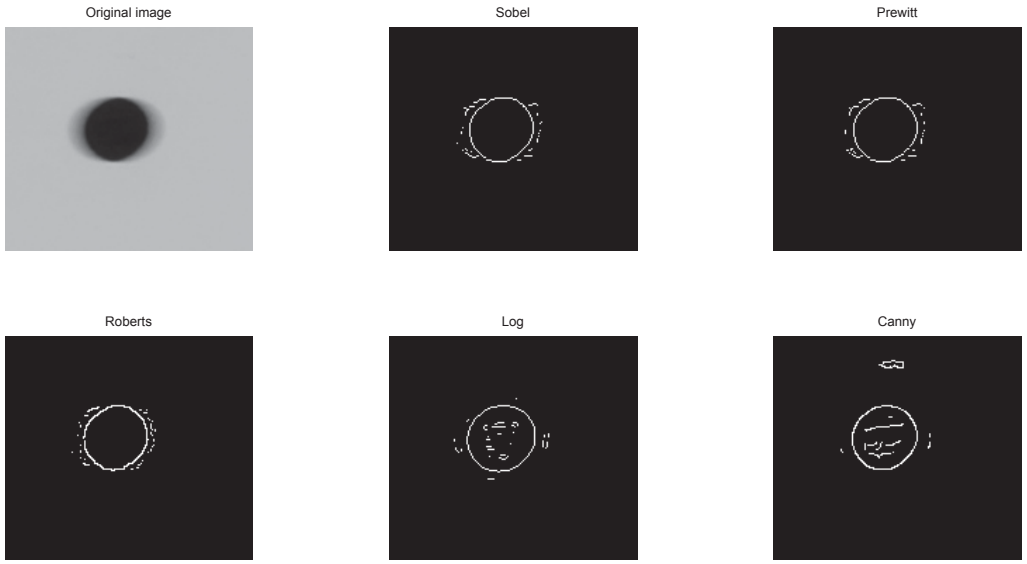

Figure 3.19: Various edge detection algorithms on a motion-blurred circular target (motion smaller than target diameter

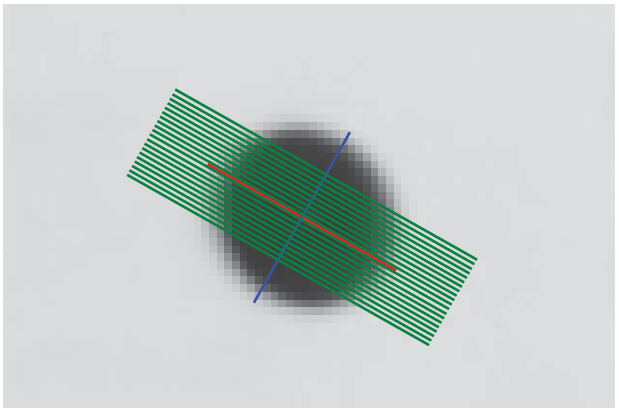

Figure 3.20: A threshold is used to identify the target, and some simple estimates about its geometry are made. The red and blue lines represent the major and minor axes, and the green lines repeat the profile lines.

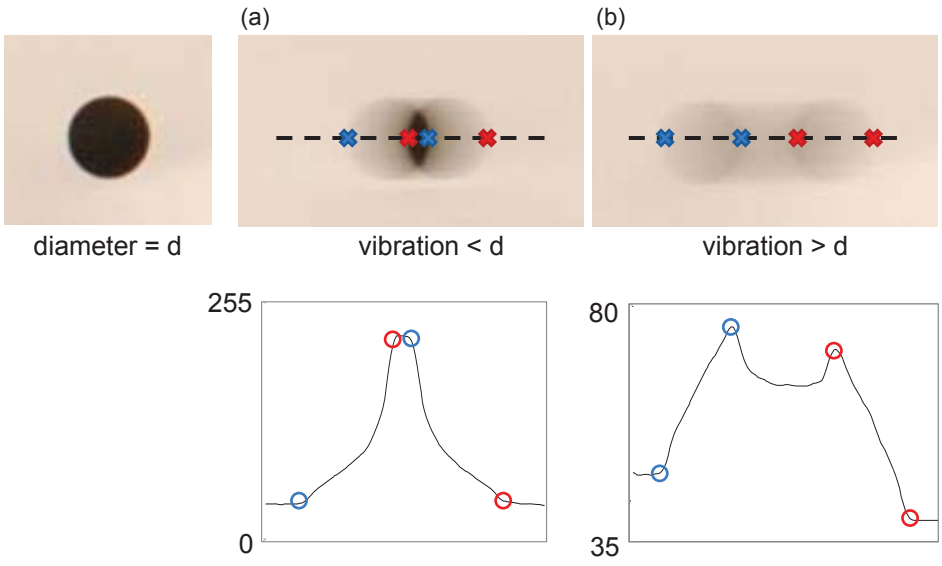

Figure 3.21: Pixel intensity profiles where target motion is (a) less or (b) greater than target diameter. Changes in gradient are marked

As the image coordinates at gradient edges are recorded, they were separated into their respective edges depending on whether they precede or follow positive or negative gradients. The collected coordinates were then used to establish two best fit ellipses. The difference in coordinate between the two centres of this ellipse were then accepted as the motion. A pair of image coordinates at either end of the motion path then existed in the ellipse fit parameters, and a statistic of the quality of fit at points to the ellipse could be calculated. From the difference in the pair of image coordinates, it was possible to determine both the length and orientation of the image motion-blur.

From a series of tests, the algorithm demonstrated reliability in the various tests that have been carried out, having shown to be capable of handling different lighting conditions, and different blur sizes. The approach was faster than the correlation technique, since iteration is not required, providing a distance and a direction in one step. Unfortunately, the approach introduced another systematic error caused by a soft edge effect, with motion blur distances being slightly overestimated. Even stationary targets produced a small displacement with this approach. This is because soft edges are found at the edge of the target caused by the imaging process, including: lens diffraction, chromatic aboration and spectral mixing. A method was found to compensate for this challenge which was developed into the proposed solution in this thesis. This solution will be now explained in the following section.

3.3 Proposed Solution (LEMBI measurement)

The pixel intensity profiles (PIP) approach was identified as being the most effective, although suffering from a systematic error. To account for the soft edge effect, a sharp unblurred image needed to be captured in addition to the blurred image. In a testing environment, this would be done before dynamic excitation is applied. An alternative would be an ordinary short-exposure image with appropriate exposure settings. By applying the PIP algorithm to the sharp image, the overestimation made due to the soft edge effect could be determined. Furthermore, testing revealed the benefits of combining the PIP approach with an iterative scheme. This involved a similar procedure for the image correlation approach introduced above substituting PIP measurements for image

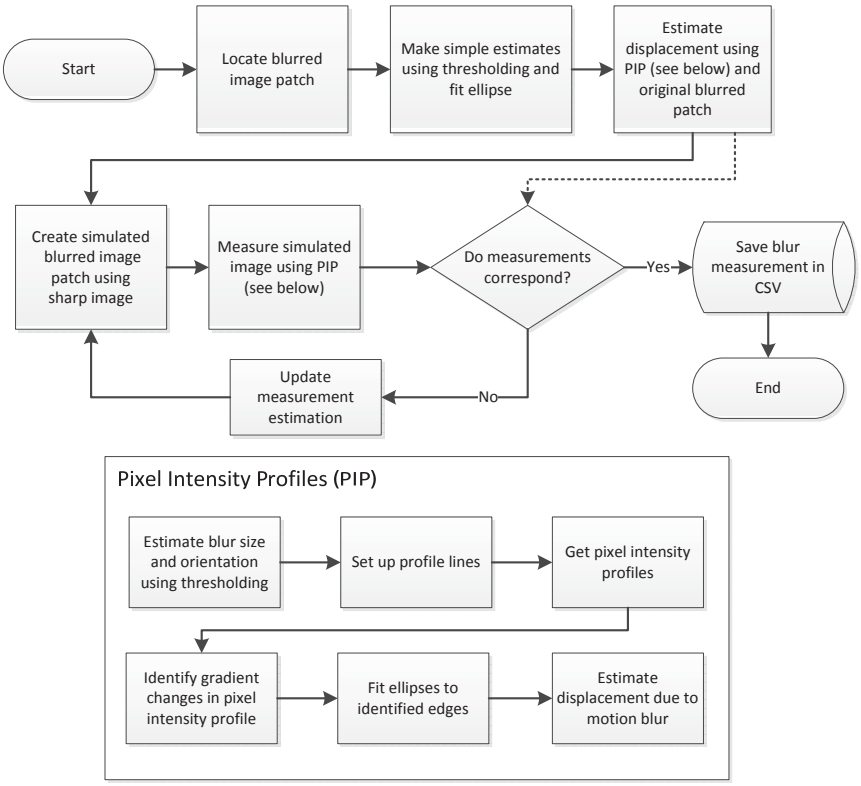

Figure 3.22: Flow chart of LEMBI measurement calculation steps.

correlation statistics. This combined solution was named long exposure motion-blurred image monitoring (LEMBI monitoring). The key algorithms that make up the LEMBI monitoring system are include in appendix C.

An initial estimate of the target's position and geometry in the blurred image was first made using a simple threshold filter. The threshold value needs to be nearer to the value of the white target background, so that the identified region would include the lighter pixels around the target periphery that are part of the motion smear. An ellipse was fitted to the detected region using least squares, and the estimated major and minor axis, and orientation allows arrangement of the profile lines for the next stage.

The PIP technique is then used to estimate the motion in the as-taken blurred image. Using this estimated motion extent and direction, a sinusoidal PSF was artificially generated (using the algorithm described in section 3.3.1). A blurred image was simulated by convolving the earlier taken short-exposure sharp image with the generated PSF.

After generating the artificially blurred image, it was compared to the as-taken blurred image. The difference to the earlier approach is that, instead of making a comparison

using a correlation statistic, the comparison was made using PIP. The result of the PIP algorithm (motion extent and direction) was compared, and the parameters used to generate the artificial image iterated until the PIP output of both artificially blurred and as-taken blurred images match (to within a user defined tolerance). Conveniently, and unlike the correlation approach, the difference in PIP outputs suggests which direction to change the parameters for the next iteration, and suggests this for motion extent and direction separately.

This approach had the precision of the PIP technique, whilst compensating for its inherent systematic error by simulating the effect of the soft edge error has on target measurement. The soft edge effect in the as-taken blurred image also existed in the simulated blurred image, and cancels out in the comparison stage. Calculation steps are summarised in figure 3.22.

LEMBI monitoring has the same requirements as the original PIP approach necessitating circular targets to be applied (section 3.2.3.5). Only a few iterations in the final stage was necessary since the discrepancy in PIP measurements closely indicated the adjustment necessary. It was necessary, however, to implement a limit on the number iterations so that the algorithm would not occasionally reach an infinite loop, in which case an error would be recorded. Such a situation could occur if an image patch was incorrectly loaded that did not contain the expected image structure.

The previously discussed correlation approach did not have a dependence on artificial targeting, whereas circular targets are a requirement of this approach. Whilst this would increase set-up time and could add practical difficulties for some test monitoring, it does offer better reliability and precision.

The developed LEMBI monitoring system relies on a static camera position. This was controlled by the camera being on a tripod, which was on a stable surface, and the camera always being activated by remote or with a long self-timer to avoid shaking the camera body. Whilst processing images, control targets were checked for consistent coordinates (in case of between-capture motion) and motion-blurred appearance (in case of inter-capture motion). Whilst some the case studies discussed in section 2.3.1 demonstrated that compensation of camera movement is possible using control targets within the image, the possibility of camera movement during the acquisition of a long-exposure image would

be more disruptive to the image, and require a more advanced compensation algorithm.

A number of input parameter had to be defined, the values of which were initially tuned during initial testing until a set of values that required no further adjustment were found. Although they were available for adjustment, it was found that target measurement would remain effective during future case studies. These parameters included constants for positioning the geometry of the intensity profile lines in relation to the target's estimated size and orientation after the initial estimate. In general, the results were not effected by their precision positioning, so long as they extended a distance outside the target edge so the edge of the target's motion path is clear. Also included was a sensitivity value for the detection of feature points in an individual PIP, expressed as a proportion of the range of pixel values within an image patch to deal with images which were darker or lighter than the test images.

3.3.1 Point spread function generation

Correct simulation of a blurred image was dependent upon the use of an appropriate point spread function (PSF) that accurately describes the motion causing the blur. Kraus (1993) discusses how the resultant blurred image differs as different forms of motion are applied (section 2.4.5).

Initally, Matlab's 'fspecial' function with the 'motion' option was used to generate PSFs for a given motion. However, the resultant PSF was one which assumed constant velocity motion, rather than sinusoidal motion, so an improved PSF function was written. This function addressed motion magnitude and rotation separately so, appropriately, a polar coordinate system was used where L is the distance and r is the rotation. This one dimensional function for motion magnitude is defined by:

$$f(x) = \begin{cases} 0, & x < \frac{L-1}{2}; \\ \left(\cos\frac{2\pi x}{L} + 1\right)\beta + \alpha, & \frac{L-1}{2} \leq x \leq \frac{L+1}{2}; \\ 0, & x > \frac{L+1}{2}; \end{cases} \tag{3.4}$$

where L is the desired motion amplitude; α is a user defined constant and $\beta = \alpha - 1$.

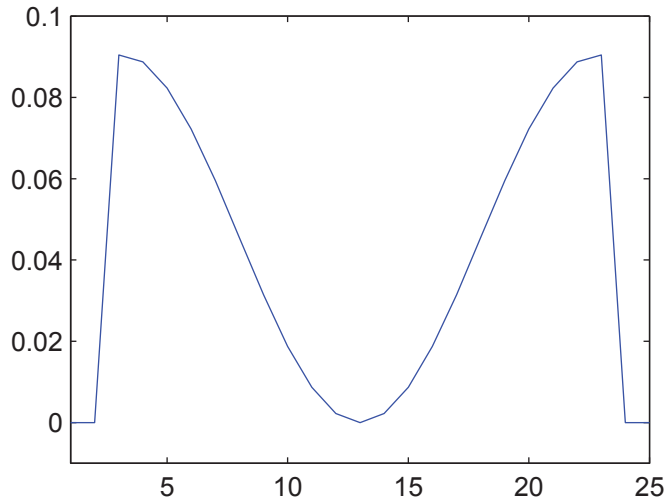

(a) Intensity profiles of linear 1D point spread function

(b) Point spread function as an image

Figure 3.23: Point spread function generation function

The one dimensional harmonic function is shown in figure 3.23a. The constant α was initially introduced to tune the shape of the harmonic curve, but tests showed $\alpha = 0$ produced the most effective results. The one dimensional function was padded to create a matrix, giving a two dimensional PSF in a horizontal direction (figure 3.23b). This PSF was then rotated by the necessary angle using Matlab's 'imrotate' function (figure 3.23c).

Finally, the sum of all values in a PSF must sum to unity, otherwise the resultant image will be darker or lighter than the original. This was achieved by dividing the by the sum of all matrix elements.

3.3.2 Gradient Change Point Identification

Detailed testing revealed that the measurement result was influenced by the method used to determine the gradient change points on the pixel intensity profiles lines. The pixel intensity profiles though a blurred target are consistent. Each pixel intensity profile requires four gradient change points to be identified. These feature points should be identified in the same location in the as-taken and simulated blurred images (figure 3.21).

Different gradient change detection algorithms were tested. The simplest used two thresholds aligned slightly below the maximum pixel value and slightly above the minimum pixel value (so as to avoid detecting sensor noise). Where the pixel intensity profile crossed these thresholds, feature points were marked. This approach provided a simple solution, particularly for the 'internal' blur case, but did not respond to the 'external' blur case or variations in image quality robustly.

A more advanced method was to differentiate the pixel intensity profile to identify changes in gradient. Changes at the start and end of positive and negative gradients were identified from peaks and troughs in the double integrated data. The resulting data was noisy and needed filtering. The algorithm was effective for both cases of 'internally' and 'externally' blurred targets.

A significant difference between the 'internally' and 'externally' blurred targets is the ordering of marked gradient points with respect to the start or end of the motion blur path. For the external blur, the two consecutive identified points correspond to one ellipse at the end of the motion path (figure 3.21). For the internal blur case, the allocation of identified points to each ellipse alternates.

Conveniently, for the differential gradient approach described above, the detected gradient change points were automatically allocated to the correct ellipse. The gradient change points for the first extremity of the target's motion were identified at the start of the first positive gradient and the start of the first negative gradient (figure 3.24). The points of the other extremity of the target's motion were identified at the end of the last positive gradient and the end of the last negative gradient. The internal blur PIP comprises only one positive gradient section and one negative gradient section, and therefore the first and last sections of the positive and negative gradients are the same sections. A significant distinguishing feature of the external blurred target PIP type is the central 'U' part of the PIP, which encompasses additional positive and negative gradient sections. The external blur PIP therefore has two positive and two negative gradient sections, and the detected gradient change points automatically adapt.

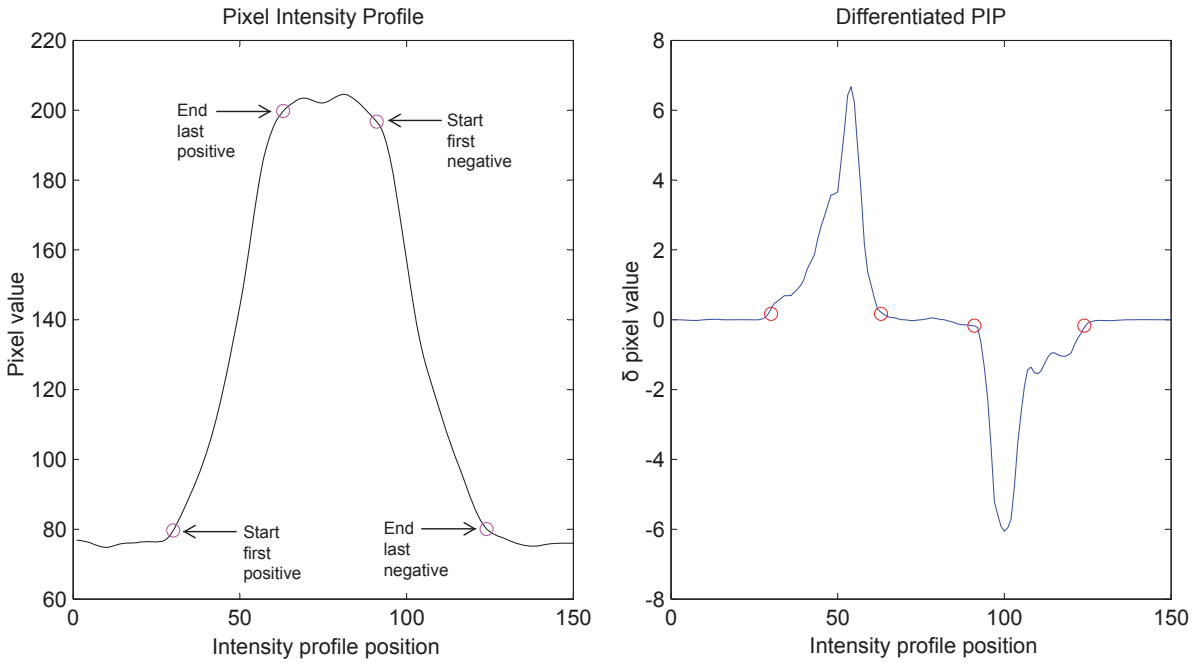

Figure 3.24: Identifying gradient change points in Pixel Intensity Profiles (PIPs)

3.4 Assessing the Accuracy of the System

As with any measurement system, an understanding of the accuracy of the system is important. Accuracy was assessed in another series of simplified tests. These tests were also used to appraise the gradient change identifications methods during their development (section 3.3.2), so that improved algorithms could be identified. Targets were mounted directly to the table surface. Since the table motion could be accurately recorded by the attached sensors (section 3.1.4), the results measured with LEMBI monitoring were compared directly with the motion recorded by the laser displacement gauge.

Four black circular targets on a white background were mounted directly to the table bed. The wooden stands introduced earlier (section 3.2.1) were used to provide control points in the image, and where positioned on either side of the table, with the control targets lying coplanar to the table-mounted targets. These were again measured by a reflectorless total station and coordinates calculated using the spreadsheet described in section 3.2.1.

The monitoring instruments described in section 3.1.4 were utilised. A Nikon D80 camera 3.1.1 was positioned on a tripod in front of the model structure so that its imaging axis was approximately perpendicular to the axis of expected motion. It was not necessary

to ensure the imaging plane is exactly coplanar to the object plane as the projective transformation will appropriately calculate object-space coordinates, taking perspective effects into account (section 2.4.3). The camera was set for manual exposure settings, with aperture set to f/22, sensitivity set to ISO-100, and an exposure time of 1 second. The camera was also attached to the double external trigger which was connected to the shake table's control computer (section 3.1.1) for convenient activation. An image was taken before any motion took place, which is required for the LEMBI measurement algorithms (section 3.3).

The shake table was programmed to carry out sinusoidal motion in a series of tests with incrementally increasing amplitude. In each test, the table received an input signal of the motion for 5 seconds, so that the table would reach steady-state motion. The shake table controller would then send a signal to the camera external trigger for the image to be taken. Once complete, the shake table controller saved the recorded sensor data to a file, and then prepare for the next incrementally higher amplitude test. The highest amplitude was 13.7 mm, which was reached in 30 increments.

Images were then processed using the LEMBI algorithm described in section 3.3. The sharp image taken when the shake table is at rest was processed using the PhotoModeler software package. PhotoModeler's automated 'RAD coded' target recognition was used for measurement of the control point targets and the coordinates were exported to a CSV file. Image coordinates for control points had previously been measured in Matlab using a weighted centroiding algorithm and identified with a target coded ring recognition algorithm. In the later implementation, PhotoModeler's own target recognition was used and coordinates exported, since PhotoModeler used least squares matching for target centroiding, which is often considered superior to the weighted centroid (Luhmann, 2011).

PhotoModeler was also used to manually identify the uncoded monitoring targets using automatic target recognition of dot targets. A 'target_coordinates.csv' file was created from this to inform the algorithm the location of the targets. Whilst the LEMBI measurement algorithm carried out accurate coordinate measurement, it must be told the approximate location of the target because the motion-blurred targets are more challenging to distinguish, identify and locate in the image from other features. Other input files included a list of target detection parameters which were identified when the algorithm

was originally created, and a list of image files to process.

The output from the bespoke image processing algorithm was a CSV file for each image containing the measured end coordinates (in image space coordinates, i.e. in pixels) for each blurred target, named '[*original image filename*]_points.csv'. Also saved in this file were values from intermediate stages of the image processing that can be used as quality estimates.

At this stage, the measured coordinates exist in image-space coordinates of pixels. It was necessary to obtain object-space coordinates that can be compared with other external independent measurements. To do this, the projective transformation was applied, making use of the earlier measured coordinates of the control points (section 2.4.3). Matlab contains a library of function for spatial transformations. Pairs of coordinates of control points for both domains are passed to the 'cp2tform' function, which generates the parameters of the spatial transform. Coordinates in either domain could then be transferred between the two using the 'tformfwd' and 'tforminv', depending on the direction required. Transformation parameters were determined using 'cp2tform' and object space coordinates determined using the 'tformfwd' function from the coordinate pairs.

The object space LEMBI measured coordinates were directly compared with the displacement recorded by laser displacement gauge. Results are given in figure 3.25. By subtracting the displacement as measured by LEMBI from measurements by the laser displacement gauge, the error in the measurement was calculated. A regression analysis of these errors was made to evaluate the accuracy. The results of the regression analysis are provided in table 3.2, with the full regression analysis results included in appendix D.

A standard deviation of ± 0.158 mm was observed, with a mean error of just -0.115 mm for a camera-object distance of 1 m. Using a 95% confidence interval, the measured distances are considered accurate to within 0.38 mm. In the image space at this scale, this represents 1.43 pixels at the 95% confidence level. Whilst the accuracy of the current measurement algorithm when expressed in pixels is poorer than conventional target measurement algorithms such as weighted centroid or ellipse fitting, images are obtained at the sensor's highest resolution without having to consider the imaging frequency limitation.

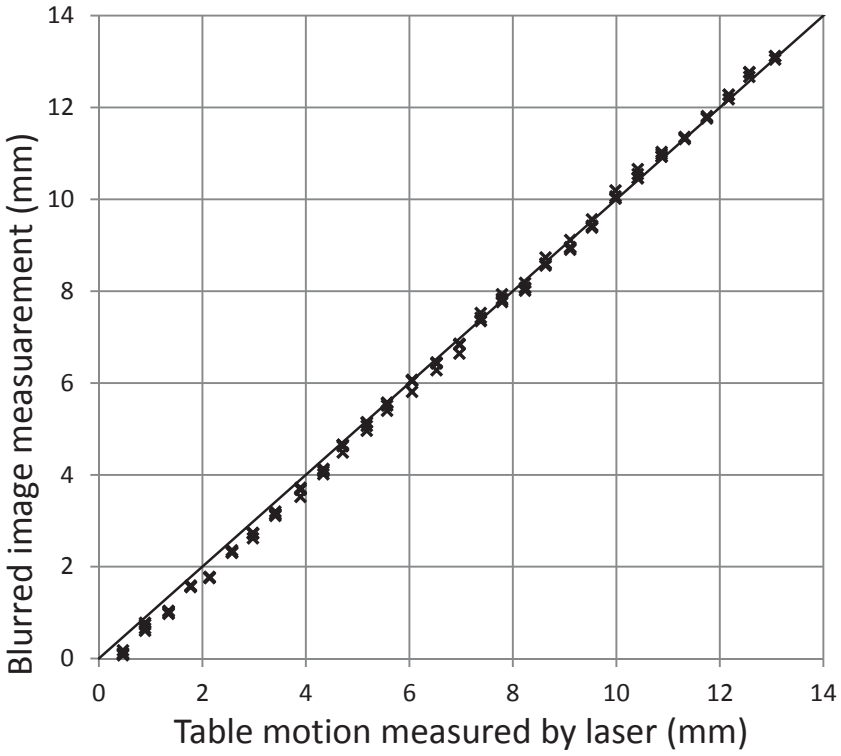

Figure 3.25: Comparison of LEMBI measurements with independent reference measurement (laser displacement gauge)

3.5 3D monitoring

The ability to extract data in 3D is a particular advantage of photogrammetry, and the potential to monitoring 3D movement is particularly relevant to structures which can experience both in-plane and out-of-plane deformations. LEMBI monitoring has been implemented for 3D monitoring also by using two camera which can be triggered simultaneously, creating a pair of motion blurred images. It was therefore important to develop the method to resolve 3D motion vectors. The original algorithm remains of use for determining target coordinates in the image, and further calculation steps (figure 3.26) were added to determine 3D coordinates.

3.5.1 Camera orientation

To determine the position of the ray projected from the projective centre of the camera to a point in the object space, the exterior orientation (EO) of the camera in that object space must be determined. Rather than carefully controlling the camera's position and

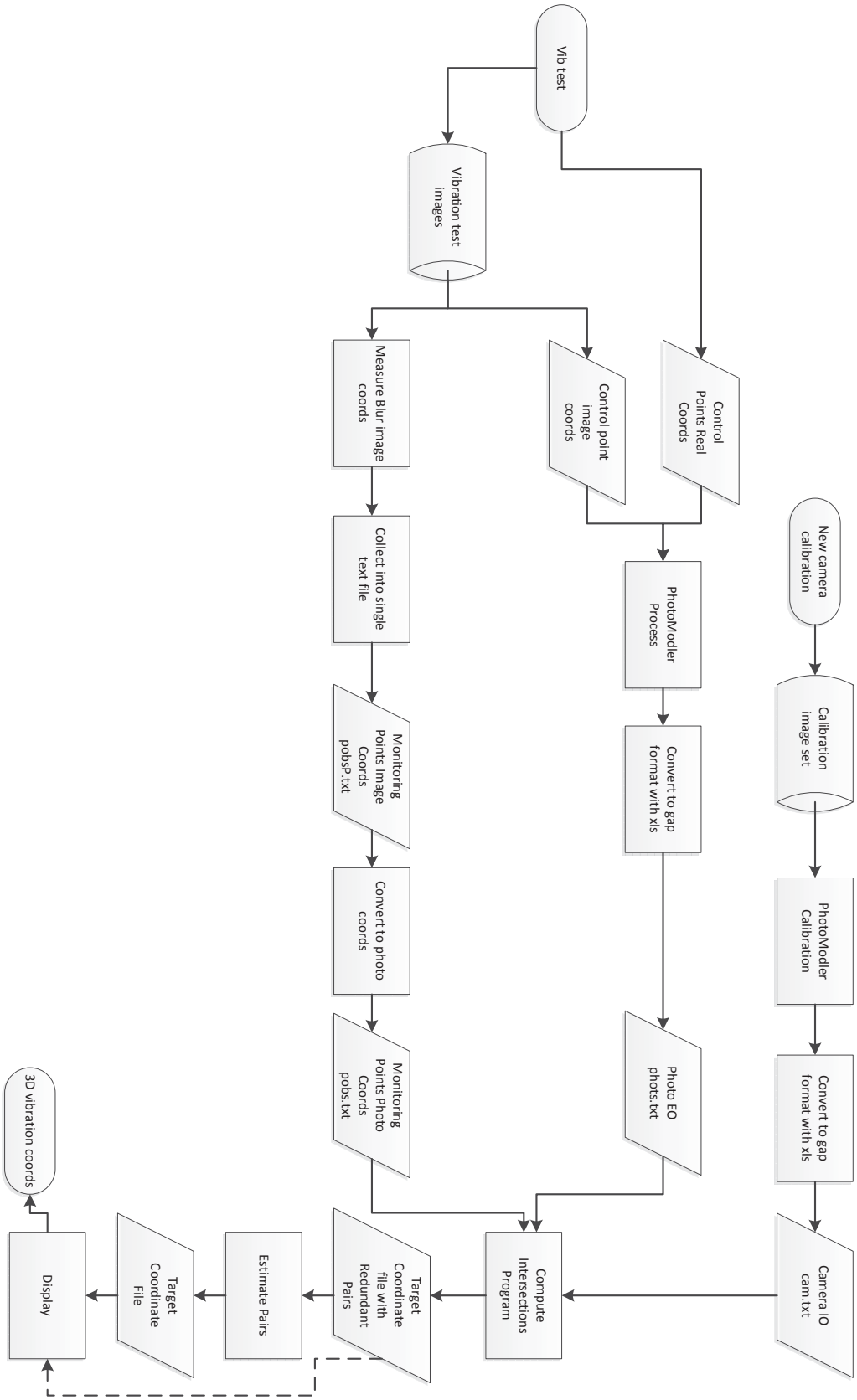

Figure 3.26: Calculation steps for 3D measurement

Summary Output

Regression	Statistics
Multiple R	0.999688
R Square	0.999376
Adjusted R Square	0.999370
Standard Error	0.095532
Observations	115

ANOVA

	df	SS	MS	F	Significance F
Regression	1	1653	1653	181105	6.096E-183
Residual	113	1.0313	0.009127		
Total	114	1653			

	Coefficients	Standard Error	t Stat	P-value
Intercept	-0.3369	0.0181	-18.600	3.501E-36
X Variable 1	1.035	0.002432396	425.6	6.0964E-183

	Lower 95%	Upper 95%	Lower 95.0%	Upper 95.0%
Intercept	-0.3727	-0.3010	-0.3728	-0.3010
X Variable 1	1.030	1.040	1.030	1.040

Table 3.2: Accuracy regression analysis summary (full results in appendix D).

orientation, it is generally more convenient to arrange the camera so as to get a suitably composed image, and then determine its orientation from coded control targets in the image. As in the 2D case, control targets are arranged in the image, and their 3D object-space coordinates recorded.

A reflectorless total station could be used to make observations to the centre of each control target. Where used here, the whole circle bearing (WCB), vertical circle (VC) and slope distance are recorded to each control target. These observations were input to a spreadsheet that calculated the 3D X, Y & Z object-space coordinates for each target. The coordinate list is converted from a CSV file to an 'INI' configuration file to be read into PhotoModeler. The sharp images captured initially were loaded in to PhotoModeler, which measures the targets in the images and, will automatically determine the EO parameters (x, y, z, ω, ϕ, κ) for each individual image in the object-space coordinate system. The coordinate system itself is arbitrary, but necessary to generate data in a real work system where scale is defined (in millimetres) and the x and y axes aligned to correspond with local gravity.

The interior orientation of the camera was determined as before using the earlier constructed camera calibration field (section 3.1.2) and the inner geometry of the D80 cameras assumed to be sufficiently stable for monitoring deformation of the structure.

3.5.2 Monitoring target marking

Whilst the sharp images are loaded in PhotoModeler, the un-coded monitoring targets are also measured. These determined centroid coordinates were not used to measure deformations, but were used to inform the blurred target measurement Matlab routine where to locate blurred targets. PhotoModeler was used because it provides convenient tools to locate and mark targets in images, although some manual intervention is necessary to correctly identify monitoring targets from other apparently circular image patches of other objects in the photo. PhotoModeler's can also be used for target matching, since it's automatic routine is efficient and saves time later. These measured coordinates are exported to PhotoModeler's 2D point table.

All coordinates are originally exported into one table, and this coordinate list is later separated in to one table per camera. Each camera's coordinate list is input to the blurred target registration algorithm along with the relevant as-taken blurred image. The motion-blurred targets are then measured using the approach described in section 3.3 above, to determine the extent and orientation (motion blur) of each target. These data are then stored, one table for each image.

3.5.3 Point matching

Each target now has four image point coordinates (in each image pair). Image 'target' and 'point' measurements may often by synonymous in photogrammetry, since each target usually has only one measurable point. With blurred imagery, however, each target is represented by two points representing either end of the target's motion. Although target matching was carried out by PhotoModeler, point matching is incomplete. Figure 3.27 illustrates the difficulty in point matching when the two image points originate from the same physical target. The problem is exacerbated since points originating from one physical target cannot be uniquely coded in the picture.

Point matching is not solved at this stage. Each possible combination of point measurements in created, which in the case of two images is two combinations. The correct combination of points will be identified later, and the additional combinations discarded

A point coordinate list is created, duplicating coordinates into the two combinations. Individual observations are given the suffixes 1A, 1B, 2A and 2B, where 1 and 2 designate the two points either end of a motion path, and A and B designate the two unknown combinations.

This list is converted and stored in a 'GAP' format 'pobs' file (Chandler and Clark, 1992). GAP format files are used hereafter for compatibility with the GAP bundle adjustment programme and other software tools already available that work in this format. GAP format files work in photo coordinates of microns, rather than image coordinates of pixels. The list is first saved as a file names 'pobsP' which contains measurements in units of pixels, and these are then converted in to the 'pobs' file by simply multiplying by a scaling constant relating the image width (in pixels) and sensors width (in millimetres). GAP format files are also created for the earlier determined camera interior orientation (in a 'cam' file), exterior orientation (in a 'phots' file).

Having all this information, a bespoke intersection program is now used to compute 3D coordinates for each point. By knowing the exterior orientation of the two cameras and applying the approximate correction for inner orientation (lens distortion) it is possible to determine the 3D position of the points in both images. This uses a well established approach known as space intersection (Luhmann *et al.*, 2006). Basic code provided by Chandler (2013) was adopted for this task.

3.5.4 Resolving the valid points

Recalling that image coordinates were duplicated earlier since the correct pairings were not known, half of the coordinate combinations are correct, and half are not, but the intersection program would create the object space coordinates in both cases. The two combination cases were denoted A and B, and image coordinate residuals were computed for each point in every combination by reprojecting points back on to the imaging plane and finding coordinate differences. The separate X and Y residuals for each point were

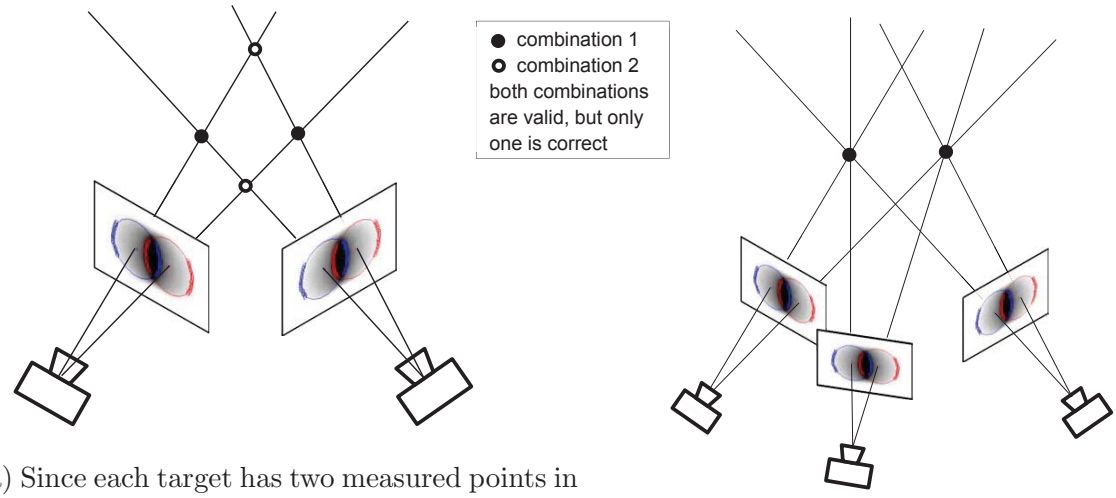

(a) Since each target has two measured points in close vicinity to each other, possible erroneous point matching must be considered

(b) Three sensor can eliminate the ambiguity

Figure 3.27: 3D Point Matching Difficulties

combined by using the Pythagorean theorem, and the combination with the lowest combined residual is accepted as the correct combination. The incorrect combination was deleted.

Having identified the valid combination of coordinates, these, together with the camera's IO and EO determined earlier are input to a bundle adjustment using the 'General Adjustment Program' (GAP) to derive final 3D coords to represent the two ends of the measured blur (Chandler and Clark, 1992).

3.5.5 Laboratory Testing

To test the 3D monitoring approach during development, further tests where carried out on the structural dynamics shake table. The two cameras used were D80 cameras with 24 mm fixed focal-length lenses. Two remote camera triggers (although potentially more could be used) had been wired together to allow cameras to be triggered simultaneously (section 3.1.1). Complete demonstrations of 3D monitoring on the shaker table are included in section 4.4.

3.5.5.1 Relative camera position problem

During tests it was observed that difficulties can arise if the deformation line in 3D space is aligned to the epipolar plane. This happens particularly when the direction of the target's motion is the same as the direction of the cameras relative positions. In this case it can become impossible to automatically determine the correct combination, since both combinations are valid and produce small residuals. A third camera could be used to resolve the ambiguity (figure 3.27b), although this would then create $2^3 = 8$ combinations of matched target measurements from which the one and only correct combination would need to be identified. This would also add redundancy to the measurement system. The correct combination could also sometimes be manually identified using engineering judgement of the likely motion.

It was found that the problem could be avoided if the likely direction of the object's motion is known a priori, and the camera arrangement selected so that the problem would not occur. In this case, motion direction was expected to be horizontal, so arranging the cameras on tripods so that they were at different heights meant that the deformation line differs from the epipolar plane, enabling the correct matching points to be easily identified.

3.5.6 Data representation

3D displacement vectors for every measuring point were stored in a matrix. Whilst an engineer might desire the full numerical displacement vectors for a few key locations in different situations, it is easier to appreciate relative movements of the whole structure graphically. A visualisation of the structure with displacement vectors overlaid could be one effective way of showing this. In fact, showing the pair of images with their individual 2D displacements overlain together may be enough to visualise the 3D movement. This approach would be suitable for printing results on paper, but would restrict the viewpoint.

In the demonstrated solution, Matlab's 'quiver3' function created 3D arrows in a rotatable viewport. Displacement vectors are typically small, and it is desirable to 'scale up' the vectors to visualise movements. The current system generates two coordinates to represent either end of the motion. The mean of the two coordinates is calculated,

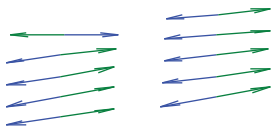

Figure 3.28: Example graphics from Matlab's quiver3 function. Two opposing vectors are drawn (scaled up) through the pair of 3D coordinates

and subtracted from the coordinates to give individual displacement vectors. The arrows produced by the 'quiver3' function are conveniently scaled to suit the display, otherwise the displacement vectors are multiplied by a constant before being displayed (figure 3.28).

3.6 Summary

This chapter has examined a range of different strategies for measurement of vibrating structures using blurred images. Different algorithms were tested for processing images, along with the different surface targets and texture types. Algorithms with accompanying target types were compared with algorithms suitable for any surface with sufficient texture.

The artificial targeting approach was considered best suited for monitoring vibrating structures. The LEMBI measurement algorithm has been developed for measuring coordinates from blurred images, making use of an additional sharp image to improve accuracy by compensating for a systematic error. The additional calculation steps necessary for determining 3D displacements have been discussed and a working solution described, which resolved additional point match difficulties not encountered in usual photogrammetric measurement using sharp images. This chosen approach will be demonstrated further in this thesis and the next chapter demonstrates the monitoring approach in a number of case studies.

Chapter 4

Results

The previous chapter derived the method developed for the monitoring of moving circular targets and assessed its accuracy. This chapter describes the application of the approach to four case studies.

In this section the terms large and small scale are used in the same sense as when photogrammetry is used in the process of map making, in that small-scale tests are of objects of large extent, which require the most scaling; and large-scale tests are of smaller objects that can often be represented with more detail.

A small 770 mm tall model was excited with 1-D motion in the lab, to demonstrate how the technique would be applied to a tall structure, and planar 2-D motion was observed and recorded. The approach was repeated on two larger tests. A wooden model 2.4 m tall was monitored outdoors, to challenge the approach with the uncontrolled lighting conditions outdoors. The approach was then also applied to a pedestrian bridge in West Bridgford, Nottingham, to demonstrate the application of the technique to a real and large structure. Finally, this chapter returns to the smaller models on the shake table which have been modified to exhibit 3-D motion, and 3-D monitoring is demonstrated. Small modifications are then made to the model to induce changes in the model's dynamic response, which are detected using the image-based monitoring approach. Each of these case studies is addressed in turn in this chapter.

4.1 Shake-table 2D

Having conducted tests using individual targets on the shake table (section 3.4), further tests were carried out to demonstrate how the approach would be applied to civil engineering case studies. The results from this test were not collected only to assess measurement accuracy, but also to demonstrate how a very high number of measurements can be recorded and used to represent the motion distribution of the test subject graphically. Models were assembled, subjected to vibrations on the shake table, and their vibration response recorded. In this initial test, the model was symmetrical and only exhibited 2D motion, with displacements being restricted to a single plane (section 3.2.1), so only 2D monitoring was necessary.

A simple 5 storey model was assembled, using a K'Nex modelling kit. The model was 770 mm tall, and each of the 5 storeys had a height matching the model's width. The K'Nex modelling kit was particularly useful for modelling simple structures as the parts 'snap' together and could be assembled and modified quickly and easily. Conveniently, the dimensions of the pieces corresponded with the spacing of threaded holes on the table, so the model could be fixed directly to the table with machine screws. Diagonal members could be added to provide bracing to any of the levels of the model, and they were added to create a partially braced frame structure. Metal plates were added to each level of the structure as a platform for sensors and accessories. Metal plates that could be placed on each level were prepared, and to prevent them from moving whilst the structure is vibrated they were fixed underneath with Blu-Tack. The metal plates were drilled with holes so that metal weight accessories could be added as necessary. For example, to induce a torsional movement with eccentric masses.

The monitoring instruments described in section 3.1.4 were utilised including, in particular, accelerometers and the laser displacement gauge (section 3.1.4).

The wooden stands introduced earlier (section 3.2.1) were used to provide control points in the image. These were measured by a reflectorless total station and coordinates calculated using the spreadsheet described in section 3.2.1. Plain black paper circular targets on white backing were used, and stuck on to the vertical members of the model using 'Blu-Tack', which held the paper firmly in place throughout tests.

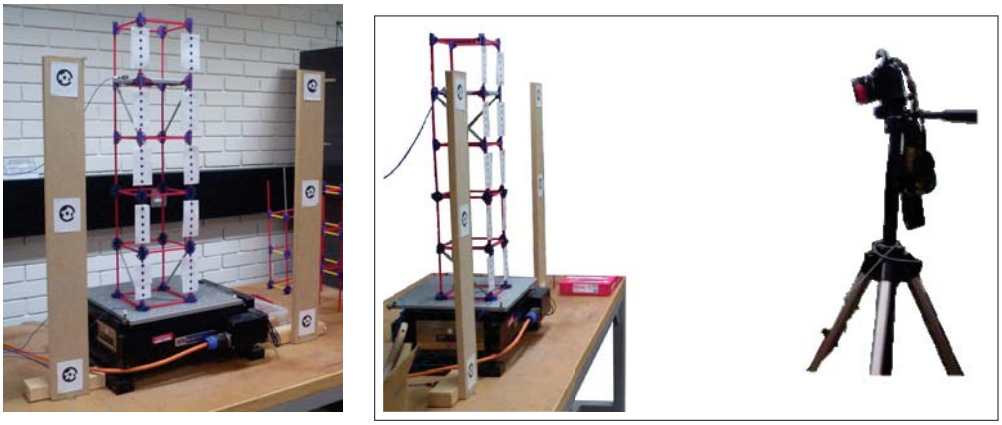

Figure 4.1: Arrangement of instruments and shaker table

The Nikon D80 10.2 MP camera was again used, and positioned on a tripod in front of the test. Exposure settings were manually set to 1 second exposure time, a time which was sufficient to capture a few vibration cycles (section 5.2.4). To get suitably exposed images for this exposure time, 100 ISO and an aperture of f/22 were used. As previously, the camera could be remotely triggered by the shake table control system, so that image capture time is known with respect to the induced and recorded vibrations.

Once the test was prepared, but before dynamic force was applied, an image was taken of the model at rest and the surrounding control targets. This sharp image was used during the later image processing (section 3.3).

4.1.1 Determining natural frequencies

Before applying vibration, it was necessary for the model structure's natural frequencies to be established. These are the frequencies at which, when excited, the model will exhibit their related vibration envelopes corresponding to the modes of vibration, known as "modal shapes", which are the properties particularly relevant to structural monitoring. To do this, one of the accelerometers was fitted on to one of the structure's horizontal metal plates using wax. The shake table was programmed with a sine sweep signal, a sinusoidal signal with constant increasing frequency, from 1 Hz up to 30 Hz (figure 4.2). This vibration was applied to the base of the model, and the acceleration-time history recorded by the accelerometer.

From the accelerometer's acceleration-time history, localised peaks in vibration am-

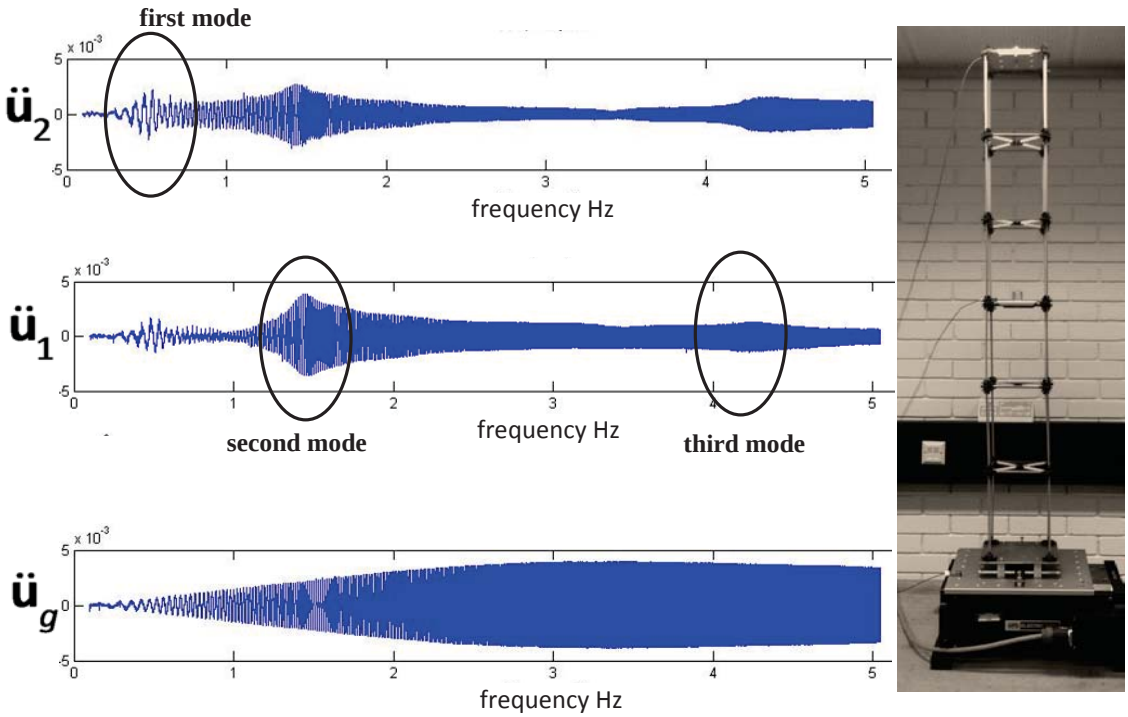

Figure 4.2: Illustrative input sine-sweep function with accelerometer histories for a model structure.

plitude can be identified. These were identified at 1.8, 3.0 & 8.1 Hz, which are accepted as the model's first three natural frequencies in this direction.

An alternative approach to identifying the natural frequencies of the model would have been to apply broadband excitation to the model. The input signal would approximately represent the superposition of many sinusoidal waveforms of different frequencies, which would appear as noise, so that all the natural frequencies of the model would be excited. The vibration response of the model, as recorded by an accelerometer, would be the superposition of the model's natural frequencies, and these natural frequencies could be identified using a Fourier transform (Clough and Penzien, 1995).

The sine sweep approach was chosen so that additional filtering of the accelerometer data and a Fourier transform was not necessary. The model's natural frequencies would be immediately apparent during the applications of motion, but for other applications the broadband excitation approach may be more suitable.

4.1.2 Model excitation

Having determined the natural frequencies of the model, image-based monitoring of the test commenced, to capture results at each of the identified natural frequencies. Sinusoidal base vibration was applied at each of the natural frequencies so that the model would exhibit its corresponding vibration envelope.

For each frequency, the signal was created, and then the motion amplitude was adjusted appropriately. The acceleration of the shake table was directly controlled by the input signal. Care needed to be exercised as the shake table was not equipped with a system to prevent damage to the table itself from inappropriate input signals, perhaps instructing the table bed to accelerate towards the end of its travel and causing it to collide with the end of its track. Consequently, it was important to adjust the gain on the signal amplifier when the frequency was changed, starting with a lower amplitude and increasing gradually. Inputting a lower frequency signal produced sinusoidal motion of greater amplitude, as the longer the frequency of vibrations, the larger the energy required to sustain the motion.

Since the table's rest position is not the same as the centre of its sinusoidal movement whilst in motion, the table was programmed to move for 4 seconds before the camera was triggered by a signal from the shake table's control system, so that the table would reach steady-state motion. When the camera's exposure had ended, the shaker table was programmed to stop.

After all images were captured, images were download from the camera, and the control target coordinates again measured by reflectorless total station; this was considered good practice to identify any possible movement of the control points during testing. The discrepancies between surveys were generally < 1 mm, within the expected accuracy of the total station. Any discrepancies much greater than this would suggest that the survey would need to be repeated.

4.1.3 Image processing

The image processing stages were carried out in the same procedure followed in section 3.4. PhotoModeler was again used to measure control and monitoring target coordinates in

the sharp image. The list of monitoring target coordinates, list of file names, and target measurement parameters were passed to the LEMBI measurement algorithm. The images were processing using the LEMBI algorithm (section 3.3), and results stored in a CSV file.

At this stage, it was possible to plot the measured end coordinates directly and rapidly on to the original image without using the control data. Since differences between pairs of coordinates at each target are very small, it is necessary to visualise the motion using a scaled vector. Matlab's 'quiver' function plots arrows, given a start coordinate and vector, so is convenient for this purpose. This type of visualisation may be sufficient for a structural engineer to understand the distribution of relative vibration amplitudes, who could then locate nodes and antinodes (locations of zero and locally maximal motion), providing qualitative information on the dynamic behaviour of the structure.

To show the vibration envelope, instead of displaying individual vectors singly, the ends of displacement vectors are linked (figure 4.3). This method outlines the vibration envelope, and the orientation of the motion is shown by the chords.

It is likely that quantitative data would also be required to facilitate a more precise analysis. At this stage, the measured displacements were in image-space coordinates and had not yet been converted into an object space coordinate system (and units of millimetres).

Parameters for the projective transformation were again determined from the control target image coordinates and planar object-space coordinates (as determined in section 3.2.1). Matlab's 'cp2tform' and 'tformfwd' functions were again used to obtain object-space coordinates for the motion extremities.

Measured displacements and orientations in the object coordinate system then existed for each target in every image frame. These results could be read either by image, where the motion of every target during a single epoch is presented, or by target, where the motion of one target at every epoch is presented. The data could then directly compared to the shake table's recorded data.

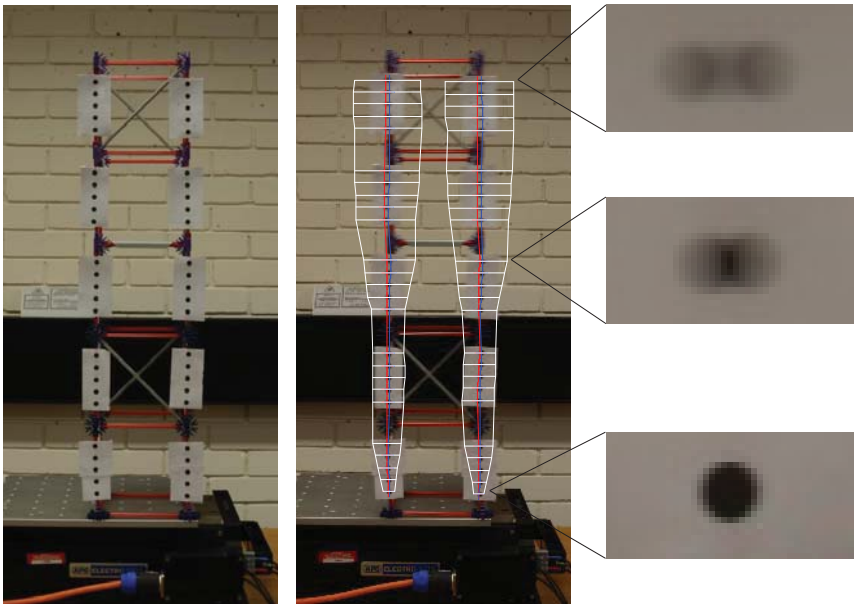

Figure 4.3: Test model with measured first vibration envelope overlain (1.8 Hz). Images on the right show target image detail.

4.1.4 Results

Graphical representations of the vibration envelope of the model as recorded by LEMBI at different excitation frequencies using the developed method follow. The measured vibration envelope is overlain onto the original image, and displacement vectors are scaled to an appropriate range.

The first case is of the model's first natural frequency at 1.8 Hz. Figure 4.3 shows the vibration envelope of the model structure. The response is as might have been expected by a structure of this type. Motion is chiefly horizontal and increases in magnitude with increasing distance from the table bed. It is also clear how the presence of a bracing system at the second and fifth levels prevents the inter-storey movement at those positions.

The target detail subfigures in figure 4.3 can be compared with general appearance of one-dimensional motion blurred targets shown in figure 3.21. The first subfigure corresponds with the target image created when motion is greater than the target diameter, whereas the second and third subfigures correspond to motion less than the target diameter. Accuracy in this arrangement was previously validated by the test results shown in figure 3.25.

The test continued, with vibration frequency being increased to 3.0 and 8.1 Hz. Re-

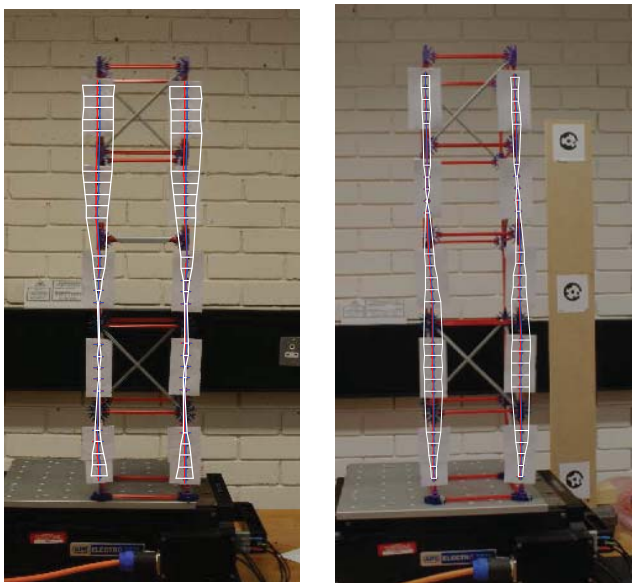

Figure 4.4: Test model with measured second (3.0 Hz) and third (8.1 Hz) vibration envelopes overlain

sults are shown in figure 4.4. As vibration frequency increased, amplitude decreased, so the gain on the signal amplifier was increased to compensate.

In these results, the ability to measure the vibration at many locations distributed across the structure is emphasised. This allows richer information than would otherwise be measured with only a single accelerometer.

Visualising the vibration envelope in this way allows detection of nodes and antinodes, and examination of the curvature of the vibration envelope. Analysis methods utilising the location of these features can be more revealing than simple static deformation measurements (section 2.1.3), and the photogrammetric approach can provide a far higher number of measurements.

If the same high quantity of data were required with only accelerometers as sensors, significantly more gauges would be required, and improved data acquisition hardware with more input channels. A method of moving the single sensor systematically to each monitoring point could be used, and since the test structure's motion is carefully controlled it would be possible, but the test would be very time consuming, and derived data would not strictly be attained from exactly the same test. Although the sensors are small and lightweight, the effect of the movement of the sensors and associated apparatus about the structure is unknown. Photogrammetric targets add negligible load, and can

remain permanently in-situ without affecting the structure.

4.2 Vertical Timber Section

A second test was designed to assess whether the approach could be applied in the outdoor environment and on a larger test structure. A vertical slender structure was selected as it may be representative of slender structures such as a wind turbine. This test would also examine how effective the approach is in natural or outdoor lighting conditions, which are not controllable in the same way as indoor lighting.

4.2.1 Test Method

An upright piece of timber 2.4 m in length was selected as the subject of the test, fixed at the bottom to a wooden base. The selected timber for the upright piece had a 20 x 67 mm section of pine. The base was a large sheet of MDF, for which a clamp was made and bolted to the centre of the sheet. The upright section could then be bolted in a vertical orientation.

The targets used for this test were 30 mm black circular target printed on white paper. This size target equated to approximately 47 pixels in the image space for the scale and camera resolution selected. Although conventional photogrammetry would have allowed smaller targets given the image scale, it has been discussed as part of the methodology (section 3.1.1) how, when the vibration amplitude was much larger than the target diameter, target detection became difficult because its image was heavily degraded by the motion blur, or when it interfered with other background objects in the image.

The camera used was the same Nikon D80 camera used in the earlier experiment (specification in section 3.1.1). The camera was located 3.5 m in front of the timber upright and was again approximately normal. 6 coded control targets on the same stands used earlier were positioned on surveying tripods either side of the timber section. The measurements of these targets were made using a reflectorless total station, and coordinates calculated using the earlier spreadsheet (section 3.2.1). The data would be used to determine appropriate projective transformation parameters to transform image coordinates to the real world system.

Figure 4.5: The upright timber used to demonstrate suitability for outdoor monitoring tasks.

Specialist excitation equipment was not available to apply controlled loads to this model. Instead, the vertical member was excited by being manually pushed in the desired direction and allowing it to spring back. The resulting motion is similar to what is expected in service due to wind loading.

4.2.2 Results

For this test accelerometers were not available, since the available hardware did not allow battery operation of the monitoring equipment (a challenge for traditional monitoring systems also—section 2.2.1). Nevertheless, LEMBI data can provide quantitative results and comparisons were made with the theoretical curvature of fixed-end column of constant stiffness. The vibration envelope of the structures would be expected to be simple, since the upright section has a constant cross section, and for homogeneous materials this would mean constant stiffness and mass. The measured deflections are therefore compared to the theoretical deflections.

Figure 4.6 provides a graphical representation of the motion of the timber upright at each excitation. Although the manual excitation cannot remain exactly constant, the

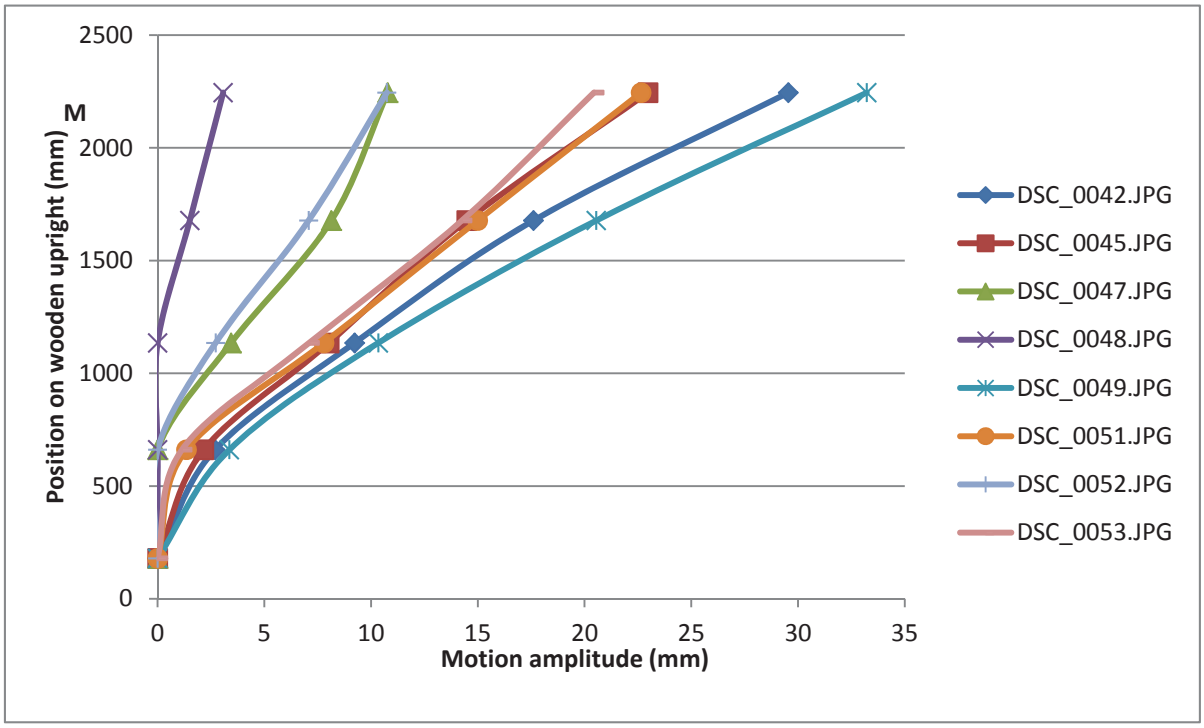

Figure 4.6: Timber upright sequential tests vibration amplitudes

curvature of the vibration envelope should remain the same, and this can be observed in the results. Making use of the control points and procedure described in section 2.4.3, the vibration amplitude of the timber upright could be quantified, but an accurate reference measurement was not available for comparison.

An comparison of the curvature of the model with the theoretical curvature for a slender section of constant stiffness can be made. Theoretical curvatures can be calculated using the equation (Clough and Penzien, 1995):

$$\phi(x) = A_1 \left[\cos ax - \cosh ax - \frac{(\cos aL + \cosh aL)}{(\sin aL + \sinh aL)} (\sin ax - \sinh ax) \right] \tag{4.1}$$

where aL is the value representing the frequency of vibration of the cantilever beam, which in this case is a constant for the first mode of vibration.

In figure 4.7, the vibration amplitude in each image has been normalised for easier comparison of the curvature, where the vibration amplitude does not remain constant in each image. The black line in figure 4.7 gives the theoretical curvature for model this model (Clough and Penzien, 1995).

Although the section was expected to be of constant stiffness, the measured vibration

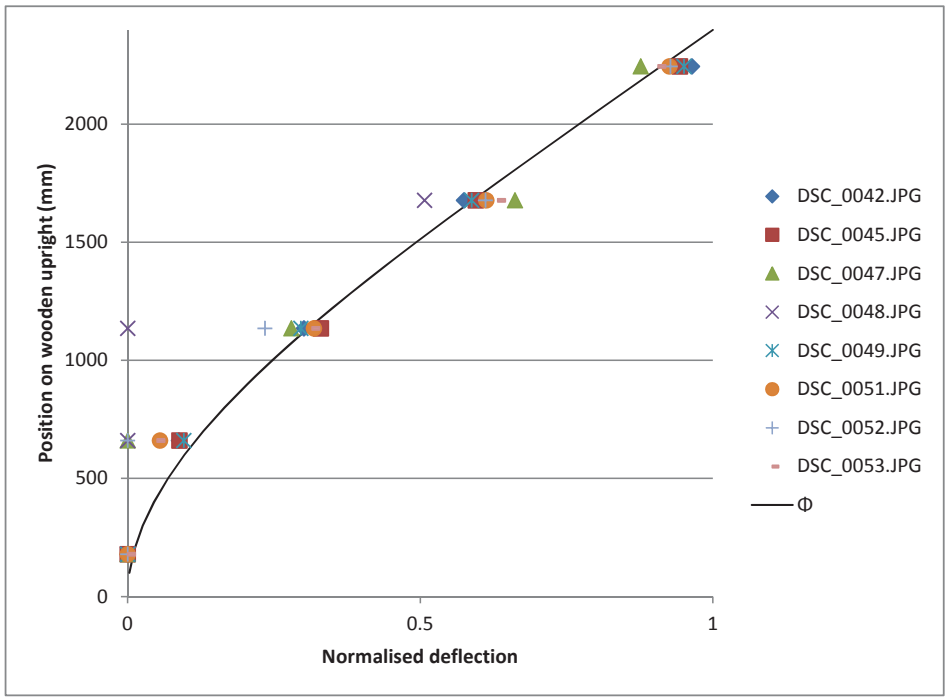

Figure 4.7: Normalised magnitude of vibration envelope of the wooden upright and the theoretical curvature of constant stiffness section

amplitudes do not always follow the theoretical curve exactly. Discontinuities in the curvature could be caused by localised variation in the stiffness of the section. As timber is a natural material, so variations in the material may exist, as do features such as knots in the wood.

Also, as a rather rudimentary method was used to excite the upright member, it is possible that modal frequencies other than the first mode were excited and the deformation may not conform exactly to the first mode of vibration.

In the figure it can be noticed that there are a few measurements where the motion amplitude is very small and has been recorded as zero (such as in 'DSC_0048.JPG'), typically located close to the base of the upright timber. This is discussed further in section 5.2.2.1.

The weakness of this case study is that there is no external reference measurement to provide an accuracy validation. But it did reveal survey design considerations for testing outdoors, which became crucial influences in the design of the later Wilford bridge case study.

4.2.3 Additional problems encountered whilst monitoring outdoors

The Nikon D80 cameras were set to manual mode, with the shutter speed set to 0.5 s and the aperture at its smallest, f/22. The sensitivity was also set to its minimum, ISO100.

On a sunny day, images were becoming overexposed and the blurred target image became disturbed. Specifically, pixels in the regions occupied by the white target border were saturated, as well as pixels at the edge of the blurred target smear which would otherwise by used in measurement (section 5.2.5). It was not possible to reduce the sensitivity or aperture further, as they were already at their minimum and maximum settings, respectively. Instead, neutral density (ND) filters were attached to the screw thread on the front of the lens, reducing the incoming light intensity to within an acceptable range for the camera. ND 2, 4 & 8 filters were purchased which reduce the light intensity evenly across all wavelengths by $^1/_2$, $^3/_4$ & $^7/_8$ respectively.

4.3 Wilford Bridge

Although the concept had been proven for test objects in a controlled situation it was decided to test another larger case study of an actual structure. This would be to demonstrate that the approach is scalable, a particular advantage of photogrammetry, and also practical for read world applications. This test would further assess the approach outdoors where the lighting condition are uncontrolled. It was not possible within the constraints of this project to identify a structure that allowed testing of the approach in pre and post-damage conditions, but a comparison of the quantitative measured displacements as well as qualitative outputs is made. Ideally a structure which allowed for pre and post damage deformation analysis would have been selected. However, the unpredictability and unlikelihood of damage occurring to a local structure suitable as a case study meant that only one state was analysed.

4.3.1 Selecting a larger case study

Different structures were considered for a larger case study. Options included bridges and wind turbines, and their size, location and material were considered.

A number of bridges within the East Midlands region were considered for suitability for a case study. An initial desk study identified 16 local bridges as possible test subjects. These bridges were visited and judged on their suitability for photogrammetric monitoring. Selection criteria included their expected dynamic performance, as well as ease of access, and likely vantage points for cameras and other sensors. The footfall of structures were also a factor, as it was judged that the general public should not unduly be inconvenienced by the planned tests. Some structures that had suitable dynamic properties were not chosen because of their crossing or close proximity to major dual carriageway roads. Many bridges crossed watercourses and at the time of selecting a case study, access to some was prevented by local flooding, so these bridges also had to be discounted. A table of the candidate structures is included in appendix B.

The bridge finally chosen was the Wilford suspension footbridge in West Bridgford, Nottingham. This suspension bridge was selected for its dynamic properties—its modal frequencies could easily be excited by pedestrians—and the vibration amplitude was also within the range suitable for the image based monitoring approach. The Wilford suspension bridge has also been the subject of a related research project assessing GPS as an alternative dynamic monitoring techniques by authors from Nottingham University (Roberts *et al.*, 2006; Meng *et al.*, 2007), allowing some form of comparison to be made.

A second candidate site included a smaller pedestrian bridge in Leicester. This cable-stayed bridge crossed a smaller river and was constructed of two box sections. The shorter length of the bridge and larger box sections made the bridge more rigid; the modal frequencies were higher and the vibration amplitude was lower. It was possible for pedestrians to excite this bridge in its vertical and horizontal axes, with the amplitude of horizontal vibrations being greater. A trial set up with camera and a few targets produced measurable images, but the Wilford bridge was considered preferable.

Wind turbines were also considered for a larger case study as they may also be subject to structural health monitoring and are associate with their own set of measurement

challenges. Nearby wind turbines were identified. Rather than artificially exciting the structure using controlled loads, excitation would be natural wind loads upon the turbine's tower, nacelle at the top of the tower, and rotor blades. A horizontal axis wind turbine on Loughborough University campus was identified as a possible case study. Although a test was scheduled and attempted, the low wind speed on the day of the test resulted in vibrations that were too small to be measured at the image scale required to capture the structure's whole height. As the LDV (section 2.2.2.5), which was to provide the independent reference measurement, was only on loan for a limited time during the Easter holiday, it was not possible to reschedule this test of a later date.

Another challenge would be locating suitable positions for control targets, which would be more difficult on a wind turbine. An optimum configuration is for control targets to be arranged around the periphery of the object so that measurements from monitoring targets will be interpolated within the area defined by the control. For camera stations located at ground level, control targets would therefore need to be highly elevated, which would not only be difficult to establish, but the stability of the control targets on tall structures themselves must also be ensured.

An alternative approach would be for the camera to be elevated, observing the wind turbine from a higher perspective. Control targets could then be located at ground level, avoiding some of the difficulties of highly elevated control. Although camera movement would be possible (where it has previously been assumed to be stationary), this would be detectable by blur measured at the control points.

An additional operational difficulty is the practical problem of fitting targets to the wind turbine column itself, which would require careful planning, and probably the use of a mobile elevating work platform. Because of these challenges and the advantages presented by the Wilford bridge, it was decided to proceed with the Wilford bridge case study only.

4.3.2 Description of the test subject

The Wilford bridge is 69 m in length and approximately 3.5 m wide, and runs approximately east-west across the River Trent (figure 4.8). Two masonry bridge abutments

Figure 4.8: Wilford Suspension Bridge

support two main cables, form which vertical suspender wires are spaced at approximately 2.2 m to the truss below the bridge deck. A timber deck spreads between the two side walls. Water and gas mains are also carried beneath the bridge deck.

The river bank of the bridge is 6.5 m below the bridge deck, and a footpath runs under the bridge in front of the abutment. This arrangement made possible observation of the underside of the bridge deck using a laser Doppler vibrometer, which only measures out-of-plane motion, and is discussed in the next section.

4.3.3 Test method

Experimental work described in past literature (Cooper and Robson, 1990; Albert *et al.*, 2002; Ronnholm *et al.*, 2009; Tasci, 2013) usually locate cameras approximately normal to the structure from an ideal monitoring point. For this structure it would not have been possible to locate the camera normal to the bridge from the north, since the river runs straight until the next bridge, 600 metres away. To the south, the river bends and the river bank is accessible, but to observe normal to the bridge, the vantage point would still have been at least 200 m from the bridge. With the maximum available focal length

Figure 4.9: Arrangement of of sensors and target for Wilford Suspension Bridge case study

lens being 200 mm, the image scale was too small at this distance.

Instead, the camera was located above the bridge's west masonry abutment, oriented to view down the bridge deck (figure 4.9). Targets were clipped to the inside of the bridge side wall. In this way the maximum target-camera distance was 70 m, and enabled a larger image scale than if the camera were normal to the structure. This configuration also permitted comparisons of different imaging scales. This could create a problem with image focus, since a very long depth of field would be required. However, the long exposure necessary to capture the blur allows the use of a very small aperature (f/18), so providing the necessary depth of field. All of the targets appeared to be sharply captured and appeared unaffected by out-of-focus blur. The masonry abutment and tripod provided a sturdy platform for the camera, which would not be affected by the vibrations of the bridge deck.

The camera used for this test was a Nikon D7000 mounted on a tripod. A 85 mm fixed focal length lens was used, fixed at its smallest aperture, f/16, and lowest sensitivity, 100 ISO. The shutter speed was selected as 0.5 s, which was considered suitable to capture the expected natural frequencies of the structure. As experienced with the timber upright test (section 4.2), it was necessary to use neutral density filters to reduce the light intensity for image exposure to remain within acceptable limits.

Targets of sizes between 20 and 40 mm were used, with the largest targets being positioned the furthest distance from the camera. Target sizes were arranged depending on the expected amplitudes (constraints between target size and expected motion amplitude

Figure 4.10: Targets used on the Wilford Bridge case study

discussed in section 5.2.2.1) and image scale as a result differing target-camera distances. The furthest targets were at least large enough to appear as circles occupying at least 10 pixels. Targets were constructed by printing black circles using a computer on to A4 acetate sheets. The acetate sheets were then glued on to white unexpanded polystyrene sheets, which could easily be scored and cut. The result was durable, weather resistant photogrammetric targets with the desired appearance (figure 4.10). To attach the targets to the bridge, right-angled metal brackets were adhered to the reverse of the targets using silicon sealant. The combined target and bracket was then fixed to the bridge parapet using simple spring clips. This method firmly held the targets in place, and no movement between the target and its fixing point could be observed.

Targets were clipped to the bridge at every second vertical member, approximately 4.4 m, with an additional target at the bridge's mid-span. Two control targets were placed at each end of the bridge, making four in total. The control targets were manufactured in the same way as the monitoring targets, so this occasion were not coded, and were instead manually located in the image during later image processing.

To provide an independent accurate reference measurement, a laser Doppler vibrometer (LDV) was kindly loaned by Polytech Inc (figure 4.11). After discussions with the instrument's manufacturer sales representative following an introduction by Dr Palmeri,

Figure 4.11: Laser Doppler vibrometer (courtesy of Polytech Inc.)

Polytech generously agreed to loan the instrument for free over the Easter holiday 2013. Polytech delivered the instrument to the University and provided training for its set-up, and collected the instrument a few days later. The test on the Wilford Suspension Bridge and the attempted wind turbine monitoring were therefore scheduled to take place this week, despite the snowfall. This device measured frequency shifts in a reflected laser beam due the Doppler effect (section 2.2.2.5). The LDV was positioned on the footpath beside the bridge abutment below the bridge deck. The measuring laser was pointed upwards at the underside of the bridge deck. The ideal arrangement would be for the measuring laser beam to be normal to the underside of the bridge deck, but this was not possible because of the river. The laser had an incident angle with the underside of the bridge which resulted in a cosine error. This angle was calculated by measuring the basic geometry of the bridge and LDV using the total station in reflectorless mode.

Accelerometers were taken to site, and connected to a Measurement Computing USB Data Acquisition Module. This data logger was selected because it could be powered through a laptop computer's USB port, whereas the NI DAQ used earlier in the lab could not be portably powered (section 3.1.3). Unfortunately, it was revealed later that, although the sensitivity of the data logger was at its maximum, it was insufficient for recording the accelerometer's signal.

Excitation was created by two pedestrians who could jump up and down on the

bridge's mid-span. Pedestrians were used to apply excitation because they were easy to arrange and available at a much lower cost than specialist dynamic excitation equipment. Since all monitoring locations on the structure were measured simultaneously, it was not necessary for excitation to remain constant, as is the case when sensors have to be moved around the structure. Meng *et al.* (2007) combined accelerometer and GPS measurements to determine three of the natural frequencies of the bridge as approximately 1.73, 2.30 and 2.93 Hz, when using accelerometer. The pedestrian exciters were instructed to jump repeatedly on the bridge at these frequencies. To control the rate at which the pedestrians were jumping, they listened to an music audio recording with its speed modified so that the music tempo would match these natural frequencies.

In experiments by Meng *et al.* (2007), 30 pedestrians jumped at mid-span to excite this bridge, and maximum deformations of 80 mm were observed. In the tests here, the two pedestrians provided adequate dynamic excitation to measure the structure's response, similarly creating a maximum deformation of approximately 80 mm. The lesser loads were easier to recruit and coordinate.

When the pedestrians started jumping, images were acquired using the DSLR camera. The camera was set to interval mode, taking images in groups of five, 1 second apart. The self-timer mode was also utilised, to minimise camera shake whilst images were being captured by physically pressing the shutter button.

With separate monitoring systems in use: image-based and LDV, it was necessary to synchronise the recorded data, for later comparison. Although both monitoring systems record timestamps alongside their data, both systems only store timestamps to the single second, which is not precise enough for the separate datasets to be correlated.

A better comparison was achieved by using a separate video camera which was set up to record the test graphically. This camera was not used in any photogrammetic processing, it only kept the DSLR camera in the foreground and the moving pedestrians on the bridge in the background to allow their timings to be compared. A freeze frame from the video is included in figure 4.12. The memory card access LED indicator on the rear of the camera body was visible in the video, and activated at the end of each exposure during data recording to the memory card. It was also possible to identify the moment that pedestrians jumped in the LDV data, which could be matched with the jumping in

Figure 4.12: Freeze frame from the video camera of the Wilford Suspension Bridge during test

the video. The video was examined in slow motion, and the time of each event (camera capture or pedestrian jump) noted. With the video camera recording at 30 frames per second, meaning images are captured every 0.0333 seconds, the two datasets could be aligned to this level of precision.

On return to the office, images were processed using the steps described earlier for LEMBI measurement (section 3.3). The result are presented below. First, figure 4.14 provides the vibration envelope at the time each image was captured along longitudinal bridge sections. Secondly, figure 4.13 provides a graphic representation of the deformation for a single target at the mid-span.

4.3.4 Results

The laser vibrometer was located below the bridge deck, pointing at a location beneath the walkway at the mid position of the bridge. The data recorded acceleration, so double integration and filtering was necessary to generate displacement history to compare with the image based deformation estimates, and the measurement must be corrected for the incident angle of the measuring beam. Figure 4.13 compares the displacement time history recorded by the LDV with the image-based measurements for the target at the

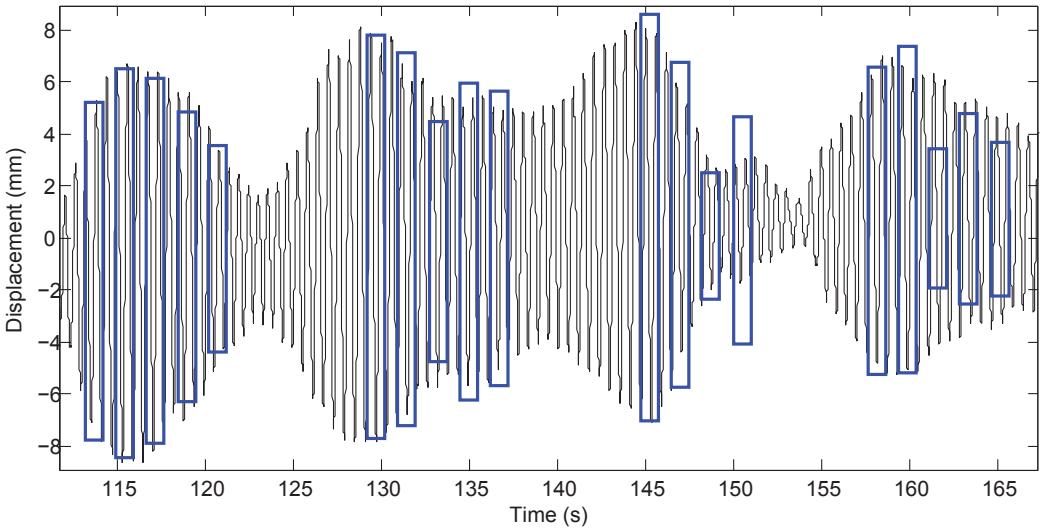

Figure 4.13: Comparison of Wilford bridge mid-span deflections measured by LDV (black line) and LEMBI measurement (blue rectangles)

bridge's mid-span for the first set of results. Image based measurements are represented on this graph by rectangles, where the height represents the magnitude of the measured vibration derived from each image, and its position in the x axis corresponds to the time the image was taken. The width of the rectangle corresponds to the time that the shutter was open. In the figure it can be seen that there is good correlation between the rectangles (representing LEMBI measurements) which outline the laser-measured motion in most cases. These reassuring results showing correspondence between an independent reference measurement and the LEMBI measurements demonstrate the effectiveness of the LEMBI approach. Figure 4.13 showing correspondence between LEMBI and reference measurements is different to the earlier figure 3.25 because the controlled motion was constant, allowing the statistical analysis of measurement differences. The true benefit of LEMBI measurements are demonstrated later when many targets are monitored simultaneously.

In some cases, the measurements don't correlate exactly. Reasons may include that the photogrammetric measurements were made along the northern wall of the bridge whilst the LDV monitoring the underside of the bridge deck was directed at the southern side. Although no torsional movements were apparent to the pedestrians on the bridge, the possibly cannot be ignored and could remain a source for error.

A second set of results is presented in figure 4.14 which provide every target's mea-

sured vibration amplitude during the first 20 measurement epochs. Each line in this graph represents the measurements obtained from an individual image and are hence each individual epochs (sequentially numbered and corresponding to those in figure 4.13). The x axis represents the chainage along the bridge starting from the furthest end, and y axis is motion amplitude. These results demonstrate how motion data from all the targets on the bridge could be captured in single images.

Looking at the results to the left of the graph and the targets nearest to the camera, the results show vibration amplitude increasing, but plateauing towards the mid-span of the bridge. Between images the motion varies in amplitude, which can be expected given the random nature of the excitation power provided by the jumping pedestrians. Whilst the amplitude varies, the form the the bridge's curvature is relatively consistent between samples, as one would expect. Towards the left of the graph where target's are greater than 30 m away, the results are more random and are almost certainly demonstrating that the measurement system is incapable of resolving motion accurately at these distances. At the furthest end of the bridge approximately 70 m from the camera, an object distance of 1 mm corresponds to 0.2 pixels in the image space, which has been shown in the shake table tests to be below the accuracy of the current blurred target measurement algorithm. For the targets are the far end of the bridge in particular, this arrangement is poorly conditioned for the desired measurements.

The case study has certainly demonstrated how LEMBI monitoring can be applied to real structures. The vibration envelope of the suspension bridge was captured using the Nikon D7000 camera, at its maximum resolution of 16 MP. If monitoring using a traditional high-speed imaging method, the sensor would capture at a maximum of only 6 frames per second at this resolution. Although being just within the constraints of the Nyquist sampling frequency criterion for the structure's natural frequencies, measurement errors can still occur because of aliasing effects (see section 2.3.5). The D7000 camera is capable of recording images in movie mode at 24 frames per second, but at this sampling frequency, would be limited to an image resolution of 2.2 MP. The lower resolution means that measurement accuracy would be less than that achievable using LEMBI.

This case study also demonstrated some of the constraints of using such an approach on a real civil engineering structure. Carrying out the test demonstrated a possible

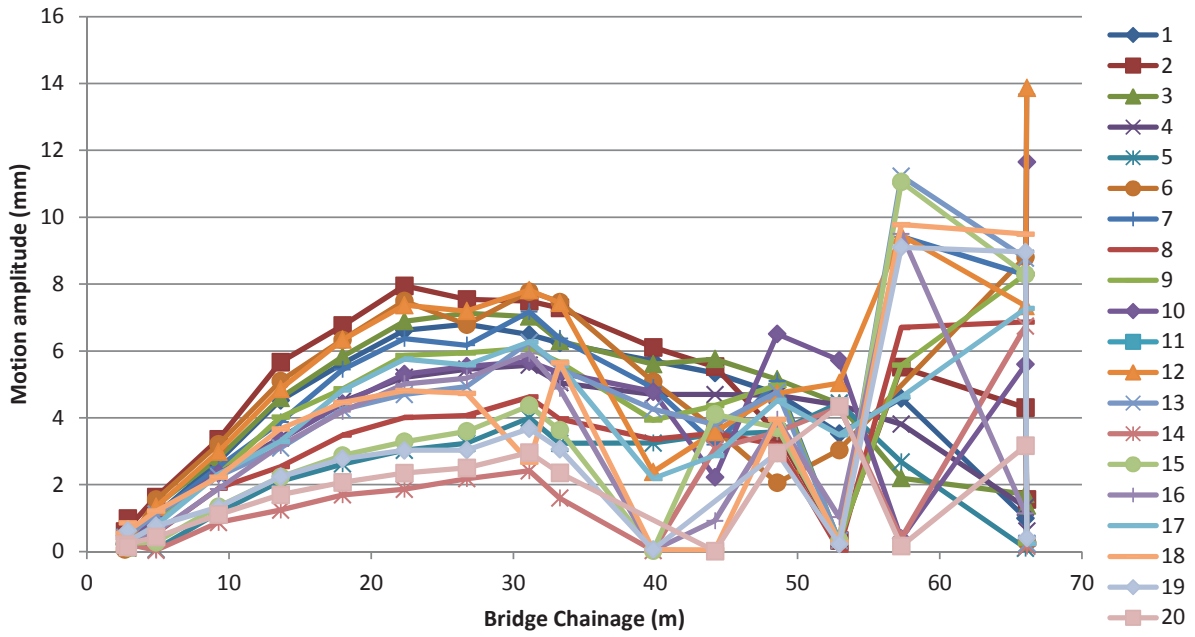

Figure 4.14: Wilford Bridge vibration amplitudes (chainage measured from the face of the south abutment on which the camera was located)

arrangement for a sensor and targets, and the use of neutral density filters for acceptable image exposure (discussed further in section 5.2.5).

4.4 Shake-table 3D model

A key development of the basic LEMBI monitoring method involved extending the approach into three dimensions using multiple cameras (section 3.5). The shake table used earlier (section 4.1) was used again using two cameras in a stereo configuration for 3D measurement. As discussed in section 3.5, although 2D measurements can be useful for monitoring plan deformations, 3D measurements would allow detection of more complicated 3D motion, which could be particularly relevant to asymmetric structures, those with complex 3D deformation, or those with unusual dynamic loads.

4.4.1 Method

The arrangement of the 3D shake table setup was broadly similar to that used in section 4.1. The large-scale plastic model was again screwed to the moving bed of the shake table. More coded control targets were added around the test structure, on the

workbench and the shake table's non-moving body, creating a volume within the control targets. The additional control points provided redundancy in the measurements. 3D object space coordinates were again established using the total station.

Two cameras were used for stereoscopic imaging, and fixed on tripods in front of the model. Motion was expected to be broadly horizontal, so the tripods were set at different heights, avoiding the situation described in section 3.5.5.1, whereby it is not possible to automatically determine the correct point matching where the deformation line and epipolar plane are coincident.

The testing procedure was carried out using the same approach described in section 3.1.3. Sinusoidal base vibration was applied separately at each frequency and images captured from both cameras simultaneously after the table had been in motion for 5 seconds (steady-state motion). Image capture was controlled using the data acquisition device described in section 3.1.4, which allowed carefully timed simultaneous activation of both cameras. The simultaneous audible click of the cameras' shutters confirmed their synchronised operation, but a small difference would not have had a significant affect since steady-state motion was reached.

The exterior orientation of the two cameras were determined using PhotoModeler, since this software package contained convenient tools for automatic target recognition and bundle adjustment. The pair of images captured before motion had started was imported into PhotoModeler, together with the the control target's object space coordinates, and the interior orientation parameters determined using a camera calibration field (section 3.5.1). The same image registration script employed for 2D motion measurement was used to determine image coordinates. Instead of using the projective transformation to determine object space coordinates, the collinearity equations were utilised, using the space intersection technique described in section 3.5.3. Figure 4.15 shows the arrangement of apparatus in the test.

4.4.2 Results

The first test involved simple 2D translation. The test was monitored using the full 3D monitoring system with stereo imagery, although only planar motion was expected.

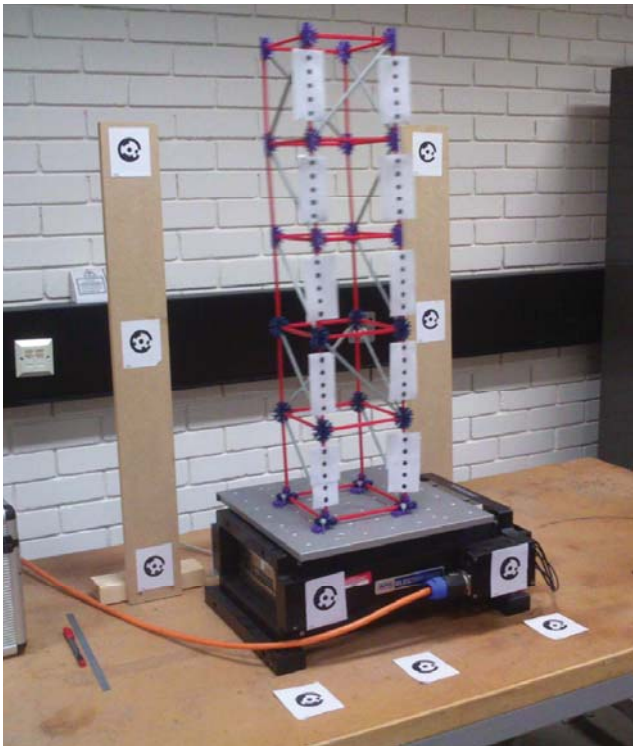

Figure 4.15: The model used for 3D monitoring

Figure 4.16(a) shows the result of a repeated test on the original model at 1.8 Hz. Unsurprisingly, the results are the same as those provided earlier in figure 4.3 in section 4.1. The vibration envelope is the same shape, with nodes (locations of no motion) apparent in the same locations and a similar curvature to that shown in figure 4.3.

As previously, vibration frequency was increased to 3.0 and 8.1 Hz, and measurement repeated. The 3D motion vectors for each frequency are given in figure 4.16(b) and 4.16(c), and are again similar to those given during planar monoscopic measurement (figure 4.4).

4.4.3 Modified Models

A particular emphasis of dynamic structural testing is the detection of structural changes, such as a loss of stiffness, that require remedial intervention to prevent failure of the structure. It is envisaged that the image based monitoring approach would be ideally suited to this task. To demonstrate the suitability for detecting structural changes, a series of modification were made to the model and measurements repeated. This test intended to simulate how changes in the structure would be reflected in changes in the

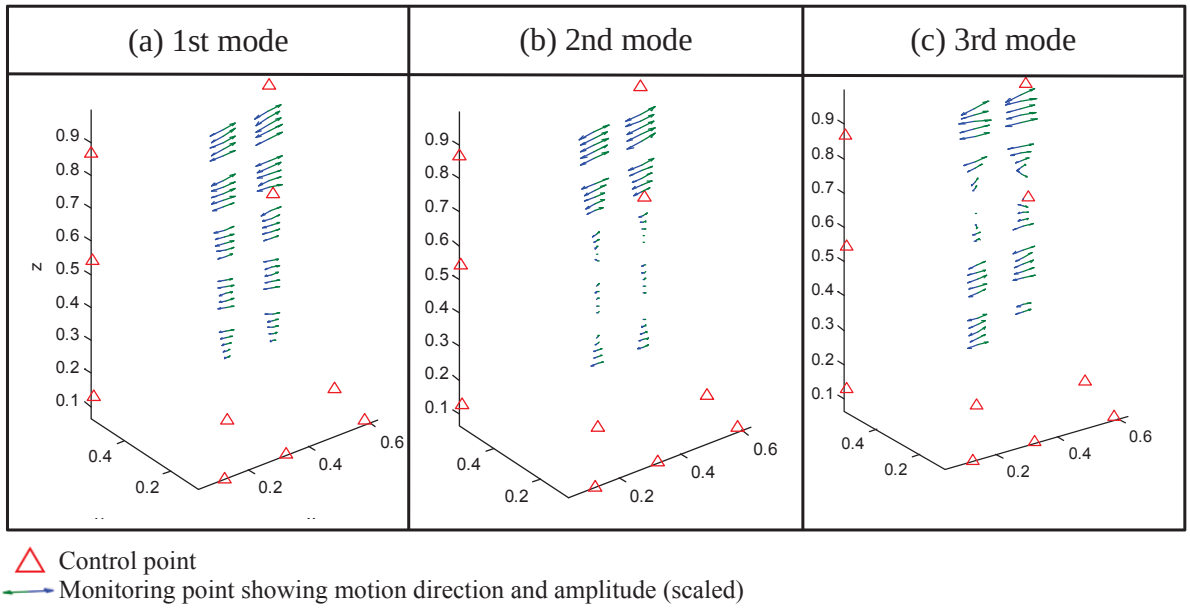

Figure 4.16: 3D measurements of the unmodified structure

measured vibration envelope, as part of the structural health monitoring scheme. Changes in either the mass or stiffness of the structure would result in changes to the structure's dynamic properties.

Modifications were made to the structure, and monitoring was repeated to compare the previous no-damage state with the post-damage state (figure 4.17). A detected change would prompt further investigation to identify the cause.

First, 48.1 g of mass (a weight weighing 36.0 g, fixed with a 12.1 g bolt) was added to the structure at the fourth level (figure 4.17). Monitoring was repeated, running through the test procedure and processing images, producing results for the first three natural frequencies. Figure 4.18a shows how the change in mass resulted in a change in the measured vibration envelope of the modified structure. In the first mode, a node is not apparent at the fourth storey where previously none were present. The location of nodes in the later two modes has also changed.

The second modification introduced to the structure involved reducing the stiffness of two of the vertical members by swapping them for some having part of the plastic section cut away (figure 4.17). By reducing the cross-section of the member, the stiffness was reduced. This is a similar effect to the failure of welds in a steel structure, which would result in a localised loss of stiffness. This modification produced unbalanced and more

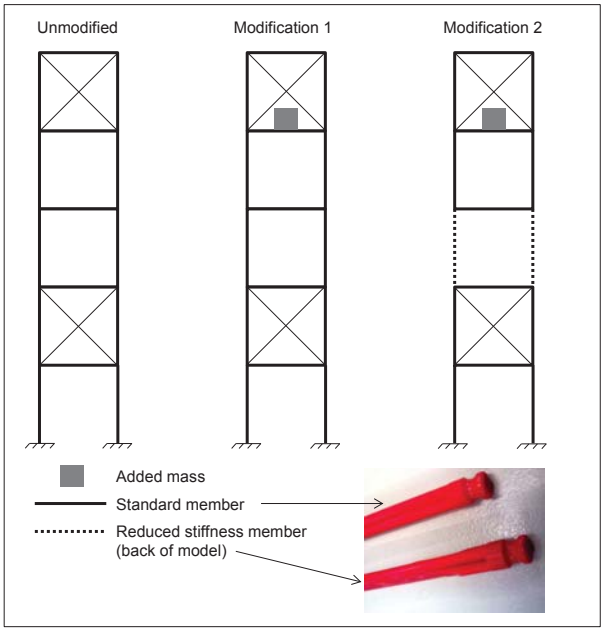

Figure 4.17: Modifications made to the model structure

interesting 3D motion. The test was repeated to see if the change was detectable and results for the modified structure are given in figure 4.18b.

Changes in the vibration envelope due to the modified stiffness of the two members can be seen. Since the model is no longer symmetrical, torsional motion can be observed. Particular attention is drawn to how changes in the location of nodes on the structure can be observed, in addition to changes in the orientation and relative magnitudes of the displacement vectors.

This case study has demonstrated the application of the image measurement approach to monitoring 3D motion, showing how an asymmetric model could be observed, including the change to orientation and magnitude progressing through the structure from the base to the top. This case study has also demonstrated how the approach could be used for damage detection within a structure, by simulating structural changes in plastic model structures resulting in modified vibration envelopes, that can be detected by the image processing approach.

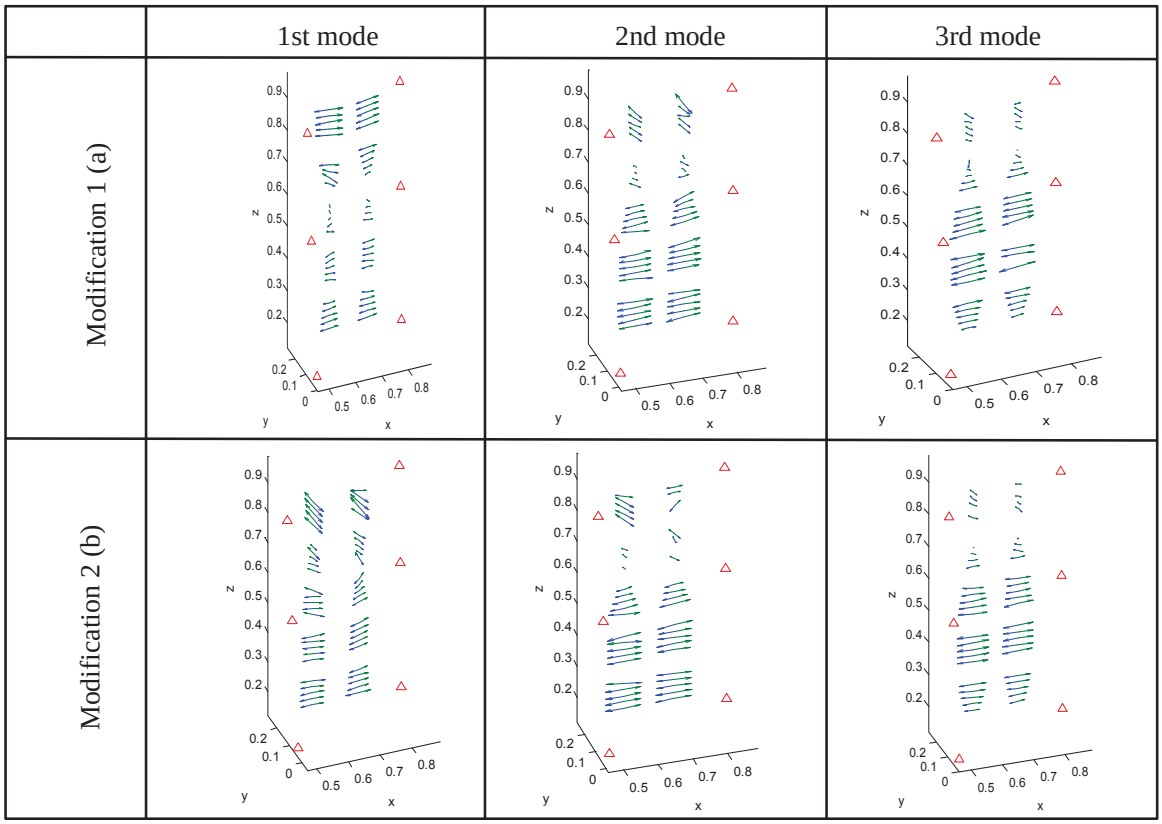

Figure 4.18: Measurements repeated after each modification to the model structure

4.5 Vertical Timber Section 3D

With the 3D monitoring routine developed, the test on the upright timber carried out in section 4.2 was repeated for 3D monitoring (figure 4.19). The goal of this case study was to verify motion could be captured in three dimensions, even outdoors. As previously, the upright timber was fixed vertically. The targets with diameters ranging from 20 to 40 mm were manufactured in the same way as those used for the Wilford Bridge (section 4.3.3). As previously, wooden stands held six coded targets to act as an external object-space control. For 3D monitoring, it is not necessary for the control points and monitoring points to be coplanar, so for this case study the control targets were not so carefully arranged, but were nevertheless carefully surveyed using total station in reflectorless mode.

Two Nikon D80 cameras were used, supported on tripods with identical settings programmed, and neutral density filters were again necessary. They were connected to the same external double trigger allowing a pair of images to be taken simultaneously when

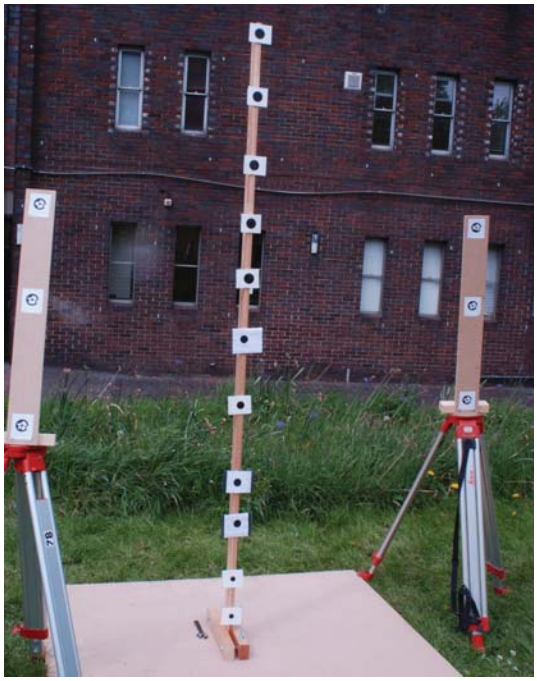

Figure 4.19: The 3D demonstration of monitoring the upright timber, with control points.

the shutter was pressed.

4.5.1 Results

The upright section was again excited by being manually pushed and allowed to oscillate. Results are presented in figure 4.21. As expected, the results appear similar to those captured in section 4.2. Again, the curvature is compared to the theoretical curvature that would be expected for the theoretical curvature of fixed end column of constant stiffness.

The timber section was excited in both it's major and minor axes (figure 4.20). As the cross section is constant along its length length, changes in relative curvature would not be expected, except if there was a change in stiffness. Figure 4.22 compares the vibration amplitude results with a theoretical curve for a section of constant stiffness. In order to represent this is 2D, the 3D data has been fit to a vertical 2D plane through the direction of the motion of the highest target. As can be qualitatively observed, the curvature of the upright's motion corresponds with the theoretical curve.

It can be seen that the lowest target on the structure is often not detected despite moving is the same way as the other targets. This is due to the minimum detectable

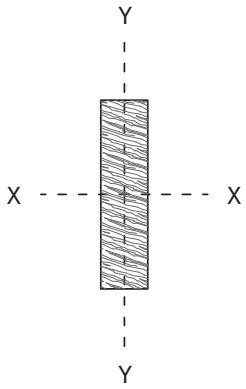

Figure 4.20: Timber upright section; definition of major (X-X) and minor (Y-Y) axes.

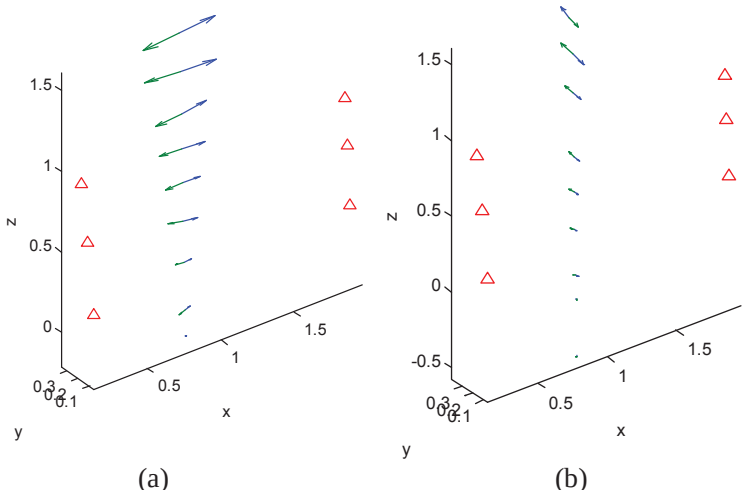

Figure 4.21: Upright Timber 3D results (a) minor axis and (b) major axis.

motion amplitude, discussed further in section 5.2.2.1. Selecting a smaller target size would result in better detection of this targets, but could cause problems if vibration amplitude is subsequently substantially increased.

This test again demonstrates monitoring in 3D, and that it remains effective out-of-doors. A comparison is made between with theoretical results, as well as noting the similarities between results obtains here, and using the earlier 2D measurement approach.

4.6 Summary

In this chapter, the efficacy of the LEMBI monitoring has been demonstrated using a series of case studies. These included large-scale models in the laboratory and smaller

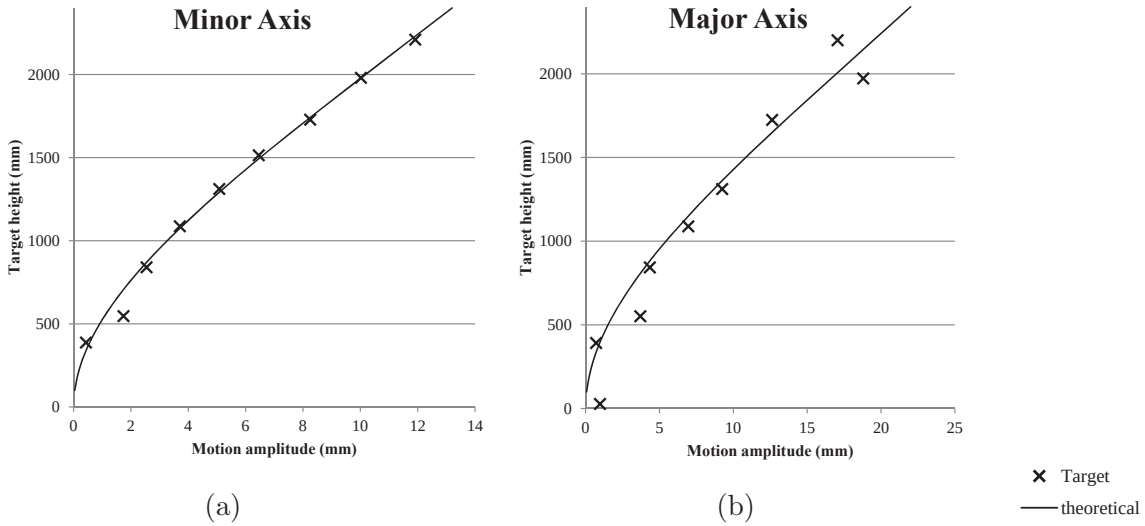

(a) (b)

Figure 4.22: Upright Timber 3D results: (a) minor axis (in-plane) and (b) major axis (out-of-plane)

case studies on a wooden model, and on an actual steel suspension bridge.

Monitoring was demonstrated initially with one camera, restricting motion to planar motion in two dimensions only. Further case studies then use the 3D monitoring extension of the developed approach to record more complex motion that is not restricted to planar displacements. Although proof of concept has been achieved in 3D, in a comparatively simple two camera stereo configuration, it is readily accepted that a multiple camera configuration would provide more robust results.

The tests on the smaller laboratory model was expanded to demonstrate how changes in the vibration envelope of the structure, caused by introducing structural changes, can be detected. This included adding accidental masses and swapping a member for those of a different stiffness, which could indicate the presence of damage in a real structure.

The following chapter assesses the quality of the proposed LEMBI measurement system. It also discusses the implications of these case studies in more detail, including encountered considerations and the implications for wider structural testing when compared with other existing monitoring approaches.

Chapter 5

Discussion

In this chapter, the results of the case studies encountered in chapter 4 are discussed in more detail. The use and implications of long exposure motion blurred images (LEMBI) for monitoring structural tests using dynamic techniques is discussed, and some of the practical considerations encountered during fieldwork are identified and addressed. This chapter then goes on to define the capabilities and identify the limitations of LEMBI monitoring. Finally, a comparison is made of the use of LEMBI monitoring with other dynamic monitoring sensors.

5.1 Data Quality

The accuracy of LEMBI measurements has been considered in section 3.4, and was shown to improve as a more advanced measurement algorithm was developed. The current working Matlab routine took several seconds to process images. There are some obvious steps that could be taken to speed up processing. For example, the current Matlab routine does not make use of parallel processing on a multiple core processor, but individual targets could be processed in parallel without significant modification to the algorithm if Matlab's parallel processing toolbox was purchased. The task would be well within the additional constraints of independent loop iteration provided by parallel processing (The MathWorks Inc., 2014b).

Adjusting the number of iterations used for motion-blurred simulated images also increased image processing time. The number of iterations was controlled the strictness

level of the measurement acceptance criteria, and the effectiveness of the algorithm to predict the parameters to use for the next iteration. Reducing the criteria speeds up image processing as fewer iterations are required, but measurement accuracy will decrease.

The accuracy of the results were also influenced by the processing options used for images and some of the exact parameters used. For example, increasing the number of pixel intensity profiles measured at each target increases processing time since each profile must be measured, and there were more points in the fitted ellipse. The dimensions of the image patch also affected the speed at which simulated images in generated, as smaller images are processed faster, but image patches must be large enough for the target in order to the measured.

Matlab is renowned for creating solutions quickly using its many built in functions and additional function libraries ('toolboxes'). Matlab also provides many tools for processing data and graphical output. However, unlike some other programming languages in which the language is compiled into an executable file, Matlab routines are stored as source code and compiled at run-time. This has the advantage of being easily edited on-the-fly and for debugging, but could increase the time necessary for image processing. An alternative would be to use a lower level language such as the C, C++ or python programming environments, which might run faster. OpenCV is a freely available library of open source functions for use in these environments with similar functionality to Matlab's libraries, and is also free (OpenCV, 2012).

5.1.1 Detecting structural changes

A demonstration of detecting structural changes was carried out after initial measurement of the unmodified state in section 4.4.3. Structures were modified, and monitoring was repeated.

If the LEMBI monitoring system were to be used as part of a structural health monitoring scheme, it would be expected that monitoring would take place, initially at the start of the scheme, and repeated at regular intervals. A change in the dynamic response from one 'epoch' to the next would indicate the need for further investigation. As the literature review discussed, this is not unlike current monitoring schemes, which aim to

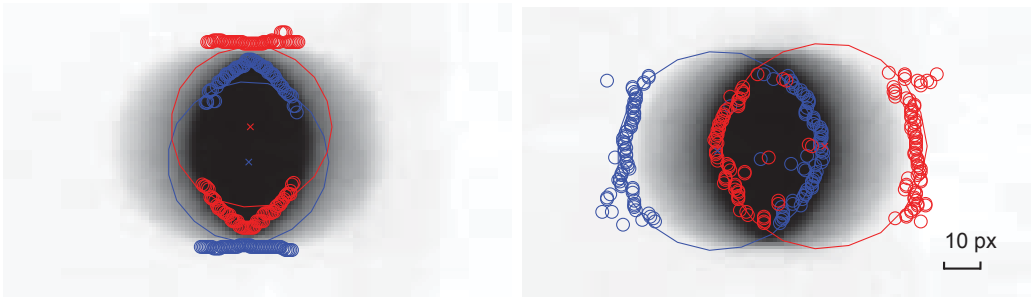

Figure 5.1: Examples of target measurement errors

detect the occurrence of a structural change.

5.1.2 Outlier measurements

Occasional outliers occured in the measurements. Outliers usually occur during measurement of image coordinates when the Pixel Intensity Profiles (PIPs) were oriented incorrectly, perpendicular to the target motion rather than parallel (figure 5.1). This could happen when the threshold used in the first step for a rapid-approximate estimate of the target's geometry is incorrect. Where these outliers occur, they were typically a result of an incorrect parameter and the error is evident in several targets in an image. The solution in this case was to modify the threshold used for identifying the blurred target smear, and repeating image processing.

Errors could also occur due to having too small a border around a physical target. If the target's motion caused it to intersect another dark area of the image, this interferes with identifying features of the blurred target smear. When this happened measured motion blur was unreliable, since the consistent target appearance that the algorithm expects is disturbed. The identified points representing the target extremes may be incorrect. The plain area around the target is therefore necessary to protect the centre target from interference.

Outliers could be reliably identified by calculating the variance of the PIP identified points from a fitted ellipse. The identified target edge points normally conform to an ellipse and typically exhibit variances from 0–1. In both of the identified cases for typical outliers, points are identified more randomly, and the variance values range from 2–30. The variance values are stored with the measured coordinates and can be used to identify

outlier measurements, which can then be removed easily.

5.1.3 Data Representation

Where the measured data must be assessed by a professional engineer, clear and concise presentation of the results is important. With a single measurement point and a traditional gauge, a time-history graph may be presented. When image-based measurements were compared with laser Doppler vibrometer, the image-based measurement is not continuous, rather in discrete intervals (section 4.3.4). In each interval, the total movement of the measurement point during the time the shutter is open is stored. Figure 4.13 illustrates one way in which the data could be compared. As discussed in section 2.1.3.1, richer information is available by comparing the relative motion amplitudes of measuring points to visualise the vibration envelope. Presenting the shape of the vibration envelope allows identification of the location of nodes and antinodes. Antinodes appear in the location of greatest motion, and nodes in location of zero motion.

For 2D planar motion, displacement vectors could be simply overlain on the original image, allowing visualisation of each displacement vector at its corresponding location on the test structure. 3D motion vectors could be drawn in a 3D rotatable and panable viewport on the computer, but it is difficult without a 3D model of the object in the figure to understand how individual vectors correspond to locations on the test structure. A simple way to present results would be to have the original stereopair images of the object with displacement vectors corresponding to the images individually. An engineer who is familiar with understanding 3D objects from multiple 2D orthographic projections of the object may find this satisfactory and the processing steps required would be no more than for planar monitoring. This type of representation would also be appropriate for printed paper. The viewport would be restricted to that of the camera, and not allow 'roaming' around the model. For complex models monitored with multiview imagery this method also becomes less efficient.

A 3D anaglyph image (an effect created by separating left and right eye images by coloured filters) of displacement vectors would also be possible. Since 3D data exists, it would be possible to render vectors in a 3D viewport, where the user would be able

to rotate the view to 'roam around' the subject, although it may be harder to visualise the correspondence between the displacement vectors and their location on a structure without the image of the structure for reference. As a compromise, the outline of the structure could be traced so that the displacement can be superimposed on a simple 3D skeleton model.

A more advanced approach would be to use standard photogrammetric techniques to create a 3D model of the test object, compromising of a point cloud or other textured surfaces making up the appearance of the test structure. This model could be manipulated in the viewport and LEMBI measured displacement vectors overlain of measurement points. Generating the point cloud for this approach would, however, increases the processing stages required to generate the output.

Alternatively, a digital 3D model of a structure may already exist, where either a Building Information Model has been created as part of a building design and management, or a Finite Element Analysis model created as part of a previous analysis. Provided the position and orientation of the model is correctly related to the measured deformation data, displacement vectors could be overlain on this model. As a surveyed point cloud of the actual structure is not used, geometric correlation between the actual structure and manually created model must be assured.

A suitable method was found to be making a 3D 'wireframe' of the model, overlain with the displacement vectors at measurement locations. The wireframe model was created using the sharp images loaded into the PhotoModeler software. Although adding manual steps to data processing, with the operator manually identifying image points at relevant corners, the commercial software package contained the tools to make this easy. A list of points describing the wireframe can be exported from PhotoModeler. These 3D lines were then plotted in Matlab and displacement vectors overlain, to produce a model to 'roam' around.

5.1.4 Number of Pixel Intensity Profiles

One of the factors affecting the accuracy of the measurement solution was the number of profile lines used for the Pixel Intensity Profile measurement (PIP) (section 3.2.3.5).

Generally, a higher number of profile lines would improve the measurement, but as the number of profile lines increased, the time taken for images to be processed increased also. Not only must the gradient change points be identified on every profile line in every iteration, but the blurred target ellipse was then fit to a larger number of coordinates. During tests, it was found that using 30 profile lines during measurement produced results that were not significantly improved with a larger number of PIPs, yet allowed acceptable image processing speed. Image processing was being carried out on a standard specification office laptop, and notably, the currently available Matlab license did not permit parallel processing (which would have been advantageous by allowing processing of different targets simultaneously).

To test the most efficient approach, using different numbers of PIPs to measure targets was tested. The number of PIPs for target measurement was increased to 100, and the Matlab routine executed. As might be expected, the routine processing duration increased. Using Matlab's 'tic' and 'toc' functions, the recorded time for image processing was 629.5 s. The measurement procedure was then repeated by reducing the number of profile lines used in measurement in increments of 10 (reducing to 2 for the fewer profile lines), and time for image processing was recorded again using the 'tic' and 'toc' functions.

The measured coordinate derived with LEMBI in each increment was compared with those measured by the shake table laser displacement gauge. Figure 5.2 shows the increase in standard deviation of errors for LEMBI measurements, as the number of profile lines decreases. Figure 5.2 also shows how the Matlab routine processing duration reduces as the number of profile lines decreases. From the graph, it can be interpreted that increasing the number of profiles lines above 30 yields little improvement in coordinate measurement, at least for the considered case studies, whilst computer processing time continues to increase. 30 profile lines was selected as a suitable compromise between measurement accuracy and image processing time.

The duration of image processing appears to slowly fall before 9 profile lines, before steadily increasing afterwards. From reviewing the results in more detail, it was found that more iterations of the PIP algorithm took place. The increase in iterations was associated with with the higher measurement standard deviations. The iteration increment acceptance threshold 5.1 was not modified to correspond to the poorer measurement ac-

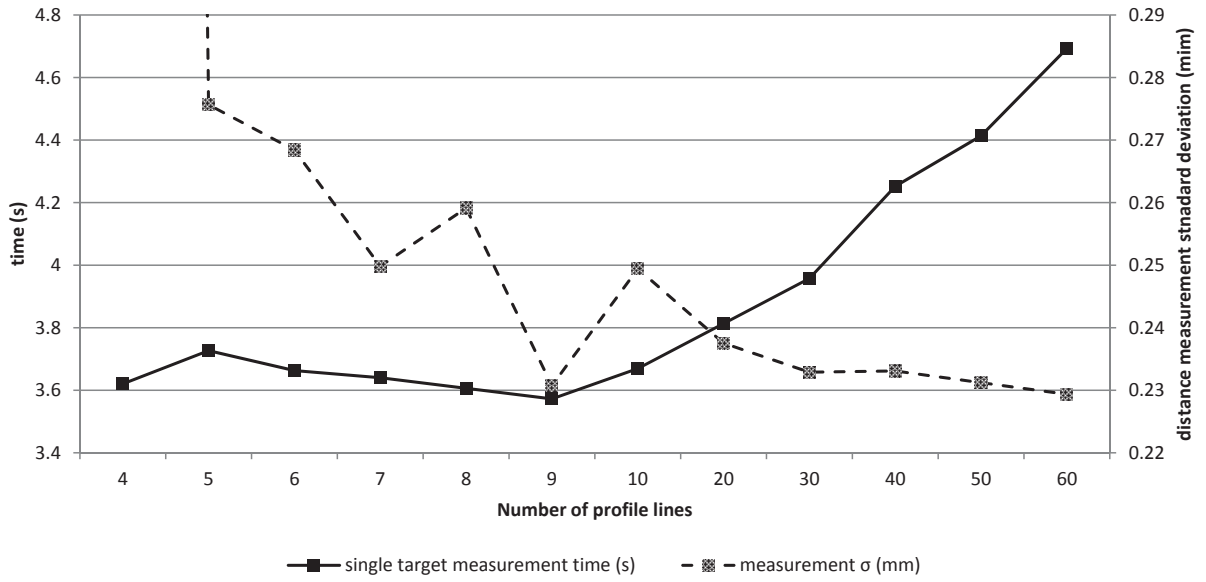

Figure 5.2: The effect of modifing the number of profile lines on image processing time and target measurement accuracy

curacy. Some further iterations were required because iteration adjustments, being based on the PIP measurements, were poorer.

It is acknowledged that, whilst the computer was not running other user applications whilst processing images, tasks often work in the background on modern operating systems and these may have been working, which could influence processing time.

It is suggested that a potential further improvement to the image processing routine would be to initially use a lower number of profile lines if the first iteration, and to increase the number of profile lines in the following iterations as the iteration estimate would be expected to be closer to the true measurement. In the final iterations, the highest number of PIPs would be used. By dynamically adjusting the number of PIPs in this way, measurement improvements may be realised with less influence on image processing speed. This is suggested as item for further investigation in the conclusion.

5.2 Survey Design Considerations

Despite the LEMBI monitoring approach having demonstrated its effectiveness, limitations exist. Like all surveying instrumentation, an understanding of how to use the instrument most effectively is important. Some notable survey design consideration and

limitations are discussed in the following.

5.2.1 Suitable Scale

Whilst a level of accuracy has been demonstrated that makes possible detection of vibrations in a civil engineering structure using the LEMBI approach, this was less at the demonstrated scales than could be achieved by other instruments specifically suited to dynamic monitoring. Consideration of the accuracy that will be achieved, with a particular camera system and object distance, should be calculated before designing the survey. Knowledge of the structure's approximate likely deformation is therefore also important. The approach may not be suitable for all structures. Particularly, it may not be suitable to those structures with higher stiffness and relatively low vibration amplitudes, such as reinforced concrete or masonry structures. The case studies were selected because they demonstrated the strengths of such a monitoring approach. Other structures would not provide as good results because their deformations would be too small, and these were deliberately not chosen.

A similar consideration is also a requirement for other instrumentation before they are installed, for correct sensor range selection and location. Accelerometers and associated data recording equipment must be selected from a range with different sensitivities, and when installed must be correctly orientated for their purpose.

5.2.2 Artificial Target Selection

Measurement is reliant on the application of circular targets with a background of contrasting colour that exceeds the expected deformation. Photogrammetric measurement projects often make use of signalised points, but technology has developed such to use untargeted features with adequate surface texture to significantly increase the density of measurements, with perhaps only a few targets to orientate images (section 2.3.4).

Nevertheless, fully targeted approaches are still used for the most accurate work, as target measurement algorithms are generally more accurate than marking of natural features. Blur measurement methods for textured features exist (section 2.4.5), and were tested (section 3.2.2), but was found to be unreliable with often irregular and incor-

rect measurement, and lacked precision, so the targeted approach was considered most workable. Not only does the use of targets improve accuracy, but allows some processing stages to be semi-automated. When images are loaded in to PhotoModeler, the signalised points are quickly recognised.

The addition of targets to the object increases set-up time and cost if these locations are not easily accessible and special access arrangements are required. Thus, consideration must be given to the location of targets, the accessibility of these location, the method of making a secure fixing, and the time taken to install the number of targets desired. A similar constraint already exists for contact gauges such as accelerometers, as well as GPS, and monitoring using high-speed photogrammetric imaging techniques with targets, but the hardware cost of photogrammetric targets is much less. Access arrangements could also be more complicated if further cabling is necessary for the accelerometers. Photogrammetric targets at a minimum are 'passive', not requiring cable infrastructure. An image processing approach would, however, require the inclusion of a remote observation location for the cameras, but allows a degree of flexibility in its location, so long as a clear view of all necessary targets is maintained. The requirement for installation of physical targets on the structure may mean the monitoring approach may not be considered 'truly' non-contact (Cooper and Robson, 1990), yet it still offers similar advantages as other non-contact approaches such as not requiring immediate stable reference.

Literature has mentioned the use of actively illuminated targets, such as individual LEDs, to permit monitoring during hours of darkness (section 2.4.2.3), where the structure's surface would not be visible unless other illumination is provided, itself having practical difficulties. In this case, the motion path of the light would be shown in light pixels in the image, with the background appearing dark.

5.2.2.1 Target Size

The size of the target must be selected during test preparation. Not only does the diameter of the circular target need to be defined, but also the dimensions of the target surround, which must exceed the measurement point's motion to avoid interference between the motion-blurred target and other background objects in the image. For the

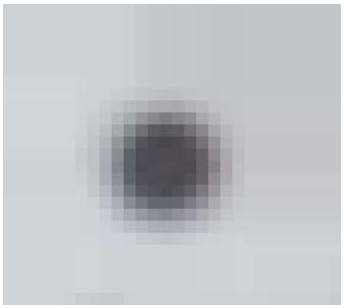

Figure 5.3: A 10 pixel diameter circular target, too small for LEMBI measurement

latter, increasing the dimensions more than necessary does not negatively impact measurement, but too large a target could be impractical, and influence a structure's wind loading.

Some knowledge about the scale of the expected deformations as well as the image scale is therefore necessary when selecting the diameter of the target. If vibration amplitude is less than approximately one tenth the target diameter, measurement becomes unreliable, with motion direction estimates becoming unreliable, and incorrect direction estimates which could result in an undesired amplitude estimate. When the motion amplitude is approximately 3 times greater than target diameter distance measurement becomes unreliable, as the range of pixel values in the blurred image patch is severely reduced. Where the blurred image of the target has a range of pixel value of only 10-15 the edges of the burred target are poorly defined. Very large targets (diameters <40 pixels) are more resilient to motion amplitude that is too large.

These limits on target diameter relative to object motion impose limits on the smallest and largest measurable motion amplitude. Subject to available object distances and lens configurations, this limit of measurable motion can be controlled by using alternative target sizes. The smallest measurable motion for a larger target is greater than for a smaller target. Therefore, the selected target size should be smaller if smaller motion is expected.

In the Wilford bridge results (section 4.3.4) is was apparent in figure 4.14 that the target distance from the camera was too great for effective measurements. With a 20 mm target at an object distance of 36.94 m, with an 85 mm focal length, the target diameter was only 10 pixels in the image space (figure 5.3). Whilst targets this size are acceptable for standard photogrammetric work, when subjected to motion, the target appearance

was too severely degraded for LEMBI measurement. Effectively a target diameter of approximately 15–20 of the expected motion is the minimum necessary, for motion up to approximately two thirds of the target diameter. Whilst the selection of target size can control the detectable motion amplitudes, the smallest measurable motion limit imposed by the image scale requires an increase in focal length to be improved, possibly reducing the object visible in field of vision.

5.2.3 Camera Location

The availability of camera locations requires consideration at an early stage of survey design. The Wilford bridge case study demonstrated how camera locations can be restricted. Locating a camera normal to the structure would have required a telephoto lens with a long focal length to be located over 100 metres away. Such lenses are available, but at greater cost. Additionally, any movement of the camera would be magnified. Whilst it is possible (and for conventional photogrammety, routine) to compensate for camera movement between captured images, compensating for camera motion during image acquisition would be particularly testing. Having a longer viewing distance would also make the instrumentation more susceptible to atmospheric conditions prevalent, such as fog, and inadvertent occlusions may be more likely over a long distance.

In the demonstration, the maximum target distance was reduced by positioning the camera so that the axis was oriented along the bridge. A 85 mm lens could then be used. This created the problem that a very long depth of field (DOF) was necessary: the furthest target being 70 m away from the camera and the nearest only 1 m away. Depth of field is controlled by adjusting the aperture, with a large aperture creating a short DOF (often a desired artistic effect), and small aperture a longer DOF, which a long exposure image can often accommodate. Smaller apertures are usually desired for photogrammetric work as more objects in the image can be in focus. Conveniently, the minimum aperture is already selected for the lowest exposure, providing the maximum depth of field.

During the Wilford bridge case study, significant degradation was not observed, when the images were viewed. Although severe out-of-focus blur is likely to degrade measure-

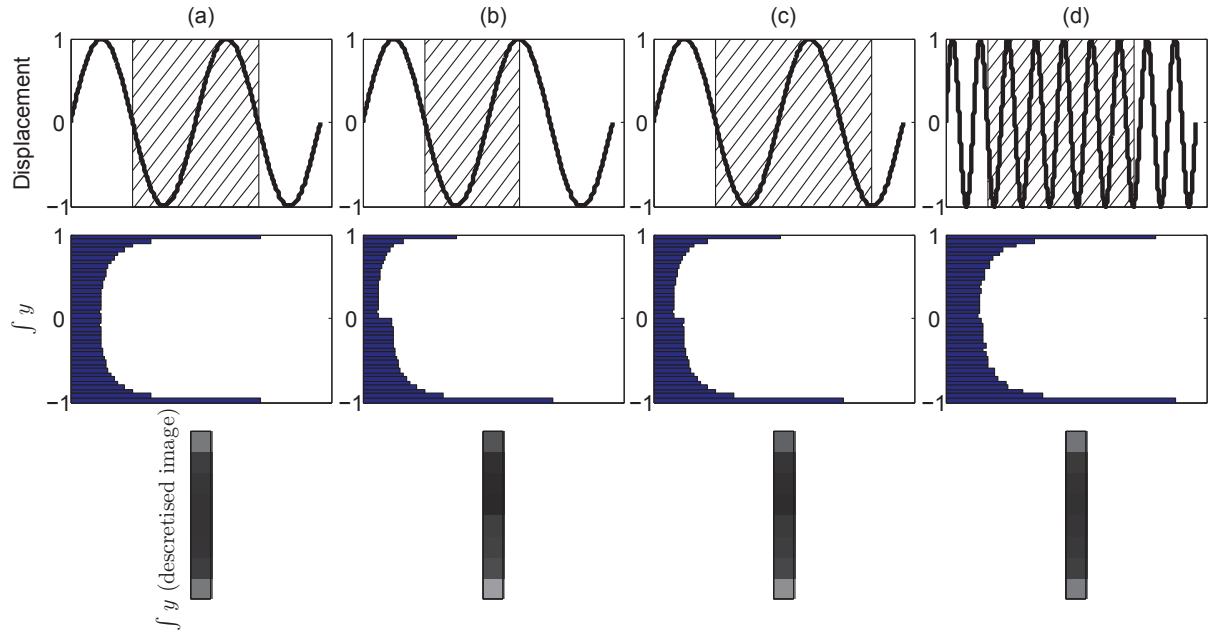

Figure 5.4: Demonstration of the effect of incomplete cycles (a) $\delta t = T$ (b) $\delta t = {}^{3}/_{4}T$ (c) $\delta t = {}^{5}/_{4}T$ (d) multiple cycles

ment accuracy, out-of-focus blur is automatically compensated by the LEMBI algorithm. Further assessment of the resolving power of the camera with objects at a range of distances and a long DOF could be made using a Siemens star in a laboratory environment.

During the Wilford bridge case study, it was noted that the LDV (which was also in use) only measures out-of-plane motion, whilst each camera sensor will only make in-plane measurement, so the availability of observation locations will have influence on the choice of sensor. During the Wilford bridge case study, the LDV could not be located in its optimum configuration, perpendicular to the bridge underside, and since the bridge spanned a river, the camera also could not be located directly parallel to the bridge centreline, again due to the course of the river.

5.2.4 Shutter Speed vs Vibration Frequency

If imaging speed is slow with respect to the vibration frequency, whole vibration cycles may not be captured. When only a partial cycle is captured, the PSF of the motion at the object during the time the shutter is open may not conform to the assumed sinusoidal pattern.

If the shutter speed is for example ${}^{3}/_{4}$ or ${}^{5}/_{4}$ of the motion period, integrating the

motion path produces a different distribution. In particular, one side of the target may appear bolder than the other and there is a discontinuity in the PSF. Figure 5.4 shows four harmonic curves of a targets motion, each with a highlighted interval during which an image would be captured. The second row shows the distribution of the objects position during that interval, and the third is a descritised PSF. Figure 5.4(a) is of an interval equal to the motion period, a whole interval is captured, and the PSF conforms to the expected sinusoidal PSF. Figures 5.4(b, c & d) shows three PSFs of incomplete periods captured. The PSFs for (b) and (c) do not conform with the sinusoidal PSF, with one 'end' being bolder than the other and a discontinuity is created in the centre. The difference is greater in (b) than (c). The harmonic patten emphasises the edges of the motion-blurred smear so that they can be measured, but an incomplete period modifies this.

Where the vibration frequency is much higher than the shutter speed, the affect of the incomplete cycle is reduced, and so the PSF does not vary significantly from the uniform sinusoidal PSF. In figure 5.4(d) the PSF appears sinusoidal again. During testing, where the imaging speed is greater than 2 motion periods, motion blur measurements appeared to remain successful.

Consideration must be given to the desired recording frequencies, so that appropriate camera exposure parameters can be set. In the tests described in section 4.1, the exposure time was set to at least twice the imposed or expected motion period, so that any 'half' cycle was not recorded. In practice for harmonic periodic motion, it was not necessary to reduce exposure time for higher test frequencies, where several complete cycles were captured.

With the exposure time fixed as specified, the camera's other parameters must be set appropriately so as to achieve suitable exposures images. Allowing too high an exposure results in saturated pixels around the target background, and some pixels around the target edge, which would otherwise form part of the target border are also saturated (figure 5.5). Too low an exposure, and the opposite is the case. ISO and aperture were set with trial and error to achieve suitable exposures. The images could be quickly review on the Nikon D80's display, and overexposured regions of the image are automatically highlighted.

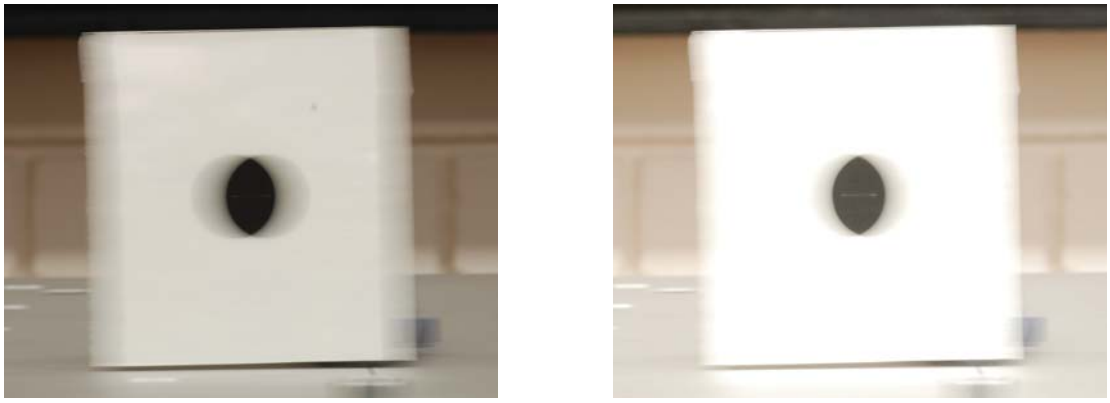

(a) Suitably exposed target image (b) An over-exposed target image

Figure 5.5: When image exposure is too high, pixels which would otherwise form part of the target border are saturated.

5.2.5 Filters

Whilst using a long shutter speed to capture motion, the camera's aperture and sensitivity had to be reduced to get suitably exposed images. Where a combination of the smallest aperture and lowest sensitivity still results in images which had overexposed regions, neutral density filters were added to the lens. This was often the case when working outdoors. Whilst bringing image exposure into a suitable range should improve measurement success and accuracy, the addition of optical elements has the potential to introduce further lens diffraction and distortions. The camera calibration procedure was repeated using the calibration field in the laboratory (section 3.1.2). The calibration was used to model the combined consumer lens and filters as a single lens system. The three ND filters available for use cost £7.50 together, so could be considered budget range filters that cannot be expected to be manufactured to the same quality as professional lenses. Distortion caused by the filter is expected, and can be modelled, so is unlikely to have significantly reduced accuracy. The assumption that the lens distortion corrections are not needed for small localised displacements because they will almost cancel out remains valid, particularly for 2D measurements (section 2.4.3).

For different sensor hardware, such as machine vision cameras, it is possible that sensitivity could be reduced further without the need for additional hardware filters. These can provide the added advantage that sensitivity can be modified without manual hardware changes as the brightness conditions change outdoors.

5.3 Comparison with alternative monitoring technologies

This section compares the LEMBI monitoring approach developed here with other dynamic monitoring approaches introduced in the literature review. Each comparison comprises not only the level of measurement accuracy, but the practical considerations of each method, such as monitoring orientation are appraised.

5.3.1 Accelerometer

Accelerometers are frequently used for dynamic monitoring. They provide a direct measurement of motion of the sensor, which is securely fixed at the monitoring point on a structure. Accelerometers are available in different sensitivities, depending on application, For instance, the accelerometer set-up used for the lab experiments had a sensitivity of 1.2×10^{-8} m/s^2 and sampled at 1652 Hz. The actual sensitivity of an accelerometer monitoring system is dependent on the particular type of sensor, the sensitivity of the data logger and any signal amplifier that may be in use.

Installation is simple where direct access to the structure is possible, unlike optical instruments which require a line of sight. Since there are no interruptions to a line of sight by occlusions, or interruptions such as poor weather, so accelerometers have higher reliability.

Significantly, an individual accelerometer will only provide measured data for the location it is fitted. For determining modal shapes where multiple monitoring are necessary, it is possible to use an accelerometer, but the sensor must be systematically moved to each monitoring location, whilst the vibration remains constant. In these scenarios, those instruments that monitor many locations simultaneously are advantageous. Each additional accelerometer adds significant cost, as the gauge is an expensive specialised gauge which is individually calibrated by the manufacturer.

The limitation of the accelerometer is that, being a contact sensor, it must be fitted at the monitoring location and connected to the data logger to either store results locally for downloading later, or relay them to a remote location. The difficulties of this were

discussed by Battista *et al.* (2011) and identified that the cabling is necessary, both for power and data transmission.

Accelerometers record data in the acceleration domain. If data in the displacement domain is desired for determining vibration amplitude, the data must be filtered and double integrated. Automated software packages exist, but manual selection of filters is necessary. This is an unreliable method of determining displacement, since the data will drift when integrated. If absolute displacements over a longer time period are desired, for example to measure static displacements in conjunction with dynamic response, the accelerometer must be supplemented by other sensors such as an LVDT (section 2.2.1.1), which would also require stable support. The image based approach, however, allows direct measurement of displacement with the same instrument arrangement as used for LEMBI monitoring.

5.3.2 Laser Doppler Vibrometer

Non-contact vibration monitoring is also possible using the Laser Doppler vibrometer, introduced in the literature review (section 2.2.2.5). The instrument that we have used for the Wilford bridge case study has a velocity measurement resolution of 0.01 µm/s (Polytech Ltd., 2014a), significantly higher than image monitoring approaches. This instrument has also no requirement for artificial targeting: a low-resolution camera built in to the instrument allows careful targeting of the measuring beam. This allows monitoring of structures where access to the measuring location is impossible. Monitoring is also possible over distances of 300 m.

Monitoring is limited to a single location, where the laser is targeted and if monitoring at several location was necessary (for modal analysis), the vibration should remain constant whilst the measuring beam is systematically moved from one monitoring point to another. A contrasting difference between the LDV and image-based measurements is that the LDV measures out-of-plane motion, and no in-plane motion is detectable. If motion is not wholly parallel to the measuring beam, measured displacements will either be subjected to a scaling error, or displacements in two directions could become confusingly combined. Where the orientation of the measuring beam limited by the avail-

able locations for the instrument, the direction of the measurable vibration is limited in turn. Image-based techniques permit only in-plane measurement (although some techniques have measured out-of-plane motion by observing changes in scale of specific targets (Chang and Xiao, 2010), but this method is less rigorous), so an image-based approach also has monitoring direction constraints.

Photogrammetric techniques also permit 3D measurement with stereo or multiview imagery. It is possible to measure in 3D using multiple LDVs, but for many applications this could be prohibitively expensive given the instrument's very high cost, the Polytech RSV-150 costing £67,000. A stereo imaging system is far cheaper and within the possibilities of many projects (section 5.4).

The LDV's interferometric measuring beam measures in the velocity domain, rather than acceleration or displacement. For applications when acceleration time history is required, differentiation of the velocity data provides the necessary acceleration data. Absolute displacements can be determined, but only by integration of the velocity data, which, like the accelerometer, requires filtering and will exhibit drift.

5.3.3 High Speed Imaging

Monitoring vibrations by measuring instantaneous position in a rapid sequence of short-exposure images is the traditional approach used to measure vibration using photogrammetry. The approach relies on well-developed techniques, and achieves accuracies similar to traditional photogrammetric measurement (Olaszek, 1999; Wahbeh *et al.*, 2003; Helfrick *et al.*, 2011). The approach is critically dependent on the camera hardware's ability to rapidly capture a sequence of images, and is successful provided suitable hardware is available.

More often, the hardware's capabilities imposes some restriction. Generally, a compromise exists between the image resolution and imaging frequency of the camera, owing to the amount of data created and the speed at which it can be stored (section 2.3.5).

Many cameras have a 'burst' mode to acquire a short rapid sequence of images and may be able to capture images in a burst mode at a higher frequency than in a continuous mode. Whilst this temporarily improves the hardware capabilities, the image capture

rate cannot be sustained for more than a short period. The length of this short period of rapid image acquisition is dependent on the size of the camera's buffer which stores images before writing to memory and once the camera's buffer is full, imaging frequency must reduce to the speed that images can be stored to the memory card. The data transfer rate of a 'UHS Speed Class 3' SD card, the current fastest performance standard, is 30 MB/s (SD Association, 2015; although some manufacturers indicate a maximum speed which is not defined by SD standards), and JPEG images from the Nikon D80 is about 3.5 MB (file size varies), so if the camera were capable of writing to the SD card at a maximum speed, less then 9 images could be captured per second, but technology advances rapidly.

At the limit of the hardware's capability, imaging frequency can become unpredictable. The imaging speed is limited by the rate at which images are written to the memory card, but since file sizes vary after JPEG compression (and the larger images files will take more time to write than the smaller) the result is unpredictable imaging frequency. Other factors affecting data storage include amplification and file fragmentation will affect the rate that data can be stored to the memory card (SD Association, 2015).

This limitation is alleviated with LEMBI measurement, which has much lower image acquisition rate, well within the capability of the SD card data transfer rate. Maximum resolution images can be stored without filling the camera's buffer.

Instead, additional time is required for the image to be processed on-board the camera before it is ready to be stored, as evidenced by the time taken for the image to be ready for display on the screen. The implication is that subsequent images cannot be captured immediately after the previous, even if space is available in the camera's buffer. Previous (Wilford bridge) results show intervals between each image capture without measurement (figure 4.13). This factor does not reduce the capability of motion measurement, since the complete motion has been captured when the shutter closes, a second image is not necessary. It does require a pause before subsequent sampling. For example, during shake table monitoring, the signal remains constant for each image to be captured, including waiting for the image to be processed and stored.

5.4 Off-the-shelf components

A notable advantage of the photogrammetric based LEMBI measurement system developed in this thesis, is that it uses off-the-shelf consumer hardware. None of the other non-photogrammetric measurement systems identified in the literature review make use of consumer hardware, as they are all dependent on specialist instrumentation constructed for commercial projects. Photographic equipment costs less than advanced specialist instruments that would usually be required for monitoring of structural dynamics. Cost savings have already been recognised when image based measurements have been used (Wahbeh *et al.*, 2003). In many instances, cost is a significant factor in projects, governing the quantity of data that can be captured. The higher availability of off-the-shelf hardware also reduces lead times for the delivery of dedicated equipment, and reduces the risk of hardware failures as sensors can be rapidly replaced.

The sensors used for image based monitoring schemes are, in general, adaptable to a variety of different applications. For example, the same hardware has been used throughout this project for case studies of different scales.

The only bespoke system hardware used for this project was the camera remote control shutter device that was adapted to trigger two cameras simultaneously (figure 3.2). This device was manufactured in-house by the department's lab technician. The relatively simple circuit's primary components consist of two ordinary single remote control cables, a relay and battery. It is likely that a similar device could be quickly recreated by any competent electrical engineer.

5.5 Implication to Structural Testing

The developed monitoring approach clearly provides an additional method for recording the vibration response of structures. LEMBI monitoring chiefly alleviates the dependence of imaging speed from vibration monitoring, allowing higher resolution sensors to be used. The implications of this are described here.

A notable strength of the approach is the number of possible measurement points measurable with only the few imaging sensors. The photogrammetric measurement ap-

proach can, therefore, be employed in scenarios requiring non-contract monitoring of a very high number of monitoring points (section 2.3).

This approach is particularly relevant to dynamic testing, where the reduced interpolation between monitoring points allows more accurate determination of the vibration envelope. The shake table case studies revealed how the vibration envelope can be recovered. Alternative strategies for determining these shapes could be a series of accelerometers. Several would be necessary, with simultaneous data logging. The advanced scanning LDV would be more convenient and allow monitoring with a single non-contact image. A significant limitation of the instrument would be the very high cost, even to hire the instrument.

It may also have been possible to determine the vibration envelope with fewer sensors, but not without increasing interpolation between monitoring points. Nodes can be located to between targets, and so the closer the spacing, the more precisely the location of the node can be determined. More subtle spatial variations can clearly only be identified by a system which reduce the need for interpolation.

5.6 Discussion on investigations into developing LEMBI monitoring further

The proposed monitoring system provides an approach to monitoring vibrations that is radically different to the monitoring systems currently in use. Further developments to LEMBI monitoring were investigated, but were not developed far enough to be incorporated into the proposed solution. The additional challenges encountered whilst attempting to extend the monitoring system are recorded here.

5.6.1 RAW image file format

Errors in the image correlation approach described in section 3.2.2.3 were attributed to a non-linear camera response function, and attempts were made to correct for this effect during image post-processing. An alternative would be to bypass the camera's internal processing and use the RAW image data directly. RAW image formats usually allow

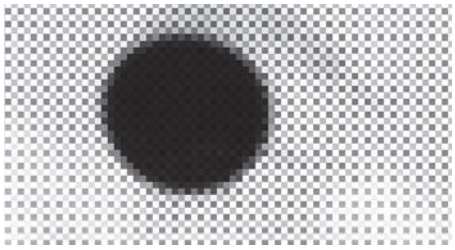

Figure 5.6: The result of the mosaic Bayer filter is clearly visible in a RAW image.

a photographer to make improvements to images because they record all of the data collected by the camera sensor without any post-processing. Manual processing of these RAW format images would allow the manufacturer's undesirable post-processing steps to be bypassed.

Depending on the hardware used, recording in RAW format may also allow higher bit-depth imagery, which would be more sensitive to the detail of gradients. This could provide better accuracy to blurred target measurement.

RAW format image files are very large since their data is not compressed, and this could delay getting results from images, so any improvements in the use of RAW images must be compared to the negative practical consequences.

Although bypassing the camera's post-processing provides the most direct measurement, interpretation of light intensities in more difficult since some post-processing steps are necessary and must be recreated. The RAW image data shown in figure 5.6 shows how a mosaic pattern exists on the image. A Bayer filter covers each pixel with a coloured filter (Russ, 2011). By knowing which pixels are coved with which coloured filter, full colour images can be reconstructed by interpolating data with neighbouring pixels of different colours, a process known as demosaicing.

5.6.1.1 Simple demosaicing

There is no single optimum algorithm for demosaicing, and many algorithms are developed for aesthetic reasons, rather than scientific accuracy. Since only greyscale images are necessary, it was attempted to create a simple demosaicing filter that assumed that, for an approximately grayscale image (such as an image patch of a blurred target) a simple factor can be applied for each colour channel. Eddins (2011) describes the steps

necessary to import the Nikon RAW images into Matlab. The Nikon NEF format is first converted in to DNG format using 'Adobe DNG Converter' (Adobe Systems Incorporated). All of the image data can then be read from the DNG file using TIFF commands. Unfortunately, demosaicing an image in this simplified way proved unsuccessful, and the mosaic pattern remained visible in the images.

5.6.1.2 Demosaicing with Adobe Photoshop

Another approach to glean the higher bit depth images was to load the RAW format images in Adobe Photoshop and allow demosaicing to be transparently carried out by the software and export the image as a 16-bit TIFF file. Although this does not allow control of the camera response function, it would preserve the higher bit-depth image. Testing this approach was time consuming, as images had to be individually loaded in to and exported from the Photoshop software package, where the files are saved in a 48 bit-depth TIFF format.

These higher bit-depth TIFF images were loaded into Matlab. By examining a histogram of pixel intensities (using Matlab's 'imhist' function) it was evident that the data was not 'true' 12-bit or even 10-bit data, but was descretised in to 683 intervals. There was, therefore, not substantially more detail than the 8-bit images that have been previously analysed. Additionally it was observed that the Nikon 'NEF' RAW format files contain a 'linearisation curve': a look-up table relating image pixel values (which have maximum value of 768) to 12-bit values (Eddins, 2011), rather than storing each pixel value in 'true' 12-bit precision. Although use of RAW imagery could improve precision of the algorithm, it was judged too problematic to create a working system, particularly it if was to be developed into a 3D solution. The potential of RAW image data to improve measurement is an area suggested for further investigation in the conclusion chapter (section 6.2).

5.6.2 Estimating velocity

It was suggested that the approach could be used to estimate the velocity of a moving object by measuring the distance travelled by the object and dividing by the duration

that the shutter was open. This could possibly be extended to estimate the frequency of the vibration. A similar approach has been used by Caglioti and Giusti (2009), who determine the distance travelled of a sports ball, and include a monoscopic 3D measurement approach by measuring an apparent change in the ball image's diameter. Lin *et al.* (2008) also measure motion-blur of cars and apply a similar method. These methods do not determine an instantaneous speed, rather an average velocity over the interval the shutter is open. Where the velocity is relatively constant, such as for a vehicle or ball in free flight, the approach has been successful (Lin *et al.*, 2008).

For the motion of structures moving at their natural frequencies, additional problems exist because the sinusoidal motion has other characteristics, that the velocity is not constant and changes direction. This complexity raises other challenges that the LEMBI approach can begin to address once a deeper understanding of changing velocity and direction are appreciated.

Changing velocity The velocity of the object, its speed in a given direction, is constantly changing as it vibrates sinusoidally. This illustrated in figure 5.7, where several intervals of the motion capture different motion amplitude. Each imaging interval is the same, but a different distance is measured in each. Calculating velocities by dividing these measured distances, Δu, by the time the shutter was open, t, would indeed give the average velocity during the time the shutter was open, but unless the phase of the wave is known, this cannot be extrapolated to find the frequency. Although the velocity is measured, it may not help with the civil engineer's analysis if the measurements cannot be transferred into a domain that can be compared.

Reversing Motion Direction Difficulties also arise where the velocity of the motion reverses, as it moves back and forth. In the first capture in figure 5.8, the average velocity during the interval, where the object start and end in the same position is zero, but this cannot be known from the image alone. Identifying the change in motion direction from the distribution of the PSF would also be insufficient, since both captures in figure 5.8 would have a similar distribution even though the measurable distance is different. To understand the motion during this interval again requires knowledge of the phase. LEMBI

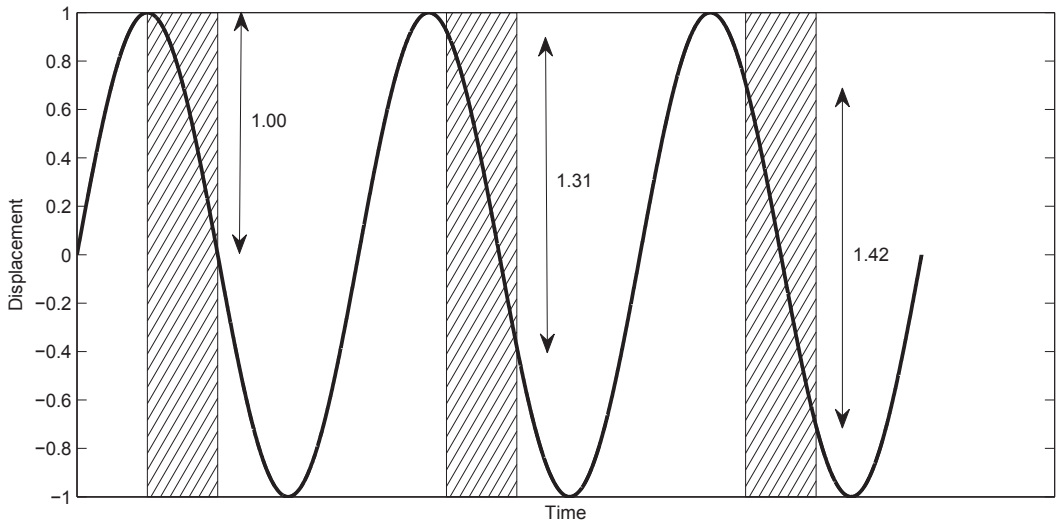

Figure 5.7: Result of different distances measured during different intervals

could be used to determine certain geometries during an initial test, followed by a more advanced test which could determine this information.

5.6.3 Measuring Different Waveforms

The vibration of civil engineering structures principally comprises of harmonic functions. During the frequency selective case studies demonstrated in this thesis, only one natural frequency is excited at a time, and so the motion is simply harmonic. If more than one natural frequency is excited, the resulting motion is the superposition of the response of the individual excited frequencies. If LEMBI measurement was extended to include motion that was not a simple harmonic function it could be applied in more scenarios, such as where frequency selective excitation is not possible. Some laboratory initial tests were conducted to test the suitability of LEMBI for monitoring motion in waveforms other than sinusoidal motion.

Square and sawtooth waves were tested (figure 5.9). Although these waveforms may not be measured successfully by the current LEMBI measurement algorithm, the appearance of the images and the difference between these and images generated by sinusoidal motion, is of interest.

Some further tests were conducted to examine the effects of differing waveforms. Tar-

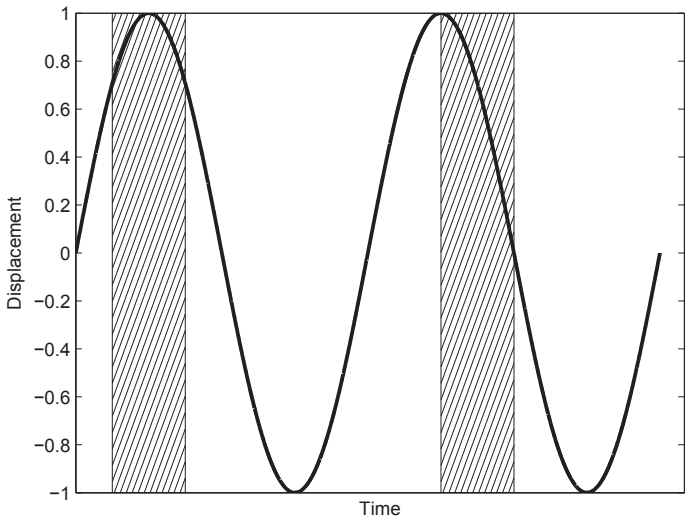

Figure 5.8: Reversing direction creates confusion; both of these measurements would give the same distribution but different amplitudes.

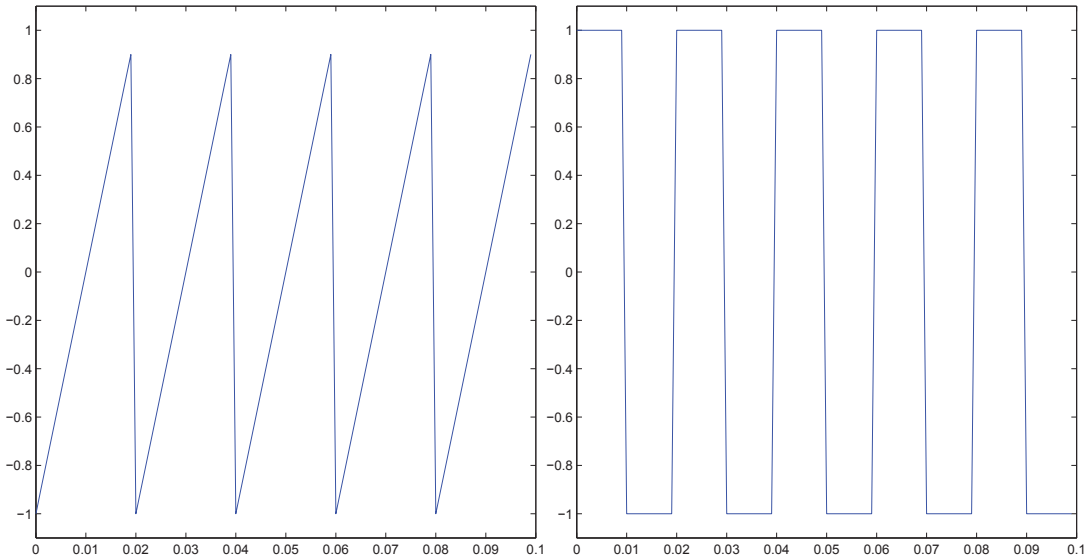

Figure 5.9: Different waveforms: (a) a square wave (b) a sawtooth wave

gets were again fixed to the shake table, which was programmed with the new waveforms. This was intended as an initial test to investigate the appearance of the images, which simply comprised of targets on the shaker table with a tripod mounted camera, and without control points. The table executed motion at the increasing programmed amplitudes, and images were captured.

On examination, the captured images did not appear significantly different to those of sinusoidal motion. On further investigation and examination of the shaker table's laser's recorded signal, although the input signal was modified to one of the above waveforms, the actual motion did not change significantly. This was because of the shaker table armature's inertia causes the shaker table to not change direction instantaneously. The input signal is proportional to the force applied to the table bed, but to reverse the direction of the table whilst it is in motion, the table must first decelerate to zero velocity before accelerating in the opposite direction.

Whilst these other waveforms are unlikely to be representative of the motion experienced by civil engineering structures, the capability of measuring other waveforms may be beneficial for monitoring broadband vibrations, where instead of frequency-selective vibration, the structure moves with more than one of its natural frequencies and the vibration of each is superimposed. Further investigation into the potential for measuring alternative waveforms using LEMBI for different applications is suggested as a subject for further investigation.

5.7 Summary

This chapter has discussed the findings made during the case studies described in chapter 4. First the factors affecting the accuracy of LEMBI measurement and the time taken for image processing were discussed. The accuracy of image measurements is dependent on some adjustable parameters, which when modified to improve accuracy, will increase the time for images to be processed. Other programming improvements that could reduce image processing were identified, but which have not been carried out within this project. The presence of outlier measurements was then discussed, and a strategy for removing outliers using the variance of coordinates fitted to an ellipse explained.

Strategies for presenting measured data as a qualitative graphic were illustrated, including approaches for 2D planar measurements and full 3D measurements.

The limitations of LEMBI monitoring were evaluated. Limitations include that the spatial measurement accuracy is less than commercial sensor systems, but this is offset by additional capabilities over other sensors, such as multiple monitoring of many monitoring points. The use of artificial targets was discussed, as this could be a practical limitation, but it permits higher accuracy than without. Suitable object scales were discussed.

The impact of low imaging speed with respect to the vibration interval was identified, including possible image processing problems as a result of incomplete sinusoidal periods that cause a PSF that does not conform to the sinusodial PSF that is assumed.

A comparison with other monitoring systems in then made: the accelerometer and laser Doppler vibrometer. A comparison with photogrammetric approaches using high speed imaging is made, which shares some of the same advantages, but crucial differences between the stored data are identified. The implications for structural testing are then evaluated. Finally, the potential for further LEMBI monitoring developments are discussed in regard to estimating the velocity or frequency of motion

Summarising, LEMBI monitoring for structural monitoring has capabilities for vibration measurement. Measurement of the vibration envelope has the potential for detecting changes to structure, as demonstrated in case study. The following concluding chapter will summarise the finding of this research project in to LEMBI monitoring and finally make recommendations for future development of the approach.

Chapter 6

Conclusion

This research project has investigated the potential for monitoring vibrations in structures using long exposure motion blurred images ("LEMBI") for dynamic structural health monitoring (SHM). The new method allows higher image resolutions than possible with existing image-based techniques, combined with higher spatial measurement accuracy and frequency invariance. The LEMBI measurement method was developed using off-the-shelf consumer hardware and bespoke image processing and space intersection algorithms. This chapter recites the objectives of this research project and demonstrates their completion.

> *Objective 1. Compose a literature review to assess current and particularly image based methods used for measuring deformations in structural testing, including both conventional and non-contact approaches.*

First, a literature review examined the existing techniques available for dynamic monitoring of structures; the motives for structural testing and the analysis techniques used were reviewed. Monitoring of structural dynamics is considered more convenient than statics by engineers for SHM. Dynamic techniques include identification of changes to a structure's modal frequencies as a result of structural changes, but the more advanced modal shape methods allow estimation of the location of changes. For this, a higher number of monitoring points is desirable to reduce interpolation, which inevitably causes loss of accuracy.

Available sensors include contact and non-contact sensors, and those that are specially intended for dynamic monitoring and those that are an extension of sensors usually used

for monitoring static properties. Most sensors are capable of monitoring in only one location at a time, i.e. the location they are fitted at, or for the laser Doppler vibrometer, the single location it is targeted at. Table 2.1 listed the properties of various sensors, and differentiated photogrammetry from other sensors in that it allows monitoring of many measurement points with sub-millimetre accuracy. Image-based monitoring techniques exist already, by measuring a structure at discrete 'epochs' and identifying deflections as a coordinate change from one epoch to the next. However, hardware capabilities limit the spatial measurement accuracy of this approach or the detectable frequencies, since a compromise exists between image resolutions and imaging speed. High resolution sensors are available at up to 50 MP (Feb, 2015), but at this resolution can capture at only 5 frames per second at the highest quality (Digital Photography Review, 2015). Video camcorders may record at 60 frames per second, but typically at only 2.07 MP ('HD' resolution). Specialist sensors that capture at even higher speeds are available, at a much greater cost.

For monitoring of static structural properties, this limitation is not significant, since the application of the deformation is generally much slower and the sensor's temporal limit is not reached. For dynamic monitoring, where the imaging speed has a direct influence on the frequency of measurable vibrations, the potential imaging speed is critical, and hence a compromise exists between measurable frequencies and measurement accuracy.

The remainder of the literature review examined image processing techniques currently in used in photogrammetry, and those used elsewhere in computer science for analysis and measurement of blurred images, both using artificial targets and natural features. Finally, the mathematical models for image geometry that allow determination of real-object coordinates in 2D and 3D from 2D images were reviewed.

> *Objective 2. Develop algorithms for measuring blur in long-exposure images captured during dynamic structural tests and design a method of incorporating these into routine structural testing.*

The methodology chapter initially introduced the hardware that would be used in this project, together with its specifications. This equipment was used to generate sample motion blurred images. An appraisal of different image processing strategies followed,

some making use of existing methods from literature, whilst others involve developing new developed Matlab algorithms. A distinction was made between natural feature-based image registration methods and those requiring artificial circular targets, with the latter favoured for better reliability and accuracy.

The proposed algorithms steps for measuring blurred circular targets are explained in full (section 3.3). First, some simple estimates about the geometry of the blur 'smear' are identified. Then, using these geometry estimates, parallel pixel intensity profile (PIP) lines are extracted, which are used to measure the motion blurred target. The third stage simulates an artificially motion-blurred image using a sharp "no-motion" image and the initial estimated motion. PIP measurements are repeated and compared to the measurement from the as-taken blurred image. Discrepancies may exist due to systematic differences between artificial and actually captured images, which are solved by iterating the estimated motion until the PIP measurement for both images (as-taken and simulated) are reduced to less than a user defined threshold.

Objective 3. Test the accuracy of such an image based system against conventional instrumentation.

The raw accuracy of the approach is demonstrated by comparing photogrammetric LEMBI measurements with the shake table's laser displacement gauge (section 3.4). The accuracy of the system is fully assessed (section 4.1, 4.2, 4.3) by comparing results against conventional instruments. A mean error of just ± 0.115 mm was observed for a camera-object distance of 1 m. Using a 95% confidence interval, the measured distances were considered accurate to within 0.38 mm. In the image space at this scale, this represented 1.43 pixels at the 95% confidence level.

Objective 4. Investigate potential of measuring deformation in three spatial dimensions using multiple camera locations and digital photogrammetry.

The LEMBI method was successful extended into full 3D measurement using two cameras (section 3.5). The PhotoModeler software package is used to determine the camera's exterior and interior orientations. A bespoke intersection algorithm was then used to determine the 3D coordinates. Difficulties with point matching were discussed,

where point matching is ambiguous because each target produces two coordinates in each image, at each end of its motion path, but by anticipating likely deformation directions during test set-up, the situation can be easily avoided.

Objective 5. Assess the scalability of image-based monitoring techniques for real structures using a series of case studies.

The first case study was of a simple plastic laboratory model mounted on the shake table (section 4.1). This model was initially monitored in planar-only 2D measurements at its first three modal frequencies. At each frequency, using the cameras, the vibration envelope was recoded. Later, monitoring was expanded to 3D monitoring, and the monitoring was repeated for the first three modal frequencies.

An upright wooden section of timber was used to demonstrate the approach for a longer object and outdoors (section 4.2). Monitoring was carried out in 2D, and then repeated in 3D about the timber section's major and minor axes. A comparison was made with the theoretical curvature for a section of constant stiffness. A full-scale case study was made of the Wilford Suspension bridge, West Bridgford, Nottingham (section 4.3), where measurements were compared with a laser Doppler vibrometer. This case study also demonstrated the approach on an actual civil engineering structure, and overcame obstacles for outdoor monitoring.

A study of particular relevance to SHM was the detection of modifications to the smaller shaker table using LEMBI monitoring. The vibration envelopes for the first three vibration modes were captured. The modifications consisted of adding mass to the structure, and modifying the stiffness of columns. In each case, changes to the vibration envelope were observed.

The considerations and discoveries whilst carrying out these case studies are discussed within this thesis. The quality of the data is affected by factors and parameters in the image processing, which are identified and discussed. An understanding of the limitations of LEMBI monitoring was gained through practical applications and later analysis of results, which are articulated.

A comparison is made with a range of other sensors. Conventional contact sensors are found the be more accurate, but none offer the same benefits of LEMBI monitoring.

Image-based methods permit many monitoring points and LEMBI is frequency invariant.

6.1 Achievements

This project has demonstrated a new approach for measurement of sinusoidal vibrations in civil engineering structures using long-exposure motion blurred images and it doing so has made a meaningful contribution to scientific knowledge.

The proposed method is novel, in that it uses a radically different approach to motion measurement, and the method could have wider applications than those tested here. The different approach produced data in a different format to that generally used, which emphasises a different aspect of dynamic testing which has upcoming potential for SHM (Kasinos *et al.*, 2014).

A workflow has been designed to record results using the LEMBI approach, which included the use of a new image measurement algorithm, which may be applied to other vibration measurement situations. The LEMBI technique is demonstrated by monitoring deformation using several case studies, providing information that is both cheaper and richer than is possible with conventional contact sensors.

6.2 Recommendations and possible future work

Further demonstrations of the LEMBI monitoring will serve to increase awareness of the approach and promote further developments. The three case studies used, whilst designed to be diverse, are relatively small in number, and further demonstrations will improve the understanding of the approach.

An ideal case study would be a structure that could be monitored prior to and following structural modifications or damage, most likely to be a structure that is scheduled for demolition. Farrar and Jauregui (1998) monitored a bridge as progressively severe damage was created by cutting into the bridge's supporting steel girders.

This thesis has focussed on the application of LEMBI for monitoring of civil engineering structures. The technique may have applications in other industries also; for example industrial metrology. Wang *et al.* (2007) identified vibration monitoring of com-

puter circuits as an application for image-based monitoring where difficulties exist with conventional sensors. The application of LEMBI monitoring elsewhere is encouraged. Further investigation into the measurement of different waveform motion blurred images may also be more applicable to other applications.

Improved accuracy is a constant aim when developing any monitoring system. This may be possible with a different implementation of the image measurement algorithm. Improvements could also be achieved through the use of higher bit-depth imagery, possibly gained through RAW image formats. Some work for this was made during this research project, but was not incorporated into the demonstrated measurement system, partly due to file type limitations (section 5.6.1). Improvements to the algorithms could also improve processing speed, such as by using parallel processing to dynamically adjusting the number of PIPs. Further investigation in this area or the use of different sensors could improve the measurement accuracy.

Some initial tests were conducted to test the feasibility of estimating vibration speed and frequency from single motion-blurred images. Initial testing and the included discussion identified a number of challenges for this measurement, which were not overcome in this project. Further investigations may solve this, further expanding the possibilities of LEMBI monitoring for civil engineering structures and wider applications.

This research was successful overall as answers were provided to the original objectives.

Chapter 7

References

3D Laser Mapping, 2011. *Site Monitor: Measuring and Monitoring a Changing World [Brochure].*

Abdel Wahab, M. and Roeck, G. D., 1999. Damage Detection in Bridges Using Modal Curvatures: Application To a Real Damage Scenario. *Journal of Sound and Vibration*, **226**(2), 217–235.

Adhikari, R., Moselhi, O., and Bagchi, a., 2013. Image-based retrieval of concrete crack properties for bridge inspection. *Automation in Construction*, **39**, 180–194.

Adobe Systems Incorporated, . *Adobe DNG Converter 8.4*. [online]. Available at: <http://www.adobe.com/support/downloads/detail.jsp?ftpID=5739> [Accessed 14 Sept 2014].

Al-Ghalib, A. a., Mohammad, F. a., Rahman, M., and Chilton, J., 2011. Damage Identification in a Concrete Beam Using Curvature Difference Ratio. *In: 9th International Conference on Damage Assessment of Structures (DAMAS 2011)*, volume 305, Oxford: IOP Publishing.

Albert, J., Maas, H.-g., Schade, A., and Schwarz, W., 2002. Pilot studies on photogrammetric bridge deformation measurement. *In:* Kahmen, H., Niemeier, W., and Retscher, G., (eds.) *Proceedings of the 2nd symposium on geodesy for geotechnical and structural engineering*, 133–140, Berlin.

Alvandi, a. and Cremona, C., 2006. Assessment of vibration-based damage identification techniques. *Journal of Sound and Vibration*, **292**(1-2), 179–202.

Arashloo, S. and Ahmadyfard, A., 2007. Fine Estimation of Blur Parmeters for Image Restoration. *In: 15th International Conference on Digital Signal Processing*, 427–430, IEEE.

Baldwin, L., 2011. Reconstructing an original look for damaged pier. *The Structural Engineer*, **89**(9), 8.

Banham, M. and Katsaggelos, A. K., 1997. Digital image restoration. *Signal Processing Magazine*, (March).

Battista, N. D., Westgate, R., and Koo, K., 2011. Wireless monitoring of the longitudinal displacement of the Tamar Suspension Bridge deck under changing environmental conditions. *In:* Tomizuka, M., (ed.) *Sensors and Smart Structures Technologies for Civil, Mechanical, and Aerospace Systems*, volume 7981, 79811O–15, Proceedings of the SPIE.

Ben-Ezra, M. and Nayar, S. K., 2004. Motion-based motion deblurring. *IEEE transactions on pattern analysis and machine intelligence*, **26**(6), 689–98.

Benning, W., Gortz, S., Lange, J., Schwermann, R., and Rostislav, C., 2003. An algorithm for automatic analysis of deformation of reinforced concrete structures using photogrammetry. *In: International Symposium on Non-Destructive Testing in Civil Engineering (NDT-CE 2003)*, Berlin, Germany: DGfZP.

Benning, W., Lange, J., Schwermann, R., Effkemann, and Gortz, S., 2004. Monitoring crack origin and evolution at concrete elements using photogrammetry. *In: XXth congress of ISPRS (International Society for Photogrammetry and Remote Sensing)*, volume 12, 23.

Boracchi, G., Caglioti, V., and Giusti, A., 2007. Ball position and motion reconstruction from blur in a single perspective image. *In: Image Analysis and Processing, 2007. ICIAP 2007. 14th International Conference on*, Iciap, Modena: IEEE Comput. Soc.

Bouguet, J.-Y., 2010. *Camera Calibration Toolbox for Matlab*. [online]. Available at: <http://www.vision.caltech.edu/bouguetj/calib_doc/> [Accessed 5 Apr 2011].

Brayer, J. M., 1997. *Introduction to Fourier Transforms for Image Processing*. [online]. Available at: <http://www.cs.unm.edu/~brayer/vision/fourier.html>.

British Standards Institution, 1986. *Testing concrete — Part 206: Recommendations for determination of strain in concrete*.

Brownjohn, P. J. M. W., 2011. Structural health monitoring: Examples and benefits to structure stakeholders. *The Structural Engineer*, **89**(9), 24–26.

Bungey, J., Millard, S., and Grantham, M., 2006. *Testing of Concrete in Structures*. 4th edition, London: Taylor & Francis.

Caglioti, V. and Giusti, A., 2009. Recovering ball motion from a single motion-blurred image. *Computer Vision and Image Understanding*, **113**(5), 590–597.

Carden, E. P. and Fanning, P., 2004. Vibration Based Condition Monitoring: A Review. *Structural Health Monitoring*, **3**(4), 355–377.

Castellini, P. and Tomasini, E. P., 2004. Image-based tracking laser Doppler vibrometer. *Review of Scientific Instruments*, **75**(1), 222.

Chakrabarti, A., Zickler, T., and Freeman, W., 2010. Analyzing spatially-varying blur. *In: Computer Vision and Pattern Recognition (CVPR)*, 2512–2519, San Fransisco: IEEE.

Chan, W.-S., Xu, Y.-L., Ding, X.-L., Xiong, Y.-L., and Dai, W.-J., 2006. Assessment of Dynamic Measurement Accuracy of GPS in Three Directions. *Journal of Surveying Engineering*, **132**(3), 108–117.

Chandler, J. and Clark, J., 1992. The archival photogrammetric technique: further application and development. *Photogrammetric Record*, **14**(80), 241–247.

Chandler, J. H., 2013. [Personal Communication].

Chandler, J. H., Fryer, J., and Jack, A., 2005. Metric capabilities of low-cost digital cameras for close range surface measurement. *The Photogrammetric Record*, **20**(109), 12–26.

Chang, C. C., 2007. From photogrammetry, computer vision to structural response measurement. *In:* Tomizuka, M., Yun, C.-B., and Giurgiutiu, V., (eds.) *Sensors and Smart Structures Technologies for Civil, Mechanical and Aerospace Systems*, volume 6529, 652903–652903–15, Proceedings of the SPIE.

Chang, C. C. and Xiao, X. H., 2010. Three-Dimensional Structural Translation and Rotation Measurement Using Monocular Videogrammetry. *Journal of Engineering Mechanics*, **136**, 840–848.

Chang, X. and Qunge, H., 2009. Dynamic structural monitoring using the kinematic positioning of a robotic total station. *In:* Jianping, C., (ed.) *9th International Conference on Electronic Measurement & Instruments (ICEMI'2009)*, 2–69, Beijing: IEEE.

Chang, Y. and Reid, J., 1996. RGB calibration for color image analysis in machine vision. *IEEE Transactions on Image Processing*, **5**(10), 1414–1422.

Chen, W. G., Nandhakumar, N., and Martin, W. N., 1996. Image motion estimation from motion smear—a new computational model. *IEEE Transactions on Pattern Analysis and Machine Intelligence*, **18**(4), 412–425.

Choi, H.-S., Cheung, J.-H., Kim, S.-H., and Ahn, J.-H., 2011. Structural Dynamic Displacement Vision System using Digital Image Processing. *NDT & E International*, **44**(7), 597–608.

Clough, R. and Penzien, J., 1995. *Dynamics of structures*. 2nd (revis edition, California, USA: Computers and Structures, Inc.. Available at: <http://trid.trb.org/view.aspx?id=50306>.

Cooper, M., 1984. Deformation measurement by photogrammetry. *The Photogrammetric Record*, **11**(63), 291–301.

Cooper, M., 1987. *Control Surveys in Civil Engineering*. London: Collins.

Cooper, M. and Robson, S., 1990. High precision photogrammetric monitoring of the deformation of a steel bridge. *Photogrammetric Record*, **13**(76), 505–510.

Cronk, S. and Fraser, C., 2006. Automated metric calibration of colour digital cameras. *The Photogrammetric Record*, **21**(116), 355–372.

Dai, S. and Wu, Y., 2008. Motion from blur. *In: 26th IEEE Conference on Computer Vision and Pattern Recognition*, 1, 1–8, IEEE.

Dai, S. and Wu, Y., 2009. Removing partial blur in a single image. *In: Computer Vision and Pattern Recognition*, Miami.

De Roeck, G., Peeters, B., and Marck, J., 2000. Dynamic Monitoring of Civil Engineering Structures. *In:* Papadrakakis, M., Smartin, A., and Onate, E., (eds.) *Computational Methods for Shell and Spatial Structures IASS-IACM 2000*, 1–24, Athens, Greece: ISASR-NUTA.

Debevec, P. and Malik, J., 1997. Recovering high dynamic range radiance maps from photographs. *In:* Owen, G., Whitted, T., and Mones-Hattal, B., (eds.) *Proceedings of the 24th annual conference on Computer graphics and interactive techniques*, Los Angeles, CA, USA: ACM Press.

Digital Photography Review, 2015. *Canon EOS 5DS: Specs.* [online]. Available at: <http://www.dpreview.com/products/canon/slrs/canon_eos5ds/specifications> [Accessed 21 Feb 2015].

Dilena, M. and Morassi, A., 2011. Dynamic testing of a damaged bridge. *Mechanical Systems and Signal Processing*, **25**(5), 1485–1507.

Direct Industry, 2011. *Aries Ingeniería y Sistemas: Laser Doppler vibrometer.* [online]. Available at: <http://www.directindustry.com/prod/aries-ingenieria-y-sistemas/laser-doppler-vibrometers-70745-614442.html> [Accessed 23 Jan 12].

Eddins, S., 2011. *Tips for reading a camera raw file into MATLAB.* [online]. Available at: <http://blogs.mathworks.com/steve/2011/03/08/tips-for-reading-a-camera-raw-file-into-matlab/> [Accessed 13 Sept 2014].

El-Hakim, S., 1996. Vision-Based automated Measurement Techniques. *In:* Atkinson, K., (ed.) *Close Range Photogrammetry and Machine Vision*, Caithness: Whittles.

EOS Systems Inc., 2013. *PhotoModeler Motion.*

European Commission, 2015. *EU successfully launches two Galileo satellites - Press Release.* [online]. Available at: <http://europa.eu/rapid/press-release_IP-15-4717_en.htm> [Accessed 13 Jun 15].

Fan, W. and Qiao, P., 2011. Vibration-based Damage Identification Methods: A Review and Comparative Study. *Structural Health Monitoring*, **10**(1), 83–111.

Farrar, C. R. and Jauregui, D. A., 1998. Comparative study of damage identification algorithms applied to a bridge: I. Experiment. *Smart Mater. Struct.*, (7), 704–719.

Fergus, R., Singh, B., and Hertzmann, A., 2006. Removing camera shake from a single photograph. *ACM Transactions on Graphics*, **1**(212), 787–794.

Forno, C., 1988. Deformation Measurement Using High Resolution Moiré Photography. *Optics and lasers in Engineering*, **8**, 189–212.

Fraser, C., 1997. Innovations in Automation for Vision Metrology Systems. *The Photogrammetric Record*, **15**(90), 901–911.

Gentile, C., 2009. Application of Microwave Remote Sensing to Dynamic Testing of Stay-Cables. *Remote Sensing*, **2**(1), 36–51.

González-Aguilera, D., Gómez-Lahoz, J., and Sánchez, J., 2008. A New Approach for Structural Monitoring of Large Dams with a Three-Dimensional Laser Scanner. *Sensors*, **8**(9), 5866–5883.

Grossberg, M. D. and Nayar, S. K., 2004. Modeling the space of camera response functions. *IEEE transactions on pattern analysis and machine intelligence*, **26**(10), 1272–82.

Grosse-Schwiep, M., Piechel, J., and Luhmann, T., 2014. Measurement of Rotor Blade Deformations of Wind Energy Converters with Laser Scanners. *Journal of Physics: Conference Series*, **524**, 012067.

Hampel, U. and Maas, H.-g., 2009. Cascaded image analysis for dynamic crack detection in material testing. *ISPRS Journal of Photogrammetry and Remote Sensing*, **64**(4), 345–350.

Hariharan, P., 2006. *Basics of Interferometry*. 2nd ed edition, Academic Press.

Hassiotis, S. and Jeong, G., 1993. Assessment of structural damage from natural frequency measurements. *Computers & Structures*, **49**(4), 679–691.

Helfrick, M. N., Niezrecki, C., Avitabile, P., and Schmidt, T., 2011. 3D digital image correlation methods for full-field vibration measurement. *Mechanical Systems and Signal Processing*, **25**(3), 917–927.

Hexagon Metrology, 2014. *Leica Absolute Tracker AT402: Product Brochure*. [online]. Available at: <http://www.leica-geosystems.co.uk/downloads123/m1/metrology/general/brochures/LeicaAbsoluteTrackerAT402_brochure_en.pdf> [Accessed 19 Dec 15].

Hirsch, M., Schuler, C., and Harmeling, S., 2011. Fast removal of non-uniform camera shake. *In: IEEE International Conference on Computer Vision 2011*, Barcelona: Computer Vision Centre.

Intergrated Design Tools, 2015. *M Series Cameras*. [online]. Available at: <http://www.idtvision.com/high-speed-cameras/products/cameras/m-series-cameras/> [Accessed 9 Sept 15].

Jahanshahi, M. R. and Masri, S. F., 2013. A new methodology for non-contact accurate crack width measurement through photogrammetry for automated structural safety evaluation. *Smart Materials and Structures*, **22**(3), 035019.

Jerabek, M., Major, Z., and Lang, R., 2010. Strain determination of polymeric materials using digital image correlation. *Polymer Testing*, **29**(3), 407–416.

Joshi, N., Kang, S. B., Zitnick, C. L., and Szeliski, R., 2010. Image deblurring using inertial measurement sensors. *ACM Transactions on Graphics*, **29**(4), 30:1–9.

Jurjo, D., Magluta, C., Roitman, N., and Gonçalves, P., 2010. Experimental methodology for the dynamic analysis of slender structures based on digital image processing techniques. *Mechanical Systems and Signal Processing*, **24**(5), 1369–1382.

Kalpoe, D., Khoshelham, K., and Gorte, B., 2011. Vibration measurement of a model wind turbine using high speed photogrammetry. *In:* Remondino, F. and Shortis, M. R., (eds.) *Proc. of SPIE: Videometrics, Range Imaging, and Applications XI*, volume 8085, 80850J 1–11.

Kasinos, S., Palmeri, A., and Lombardo, M., 2014. Using the vibration envelope as damage-sensitive feature in composite beam structures. *Structures*, **1**(February), 67–75.

Kearney, A. and Forno, C., 1989. A large scale deformation study using moiré photography. *Photogrammetric Record*, **13**(74), 217–224.

Kijewski-Correa, T., Kareem, A., and Kochly, M., 2006. Experimental Verification and Full-Scale Deployment of Global Positioning Systems to Monitor the Dynamic Response of Tall Buildings. *Journal of Structural Engineering*, **132**(8), 1242–1253.

Kim, S., Tai, Y.-W., Kim, S. J., Brown, M. S., and Matshushita, Y., 2012. Nonlinear camera response functions and image deblurring. *In:* Chellappa, R., (ed.) *IEEE Computer Society Conference on Computer Vision and Pattern Recognition*, 25–32, Providence, RI, USA: IEEE.

Kraus, K., 1993. *Photogrammetry: Vol. 1 Fundamentals and Stardard Processes.* Bonn: Ferdinand Dümmels Verlag.

Lange, J. and Benning, W., 2006. Crack detection at concrete construction units from photogrammetric data using image processing procedures. *In:* Kerle, N. and Skidmore, A., (eds.) *Proceedings of the ISPRS Commission VII Symposium 'Remote Sensing: From Pixels to Processes'*, Enschede, The Netherlands.

Lee, J.-J., Fukuda, Y., and Shinozuka, M., 2006. Dynamic displacement measurement of bridges using vision-based system. *In: Proceedings of SPIE: Smart Structures and Materials 2006*, volume 6174, 1–9, SPIE.

Lee, J.-J. and Shinozuka, M., 2006a. A vision-based system for remote sensing of bridge displacement. *NDT & E International*, **39**(5), 425–431.

Lee, J.-J. and Shinozuka, M., 2006b. Real-Time Displacement Measurement of a Flexible Bridge Using Digital Image Processing Techniques. *Experimental Mechanics*, **46**(1), 105–114.

Leica Geosystems, 2014. *Leica ScanStation P20*. [online]. Available at: <http://www.leica-geosystems.co.uk/en/Leica-ScanStation-P20_101869.htm>.

Leica Geosystems, 2015. *Leica Absolute Tracker AT402*. [online]. Available at: <http://www.leica-geosystems.co.uk/en/Leica-Absolute-Tracker-AT402_81625.htm> [Accessed 28 Nov 15].

Leitch, K. R., 2010. *Close-Range Photogrammetric Measurement Of Bridge Deformations*. Saarbrücken, Germany: Lambert Academic Publishing.

Li, Q., Wang, S., Guan, B., and Wang, G., 2007. A machine vision method for the measurement of vibration amplitude. *Measurement Science and Technology*, **18**(5), 1477–1486.

Li, Z. and Liu, M., 2010. Research on Decoding Method of Coded Targets in Close-range Photogrammetry. *Journal Of Computational Information Systems*, **8**, 2699–2705.

Lin, H.-Y., Li, K.-J., and Chang, C.-H., 2008. Vehicle speed detection from a single motion blurred image. *Image and Vision Computing*, **26**(10), 1327–1337.

Lovse, J. W., Teskey, W. F., Lachapelle, G., and Cannon, M. E., 1995. Dynamic Deformation Monitoring of Tall Structure Using GPS Technology. *Journal of Surveying Engineering*, **121**(1), 35–40.

Luhmann, T., 2011. 3D Imaging - How to Achieve Highest Accuracy. *In:* Remondino, F. and Shortis, M. R., (eds.) *Proc. of SPIE: Videometrics, Range Imaging, and Applications XI*, volume 8085, 808502–1–11, Munich, Germany.

Luhmann, T., Robson, S., Kyle, S., and Harley, I., 2006. *Close range photogrammetry: principles, techniques and applications*. Dunbeath: Whittles.

Maas, H.-g., 1998. Photogrammetric techniques for deformation measurements on the reservoir walls. *In: The Proceedings Of The IAG Symposium On Geodesy For Geotechnical And Structural Engineering, Eisenstadt, Austria*, 319–324.

Maas, H.-g. and Hampel, U., 2006. Photogrammetric Techniques in Civil Engineering Material Testing and Structure Monitoring. *Photogrammetric Engineering & Remote Sensing*, **72**(1), 39–45.

Meng, X., Dodson, A., and Roberts, G. W., 2007. Detecting bridge dynamics with GPS and triaxial accelerometers. *Engineering Structures*, **29**(11), 3178–3184.

Meng, X., Roberts, G. W., Dodson, A. H., Cosser, E., Barnes, J., and Rizos, C., 2004. Impact of GPS satellite and pseudolite geometry on structural deformation monitoring: analytical and empirical studies. *Journal of Geodesy*, **77**(12), 809–822.

Metrolaser Inc., 2011. *VibroMet 500 SLDV (Scanning Laser Doppler Vibrometer): Specifications*. [online]. Available at: <http://www.metrolaserinc.com/vibromet500-SLDV_specifications.htm> [Accessed 23 Jan 12].

MicroSurvey, 2011. *STAR*NET-PRO*.

Mikhail, 2001. *Introduction to modern photogrammetry*. Chichester: John Wiley & Sons.

Morassi, A., Nakamura, G., Shirota, K., and Sini, M., 2007. A variational approach for an inverse dynamical problem for composite beams. *European Journal of Applied Mathematics*, **18**(01), 21.

Morassi, A. and Tonon, S., 2008. Experimental and Analytical Study of a Steel-concrete Bridge. *Journal of Vibration and Control*, **14**(6), 771–794.

Morlier, J., Salom, P., and Bos, F., 2007. New Image Processing Tools for Structural Dynamic Monitoring. *Key Engineering Materials*, **347**, 239–244.

Moschas, F. and Stiros, S. C., 2011. Measurement of the dynamic displacements and of the modal frequencies of a short-span pedestrian bridge using GPS and an accelerometer. *Engineering Structures*, **33**(1), 10–17.

Moss, R. and Matthews, S., 1995. In-service structural monitoring: a state-of-the-art review. *The Structural Engineer*, **73**(2), 23–31.

Nakamura, S.-i., 2000. GPS Measurement of Wind-Induced Suspension Bridge Girder Displacements. *Journal of Structural Engineering*, **126**(12), 1413–1419.

Nassif, H. H., Gindy, M., and Davis, J., 2005. Comparison of laser Doppler vibrometer with contact sensors for monitoring bridge deflection and vibration. *NDT & E International*, **38**(3), 213–218.

Nickitopoulou, A., Protopsalti, K., and Stiros, S. C., 2006. Monitoring dynamic and quasi-static deformations of large flexible engineering structures with GPS: Accuracy, limitations and promises. *Engineering Structures*, **28**(10), 1471–1482.

Ogleby, C., Papadaki, H., Robson, S., and Shortis, M., 1999. Comparative camera calibrations of some "off the shelf" digital cameras suited to archaeological purposes. *Proceedings, International Archives Photogrammetry and Remote Sensing,*, **32**(B5), 69–75.

Olaszek, P., 1999. Investigation of the dynamic characteristic of bridge structures using a computer vision method. *Measurement*, **25**(3), 227–236.

Omega Engineering, 2011. *Positioning Strain Gages to Monitor Bending, Axial, Shear, and Torsional Loads*. [online]. Available at: <http://www.omega.co.uk/techref/pdf/Positioning_Strain_Gages.pdf> [Accessed 11 Mar 11].

OpenCV, 2012. *OpenCV Wiki - Welcome*. [online]. Available at: <http://opencv.willowgarage.com/wiki/> [Accessed 14 May 12].

Orr, J., Darby, A., Ibell, T., and Evernden, M., 2012. The shear behaviour of non-prismatic reinforced concrete beams determined using digital image correlation. *In: 5th Internation Conference on Optical Measurement Techniques*, 1–10, Antwerp, Belgium: Shaker Publishing.

Pandey, A., Biswas, M., and Samman, M., 1991. Damage detection from changes in curvature mode shapes. *Journal of Sound and Vibration*, **145**(2), 321–332.

Paramanand, C. and Rajagopalan, A. N., 2012. Depth from motion and optical blur with an unscented kalman filter. *IEEE transactions on image processing*, **21**(5), 2798–811.

Park, H. S., Lee, H. M., Adeli, H., and Lee, I., 2007. A New Approach for Health Monitoring of Structures: Terrestrial Laser Scanning. *Computer-Aided Civil and Infrastructure Engineering*, **22**(1), 19–30.

Park, J.-W., Lee, J.-J., Jung, H.-J., and Myung, H., 2010. Vision-based displacement measurement method for high-rise building structures using partitioning approach. *NDT & E International*, **43**(7), 642–647.

Polytech Ltd., 2014a. *RSV-150 Remote Sensing Vibrometer*. [online]. Available at: <http://www.polytec-ltd.co.uk/uk/products/vibration-sensors/special-application-vibrometers/rsv-150-remote-sensing-vibrometer/> [Accessed 10 Nov 14].

Polytech Ltd., 2014b. *UHF-120 Ultra High Frequency Vibrometer*. [online]. Available at: <http://www.polytec-ltd.co.uk/uk/products/vibration-sensors/microscope-based-systems/uhf-120-ultra-high-frequency-vibrometer/> [Accessed 10 Nov 14].

Psimoulis, P. a. and Stiros, S. C., 2008. Experimental Assessment of the Accuracy of GPS and RTS for the Determination of the Parameters of Oscillation of Major Structures. *Computer-Aided Civil and Infrastructure Engineering*, **23**(5), 389–403.

Qiqiang, F. and Xin, C., 2009. Fast Recognition and Precise Centroiding of Artificial Targets. *Surveying And Mapping*, 2–5.

Rastogi, P. K., 2001. Measurement of Static Surface Displacements, Derivatives of Displacement, and Three-dimensional Surface Shapes — Examples of Applications to Non-destructive testing. *In:* Rastogi, P. K., (ed.) *Digital Speckle Pattern Interferometry and Related Techniques*, chapter 3, 141–224, Chichester: John Wiley & Sons.

Roberts, G. W., Meng, X., Brown, C. J., and Dallard, P., 2006. GPS measurements on the London Millennium Bridge. *Proceedings of the ICE - Bridge Engineering*, **159**(4), 153–161.

Roberts, G. W., Meng, X., and Dodson, A. H., 2004. Integrating a Global Positioning System and Accelerometers to Monitor the Deflection of Bridges. *Journal of Surveying Engineering*, **130**(2), 65–72.

Robins, P., Austin, S., Chandler, J. H., and Jones, P., 2001. Flexural strain and crack width measurement of steel-fibre-reinforced concrete by optical grid and electrical gauge methods. *Cement and Concrete Research*, **31**(5), 719–729.

Ronnholm, P., Nuikka, M., Suominen, A., Salo, P., Hyyppa, H., Pontinen, P., Haggren, H., Vermeer, M., Puttonen, J., and Hirsi, H., 2009. Comparison of measurement techniques and static theory applied to concrete beam deformation. *The Photogrammetric Record*, **24**(128), 351–371.

Russ, J. C., 2011. *The Image Processing Handbook*. Sixth edit edition, Boca Raton, FL: CRC Press.

Schmidt, T., Tyson, J., and Ganaulis, K., 2003. Full-field Dynamic Displacement and Strain Measurement using Advanced 3D Image Correlation Photogrammetry: Part I. *Experimental Techniques*, (June), 47–50.

Scott, P., 1978. Structural deformation measurement of a model box girder bridge. *The Photogrammetric Record*, **9**(April), 361–376.

SD Association, 2015. *About Speed Class and Benefit*. [online]. Available at: <https://www.sdcard.org/consumers/speed/> [Accessed 31 Aug 15].

Shortis, M. R., Clarke, T., and Robson, S., 1995. Practical testing of the precision and accuracy of target image centring algorithms. *In:* Shortis, M. R., (ed.) *Videometrics IV*, volume 2598, 65–76, Philadelphia, Pennsylvania: SPIE.

Shortis, M. R., Clarke, T., and Short, T., 1994. A comparison of some techniques for the subpixel location of discrete target images. *In:* Clarke, T., (ed.) *Videometrics III*, volume 2350, Boston: SPIE.

Shortis, M. R., Ogleby, C., and Robson, S., 2001. Calibration modelling and stability testing for the Kodak DC200 series digital still camera. *Proceedings of SPIE*.

Shortis, M. R., Seager, J., and Robson, S., 2003. Automatic recognition of coded targets based on a Hough transform and segment matching. *In:* El-Hakim, S. F., Gruen, A., and Walton, J. S., (eds.) *Videometrics VII*, volume 5013, 202–208, Santa Clara, California: SPIE.

Solomon, C. and Brekon, T., 2011. *Fundamentals of digital image processing: A practical approach with examples in Matlab*. Chichester: John Wiley & Sons.

Sorel, M. and Flusser, J., 2008. Space-variant restoration of images degraded by camera motion blur. *In: IEEE transactions on image processing*, volume 17, 105–16.

Srinivasan, G. N. and Shobha, G., 2008. Segmentation Techniques for Target Recognition. *WSEAS Transactions on Computers*, **7**(10), 1555–1563.

Stanbridge, A. B., Martarelli, M., and Ewins, D. J., 2004. Measuring area vibration mode shapes with a continuous-scan LDV. *Measurement*, **35**(2), 181–189.

Sunny Instruments Singapore, 2009. *LV-S01 Laser Doppler Vibrometer*. [online]. Available at: <http: //www.sunnyinstruments.com.sg/English/proxx.jsp?kind_num=007001001&id=1> [Accessed 23 Jan 12].

Tao, G. and Xia, Z., 2005. A non-contact real-time strain measurement and control system for multiaxial cyclic/fatigue tests of polymer materials by digital image correlation method. *Polymer Testing*, **24**(7), 844–855.

Tasci, L., 2013. Deformation Monitoring in Steel Arch Bridges Through Close-Range Photogrammetry and the Finite Element Method. *Experimental Techniques*, **39**(3).

The MathWorks Inc., 2014a. *graythresh: Global image threshold using Otsu's method*. [online]. Available at: <http://www.mathworks.co.uk/help/images/ref/graythresh.html>.

The MathWorks Inc., 2014b. *parfor: Execute loop iterations in parallel*. [online]. Available at: <http://www.mathworks.co.uk/help/distcomp/parfor.html>.

Thomas, H. and Cantré, S., 2009. Applications of low budget photogrammetry in the geotechnical laboratory. *The Photogrammetric Record*, **24**(December), 332–350.

Trouve, P. and Champagnat, F., 2011. Single image local blur identification. *In: 18th IEEE International conference on Image Processing*, 613–616, Brussels, Belgium: IEEE.

Uhl, T., Kohut, P., Holak, K., and Krupinski, K., 2011. Vision based condition assessment of structures. *In:* Ouyang, H., (ed.) *9th International Conference on Damage Assessment of Structures (DAMAS 2011)*, volume 305, 012043, Oxford, UK: IOP Publishing.

Valença, J., Júlio, E., and Araújo, H., 2012. Applications of Photogrammetry to Structural Assessment. *Experimental Techniques*, **36**(5), 71–81.

Wackrow, R. and Chandler, J., 2007. Geometric consistency and stability of consumer-grade digital cameras for accurate spatial measurement. *The Photogrammetric Record*, **22**(118), 121–134.

Wahbeh, A., Caffrey, J., and Masri, S., 2003. A vision-based approach for the direct measurement of displacements in vibrating systems. *Smart materials and structures*, **12**, 785–794.

Wang, S., Guan, B., Wang, G., and Li, Q., 2007. Measurement of sinusoidal vibration from motion blurred images. *Pattern Recognition Letters*, **28**(9), 1029–1040.

Warren, C., Niezrecki, C., Avitabile, P., and Pingle, P., 2011. Comparison of FRF measurements and mode shapes determined using optically image based, laser, and accelerometer measurements. *Mechanical Systems and Signal Processing*, **25**(6), 2191–2202.

Whiteman, T., Lichti, Derek, D., and Chandler, I., 2002. Measurement of deflections in concrete beams by close-range digital photogrammetry. *In:* Armenakis, C. and Lee, Y., (eds.) *Symposium on Geospatial Theory, Processing and Applications*, volume 34, Ottawa: ISPRS.

Wolf, P. R. and Dewitt, B. A., 2000. *Elements of Photogrammetry*. 3rd edition, Boston: McGraw-Hill.

Xiaojuan, W. and Xinlong, W., 2011. Multiple blur of star image and the restoration under dynamic conditions. *Acta Astronautica*, **68**(11-12), 1903–1913.

Xie, J., Lin, W., Li, H., Guo, K., Jin, B., Zhang, Y., and Liu, D., 2011. A new algorithm for improving Deblurring effects and addressing spatially-variant blur problems for image motion deblurring. *2011 4th International Congress on Image and Signal Processing*, 651–655.

Yi, T., Li, H., and Gu, M., 2010a. Full-scale measurements of dynamic response of suspension bridge subjected to environmental loads using GPS technology. *Science China Technological Sciences*, **53**(2), 469–479.

Yi, T., Li, H., and Gu, M., 2010b. Recent research and applications of GPS based technology for bridge health monitoring. *Science China Technological Sciences*, **53**(10), 2597–2610.

Yilmazturk, F. and Kulur, S., 2012. A Photogrammetric System Design to Determine the Load-Deflection Behaviors of Materials in Civil Engineering. *Journal of Testing and Evaluation*, **39**(4), 1–8.

Yoneyama, S., Kitagwa, A., Kitamura, K., and Kikuta, H., 2005. Deflection distribution measurement of steel structure using digital image correlation. *In:* Hanssen, L. M. and Farrell, P. V., (eds.) *Optical Diagnostics*, volume 5880, 58800G 1–8, SPIE.

Appendix A

Conference contributions

Two conference contributions were accepted for oral presentations at international conferences after a peer review process during the course of this research project:

- McCarthy, D.M.J., Chandler, J.H. & Palmeri, A., 2013. Monitoring Dynamic Structural Tests Using Image Deblurring Techniques. In: Biswajit, B. (ed.) *10th International Conference on Damage Assessment of Structures* (DAMAS 2013), Dublin, 8–10 July 2013. Zurich: Trans Tech Publications Inc., pp. 932-939. doi: 10.4028/www.scientific.net/KEM.569-570.932

- McCarthy, D.M.J., Chandler, J.H. & Palmeri, A., 2014. 3D Case Studies of Monitoring Dynamic Structural Tests using Long Exposure Imagery. In: F. Remondino & F. Menna (eds.) ISPRS Technical Commission V Symposium 2014 Int. Arch. Photogramm. *Remote Sens. Spatial Inf. Sci.*, XL-5, 23–25 June 2014, Riva del Garda, Italy, pp. 407-411. doi: 10.5194/isprsarchives-XL-5-407-2014

One journal paper has been submitted for consideration for publication, and has been accepted subject to revision.

- McCarthy, D.M.J., Chandler, J.H. & Palmeri, A., 2015. Monitoring 3D Vibrations in Structures using High Resolution Blurred Imagery.

Monitoring Dynamic Structural Tests using Image Deblurring Techniques

D.M.J.McCarthy[1, a], J.H.Chandler[1,b] and A.Palmeri[1,c]

[1]School of Civil and Building Engineering, Loughborough University, Loughborough, Leics, LE11 3TU

[a]D.McCarthy@lboro.ac.uk, [b]J.H.Chandler@lboro.ac.uk, [c]A.Palmeri@lboro.ac.uk

Keywords: Dynamic testing, Image processing, Structural health monitoring, Image deblurring, Point spread function, Close range photogrammetry, Vibration measurement.

Abstract. Photogrammetric techniques have demonstrated their suitability for monitoring static structural tests. Advantages include scalability, reduced cost, and three dimensional monitoring of very high numbers of points without direct contact with the test element. Commercial measuring instruments now exist which use this approach.

Dynamic testing is becoming a convenient approach for long-term structural health monitoring. If image based methods could be applied to the dynamic case, then the above advantages could prove beneficial. Past work has been successful where the vibration has either large amplitude or low frequency, as even specialist imaging sensors are limited by an inherent compromise between image resolution and imaging frequency. Judgement in sensor selection is therefore critical. Monitoring of structures in real-time is possible only at a reduced resolution, and although imaging and computer processing hardware continuously improves, so the accuracy demands of researchers and engineers increase.

A new approach to measuring the vibration envelope is introduced here, whereby a long-exposure photograph is used to capture a blurred image of the vibrating structure. The high resolution blurred image showing the whole vibration interval is measured with no need for high-speed imaging. Results are presented for a series of small-scale laboratory models, as well as a larger scale test, which demonstrate the flexibility of the proposed technique. Different image processing strategies are presented and compared, as well as the effects of exposure, aperture and sensitivity selection. Image processing time appears much faster, increasing suitability for real-time monitoring.

Introduction

Image-based monitoring using photogrammetric techniques has been demonstrated for structural testing. The approach allows non-contact monitoring of a high number of points with one (for 2D monitoring) or two or more (for 3D deformations) imaging sensors. The approach is scalable, and for the amount of data collected, relatively inexpensive.

The approach has been demonstrated for monitoring dynamic structural tests, but monitoring is limited by a compromise between sensor resolution and sampling frequency. Real-time monitoring is possible but only at a reduced resolution because of the huge amount of data produced by high speed imaging sensors. To improve measurement accuracy, telephoto lenses have been used to 'zoom-in' on a single target [1], but the advantage of many monitoring points is lost.

A new approach is introduced in this paper where a long-exposure image is used to capture the whole vibration. The vibration interval is recorded within the single image and an algorithm for its measurement demonstrated. The camera sensor can be of higher resolution than those previously used as there is no requirement for high speed imaging, allowing more accurate spatial measurement.

Structural Testing

Structural testing is used to evaluate the performance of structural members, both of in situ structures and in the laboratory environment. Structural testing may be carried out to test correlation

with analytical models of structural behaviour. Typically, loads are applied to test structural elements, and their performance monitored as the load increases to the target limit. Some tests may demand more advanced monitoring systems to record complex deformation patterns

The integrity of existing structures may also wish to be tested. The structure may be overloaded above its intended working load and based on its performance, deemed safe for its intended use. The record of the test serves as evidence of the structure's integrity. A structure may also be tested if, for example, a change of use is desired, to verify its integrity following a potentially damaging event, or if the quality of repair work needs to be verified. Structural health monitoring programs for monitoring the long-term status of structures are becoming more common.

Dynamic structural testing. Dynamic testing techniques, whereby the structural vibration is recorded, are a prevailing approach for structural health monitoring. The testing approach can be considered convenient for long-term monitoring, as light structural changes can be detected without the associated inconvenience of static testing. Interpreting the vibration response data could be, however, more complicated and specialised expertise is required to quantify damage.

Typically, changes in natural frequencies would be detected, which would indicate some change in stiffness. The more advanced algorithms use discontinuities in mode shapes to predict location and estimate severity [2]. Structural mode shapes are found by monitoring at several locations on a structure. For these methods, a higher number of sensors provides the most accurate results [3,4].

Accelerometers, commonly used for structural testing, are relatively inexpensive and simple to use. However, installing a number of them on to a structure becomes expensive, with associated cabling infrastructure for power and data and/or additional wireless equipment. Data from standard accelerometers may also not measure very low frequency vibrations [5].

Imagery-based monitoring of structures

Image-based monitoring has proven its application in the past to monitoring structural tests [5-8]. A structure is measured using photogrammetric techniques and data compared at different time intervals to calculate displacements. Advantages include: measurement can be made without contact with the structure, making it suitable for difficult measuring tasks where there is no stable support for displacement gauges. A very high number of points can be measured by a single camera sensor, limited only by sensor resolution, allowing monitoring of complex deformation patterns. Multiple camera sensors can monitor deformation in three dimensions.

While the most accurate measurement work still requires targets to be fixed to structures, digital image correlation (DIC) makes possible measurement of structures without targets fitted, provided their surface has sufficient natural texture [5]. Not needing to measure individually fitted targets allows very densely distributed measuring points and ‘full-field’ measurement. This allows visualisation of, for example, strain gradients, without long preparation and time on-site.

The scalability of image processing means measurements of large structures are possible to sub-millimetre accuracy while the accuracy of measuring small scale laboratory tests can be in the order of microns. Demonstrations give laboratory-scale examples of monitoring complex deformation in beam load tests as well as measuring the width of small scale hairline cracks in concrete [6-8]. Mass and Hampel [8] also give examples of large scale monitoring of complex structures such as buildings, bridges and reservoir dams.

GPS has also been proposed as an approach for monitoring static and dynamic structural testing [9]. Although requiring a base station receiver near the structure in addition to the receiver on the structure, line-of-sight between the two is not required. The instruments necessary for a usable accuracy are expensive and specialised and additional monitoring points radically increase costs.

Proposed Vibration Measurement Methodology

The advantages of photogrammetric image processing for monitoring structural testing can be taken advantage of in the dynamic case also. In dynamic testing, the principle remains the same, but the rate of image acquisition is increased to many pictures per second. This has been demonstrated

[10-12] but current hardware is limited by a compromise between sensor resolution and the number of frames per second that can be recorded. The choice of sensor is important, as the number of frames per second will limit the frequency of vibrations that can be recorded and an inadequate sensor resolution will fail to detect low amplitude vibration. The Nyquist sampling theorem states that in order to measure a vibration, the sampling frequency must be at least two times the vibration frequency. Very high resolution sensors can measure many targets over a whole structure, but need to record at below 10 Hz. Other sensors can record at up to 1000 kHz, but can only measure a very limited number of targets within close proximity.

The proposed approach. Our approach involves capturing a long-exposure blurred image of circular targets marked on the structure. High-speed imaging is not necessary as a 'smear' of the whole blur interval is captured in the single image. The vibration amplitude at a high number of points on the structure is measured and this information can be subsequently related to the expected performance of the structural system under the test load. Our implementation involves capturing a sharp image through a fast exposure as well as the blurred, which are processed in combination.

Measuring blur in computer science. A keen research area in computer science is that of 'image deblurring'. Algorithms exist that take a single blurred image and impressively 'de-blur' it. Rather than simply sharpening edges in images, these de-blurring algorithms first estimate the motion that caused the blur before applying a correction based on the estimated blur shape and size [13]. Artificial markings are not always required, but there is dependence on sufficient object texture.

The first stage of estimating the motion causing the blur is key to a successful 'deblur', and there are many advanced algorithms published. After estimating motion, other algorithms exist that estimate the spatial movement such as the speed of moving balls in sports [14]. The size and shape of the estimated motion is conveniently described by the point spread function (PSF) and measuring the estimated PSF provides the extent of motion at that point in an image. The PSF also contains data about the amount of time the moving object spent in each position. This approach, while alleviating the need for object targets, is computationally intensive, requiring several minutes to iteratively estimate the motion at a single point; this long processing time precludes real-time monitoring. Incorrect results are also common where surface texture is poor, yet it is difficult to identify these incorrect motion estimations.

Matlab Implementation. Our Matlab implementation processes images containing circular targets in three stages with increasing accuracy (but decreasing speed).

First: Estimate with threshold. First, a threshold filter is used to quickly identify the centre of the blurred target and estimate of the size and shape of the blur (Fig. 1a). This step also determines

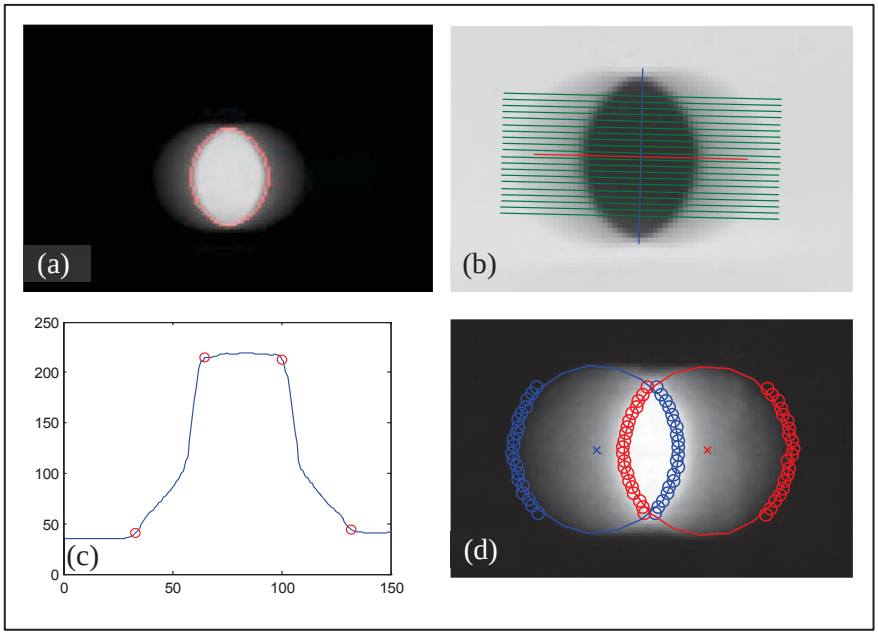

Figure 1: Estimate for blur dimensions using pixel intensity profiles. (a) First shape estimate, (b) Produced profile lines, (c) Individual intensity profile with identified blur edges, (d) Measured blur dimensions.

whether the blur is an ‘internal’ blur, where the vibration amplitude is less than the diameter of the circular target, or an ‘external’ blur, where the vibration amplitude is greater. In the first case, part of the image is always occupied by the circular target and a patch of low intensity pixels will exist, in the second case there is a smaller range of pixel values. For internal blurs, an ellipse fit to this low intensity patch will have a major axis roughly perpendicular to the blur orientation (Fig. 1a).

Second: Pixel intensity profiles. We then use the approach proposed by Boracchi *et al.* [15] for estimating the motion of sports balls. The algorithm is initialised by using a simple threshold filter with a higher threshold to better estimate the size and orientation of the blur (Fig. 1b). A number of intensity profiles are made within the blur. Four points of interest are picked from the profile: at the start and end of the positive gradient, and the start and end of the negative gradient (Fig. 1c). The algorithm that picks these points is the same for both internal and external blur cases. An ellipse is fit to each set of points for each edge of the blur and the difference between the centres of the two ellipses identifies the amplitude of the vibration.

Although the shape of intensity profiles are consistent, the current implementation is susceptible to some image noise, resulting in some outliers. A quality check is important so that these outliers can be detected and corrected or removed.

Third: Simulated blur smears. To improve upon the previous analysis, the third proposed stage reverses deblurring algorithms by iteratively simulating different blur dimensions of the sharp image and correlating with the observed blurred image (Fig. 2). This builds on the assumption that a blurred image can be represented as an un-blurred image filtered by some motion filter. This provides sub-pixel (and depending on scale, sub-millimetre) accuracy as well as a measure of quality.

Initial Experiments

To test the algorithm, simulations were carried out on a small (30×30 cm) shake table at Loughborough University (Fig. 3). Small plastic models were built, and targets adhered on to them. A single Nikon D80 DSLR camera was set up on a tripod to monitor the model. The vibration of the structure was measured by accelerometers, and the table bed position was also monitored by a laser sensor.

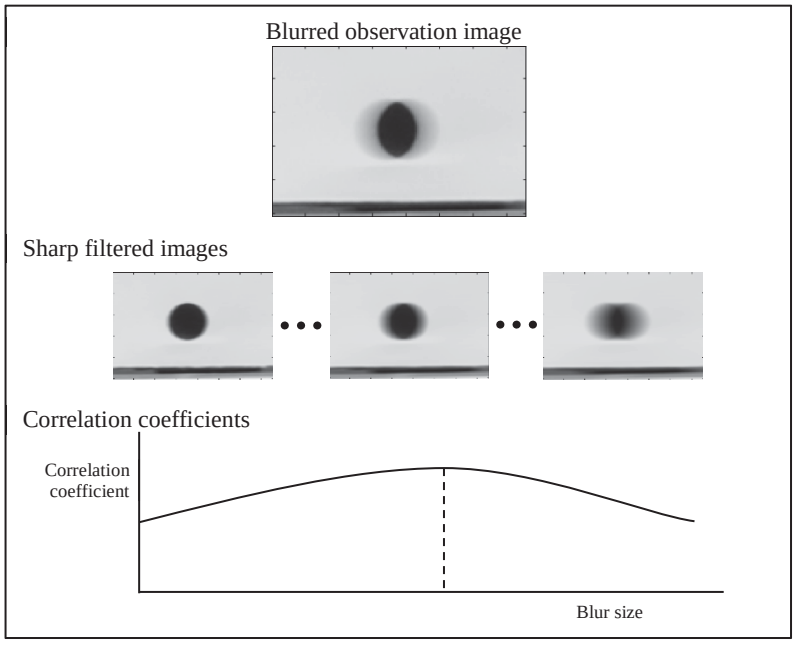

Figure 2: Blur measurement by simulation for sub-pixel precision and validation

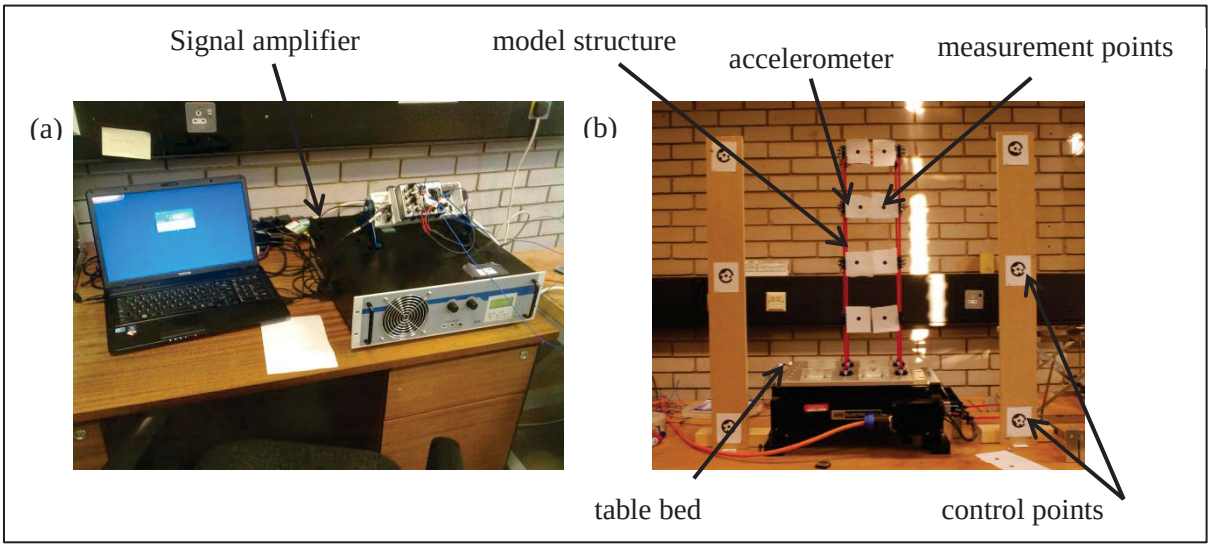

Figure 3: Shake table experiments at Loughborough University (a) table control equipment (b) sample image

The two wooden stands either side of the shake table support control points, stationary targets used to provide scale. In this instance, only planar movements were recorded, as all targets lay in a single plane. Displacements measured in the image space were transformed to real word coordinates in millimetres using the projective transformation. The control targets were measured using a Leica TCR400 reflectorless total station.

To assess the accuracy of the measured blurs, the shake table was programmed to vibrate with simple harmonic motion of varying amplitudes. Using the displacement laser and double integrating the accelerometer data, the vibration amplitude measured by the image processing approach is compared in Fig 4. Accuracies of 0.25mm are achieved (using a 95% confidence interval), which is further discussed in the following section. It is worth noting that we are interested in the envelope of the dynamic response of the sample structure, independently of the frequency of vibration.

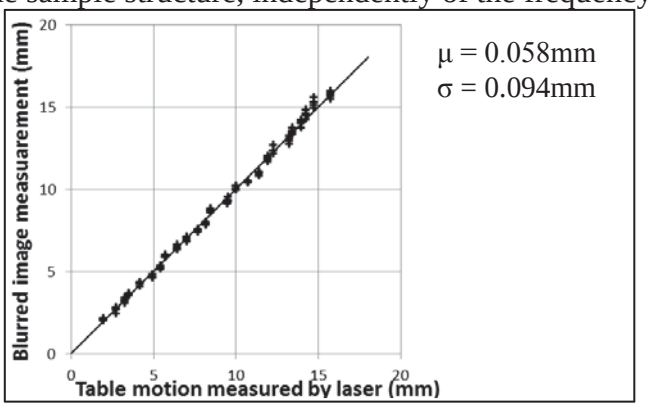

Figure 4: Results (at present scale, 1 mm ≈ 3 pixels)

Discussion

The spatial accuracy of photogrammetric measurements is dependent upon the scale of the test, so accuracy in pixels can be used to compare to other photogrammetric work. At the scale used, an accuracy of 0.25 mm (using a 95% confidence interval) is about 0.64 pixels in the image space which is unimpressive when compared with that of traditional photogrammetry using sharp images [16], but because recording dynamic tests with high-speed cameras necessitates lower image resolutions, even with specialist imaging sensors, the actual real-space measurement accuracy is higher than that previous achieved. It was noted that the accuracy of the largest vibration amplitudes had the highest measurement error, probably due to low range of pixel intensity values in the fainter image and lower signal-to-noise ratio.

The output is also frequency-independent, as the measureable vibration is not dictated by the Nyquist criterion, and aliasing, whereby a peak of vibration is missed, does not occur.

Demonstrations here use only a few targets, but the number of possible targets is limited only by practical considerations of attaching them to the structure, allowing many more. Increasing the number of targets would allow more accurate measurement of mode shapes with less interpolation. Increasing targets further, especially in a laboratory environment, approaches full-field measurement. If accelerometers or GPS were used, additional hardware would be necessary for each monitoring point, and this solution is much less expensive that the multiple-point-monitoring scanning laser Doppler vibrometer alternative.

Low frequency vibrations (<1Hz) are measured in the same way by using a longer shutter speed. Shutter speeds of several seconds cause images to become overexposed, but this is mitigated with lens filters. The same setup is also suitable for monitoring of static properties of the bridge using well-known photogrammetric techniques. These properties when measured with an accelerometer are susceptible to inaccuracies due to 'drift' in the accelerometer data [1].

Practical considerations. The imaging hardware used is a consumer grade DSLR camera, and processing is carried out with an average specification PC. Such an approach allows a flexible monitoring scheme using off-the-shelf components. The current setup requires fixing targets in visible positions on the structure and control targets around the outside, which are then measured by total station. However, a simple scale constraint could be the only control required, provided by a simple scale ruler. Time to set up is comparable to other non-contact optical monitoring techniques which do not require the cabling infrastructure of many individual sensors.

The approach is, however, limited in its requirement of a suitable imaging station. The fixed control is also necessary to monitor for any camera movement in between measurement epochs. The requirement for control on a stable reference may be restrictive in outdoor applications, as a stable reference near tall structures may not be available. The targets demonstrated here would only be visible during daylight hours, although 'active' targets containing LEDs have been proposed and evaluated by others [1].

Image processing considerations. Processing time is a matter of seconds on an average specification computer. While not producing immediate real-time results to the user, it does produce results rapidly.

The current implementation requires the user must manually specify the initial region of interest and a small number of parameters. After this, processing of a number of similar images is automated, even where there is a high number of measuring points within the image. It is anticipated that the few manual parameters which relate to, for example, the lighting and colour of target against the background, could also be set automatically.

Camera exposure and response function. Particular care has to be given to selecting the correct exposure setting of the camera. Saturated areas of the image, whereby some pixels are over-exposed, are not unlikely to occur when using long exposure images, and the overexposed area contains no gradient information. The solution is to reduce the exposure, but this can only be realised after the first image has been taken. In the anticipated real-time processing solution, saturation will be automatically realised after the first image is taken and the exposure time can be quickly corrected.

Borracchi *et al.* [15] suggested that most cameras do not apply a linear relationship between the amount of light at each pixel on the sensor and final pixel value recorded. This was particularly apparent when comparing the blurred observation image with the sharp filtered image. Although the two images were very similar (Fig. 2), containing similar edges, gradients and artefacts, the overall intensity of the 'smear' differed. Borracchi *et al.* [15] suggest that modelling the camera's transfer function for pixel intensity values will correct for this.

The blur distance measured by pixel intensity profiles, as was proposed by Boracchii *et al.* [15], regularly overestimates the actual vibration interval. This is because, although most of the gradient from target to background is caused by the motion 'smear', some gradient with a width of about 1-2 pixels is normally present around ordinary images of photogrammetric targets. This is evident when using the same algorithm on stationary targets, were movement is estimated of about the width of the target fringe. This systematic error may have been insignificant in Boracchii *et al.*'s

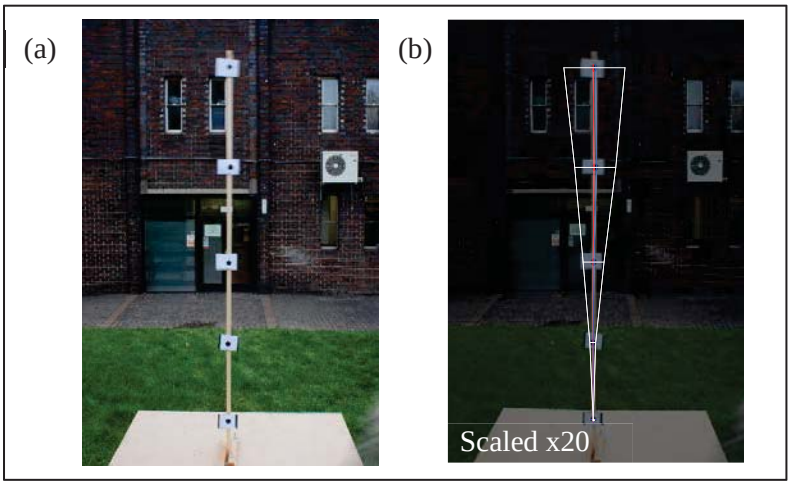

Figure 5: Demonstration capturing a motion-blurred image outdoors (a) the tested column (b) the measured vibration envelope (scaled x20)

work which used images of a different scale, but for our work it should be anticipated and corrected. In our solution, the iterative simulation method used for sub-pixel measurement has the further advantage that it does not contain this systematic error.

Future applications

The scalability of the approach allows image processing to be carried out by the same algorithm on small as well as larger-scale structures. The approach will now be tested on larger full-scale structures.

Feasibility test for larger structures. The accuracy for small-scale tests shown above was approximately 0.2 mm for a 0.5 m tall model observed at about 2 m. In the image space, this is an accuracy of 0.6 pixels. A larger structure, for example with a height of 5 m, could be observed with the same lens hardware and an accuracy of less than a millimetre would be expected.

A likely additional challenge would be the lack of control over lighting conditions, although it is anticipated that adjusting camera exposure settings will account for this. Sample images of simple outdoor structures (Fig. 5) indicate that image processing is successful, with careful selection of exposure settings.

In comparison to GPS monitoring of structures, the measurement of vibration amplitude would be expected to be more accurate. Like photogrammetry, GPS is also suitable for static and semi-static monitoring approaches, but it is only sensitive to vibration with amplitudes above about 5-10 mm. While GPS data does contain frequency information, the proposed image processing approach would allow measurement of structures with lower vibration amplitudes.

Estimating the frequency of the dominant mode. Current exposure times for the current demonstrations have been large enough to capture the whole vibration interval. If the exposure time is reduced, and a structure's vibration remains constant, the image will record only part of the structure's vibration. It is suggested that there is potential for estimating the frequency of a dominant mode of a structure by measuring how much of a structure's whole vibration interval is occupied within the time the shutter is open.

Conclusion

An approach to estimating the vibration envelope using long-exposure single images has been proposed. Previous image monitoring systems have been limited by a compromise between spatial resolution and imaging frequency, even when using specialist sensors. This frequency-independent approach avoids this limitation and has been demonstrated using consumer-grade imaging hardware. An algorithm for correlating the observed image with simulated images has demonstrated the efficacy of the approach.

When used with frequency-selective narrowband excitation, the approach provides spatial measurement of vibration amplitudes more accurately than previous high-speed imaging solutions. The high number of possible measurement points with image-based techniques is highlighted as of potential benefit to determining mode shapes as it reduces the distance between measurement points that otherwise requires interpolation.

Consideration should be given to the relatively low cost of the instruments used and the scalability of the approach. Because measurement is frequency-independent, hardware is not limited to certain frequency ranges. Initial tests on small-scale models have shown the approach can measure with 0.25 mm accuracy, which is scalable to structures of other sizes. The feasibility of monitoring larger full-scale structures has been tested and accuracy estimated. Finally, further work to assess the potential for frequency measurement has been introduced.

References

[1] Wahbeh, A.M., Caffrey, J.P. & Masri, S.F., A vision-based approach for the direct measurement of displacements in vibrating systems. Smart materials and structures. 12 (2003) 785–794.

[2] Pandey, A., Biswas, M. & Samman, M., Damage detection from changes in curvature mode shapes. Journal of Sound and Vibration. 145(2) (1991) 321–332.

[3] Carden, E.P., Vibration Based Condition Monitoring: A Review. Structural Health Monitoring. 3(4) (2004) 355–377.

[4] Dilena, M. & Morassi, A., Dynamic testing of a damaged bridge. Mechanical Systems and Signal Processing. 25(5) (2011) 1485–1507.

[5] Warren, C., Niezrecki, C., Avitabile, P. & Pingle, P., Comparison of FRF measurements and mode shapes determined using optically image based, laser, and accelerometer measurements. Mechanical Systems and Signal Processing. 25(6) (2011) 2191–2202.

[6] Robins, P., Austin, S., Chandler, J.H. & Jones, P., Flexural strain and crack width measurement of steel-fibre-reinforced concrete by optical grid and electrical gauge methods. Cement and Concrete Research. 31(5) (2001) 719–729.

[7] Lange, J. & Benning, W., Crack detection at concrete construction units from photogrammetric data using image processing procedures, in: N. Kerle & A. Skidmore, (Eds.), Proceedings of the ISPRS Commission VII Symposium “Remote Sensing: From Pixels to Processes”, Enschede, The Netherlands, 2006.

[8] Maas, H. & Hampel, U., Photogrammetric Techniques in Civil Engineering Material Testing and Structure Monitoring. Photogrammetric Engineering & Remote Sensing. 72(1) (2006) 39–45.

[9] Roberts, G.W., Meng, X., Brown, C. J. & Dallard, P. GPS measurements on the London Millennium Bridge. Proceedings of the ICE - Bridge Engineering. 159(4) (2006) 153–161.

[10] Lee, J.-J. & Shinozuka, M., Real-Time Displacement Measurement of a Flexible Bridge Using Digital Image Processing Techniques. Experimental Mechanics. 46(1) (2006) 105–114.

[11] Park, J.-W., Lee, J.-J., Jung, H.-J. & Myung, H., Vision-based displacement measurement method for high-rise building structures using partitioning approach. NDT & E International. 43(7) (2010) 642–647.

[12] Choi, H.-S. Cheung, J.-H., Kim, S.-H., & Ahn, J.-H., Structural Dynamic Displacement Vision System using Digital Image Processing. NDT & E International. 44(7) (2011) 597–608.

[13] Fergus, R., Singh, B. & Hertzmann, A., Removing camera shake from a single photograph. ACM Transactions on Graphics. 1(212) (2006) 787–794.

[14] Caglioti, V. & Giusti, A., Recovering ball motion from a single motion-blurred image. Computer Vision and Image Understanding. 113(5) (2009) 590–597.

[15] Boracchi, G., Caglioti, V. & Giusti, A., Ball position and motion reconstruction from blur in a single perspective image, in: Image Analysis and Processing. Modena: IEEE Comput. Soc., 2007.

[16] Luhmann, T., 3D Imaging - How to Achieve Highest Accuracy, in: F. Remondino & M. R. Shortis, (Eds.), Proc. of SPIE: Videometrics, Range Imaging, and Applications XI, Munich, Germany, 2011, pp. 808502–1–11.

3D CASE STUDIES OF MONITORING DYNAMIC STRUCTURAL TESTS USING LONG EXPOSURE IMAGERY

D. M. J. McCarthy [a], J. H. Chandler [a], A. Palmeri [a]

[a] School of Civil and Building Engineering, Loughborough University, UK -
(d.mccarthy, j.h.chandler, a.palmeri)@lboro.ac.uk

Commission V, WG V/1

KEY WORDS: Vibration, Engineering, Monitoring, Long Exposure Imagery, Image Processing, Close Range Photogrammetry

ABSTRACT:

Structural health monitoring uses non-destructive testing programmes to detect long-term degradation phenomena in civil engineering structures. Structural testing may also be carried out to assess a structure's integrity following a potentially damaging event. Such investigations are increasingly carried out with vibration techniques, in which the structural response to artificial or natural excitations is recorded and analysed from a number of monitoring locations. Photogrammetry is of particular interest here since a very high number of monitoring locations can be measured using just a few images. To achieve the necessary imaging frequency to capture the vibration, it has been necessary to reduce the image resolution at the cost of spatial measurement accuracy. Even specialist sensors are limited by a compromise between sensor resolution and imaging frequency.

To alleviate this compromise, a different approach has been developed and is described in this paper. Instead of using high-speed imaging to capture the instantaneous position at each epoch, long-exposure images are instead used, in which the localised image of the object becomes blurred. The approach has been extended to create 3D displacement vectors for each target point via multiple camera locations, which allows the simultaneous detection of transverse and torsional mode shapes. The proposed approach is frequency invariant allowing monitoring of higher modal frequencies irrespective of a sampling frequency. Since there is no requirement for imaging frequency, a higher image resolution is possible for the most accurate spatial measurement. The results of a small scale laboratory test using off-the-shelf consumer cameras are demonstrated. A larger experiment also demonstrates the scalability of the approach.

1. INTRODUCTION

In civil engineering, it is often necessary to detect long-term degradation phenomena in existing structures using structural health monitoring programmes. Structural testing may also be required to assess integrity due to a change of use or following a potentially damaging event. The development of new materials also demand advanced monitoring instrumentation to more fully understand the processes involved.

The benefits of photogrammetric monitoring can be realised for structural testing. The approach allows non-contact monitoring of displacements at many monitoring locations distributed across the structure. For monitoring of vibrations the same approach has been used, but the potential is limited by the capabilities of imaging hardware. This paper describes the use of an alternative approach using longer exposures to capture the motion within motion-blurred images, which are processed with a bespoke algorithm. The approach has now been extended in to three dimensions. Two case studies are contained in this paper, demonstrating the approach for monitoring vibrations in model structures in 3D. Visualisations of the 3D motion vectors demonstrate the captured detail.

2. DYNAMIC STRUCTURAL TESTING

2.1 Monitoring structures

When testing civil engineering structures, non-destructive test techniques are usually utilised for most existing structures. Dynamic test techniques are of particular interest, since the vibration response is sensitive to more subtle structural properties. The vibration response to artificial or natural excitation is recorded and analysed using specialised approaches. For instance, a reduction in modal frequencies would possibly indicate a concentrated loss of stiffness due to the presence of damage, but this information alone cannot determine the location or severity of damage and would require further investigation. Richer information comes from the analysis of the modal shapes, as changes in the curvature of the modal shape or in the position of nodes and antinodes may allow estimates of the location and severity of the structural damage (Pandey et al., 1991).

In order to detect these modal shapes, a number of sensors are distributed on a structure. A higher number of monitoring locations is desirable since interpolation is necessary between data points. Past studies also show that the best results are found with a higher number of sensors (Carden & Fanning, 2004). Contact accelerometer gauges are conventionally used, but practical limitations exist as each additional accelerometer adds hardware cost and requires cabling and data collection infrastructure. The highly specialised laser Doppler vibrometer (an optical instrument that measures vibration by detecting frequency shifts in a reflected laser beam) can be used, but remains expensive and takes time for the measuring laser beam to be moved systematically to each monitoring location. Photogrammetry is of interest here since a high number of monitoring locations can be measured using just a few imaging sensors.

This contribution has been peer-reviewed.
doi:10.5194/isprsarchives-XL-5-407-2014

3. PHOTOGRAMMETRIC MONITORING OF STRUCTURAL DYNAMICS

Photogrammetry has proven capabilities for accurate spatial measurement. Advantages include that it is non-contact, relatively inexpensive for the amount of data collected, and the capability of measuring many locations simultaneously. Photogrammetry has been used for monitoring static deformations in structural testing by making repeated measurements, and calculating the change in measurements between subsequent measurement epochs. (Maas & Hampel, 2006; Yoneyama et al., 2007; Ronnholm et al., 2009).

Since monitoring of dynamic structural properties is emerging as a tool for structural assessment, it is natural progression to apply photogrammetric monitoring to the dynamic monitoring case. Studies have already applied photogrammetric monitoring to tests utilising dynamic techniques (Olaszek, 1999; Jurjo et al., 2010; Choi et al., 2011). The principle has remained the same, but imaging frequency is increased to many frames per second in order to capture vibrations. The Nyquist criterion states that, to be able to detect vibrations of a given frequency, it is necessary to sample the data at double the vibration frequency or more (Morlier et al, 2007). Where photogrammetric monitoring has been applied using sensors capable of higher imaging frequencies, structural properties have been successfully identified, however, it is often necessary to reduce the image resolution at a cost of spatial measurement accuracy due to hardware limitations.

Consumer-grade DSLR cameras are capable of very high image resolutions, including up to 30MP, but at this resolution they are limited to recording only a few continuous image frames per second (fps), insufficient for monitoring most vibrations. Consumer grade video cameras, which record at up to 60 fps and are more suitable to monitoring vibrations, but these sensors tend to be limited to 2MP ('HD' 1080p resolution). Even specialist sensors are limited by a compromise between sensor resolution and imaging frequency.

Some authors have improved measurement accuracy by 'zooming-in' to individual measurement points. Whilst providing sufficiently accurate measurement at these locations, the advantage of simultaneous monitoring of multiple points, a particular advantage of photogrammetric monitoring, is lost. The literature review noted how for structural assessment using dynamic techniques, 'modal-shapes' are most accurately determined where interpolation is reduced with a higher number of monitoring points.

4. METHODOLOGY

To alleviate this compromise, a different approach has been developed. Instead of using high-speed imaging to capture the instantaneous position at each epoch, long-exposure images are used in which the localised image of the object becomes blurred (McCarthy, 2013). This paper describes tests where the approach has been further developed to demonstrating 3D.
Ordinary circular targets are used since their motion-blurred appearance is predictable. A bespoke Matlab routine using Matlab's image processing toolbox determines two image coordinates at each target (Figure 1). 3D displacement vectors can be determined with multiple camera locations, which is of interest since simultaneous detection of transverse and torsional mode shapes is then possible.

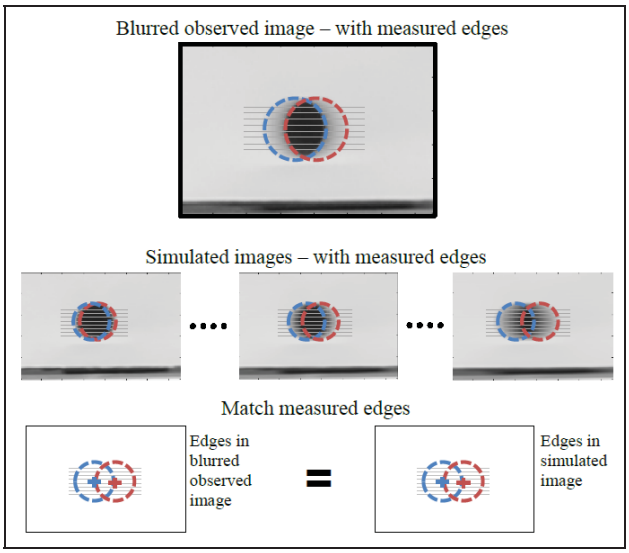

Figure 1. Motion-blurred target measurement algorithm

4.1 Experimental approach

Model structures were built in a laboratory and testing methodology developed. Ordinary circular targets were placed on the model in the conventional way. These targets were not coded, since the broken ring of a motion-blurred coded target disturbs the appearance and measurement of the centre circle. Other coded control targets are arranged around the test subject for independent reference in the conventional way. In our implementation, an unblurred image is also captured which is used by the target measurement algorithm to improve accuracy. This sharp image may be taken before dynamic excitation is applied or, in the case of natural excitation, simply a short exposure image with appropriately adjusted exposure settings.

Two or more cameras are arranged on tripods to achieve a suitable base-to-distance ratio as is normally desired in photogrammetric measurement. The control targets located in images remain stationary and unblurred, and are read into the PhotoModeler Motion software package (EOS Systems, 2014) for determining the cameras exterior orientation. Interior orientation is also determined using PhotoModeler's automated camera calibration and a camera calibration field.

Registration of the motion-blurred images is done using the Matlab script. After determining 2D image coordinates, a space intersection algorithm then determines 3D coordinates at either end of each target's motion path. From this pair of 3D coordinates, the motion distance and direction are determined and plotted on to a figure.

Difficulty referencing measurements between images was encountered, since at each target in each image where there would normally be only a single measurement, two measurements exist at either end of the motion path (figure 2). This was further complicated by the fact that there is no possibility for unique coding, since they originate from the one same physical target. Figure 3 shows the results produced by both combinations and how it produces motion vectors in different directions. It is possible in some cases to determine the correct combination by engineering judgement, but a more reliable approach was to select the combination that produced the smallest image residuals.

Care had to be taken arranging cameras when only two are in use, since if the relative positions of two cameras are in the same direction as the test subject's motion, the image residuals of both combinations will be similarly small. In these case studies the motion was expected to be broadly horizontal, so the cameras were arranged at different levels on different height tripods.

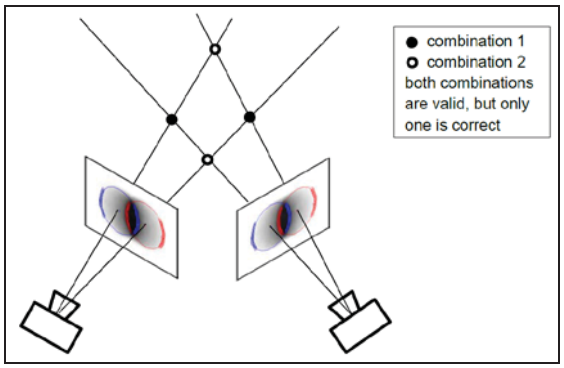

Figure 2. Ambiguity exists in matching motion 'ends' which exist from the same target.

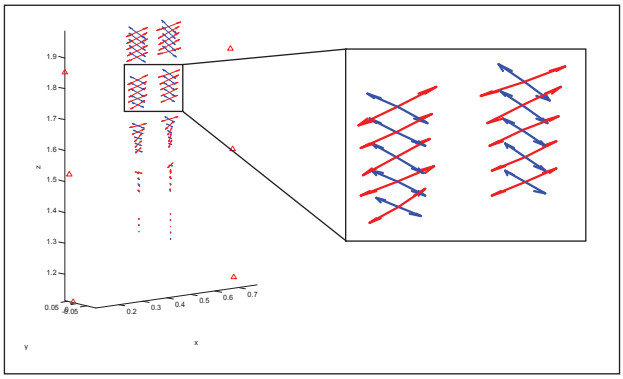

Figure 3. Unresolved measurement matching produced two possible motion vectors.

5. CASE STUDIES

5.1 Small scale shaker table models

A 780 mm tall 2D plastic model was fitted on to a structural dynamics shaker table, to observe its response to different vibrations (figure 4). The shaker table used was a 1 dimensional APS400 shaker table. The table can induce vibration of varying frequencies, amplitudes and waveforms to model structures fitted to its surface. The movement of the table is controlled by a laptop and a Matlab routine. Different types of accelerometer are available in the structural dynamics laboratory and the motion of the table is accurately monitored by a laser displacement gauge.

The cameras used were two Nikon D80 10.2 megapixel cameras with 24 mm fixed focal length lenses. Both cameras were connected to the same remote shutter so that they are both triggered simultaneously. Black circular 8 mm targets with a white background were distributed over the model structure, as well as on the table surface itself. A number of coded control targets were supported on stands around the model, and their positions measured using a total station in reflectorless mode.

The natural frequencies of the model were determined using an accelerometer. Vibration was applied at these frequencies and images were captured recording the structure's response to each motion. Images were then processed using the process described above to determine image coordinates, and 3D object-space coordinates were determined using the space intersection algorithm.

The shaker table can apply only 1D excitation, but 3D motion can be created with an appropriately asymmetric physical structure. Figure 5 shows three vibration envelopes exhibited by the model structure when vibrated at different frequencies on the shaker table. Figures 5a and 5b both show lateral motion of the model, and 5b shows the detail of the model's curvature. Figure 5c, shows how the top of the model is exhibiting 3D torsional motion.

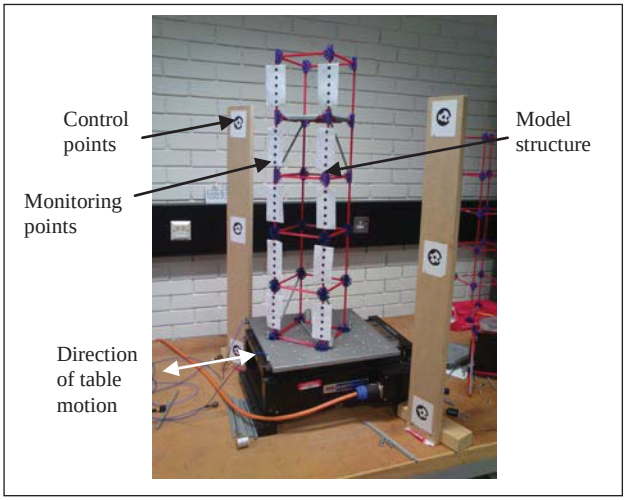

Figure 4. Rotated model fitted to the shaker table

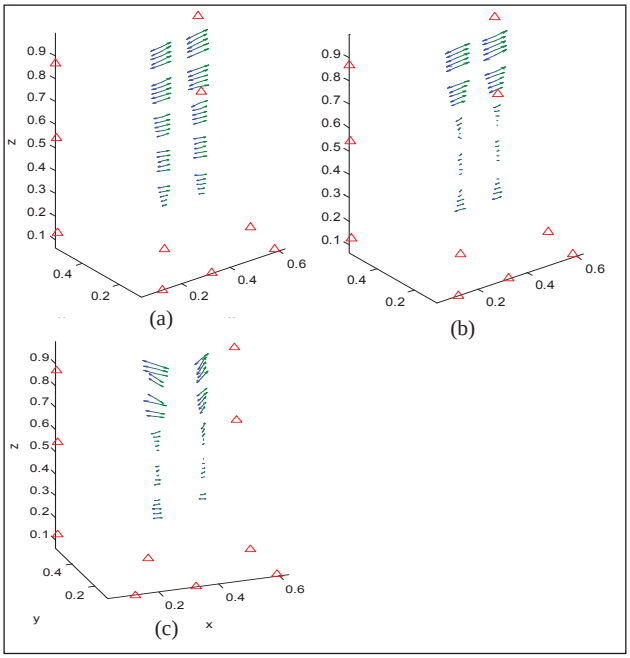

Figure 5. Captured vibration envelopes of the model structure.

The model was repositioned on the shaker table so that the table motion was diagonally across the model (figure 4). Figure 6 shows further vibration envelopes that were captured. In particular, Figure 6a shows how the torsional curvature of the

modal, which starts in the direction of the applied diagonal motion at the base of the structure, and ends at the top of the structure where the motion is across the model's axis.

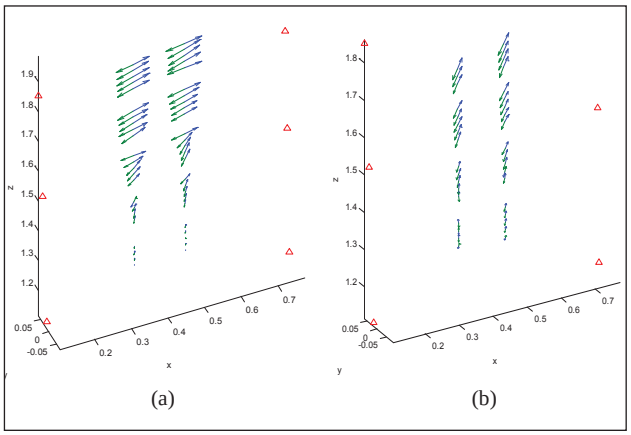

Figure 6. Captured vibration envelopes of the rotated model structure.

5.2 Vertical timber section

A larger model was constructed to demonstrate how the approach is scalable and how the test remains effective in outdoor conditions. This larger model was a 2.4 m tall vertical timber section which was fixed to another flat piece of wood. As before, D80 cameras were used, coded control targets were placed either side of the test subject and their coordinates were measured using total station in reflectorless mode. Larger monitoring targets were used to reflect the changed image scale (figure 7).

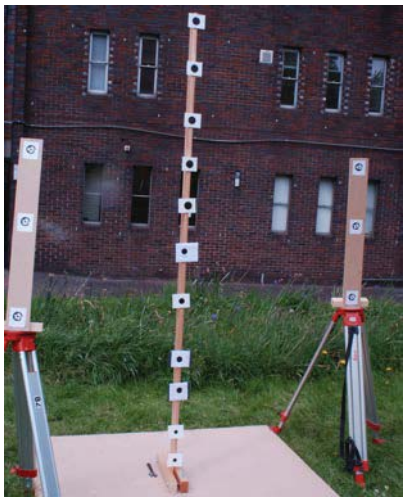

Figure 7. Timber upright outdoor model.

The timber upright was excited manually in the X and Y axis. The objective here was to examine the curvature of the vibration envelope rather than identify nodes. Figure 8 gives the motion vectors for motion in the X and Y directions. Since the stiffness of the section in the minor axis is greater than the major axis, it would be expected that the vibration amplitude is more in this direction with a similar excitation.

It was found that whilst working outside, images would be overexposed by the brighter sunlight, even on the camera's lowest sensitivity settings. Neutral density filters were used to bring sensor exposure into an acceptable range.

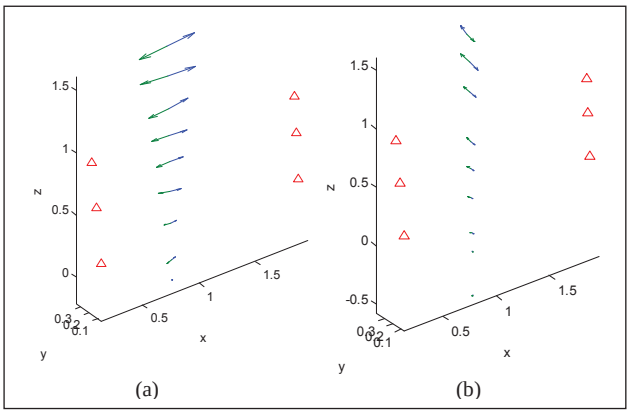

Figure 8. Captured vibration envelopes of the vertical timber as a result of excitation in the (a) X and (b) Y axis.

6. DISCUSSION

These experiments have demonstrated how long exposure imagery can be used for monitoring dynamic tests of vibrating structures. The approach overcomes inherent limitations in the high frequency imaging for monitoring vibrations which is limited to lower image resolutions.

The 3D experiments demonstrate the advantage of the photogrammetric technique over traditional sensors such as accelerometers. The approach is frequency independent, and frequencies up to 12 Hz have been recorded successfully, beyond the Nyquist frequency of 1.5 Hz (considering the 3 fps the Nikon D80 camera is capable of). The cameras used were off-the-shelf DSLR cameras, making the cost of the system considerably less than the highly specialised laser Doppler vibrometer, or using many accelerometers.

Accelerometers are contact sensors, so many are required to record the varying vibration throughout a structure. Alternatively, it is possible to systematically move an accelerometer to each monitoring location if vibration can remain constant. If multiple sensors are used, each additional monitoring location requires additional hardware, and requires cabling infrastructure and data logging hardware, increasing cost and set up time. Each additional monitoring point in this case requires only the addition of adhesive paper targets, so increased cost and set-up time is very low. The simplest accelerometer is one-dimensional, although three-dimensional accelerometers are available at additional cost. The laser Doppler vibrometer overcomes some of the limitations of accelerometers by making optical measurements from a remote observation point, but this instrument is limited to measuring out-of-plane movement only, and remains expensive.

All the motion vectors presented in the paper are represented by double-ended arrows. This is because it is not possible to determine the direction of the motion at the time the image is captured. Although the traditional high speed imaging approach allows instantaneous motion direction to be discerned between successive images, but it has not prevented the vibration envelope from being visualised with this approach.

The motion-blurred target measurement algorithm is less accurate than methods used for measurement of ordinary sharp images. However, alleviating the need for high speed imaging allows different hardware to be used, and images can be of a

higher resolution than would otherwise be possible. The image resolution of consumer level DSLR cameras is much higher than that used by camcorders that have previously been used for their higher imaging frequency. Unfortunately, the bespoke algorithm for measuring motion-blurred targets also has a longer duration than conventional sharp circular target measurement algorithms. However, the whole motion is captured within a single image so only the one image needs to be processed, rather than a long sequence of images. This also has advantages in terms of data storage and transmission, since the total file size for a long sequence of images would be very large.

Having fewer image files is also advantageous to real-time monitoring, which requires images to be downloaded to a computer and processed at the same rate at which they are acquired. Real time monitoring using the conventional approach has only been demonstrated possible at a reduced image resolution. The arrangement of artificial monitoring and control targets, and camera observation positions, is almost the same to that previously used for the monitoring of static deformation (Lange & Benning 2006; Ronnholm et al. 2009). In this way, the monitoring scheme can be used to monitor any static deformations also.

An additional constraint in camera positioning existed due to the difficulty in matching measured target 'ends'. As noted in figure 2, only one combination is correct, and this combination can usually be identified by selecting the case that produced the smallest image residual measurements. However, if only two cameras are used, and the cameras were arranged so that their relative positions are in the same direction as the motion of the test subject, both combinations produce similarly small coordinate residuals. This situation can be avoided by using more than two cameras, or by having 'a-priori' knowledge of expected vibration directions and suitably arranging the cameras.

The determined data is different to the traditional monitoring approach which determines natural frequencies by analysing acceleration history with a discrete Fourier transform, rather emphasising measurement of the vibration envelope. This approach could accompany traditional acceleration gauges for more detailed data, or used with frequency-selective excitation, where tests make use of artificial exciters. In this way it is not a complete replacement for traditional specialist dynamic monitoring instruments, indeed the approach currently does not provide the same level of accuracy, but aims to provide more detailed information.

7. CONCLUSIONS

This paper has presented two case studies of photogrammetric monitoring of vibrating structures using localised motion-blurred image patches. The case studies have shown how the measurement approach provides richer 3D detail for visualising the vibration envelope, using consumer grade imaging hardware. The scalability of the approach is demonstrated.
The frequency invariance means that monitoring of higher frequency vibrations, where photogrammetric monitoring has in been limited to lower image resolutions in the past, is possible with higher image resolutions, and hence better spatial measurement accuracy. They approach has been effectively used to record vibrations of up to 12 Hz.

Additional measurement matching complications not normally found in photogrammetric monitoring were identified, and how they can normally be resolved discussed. Although each target itself can be easily matched between images, the 'end' of each target's motion path cannot be uniquely coded, and selecting the combination with the smallest target residuals was effective in most cases. Another complication was the outdoor brightness level which caused images to be overexposed, which was overcome by using Neutral Density filters.

8. REFERENCES

Carden, E.P. & Fanning, P., 2004. Vibration Based Condition Monitoring: A Review. *Structural Health Monitoring*, 3(4), pp. 355–377.

Choi, H.-S., Cheung, J.-H., Kim, S.-H., Ahn, J.-H., 2011. Structural Dynamic Displacement Vision System using Digital Image Processing. *NDT & E International*, 44(7), pp. 597–608.

EOS Systems, 2015. PhotoModeler Motion Overview, Vancouver, Canada http://www.photomodeler.com/products/motion/default.html (14 Apr. 2014).

Jurjo, D.L.B.R., Magluta, C., Roitman, N., Gonçalves, P.B., 2010. Experimental methodology for the dynamic analysis of slender structures based on digital image processing techniques. *Mechanical Systems and Signal Processing*, 24(5), pp. 1369–1382.

Lange, J. & Benning, W., 2006. Crack detection at concrete construction units from photogrammetric data using image processing procedures. In: *Proceedings of the ISPRS Commission VII Symposium "Remote Sensing: From Pixels to Processes."* Enschede, The Netherlands. Vol. XXXVI, Part 7, pp. 15-19.

Maas, H. & Hampel, U., 2006. Photogrammetric Techniques in Civil Engineering Material Testing and Structure Monitoring. *Photogrammetric Engineering & Remote Sensing*, 72(1), pp. 39–45.

McCarthy, D.M.J., Chandler, J.H. & Palmeri, A., 2013. Monitoring Dynamic Structural Tests Using Image Deblurring Techniques. In: *Key Engineering Materials*. Dublin, Ireland, pp. 932–939.

Morlier, J., Salom, P. & Bos, F., 2007. New Image Processing Tools for Structural Dynamic Monitoring. In: *Key Engineering Materials*. Oxford, UK, pp. 239–244.

Pandey, A., Biswas, M. & Samman, M., 1991. Damage detection from changes in curvature mode shapes. *Journal of Sound and Vibration*, 145(2), pp. 321–332.

Olaszek, P., 1999. Investigation of the dynamic characteristic of bridge structures using a computer vision method. *Measurement*, 25(3), pp. 227–236.

Ronnholm, P., Nuikka, M., Suominen, A., Salo, P., Hyyppa, H.,Pontinen, P., Haggren, H., Vermeer, M., Puttonen, J., Hirsi, H., 2009. Comparison of measurement techniques and static theory applied to concrete beam deformation. *The Photogrammetric Record*, 24(128), pp. 351–371.

Yoneyama, S., Kitagawa, A., Iwata, S., Tani, K., Kikuta, H, 2007. Bridge deflection measurement using digital image correlation. *Experimental Techniques*, 31(1), pp. 34–40.

Photogrammetric Record, 17(9#): 000–000 (April / October 200#)

MONITORING 3D VIBRATIONS IN STRUCTURES USING HIGH RESOLUTION BLURRED IMAGERY

By DAVID M.J. MCCARTHY (d.mccarthy@lboro.ac.uk),
JIM H. CHANDLER (j.h.chandler@lboro.ac.uk)
and ALESSANDRO PALMERI (a.palmeri@lboro.ac.uk)
Loughborough University

Abstract

Photogrammetry has been used in the past to monitor the laboratory testing of civil engineering structures using multiple image based sensors. This has been successful, but detecting vibrations during dynamic structural tests has proved more challenging. Detecting vibrations during dynamic structural tests usually depend on high speed cameras, but these sensors often result in lower image resolutions and reduced accuracy.

To overcome this limitation, a novel approach described in this paper has been devised to take measurements from blurred images in long-exposure photos. The motion of the structure is captured in individual motion-blurred image, without dependence on imaging speed. A bespoke algorithm then determines each measurement point's motion. Using photogrammetric techniques, a model structure's motion with respect to different excitation frequencies is captured and its vibration envelope recreated in 3D. The approach is tested and used to identify changes in the model's vibration response.

KEYWORDS: Vibration, Deformation, Motion-blur, Engineering, Structural Health Monitoring, Close Range Photogrammetry

INTRODUCTION

CIVIL engineering structures often need to be tested to verify their performance and integrity. This requires meticulous planning, so that sufficient data is collected with the sufficient number of carefully positioned sensors. Contact transducers are often used, though they have some limitations, particularly if access to the structure is difficult. In the case of structural testing using dynamic test techniques, advanced sensors allow more detailed measurement. This approach is particularly convenient, as the presence of damage tends to result in a

localised change in the stiffness within the structure, which can then affect the vibration response elsewhere.

The advantages of photogrammetry can be realised when applied to structural testing, as a very high number of points can be recorded with few sensors, without any contact with the structure. This is of primary relevance when measuring dynamic mode shapes, since interpolation is necessary between each measuring point. Current hardware, however, limits the potential for this type of dynamic monitoring, which necessitates much higher imaging speeds.

In this paper, a novel approach is developed to directly measure the blur created by a deliberately long exposure. This is explained and tested after the importance and prior work is reviewed. The approach has built on previous developments (McCarthy et al., 2013, 2014) and the results of enhanced case studies are included here.

STRUCTURAL TESTING

ASSESSMENTS of structural integrity are often necessary for a variety of reasons. New materials under development in the laboratory environment may demand complex monitoring schemes to understand deformation patterns. Testing may also be prescribed during construction as verification of some critical elements. Testing of existing structures may be needed for evaluation prior to a change of use, or following a potentially damaging event. Long term structural health monitoring schemes are necessary on some structures to detect any potential deterioration.

Conventional structural tests apply increasing load to a structure while its performance is monitored by gauges. Subject to acceptable results, the structure is then deemed suitable for its working loads. The load would be applied with, for example, test weights on a slab or large vehicles on a bridge. This testing of 'static' structural properties may be considered inconvenient since the test would necessitate taking the structure out of service, in addition to the logistical problems of transporting and moving loads. Care must also be taken to not increase load above the structure's elastic limit, otherwise damage may occur from the test itself.

Dynamic structural monitoring is now emerging as a viable and effective approach for assessing structural performance (Brownjohn, 2011). Data collection is considered more convenient since much lower loading is necessary and monitoring can take place without taking the structure out of service. However, data analysis can be complicated and specialist expertise is necessary to interpret the vibration response. Several approaches exist to identify structural changes from the measured vibration response (Kasinos et al., 2014) and comparative studies score these approaches on their ability to identify, locate and quantify damage (Carden & Fanning, 2004). Generally, those approaches which take advantage of a higher number of monitoring points produce the most reliable results (Carden & Fanning, 2004).

MONITORING OF STRUCTURAL TESTS

ENGINEERS must select and distribute sensors appropriately to collect sufficient data to understand forces and deformations within a structure. Traditional contact sensors measure displacements or strains. For example, linear variable displacement transducer (LVDT) sensors can be used to measure displacement at various points of the structure, usually at a beam's mid-span or other equally spaced locations. Foil strain gauges measure strain in the material, the dimensionless measure of extension in a given direction.

Traditional contact gauges are reliable, well understood and often prescribed by engineers, but in many cases their effectiveness is limited by the fact that they only record the structure's performance in a single location, at the position where they are fitted. The possibility of individual gauges being affected by local variations in the material, or local strain concentrations should be recognised. Strain gauges are also susceptible to daily and seasonal environmental changes, being a significant limiting factor in long term structural health monitoring. Furthermore, each additional sensor costs money, takes time to fit and requires cabling infrastructure, and many sensors only measure in one dimension unless the more expensive multidimensional counterparts are used. Harvey (2008) noted the importance of carefully locating sensors, as a poorly sited sensor may not measure anything useful.

More advanced non-contact sensors can be used, including a total station or terrestrial laser scanner. These sensors can collect optical measurements from several monitoring points, but the latter is unable to measure true instantaneous point deformation. In addition, they take time to traverse the whole structure, making them suitable for testing of static properties only (Psimoulis and Stiros, 2008; Ronnholm et al., 2009). Differential GPS can monitor deformation without line of sight, but each individual monitoring point adds considerable cost (Roberts, 2004). The laser Doppler vibrometer (LDV) is a specialised optical dynamic sensor for monitoring vibrations. Changes in the wavelength of a reflected laser beam are related to the velocity of a moving surface. The instrument is very precise, but measures only at the location it is targeted at.

Photogrammetry has demonstrated its potential for monitoring structural tests in the past (Cooper, 1990; Maas, 1998; Benning, 2006). In particular, it allows instantaneous measurement of a very high number of monitoring points with a single arrangement of image sensors. These points may be monitored in 3D if using stereo or multiview imagery, whereas many contact gauges are one dimensional, or have more expensive 3D variants. Other advantages include that it is non-contact, meaning that the monitoring instruments do not add load to the test subject, and a stable reference on which to support contact gauges is not required. In particular, the photogrammetric approach is scalable, and suitable for a wide range of applications from small-scale laboratory tests (Thomas & Cantré, 2009) to full-size structures.

Photogrammetry has also been shown suitable for monitoring dynamic tests. Since all monitoring points within an image are measured simultaneously, additional points can be added, and the distance between each monitoring point reduced, with little additional cost. Vibrations can be captured by increasing

imaging speed to many frames per second (fps). The Nyquist sampling theorem dictates that, in order for certain frequencies to be detected, data must be sampled at least twice the desired frequency range. Olaszek (1999) notes that an even higher sampling frequency may be desirable, since even if the Nyquist theorem is satisfied, aliasing effects can cause the peak amplitude in the frequency domain to be missed.

Structural engineers always desire measurements that are as accurate as possible. Clearly the use of the highest resolution cameras is desirable to achieve the highest precision measurement but, as noted above, high imaging speed is normally necessary to capture and hence measure vibration at the required frequencies. When selecting camera hardware for monitoring tests of static properties (which take place over several minutes or a few hours), potential speed of continuous imaging may not need to be considered. In contrast, for dynamic tests with relatively fast variations in the deformed state of the structure, consideration must be given to both the image resolution and the potential continuous imaging speed of the camera.

When selecting a camera, current sensor hardware requires a compromise to be made between the image resolution and temporal resolution of the sensor. Digital single lens reflex (DSLR) cameras are available with image resolutions over 30 MP and consumer camcorders typically record at up to 60 frames per second. However, a DSLR camera at its highest resolution setting can only sustain at most a few images per second. Consumer camcorders acquire images at higher frequencies, but only capture at much lower image resolutions, typically 2.1 MP ('HD' resolution). Specialist machine vision camera sensors exist in a wide variety of configurations, but even these sensors are limited by a trade-off between spatial resolution and imaging frequency, and are expensive. Although the capabilities of image sensors are continually improving, so too do the demands of engineering researchers.

Real-time monitoring is very often desired for monitoring structural tests, since the engineer can appreciate the structure's performance as the tests takes place. When high speed imaging is used for monitoring, the images must be processed at the same rate that they are acquired, otherwise the real-time detectable vibration frequencies are limited by the processing speed. Real-time monitoring at acceptable speeds is possible, but only at a reduced image resolution and hence reduced spatial accuracy or by reducing the number of points (Jurjo, 2010), increasing undesirable interpolation.

Capturing a very high number of high resolution images also has practical difficulties. A considerable amount of data is generated and bottlenecks exist when images are stored to an internal memory card or uploaded to external file storage, or another computer for processing. If images are post-processed, or are to remain as documentary evidence, a large amount of data storage space is required.

PROPOSED MEASUREMENT APPROACH

AIMED at alleviating this penalising compromise between image resolution and imaging frequency, a radically new approach is presented in his paper, in which the structural vibration is captured within long-exposure images. Indeed, the motion of the vibrating structure causes localised blur within the image, and this can be measured using automated image processing methods.

Motion blurred imagery has been examined in Computer Science literature, and many algorithms have been published for extracting data from these seemingly poor quality images (Yitzhaky & Boshusha, 2000; Wang et al., 2007). It is often assumed that a motion blurred image is created from an ordinary sharp scene which is degraded my some blurring function. This blurring can be expressed using (Banham & Katsaggelos, 1997):

$$\mathbf{Y}(i,j) = \sum_{k=1}^{m}\sum_{l=1}^{n}\mathbf{H}(i,j;k,l)\mathbf{F}(k,l) + \mathbf{N}(i,j) \quad (1)$$

where, $\mathbf{F}(k,l)$ is an ordinary m x n sharp image; $\mathbf{H}(i,j;k,l)$ is the point spread function; $\mathbf{Y}(i,j)$ is the resultant blurred image; and $\mathbf{N}(i,j)$ represents noise.

The point spread function, **H**, contains information about the motion that caused the blur, including its extent, direction, and distribution. Some algorithms are capable of 'blind deconvolution' i.e. recovering the point spread function without prior knowledge of the motion that caused the blur.

In our implementation, an algorithm measures the motion blur exhibited by ordinary circular targets (McCarthy et al., 2014). Both the amplitude of the motion causing the motion blur and direction of the motion path are measured. A sinusoidal motion is assumed, as is expected during frequency selective dynamic structural testing (e.g. Chopra, 2007; Clough & Penzien, 2010; Palmeri & Lombardo, 2011). Black circular targets with a white background are arranged at necessary monitoring points on the test subject in the conventional way. Our implementation also requires a single sharp image of the test structure from the same cameras. This may be before dynamic excitation is applied, or in the case of a structure with environmental loading which vibrates continuously, simply an image taken with an appropriately fast shutter speed.

When the test structure vibrates, either artificially by manually applying force, or naturally under environmental loads such as wind, a single long exposure image is taken. As a result, the whole vibration of the structure during the time that the shutter is open is captured within the single image. The motion amplitude and direction at each monitoring point can then be measured by processing these long exposure images with a bespoke algorithm, implemented in MATLAB.

A set of preliminary tests were carried out on circular targets, which have demonstrated that their blurred images take a consistent form, exhibiting the same edges, shapes and gradients. Interestingly, two cases exist whereby the motion amplitude is either less or greater than the diameter of the circular target (Figure 1). In the former case, a small region of the image is occupied by the target throughout the exposure, and the pixels in this region remain the same

intensity as the black sharp target exhibiting no motion. Other image pixels which are occupied by the target for only part of the whole exposure, generate a pixel value with a value between the black target and the white border, proportional to the amount of time occupied by the target. In the latter case, every region of the image is exposed to the white target border for at least some of the time that the shutter is open, so the pixel value measured by every pixel within the blurred target image is in between the black of the target and white of the target background.

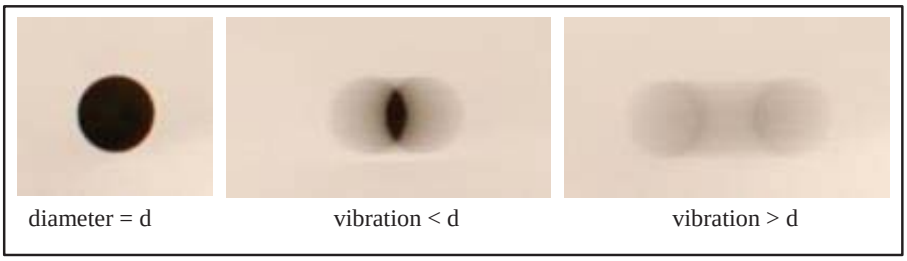

Figure 1: Appearance of motion blurred circular targets

IMAGE PROCESSING PROCEDURE

THE KEY steps in the bespoke image processing algorithm are summarised in Figure 2. The proposed procedure uses MATLAB's image processing toolbox. Three measurements are estimated using different techniques, each achieving increasing accuracy, but at decreasing speed.

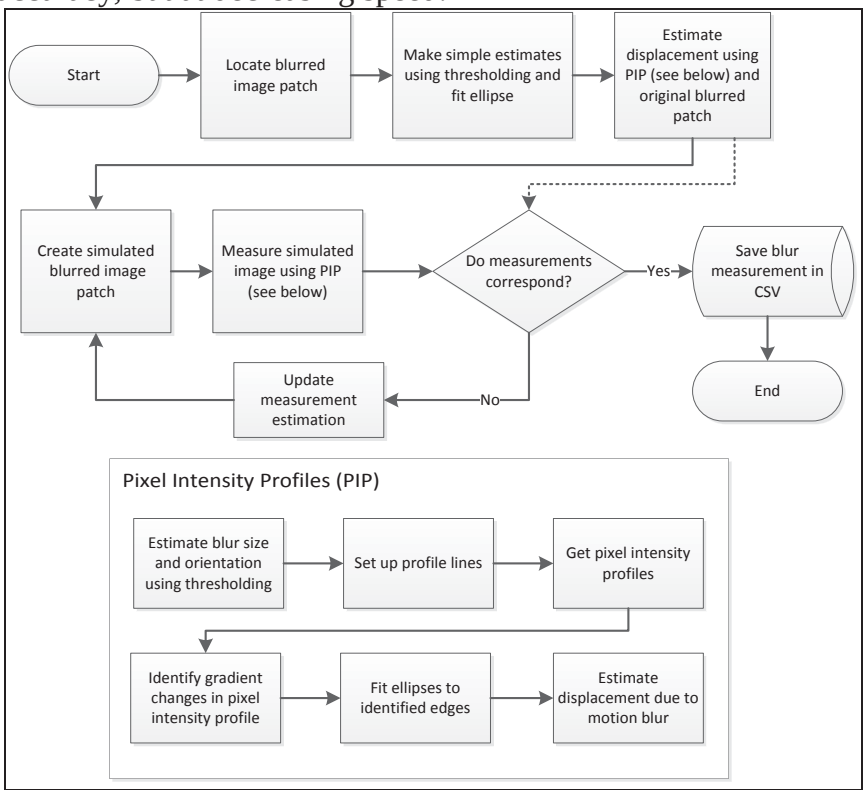

Figure 2: Blur measurement calculation flowchart

The blur measurement algorithm assumes the approximate location of each target is already known, since blurred targets in an image are more difficult to locate than a sharply defined target. This is achieved by detecting targets in the additional sharp image, in which circular targets are easily identified, and a list of coordinates passed to the blur measurement algorithm.

After locating the image patch of the blurred target, a rapid approximate estimate about the geometry of the image is determined with a simple thresholding algorithm. The chosen threshold needs to be nearer in value to the white of the target background, so that the detected region includes the grey regions at the edge of the blurred target. An ellipse is fitted to the detected region using least squares, and the estimated major and minor axis, and orientation allows arrangement of the profile lines for the next stage (Figure 3).

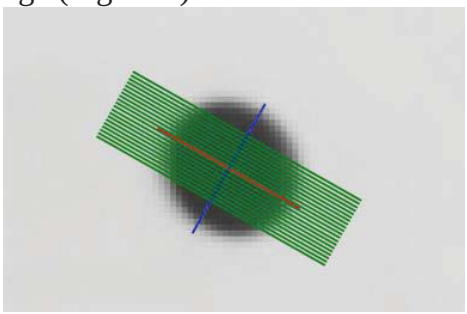

Figure 3: Major and minor axis (red and blue) of the target with arranged pixel intensity profile lines (green)

Secondly, parallel Pixel Intensity Profiles (PIPs) are extracted from the image through the major axis of the blur. The PIP process is adapted from an approach proposed by Boracchi et al. (2007). The number of profiles can be adjusted, but 20 was found to be a suitable balance between measurement accuracy and processing time. An example pixel intensity profile appears as in Figure 4b (The signal is inverted so that target pixels result in a peak), and points can be identified at abrupt changes in the gradient of the intensity profile which relate to features on the blur smear (Figure 4a). The algorithm identifies these features twice differentiating the intensity profile and locating peaks in the resulting function. These features are allocated to two groups (shown in red and blue in the figure), depending on where they follow or precede positive or negative gradients, and ellipses are fitted to each group of points (Figure 4c). The distance and angle between the centre coordinates of these ellipses is taken as the estimated motion occurring at that monitoring point on the structure. Tests demonstrated that this method provides pixel level accuracy of the motion amplitude.

The pixel intensity profile algorithm is effective in both cases, where motion amplitude is both smaller and larger than the target diameter (Figure 1); the algorithm identifies changes in gradient rather than changes in absolute pixel value. The type of blurred target is automatically identified by the presence of the dark centre region, since this has an effect on the allocation of feature points in the pixel intensity profiles into the two ellipses.

In tests, the pixel intensity profiles method alone regularly over-estimated the exhibited motion and did not provide adequate accuracy due to a specific systematic effect. Motion was overestimated because at the edge of targets there is

a gradient in pixel values, caused by chromatic aberration and lens diffraction. This was evident when an image of a stationary target exhibited an apparent displacement of approximately 1 pixel. A subsequent step was included therefore to improve accuracy.

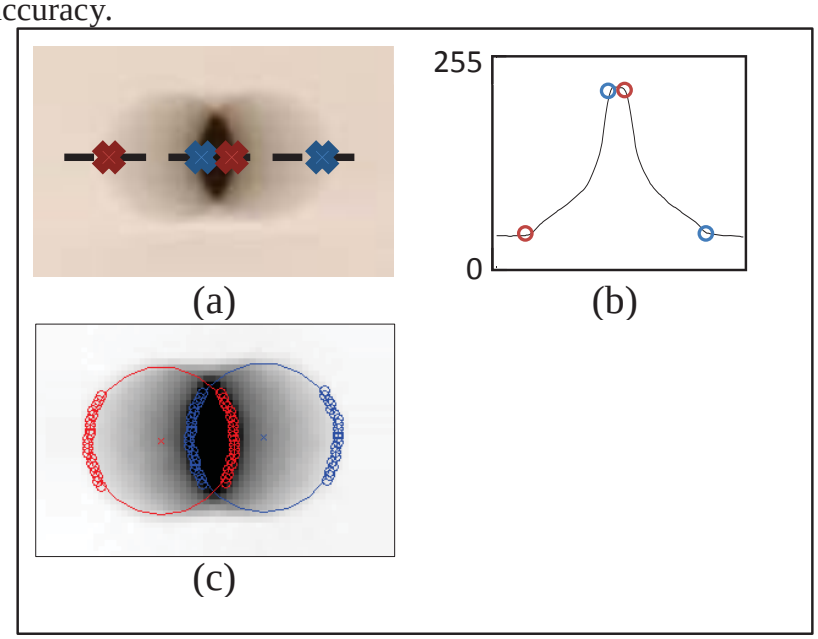

Figure 4: Resultant Blur Measurement

To achieve superior accuracy an iterative procedure was introduced. Here, a simulated blurred image patch is generated using the blur function (equation 1), using a sinusoidal point spread function of the first estimated motion and the earlier taken sharp image. The equation used to describe the point spread function, **H**, is defined by:

$$f(x) = \begin{cases} 0, & x < \frac{L-1}{2}; \\ \cos\frac{2\pi x}{L}+1, & \frac{L-1}{2} \le x \le \frac{L+1}{2}; \\ 0, & x > \frac{L+1}{2}; \end{cases} \quad (2)$$

where, L is the estimated motion amplitude. This function is discretised into units of a pixel by applying the trapezium rule over pixel intervals. The result of this function is spatially rotated by the estimated motion angle using MATLAB's imrotate function set to use bilinear interpolation. Finally, the matrix is divided by the sum of its elements, so that the elements of the final **H** sum to unity.

Pixel intensity profiles of this simulated image are measured and compared with the as-taken blurred image. If the initial measurement was correct, the as-taken and simulated image would correspond closely. If a discrepancy between the two remains, the amplitude and angle parameters of the point spread function are iteratively adjusted by the measurement discrepancy until the difference between the measured motion in both the original and simulated image patches is less than a user set threshold (Fig 5). The motion amplitude and angle used to create a simulated image that matched the as-taken image, is then accepted as the vector describing the distance and direction of the motion at that point on the test subject.

TRANSFORMATION INTO OBJECT SPACE

Having measured image coordinates in units of pixels, the distance and direction can be immediately represented graphically by superimposing displacement vectors on to the original images. By also superimposing the envelope of the motion, the output is similar to that produced by finite element software packages that might be used to predict forces and deformations in the structure. By showing displacement vectors together with an image of the structure, the engineer can appreciate which parts of the structure have the greatest motion, as well as observing the distribution, and possibly spot any anomaly.

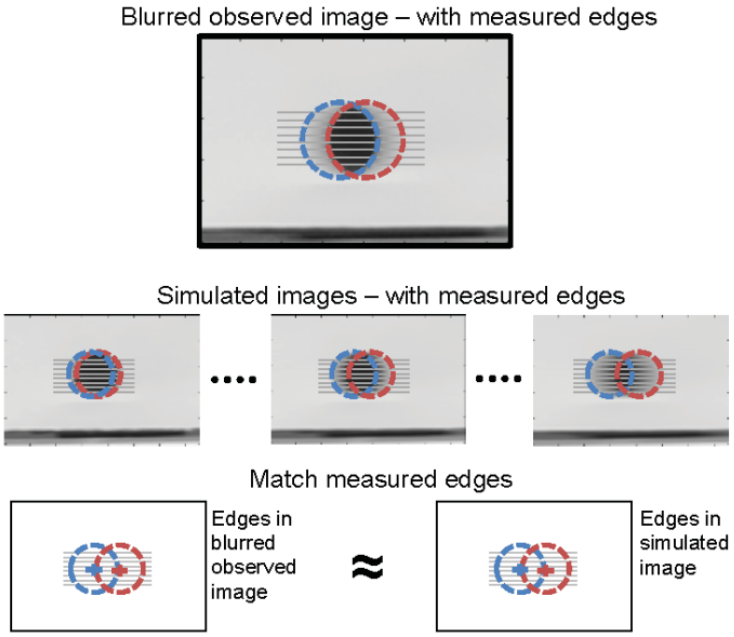

Figure 5: Iteratively improving accuracy using both the original blurred and simulated image patches.

2D Planar Measurement

It is also likely that an engineer would desire these measurements transformed into an appropriate object-space system (in millimetres) for more precise comparisons and analysis. With only a single camera, it is possible to provide 2D measurements, so long as it is known that any movement is planar and the focal plane of the camera is aligned approximately to the same plane. In this scenario, the perspective transformation (Luhmann et al., 2006) can be used to transform coordinates from image space to object space. However, if any out-of-plane movement were to occur, this could cause a scaling error in the measured results. It is recognised that radial and tangential distortion cause a displacement of a projected object point in the image plane. However, if individual monitored points are displaced relative to a fixed camera, then computed object displacements are almost identical, whether a lens model is explicitly incorporated or not. However, the effects of lens distortion can be easily corrected following

camera calibration (eg. Luhmann et al., 2006) and a correction for this simple systematic effect should be incorporated.

Coded control targets can simply be arranged around the test object (coplanar to the monitoring targets) and their object-space coordinates measured using a reflectorless Total Station. Coordinates in an arbitrary 3D object space are calculated. For calculating planar deformations, plane space coordinates for each control point are determined (Fig 6). The plane is defined by the object-space *X* and *Y* coordinates, to which linear regression is used to define an object space plan gradient and intercept. The distance from the intercept to the nearest point along the regression line of each control point is taken as its plane-space *x* coordinate. The earlier determined object-space *Z* coordinates become corresponding plane-space vertical *y* coordinate. Projective transformation parameters are determined with the paired plane-space and image-space control target coordinates, which are used to apply the projective transform to the earlier measured image-space monitoring point coordinates.

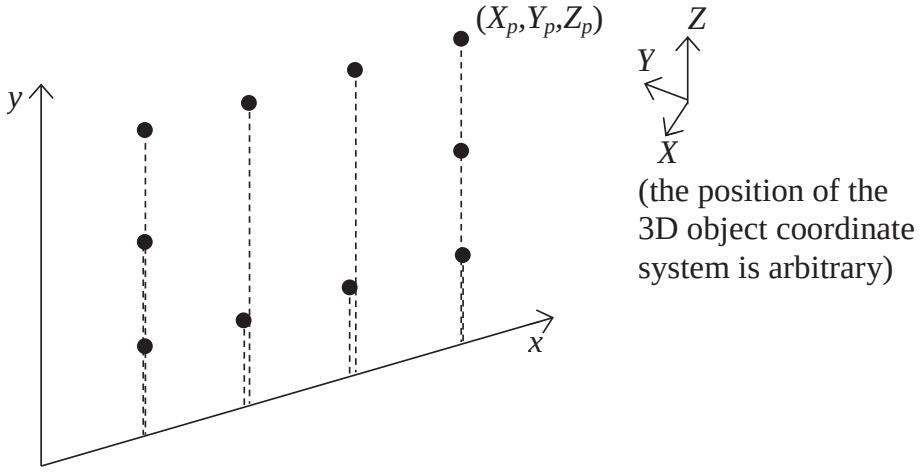

Figure 6: Definition of planar coordinates from 3D control point coordinates

Measurement in 3D

3D measurement has been highlighted in the past as a strength of photogrammetric measurement for monitoring of structures. The monitoring approach was expanded to fully 3D measurement that also allows non-planar motion to be recorded (McCarthy et al., 2014). For a moving target, two 3D object points will be created on any image, representing the target at each end of its motion. A 3D approach requires the use of two or more sensors and their shutters must be interconnected so that they capture images simultaneously. Additional calculation steps for finding 3D coordinates are shown in figure 7.

The exterior orientation (EO) of the cameras needs to be known and was achieved using the PhotoModeler software package (version 2013.0.3.113 64-bit, July 2013; EOS Systems Inc., Vancouver, Canada). This software is convenient because it automatically recognises coded control targets in images, and object space coordinates for the control points can be loaded using a PhotoModeler coded coordinate file. PhotoModeler's automated camera calibration was also used to determine appropriate interior orientation (IO) parameters, including

deriving an appropriate lens model, allowing accurate coordinates for the monitoring points to be determined. These object points allow approximate image coordinates to be computed, which are then used by the blur measurement algorithm to assist locating targets in images. Target matching can also be carried out by PhotoModeler.

Image coordinates for the motion blurred targets are measured as before using the image processing algorithm described above and stored in a CSV file. As mentioned above, a new challenge at the point matching stage occurs, since each target, which would normally have a single measurement in each image, instead has two coordinates measured, at either end of its motion path. Unlike traditional photogrammetry, the image coordinates relating to a 3D point cannot be uniquely matched with coded targets since they originate from one physical target which changes position. Figure 8 shows how two image coordinates exist for each target, and how different pairs of candidate object points can be created.

To solve this ambiguity for all objects/camera configurations, two candidate combinations of the pairs of coordinates for each target should be considered, since it is not yet known which combination is correct. 3D coordinates are therefore calculated for both combinations using a bespoke space intersection program, using Photomodeler's earlier derived EO and IO, which explicitly corrects for lens distortion. Residual image coordinates for the incorrect combination are usually significantly higher, depending on the exact arrangement (although, where the direction of target motion approaches the epipolar plane, they become similar, as discussed below). Residual coordinates are then calculated through reprojection of the 3D point onto the image, using the known camera orientations. In tests, it was found that selecting the combination of image coordinates which produces the smallest residual measurements overall, usually identified the correctly matched pair.

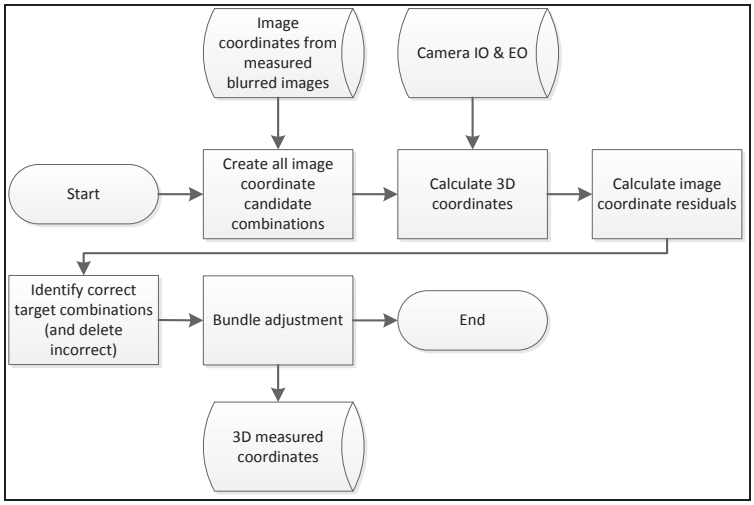

Figure 7: 3D calculation flow chart

Although this method has proven successful, in a particular case the correct combination cannot be automatically determined; where the orientation of the both measured points lie on the same epipolar plane. It may be possible to determine the most likely combination using engineering judgement, but if "a priori"

knowledge of the likely motion is available, then the two cameras can be arranged obliquely, such that this situation does not occur. It is therefore helpful to consider likely target movement direction when selecting camera positions. This ambiguity could also be solved by adding a third camera to the system, although there would then be $2^3 = 8$ combination of coordinates to consider for a single target.

Once 3D coordinates are determined, all of this data were then input to a bundle adjustment ('General Adjustment Program' (GAP), Chander & Clarke, 1992) to calculate final 3D coordinates in the object space.

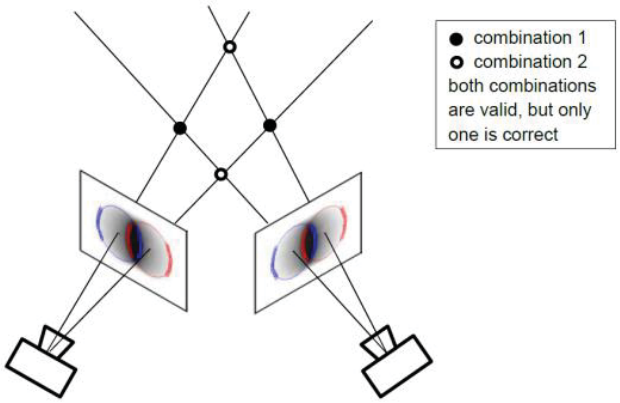

Figure 8: Point matching difficulties for a single target

PRACTICAL TESTS AND RESULTS

A ONE dimensional shaker table was used to test and demonstrate the proposed approach. The APS 'Electro-Seis' 400 is a long-stroke shaker capable of carrying out programmed one-dimensional motions up to 150 mm described in McCarthy et al. (2013, 2014). In its normal use, models are fitted to the 455 x 455 mm table bed which is programmed with vibrations of varying frequencies and amplitudes. As the model is subjected to base vibration, data would be recorded about the model's dynamic response using accelerometers and a laser displacement gauge.

Two Nikon D80 DSLR cameras were available for image capture, each camera equipped with 24 mm fixed focal length lenses and focus fixed at the appropriate distance (Figure 9a). The cameras have a sensor resolution of 10.2 MP. The shutter speed was fixed at 1 second in order to capture the whole vibration cycle, and the aperture and sensitivity were set to F32 and ISO 100 to provide clear images with appropriate contrast. The external shutter release for each camera was connected to the shaker table's control system (Figure 9c) so that the exact time they are triggered is recorded alongside the sensor data so that a direct comparison can be made.

Simple plastic model structures with a height of 760 mm were rigidly fixed with bolts to the shaker table (Figure 9b). The columns on the structure were marked with circular targets. Black 8 mm circles were printed on white paper backing with sufficient white space around the target so that the white space was sure to exceed the expected motion amplitude. Conventional coded targets were

arranged around the shake table to provide control points, and their positions were measured by total station in reflectorless mode. For 2D monitoring, these must be in the same plane as the monitoring targets, whilst for 3D tests these define a volume occupied by the model structure.

Testing 2D monitoring

For the first test, 2D measurements were made with a single camera positioned in front of the structure. The model structure was subjected to one dimensional

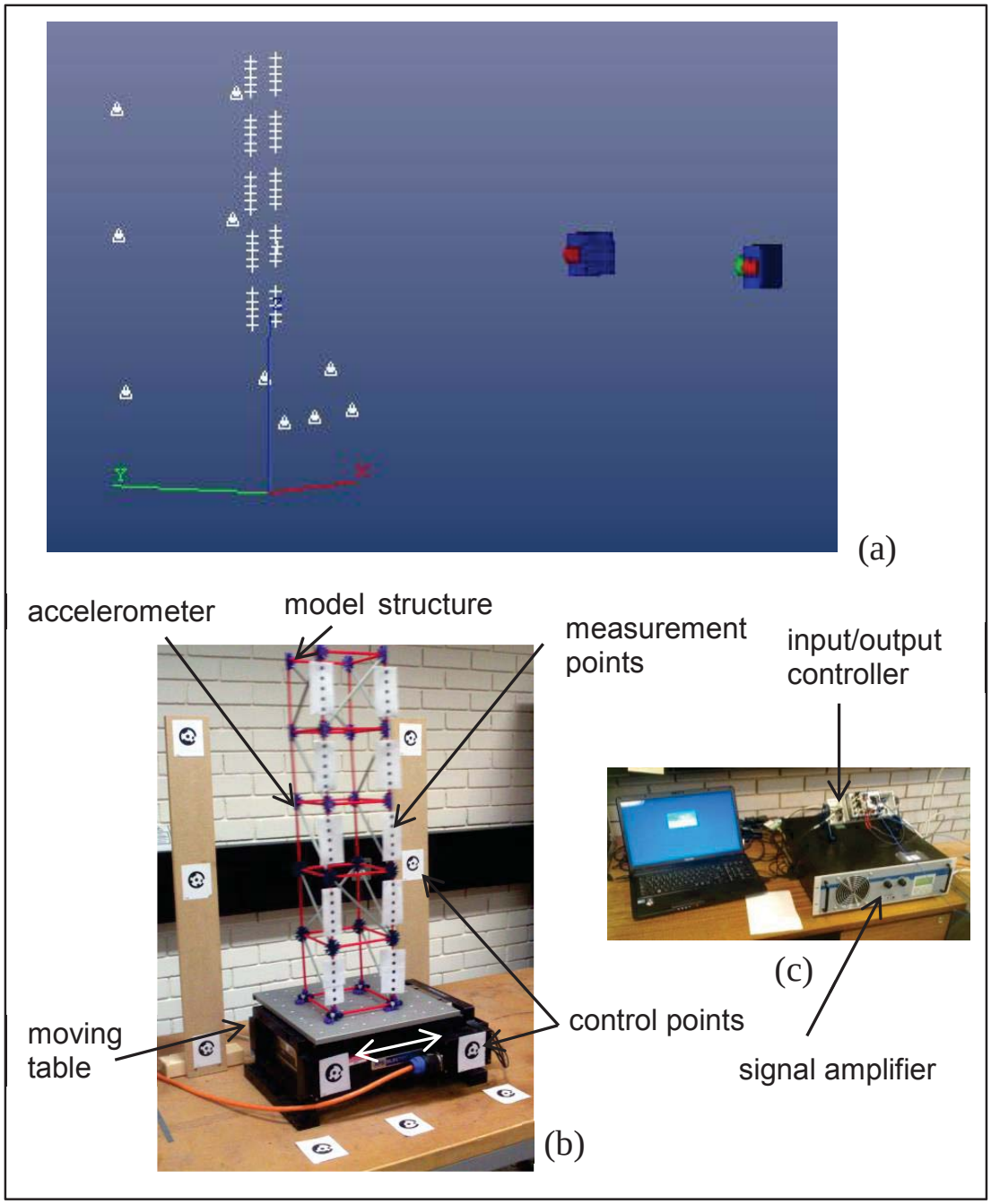

Figure 9: (a) experimental set up, (b) detail of vibration test subject, (c) detail of shaker table control system.

motion of varying frequencies. In particular, the model was excited with sinusoidal vibration at its natural frequencies (established separately using an accelerometer with a 'sine sweep' input table motion) so that the model would exhibit its vibration envelope for these modal frequencies. These are of interest for looking at the curvature of the vibration envelope, and locating nodes and antinodes (Abdel Wahab, 1999). Figure 10 shows recorded images overlain with the 2D measurements established using the image processing routine described in the previous section ("2D Planar Measurement").

The shape of the first vibration mode at 5 Hz may be expected for a structure of this type. The higher vibration mode shapes are less predictable since they are more sensitive to local variations in the structural properties. These higher modes are therefore also more likely to be able to indicate any changes in stiffness caused by damage or degradation of a structure.

Testing 3D Monitoring

Taking advantage of appropriate photogrammetric procedures and processes, further tests were carried out of the same model to demonstrate the 3D deformation measurement system developed. The second camera was introduced, and cameras rearranged to achieve appropriately convergent images. Both camera's external triggers were connected to the shaker table's control system, so that they would both be triggered simultaneously. The same motion was reapplied to the model. Following data capture, the images were processed as before using the blur measurement algorithm. The steps described in the previous section "Measurement in 3D" for determining the camera's orientations were followed, and 3D coordinates generated. Figure 11a shows the results from the repeated test

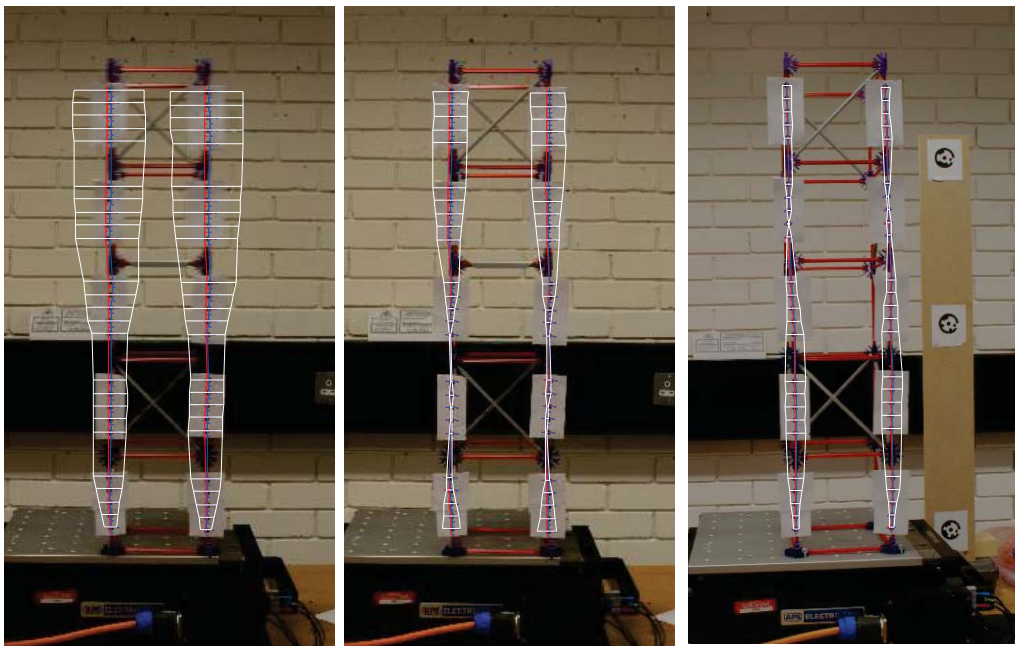

1st mode (5 Hz) 2nd mode (8 Hz) 3rd mode (12 Hz)

Figure 10: Measured vibration envelopes (horiz. scale enlarged by factor of 20)

which are similar in form to those measured in the first test (Figure 10).

Detecting structural changes

To assess the potential for detecting structural changes using the measured image data, a further test was designed using the same model structure. As shown in Figure 12, the structure was modified by adding mass to the structure on the 4th level. The test was repeated with the first three mode shapes being captured. Figure 11b shows the change in the dynamic response of the modified structure can be appreciated by a change in the measured vibration envelope. In particular, more significant three-dimensional changes are observed at the higher modes.
The second modification involved substituting two vertical members with replacements that had part of their cross section cut away (figure 12). By reducing

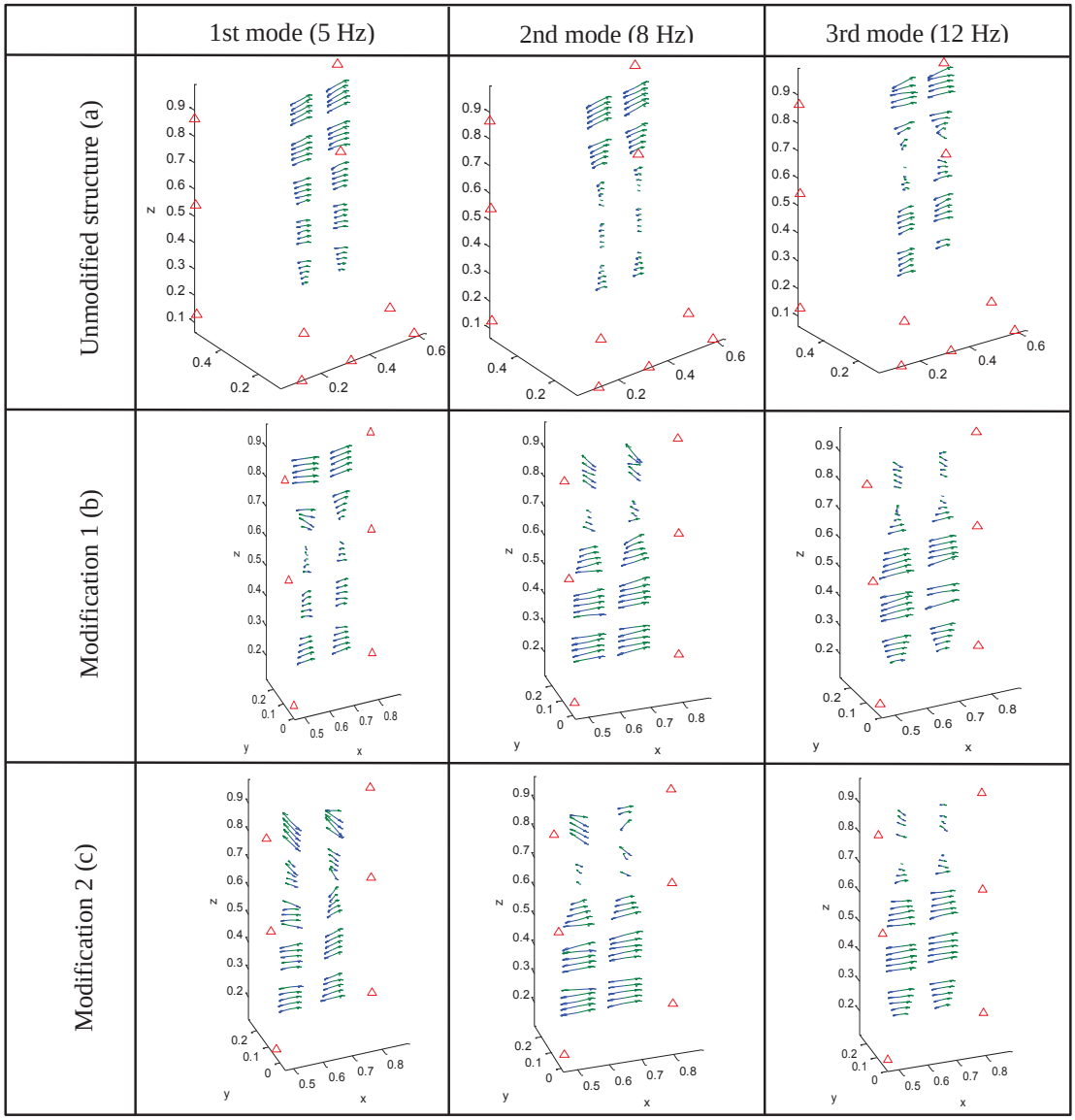

Figure 11: Measured change in vibration envelope from structural modifications. Blue/green vectors represent individual target displacements, whilst red triangles represent control points.

the cross-sectional area of the member, the stiffness was reduced. This is a similar affect to the failure of welds in a steel structure, which would result in a loss of stiffness. Changes can be observed in the locations of nodes and anti-nodes, the positions where the amplitude is smallest and largest. In a practical setting, identifying a change in the vibration envelope when one was not expected would prompt further investigation as to the underlying cause, possibly prompting repair work (Kasinos et al., 2014).

Testing was repeated again and results are presented in Figure 11c. It is interesting to note how the analysis of the unmodified model (Figure 11a) reveals a motion which is essentially planar in all the three modes of vibration; while the two modifications (Figures 11b and 11c) induces some significant torsional effects. Such changes in orientation of the vibration envelope may not ordinarily be detectable with conventional single axis accelerometers.

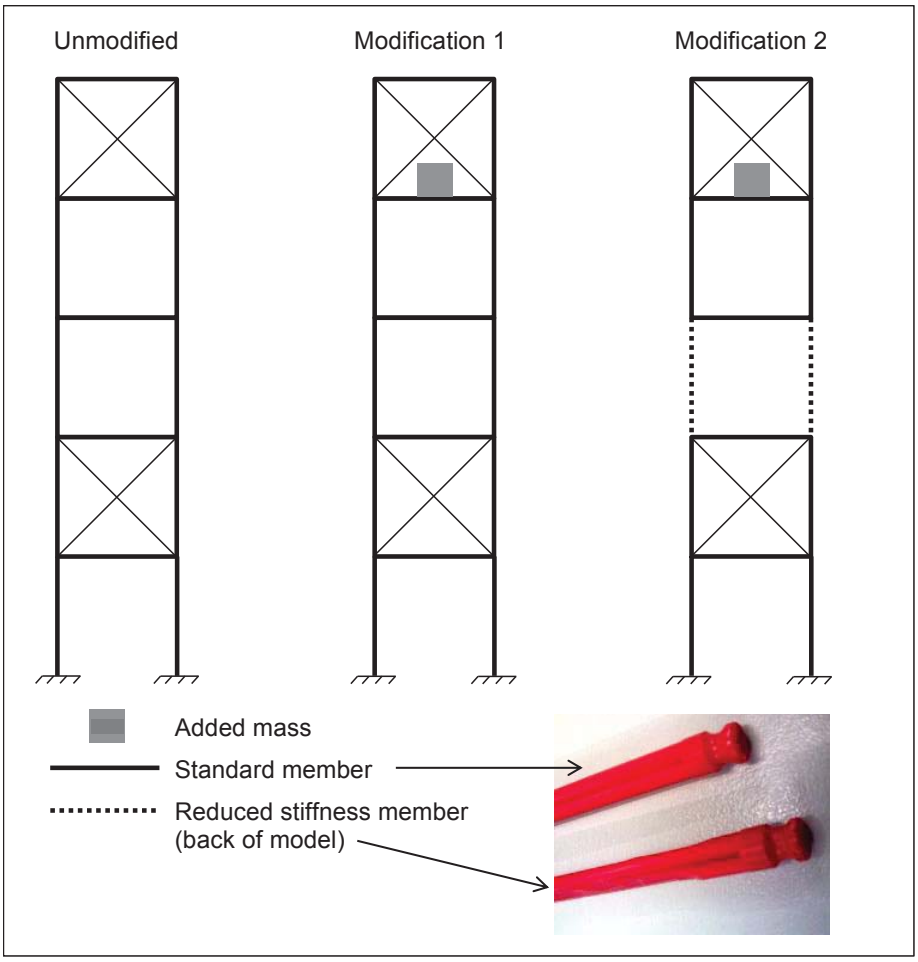

Figure 12: Modifications made to model structure

DISCUSSION

THIS paper demonstrates the potential for using controlled blurred images to monitor structural tests using off-the-shelf low cost equipment and digital photogrammetry. It may be used for a wide range of applications where imaging

hardware provides sufficient image and temporal resolution. The proposed solution further extends the capabilities of photogrammetric monitoring by allowing vibration patterns to be identified without the requirement of high imaging speed sensors, which are expensive.

Assessing the accuracy of the system

An important question is always the accuracy, and this was assessed in another series of simplified tests. Individual targets were mounted directly to the table surface. Since the table motion could be accurately recorded by laser displacement gauge and accelerometers, these can be directly compared with the recorded motion. Various different amplitudes and target sizes were tested, along with different sized circular targets.

Results for errors between laser displacement gauge measurement and the image-based distance measurement are given in figure 13. A standard deviation of ±0.158 mm was observed, with a mean error of just -0.115 mm for a camera-object distance of 1 m. Using a 95% confidence interval, the measured distances are considered accurate to within 0.38 mm. In the image space at this scale, this represents 1.43 pixels at the 95% confidence level. Whilst the accuracy of the current measurement algorithm when expressed in pixels is poorer than conventional target measurement algorithms such as weighted centroid or ellipse fitting, images are obtained at the sensor's highest resolution without having to consider the imaging frequency limitation.

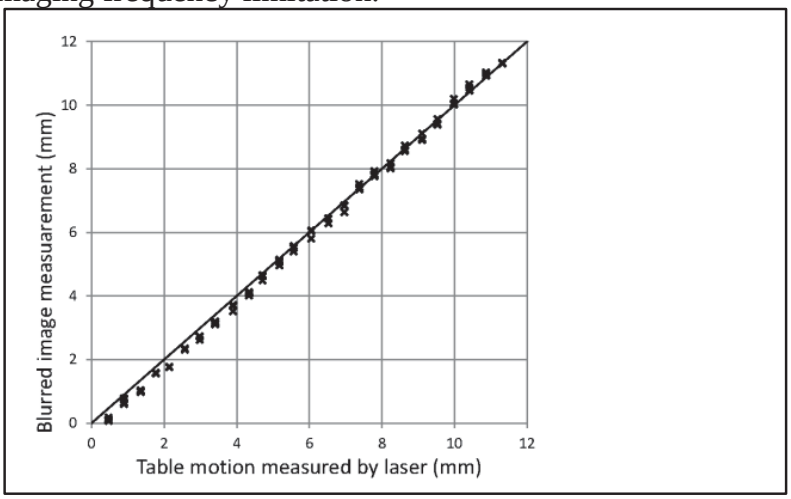

Figure 13: Results of accuracy assessment

The D80 cameras have a sensor resolution of 10.2 MP, at which resolution they were found to have a maximum continuous rate of 3 fps. These sensors would be limited to recording vibrations of less than 1.5 Hz at their maximum resolution due to the Nyquist sampling theorem. Utilising the proposed method, these sensors demonstrated the ability to measure the amplitude and shape of the dynamic response of structures at a frequency of 12 Hz. This approach also allows this to be achieved very efficiently, using a minimum number of images and sensors.

Tests have demonstrated how the approach may be used to identify the changes in the vibration envelope of structures, which in turn may be used to identify structural changes, e.g. the presence of localised damage.

The photogrammetric arrangement makes possible monitoring of displacements to assess static properties of the structure as well as dynamic. Although it is possible to calculate absolute displacements from acceleration measurements by double integration, the result usually exhibits a drift, and alternative sensors are normally necessary for monitoring of static structural properties. The arrangement of image sensors and targets makes possible recording of overall displacements of a structure, for assessment of the structure's static properties.

Imaging sensors have been used for monitoring vibrations in the conventional way by recording displacement-time history, from which frequency information can be identified using the discrete Fourier transform (Choi et al., 2011; Helfrick et al., 2011; Warren et al., 2011). This monitoring requires cameras with higher speeds at the cost of lower image resolutions. It is possible to improve measurement accuracy by 'zooming-in' on a single target, but the advantage of multiple monitoring points would be lost. The advantage of a very high number of monitoring points is of particular interest in the dynamic case. Maintaining a larger image scale allows the higher number of monitoring points, reducing undesirable interpolation.

Control of the image acquisition time and knowledge of the anticipated motion frequency is necessary to ensure that an appropriate shutter speed is selected. A shutter speed too short results in recorded motion that does not confirm to the sinusoidal pattern. In practice, relatively fast motion can be easily measured as the camera speed can be adjusted and the image exposure will remain acceptable. The shutter speed can be extended for slower vibration, but this may result in images being unacceptable overexposed. In case studies, neutral density filters have been used to reduce image exposure, allowing shutter speeds in the order of seconds to be used. Vibrations with a period of a second have been recorded successfully, but possible frequencies are limited by the imaging system.

While many techniques for interpreting dynamic response make use of frequency information, the proposed approach is frequency independent, rather emphasising spatial measurement of the vibration envelope. The acceleration time history from accelerometer data would usually be used for the identification of multiple frequencies in broadband excitation. When used with frequency-selective excitation, direct spatial measurement of the vibration envelope exhibits nodes, antinodes and shape curvature that can be used for dynamic assessment (Abdel Wahab & De Roeck, 1999). Although only a sinusoidal function has been used in this study to simulate the blur of the target, other functions could be used, depending on the particular regime of motion expected for the structure under observation.

For measurement in 3D, it was recognised that difficulties in target matching exist and how they were overcome has been described. In many static structural testing scenarios, the deformation shape of structure is relatively easy to predict, since the structure usually deforms in the direction of the applied load, and the use of one-dimensional gauges is often suitable. Out-of-plane movement is more

likely to be encountered during dynamic testing, since excited vibration modes could be longitudinal, transverse or torsional. Therefore, 3D monitoring, such as that presented here, may be desirable in more dynamic testing cases. Triaxial variants of accelerometers are also available, but each sensor is upgraded at added cost and more data-acquisition channels are needed, whilst each individual photogrammetric target is relatively inexpensive.

Accelerometers are more sensitive than the proposed image-based approach. Their high sensitivity and frequency information allows detection of vibrations of very low amplitude and high frequency. When photogrammetry is used for monitoring structural tests it is often commented that traditional contact gauges are known to be more accurate, and are usually used to assess the accuracy of the photogrammetric measurement system (Yoneyama et al., 2005; Ronnholm et al., 2009). However, the cost of an individual accelerometer is high, and extensive cable infrastructure and data monitoring hardware is required. Since individual accelerometers add significant cost to a monitoring system, as well as time to install, fewer sensors are usually possible than the image based approach used here. When determining modal shapes it is desirable to reduce the interpolation necessary between monitoring points by increasing their number (Carden & Fanning, 2004).

If employed for monitoring outdoors, the approach could clearly be affected by factors such as poor weather. Active targets built from high-intensity L.E.D.s have been discussed by Wahbeh et al. (2003) to allow improved monitoring during night hours and in dull weather. The image processing algorithm used is likely to be successful on this kind of similar images, and this may be an area for future investigation. Other sensors that do not rely on line-of-sight are not without their own difficulties, and Battista (2011) commented on experiencing missing data due to cable infrastructure problems.

CONCLUSION

THIS paper has presented a novel approach to identifying vibration patterns in civil engineering structures using long-exposure images, in which the targets appear blurred because of the motion of the structure. Photogrammetry has already demonstrated its use for monitoring of structural tests where hardware has sufficient imaging speed. The proposed approach aims to directly record the envelope of sinusoidal vibration, rather than instantaneous deformed shapes. This allows sensors with higher image resolutions to be used and at smaller scale in the field environment. Laboratory tests demonstrate the high quantity of measurements that can be achieved with only a few sensors, and the accuracy of the measurements has been assessed.

The data collected using the blurred-image approach has been compared with the traditional dynamic monitoring instruments. It has also been demonstrated how the approach can be used to detect structural changes in a series of model structures. The new frequency independent approach expands the capabilities of existing sensors which have otherwise had their applications restricted by their imaging frequency.

REFERENCES

ABDEL WAHAB, M.M. & DE ROECK, G., 1999. Damage Detection in Bridges Using Modal Curvatures: Application To a Real Damage Scenario. *Journal of Sound and Vibration*, 226(2): 217–235.

BANHAM, M. & KATSAGGELOS, A.K., 1997. Digital image restoration. *Signal Processing Magazine*, (March): 24–41.

BATTISTA, N. DE, WESTGATE, R. & KOO, K., 2011. Wireless monitoring of the longitudinal displacement of the Tamar Suspension Bridge deck under changing environmental conditions. *In:* M. TOMIZUKA, ed. *Sensors and Smart Structures Technologies for Civil, Mechanical, and Aerospace Systems* Proceedings of the SPIE: 79811O–15.

BORACCHI, G., CAGLIOTI, V. & GIUSTI, A., 2007. Ball position and motion reconstruction from blur in a single perspective image. *In: 14th International Conference on Image Analysis and Processing*. Modena: IEEE Comput. Soc.

BROWNJOHN, P.J.M.W., 2011. Structural health monitoring: Examples and benefits to structure stakeholders. *The Structural Engineer*, 89(9): 24–26.

CARDEN, E.P. & FANNING, P., 2004. Vibration Based Condition Monitoring: A Review. *Structural Health Monitoring*, 3(4): 355–377.

CHOI, H.-S., CHEUNG, J.-H., KIM, S.-H. & AHN, J.-H., 2011. Structural Dynamic Displacement Vision System using Digital Image Processing. *NDT & E International*, 44(7): 597–608.

CHOPRA, A., 2007. *Dynamics of Structures*, 3nd Edition, Prentice Hall: Upper Saddle River, NJ (USA).

CLOUGH, R. & PENZIEN, J. 2010. *Dynamics of Structures*, 2nd Edition (Revised), Computers and Structures: Berkeley, CA (USA).

CROSS, E.J., KOO, K.Y., BROWNJOHN, J.M.W., & WORDEN, K., 2013. Long-term monitoring and data analysis of the Tamar Bridge. *Mechanical Systems and Signal Processing*, 35(1-2): 16–34.

HARVEY, B., 2008. Testing and monitoring of structures: traps for the unwary. *Structural Engineer*, (October): 22–24.

HELFRICK, M.N., NIEZRECKI, C., AVITABILE, P. & SCHMIDT, T., 2011. 3D digital image correlation methods for full-field vibration measurement. *Mechanical Systems and Signal Processing*, 25(3): 917–927.

KASINOS, S., PALMERI, A. & LOMBARDO, M., 2015. Using the vibration envelope as damage-sensitive feature in composite beam structures, *Structures*, 1:67-75.

LANGE, J. & BENNING, W., 2006. Crack detection at concrete construction units from photogrammetric data using image processing procedures. *In:* N. KERLE & A. SKIDMORE, eds. *Proceedings of the ISPRS Commission VII Symposium "Remote Sensing: From Pixels to Processes"*. Enschede, The Netherlands.

LUHMANN, T., 2011. 3D Imaging - How to Achieve Highest Accuracy. *In:* F. REMONDINO & M. R. SHORTIS, eds. *Proc. of SPIE: Videometrics, Range Imaging, and Applications XI*. Munich, Germany, 808502–1–11.

LUHMANN, T., ROBSON, S., KYLE, S., HARLEY, I. 2006. *Close range photogrammetry: principles, techniques and applications*, Dunbeath: Whittles.

MCCARTHY, D.M.J., CHANDLER, J.H. & PALMERI, A., 2013. Monitoring Dynamic Structural Tests Using Image Deblurring Techniques. *In:* B. BASU, ed. *Key Engineering Materials*. Dublin, Ireland: Trans Tech Publications, 569–570:932–939.

MCCARTHY, D.M.J., CHANDLER, J.H. & PALMERI, A., 2014. 3D Case Studies of Monitoring Dynamic Structural Tests using Long Exposure Imagery. *International Archives of Photogrammetry, Remote Sensing and Spatial Information Sciences*, XL-5, 23–25 June 2014, Riva del Garda, Italy, pp. 407–411.

OLASZEK, P., 1999. Investigation of the dynamic characteristic of bridge structures using a computer vision method. *Measurement*, 25(3): 227–236.

PALMERI, A. & LOMBARDO, M., 2011. A new modal correction method for linear structures subjected to deterministic and random loadings, *Computers and Structures*, 89(11-12):844-854.

PSIMOULIS, P. A. & STIROS, S.C., 2008. Experimental Assessment of the Accuracy of GPS and RTS for the Determination of the Parameters of Oscillation of Major Structures. *Computer-Aided Civil and Infrastructure Engineering*, 23(5): 389–403.

ROBERTS, G.W., MENG, X. & DODSON, A.H., 2004. Integrating a Global Positioning System and Accelerometers to Monitor the Deflection of Bridges. *Journal of Surveying Engineering*, 130(2): 65–72.

Ronnholm, P., Nuikka, M., Suominen, A., Salo, P., Hyyppa, H. & Pontinen, P., 2009. Comparison of measurement techniques and static theory applied to concrete beam deformation. *The Photogrammetric Record*, 24(128): 351–371.

Thomas, H. & Cantré, S., 2009. Applications of low budget photogrammetry in the geotechnical laboratory. *The Photogrammetric Record*, 24(December): 332–350.

Wahbeh, A.M., Caffrey, J.P. & Masri, S.F., 2003. A vision-based approach for the direct measurement of displacements in vibrating systems. *Smart materials and structures*, 12: 785–794.

Wang, S., Guan, B., Wang, G, Li, Q., 2007. Measurement of sinusoidal vibration from motion blurred images. *Pattern Recognition Letters*, 28(9):1029–1040.

Warren, C., Niezrecki, C., Avitabile, P., Pingle, P., 2011. Comparison of FRF measurements and mode shapes determined using optically image based, laser, and accelerometer measurements. *Mechanical Systems and Signal Processing*, 25(6): 2191–2202.

Yitzhaky, Y. & Boshusha, G., 2000. Restoration of an image degraded by vibrations using only a single frame. *Optical Engineering*, 39(8):2083-2091.

Yoneyama, S., Kitagwa, A., Kitamura, K., Kikuta, H., 2005. Deflection distribution measurement of steel structure using digital image correlation. *In:* L. M. Hanssen & P. V. Farrell, eds. *Optical Diagnostics*, 58800G 1–8.

Résumé

Zusammenfassung

Appendix B

Larger case study candidate structures

The following page lists the structures which were considered whilst selection a case study for this project. The bridges were either visited on site or, for those further afield, considered remotely using sources such as Google Earth.

After reducing the shortlist, two preferred candidate structures were identified, in Nottingham and Leicester. The Wilford Suspension Bridge in Nottingham was selected.

1	Wilford Suspension Bridge, Welbeck Road, Nottingham Good candidate
2	Kensington Avenue, Loughborough – steel truss footbridge Maybe – short span – high frequency but fairly low amplitude, local
3	Sandringham Drive, Loughborough - footbridge Maybe – short span – high frequency but fairly low amplitude, local
4	Thurcaston Road, Leicester. Near abbey lane intersection Red Hill way 2 span pedestrian bridge Nick's suggestion – Dave Twigg looked at before?
5	http://www.foxysislandwalks.co.uk/Leicester-Canal-Arm.html canal footbridge 14 REJECT: In Northamptonshire
6	footbridge over the River Wreake between Brooksby and Hoby. http://www.leics.gov.uk/index/highways/road_pathway_maintenance/commercial_services/rights_of_way_services.htm
7	http://www.pwpeics.se/england_l.htm Leicester: Holden Street footbridge, Belgrave. Steel suspension bridge http://www.foxysislandwalks.co.uk/GUJC-Leicester.html pictures at end Mill Hill, Leicester Reason for rejection: Too rigid – wider than others
8	http://www.pwpeics.se/england_l.htm Leicester: Footbridge across Hamilton Way
9	Waterside Inn, Sileby Road, Mountsorrel, go east, footbridge under A6. Reason for rejection: Flooded on visit
10	Waterside Inn, Sileby Road, Mountsorrel, go east, bridge over weir Reason for rejection: Flooded on visit
11	Sileby Mill boatyard Reason for rejection: Flooded on visit
12	Castle Gardens, The Newark, Leicester. Suspension bridge http://www.foxysislandwalks.co.uk/GUJC-Leicester.html Leicester, Footbridge No.111A - River Soar http://www.pwpeics.se/england_l.htm Leicester: Footbridge at Castle Garden across Grand Union Canal by 'Colorworks' bar and restaurant steel suspension bridge Good candidate, more lateral vibration than vertical
13	Waterside Inn, Sileby Road, Mountsorrel, go west 0.4mi Reason for rejection: Flooded on visit
14	http://www.foxysislandwalks.co.uk/GUJC-Leicester.html Swan's Nest bridge 10 Mill Hill, Leicester, then 0.2mi south Reason for rejection: Flooded on visit
15	Footbridge over A6 at Quorn Reason for rejection: too rigid, access difficult.
16	Footbridge over Trent at Burton-on-Trent Wetmoor Lane Suggested by Nick

Appendix C

Key Matlab algorithms

This appendix lists and describes the function of the key Matlab algorithms for LEMBI monitoring.

routine This is the main function, in which variables are defined, images loaded from disk and the other main functions are called.

scanlines_estimate This algorithm carries out PIP measurement, and returns the PIP measurement result.

refine_with_simulation3 Is provided with the motion initially estimated by the scanlines_ estimate function, and manages iterations of the verify_ with_ simulation function as the more accurate blurred target measurement is found.

verify_with_simulation Takes a blurred and unblurred image, artificially blurs the sharp image using the provided motion estimate. This algorithm initially calculated a correlation statistic, but was then modified to call the scanlines_ estimate function.

sinusoidal_blur_kernel5 This function generates the point spread function used to generate artificially motion blurred images. Its output is illustrated in figure 3.23.

C.1 'routine'

```
% clear all
close all
% UserLoopFinished = false;
PointSelectionMode = 'auto';
window_size = [80, 140];
% window_size = [50, 40];
clear crop_rectangle selection_x selection_y % Clear previous target
failed_targets = zeros(1,2);
AutoResponse = 3;        % 3 to accept
AutoAcceptParameters = true;
acknowledge_each_new_image = false;
strict_target_coords_Iblurred = false;
% strict_target_coords_Isharp = true;
coordinate_for_sharp_target = 'as blurred'; % 'search'  'coordinate'  'as blurred'  'sharp_target_coordinates'

PathName = 'C:\Users\cvdm7\Personal Documents - Not Backed Up\Upright 13.2.13';
SharpFileName = 'DSC_0035.JPG';

% Load image names
imagenames_fid = fopen(fullfile(PathName,'image_names.txt'));
FileNameCell = textscan(imagenames_fid,'%s');
FileName = FileNameCell{1}';
fclose(imagenames_fid);
% load(fullfile(PathName,'folder_ImageNames'))

if ~exist('sharp_target_coordinates','var')
    sharp_target_coordinates = csvread(fullfile(PathName,'target_coordinates.csv'));
end
% save(fullfile(PathName,'folder_ImageNames'),'FileName')
% FileName{1} = 'ARL_5289.JPG';

if ~exist('FileName','var')
    [FileName, PathName] = uigetfile({'*.jpg;*.tif;*.png;*.gif','All Image Files'}, ...
    'Select the BLURRED image','\\staff-fs\cv-staff-home\cvdm7\Shaker table 19.11.12');
end
if ~exist('SharpFileName','var')
    [SharpFileName, PathName] = uigetfile({'*.jpg;*.tif;*.png;*.gif','All Image Files'}, ...
    'Select the SHARP image for verification','\\staff-fs\cv-staff-home\cvdm7\Shaker table 19.11.12');
end
%% Create task list
image_nos_to_loop = 1:length(FileName);
target_nos_to_loop = 1:5;

if ~exist('tasklist','var')
    number_of_tasks = length(image_nos_to_loop)*length(target_nos_to_loop);
    tasklist = cell(number_of_tasks,1);
```

```
47      for ii = 1:length(image_nos_to_loop)
48          for p = 1:length(target_nos_to_loop)
49              tasklist{p+(ii-1)*length(target_nos_to_loop),1} = ...
50                  struct('image_number',image_nos_to_loop(ii), ...
51                  'target_number',target_nos_to_loop(p), ...
52                  'task_status','queued', ...
53                  'FileName',FileName{image_nos_to_loop(ii)});
54          end
55      end
56  end
57
58
59  %% Main task loop
60  % image_nos_to_loop = 1:length(FileName);
61  % target_nos_to_loop = 8:17;
62
63  waitbarHandle = waitbar(0,'Starting...','Name','Routine081112_progress');
64
65  for task_no = 1:number_of_tasks
66      switch tasklist{task_no}.task_status
67          case 'completed'
68              disp(['Task_number_' num2str(task_no) '_has_status_completed'])
69              continue
70          case 'error'
71              disp(['Task_number_' num2str(task_no) '_has_status_error'])
72              continue
73          case 'queued'
74              disp(['Task_number_' num2str(task_no) '_starting'])
75          otherwise
76              disp(['Task_number_' num2str(task_no) '_has_unrecognised_status
                    '])
77              continue
78      end
79
80      %% Single point loop
81      try
82          if exist(fullfile(PathName,strcat(tasklist{task_no}.FileName(1:8),'
                _target_coordinates.csv')),'file')
83              disp('New_array_of_target_coordinates_for_this_image')
84              target_coordinates = csvread(fullfile(PathName,strcat(tasklist{
                    task_no}.FileName(1:8),'_target_coordinates.csv')));
85          end
86
87          image_loop_number = tasklist{task_no}.image_number;
88          point_loop_number = tasklist{task_no}.target_number;
89              waitbar((task_no-1)/number_of_tasks,waitbarHandle,['Task:_'
                    num2str(task_no) '/' num2str(number_of_tasks) '_Image:'
                    num2str(image_loop_number) '_Target:' num2str(
                    point_loop_number)]);
90
91          PointLoopFinished = false;
92          while ~PointLoopFinished  % Start the single point loop
93              close all
94
95              %% Load in the images and user identifies the targets
```

```
96              fprintf('\n\n*** Next target ***\n')
97              disp(['Image: ' num2str(image_loop_number) ' Point: ' num2str(
                    point_loop_number)])
98
99              % Load blurred image
100             Iblurred = imread(fullfile(PathName,FileName{image_loop_number
                    }));
101             Iblurred = rgb2gray(Iblurred);
102             Iblurred = 255 - Iblurred;
103             disp(['Routine081112: Image loaded from ' FileName{
                    image_loop_number}]);
104
105             % User crops image
106             disp('Routine081112: Crop the image')
107
108             switch PointSelectionMode
109                 case 'manual'
110                     % Crop
111                     % crop_rectangle = [];
112                     if exist('crop_rectangle','var')
113                         [Iblurred, crop_rectangle] = imcrop(Iblurred,
                                crop_rectangle);
114                     else
115                         [Iblurred, crop_rectangle] = imcrop(Iblurred);
116                     end
117                     Isharp_crop_corner = crop_rectangle([2 1]);
118                     Iblurred_crop_corner = crop_rectangle([2 1]);
119                     close
120
121                     % User selected object in blurred image
122                     if exist('selection_x','var')
123                         Iblurred_user_selected_point = [selection_y,
                                selection_x];
124                     else
125                         disp('Routine081112: Click on the target in the
                                BLURRED image')
126                         figure
127                         imshow(Iblurred)
128                         hold on
129                         [selection_x, selection_y] = ginput(1); % user
                                selects the 'blob'
130                         Iblurred_user_selected_point = [selection_y,
                                selection_x];
131                         close
132                     end
133                 case 'auto'
134                     if exist(fullfile(PathName,'target_coordinates.csv'),'
                            file')
135                         target_coordinates = csvread(fullfile(PathName,'
                                target_coordinates.csv'));
136                     elseif exist(fullfile(PathName,'target_coordinates.mat'
                            ),'file')
137                         load(fullfile(PathName,'target_coordinates'));
138                     else
139                         error('Routine: No target coordinates defined');
```

```
140                     end
141                     %         save(fullfile(PathName,'target_coordinates')
                            ,'target_coordinates');
142                     Iblurred_user_selected_point = target_coordinates(
                            point_loop_number,:);
143                     Iblurred_crop_corner = Iblurred_user_selected_point -
                            round(window_size./2);
144                     Isharp_crop_corner = Iblurred_crop_corner;
145                     crop_rectangle = [ Iblurred_crop_corner([2 1]) ,
                            window_size([2 1]) ];
146                     [Iblurred, crop_rectangle] = imcrop(Iblurred,
                            crop_rectangle);
147                     Iblurred_user_selected_point =
                            Iblurred_user_selected_point - ...
148                     Iblurred_crop_corner;
149                 end
150
151
152                 % Recentre the blurred image
153                 if strict_target_coords_Iblurred
154                     Iblurred_estimated_centre = Iblurred_user_selected_point;
155                 else
156                     Iblurred_estimated_centre = search_for_target_in_image(
                            Iblurred, ...
157                     Iblurred_user_selected_point);
158                 end
159                 Iblurred = imread(fullfile(PathName,FileName{image_loop_number
                        }));
160                 Iblurred = rgb2gray(Iblurred);
161                 Iblurred = 255 - Iblurred;
162                 Iblurred_estimated_centre = Iblurred_estimated_centre +
                        Iblurred_crop_corner;
163                 [Iblurred, Iblurred_crop_corner, Iblurred_estimated_centre] =
                        RecenterCroppedImage(...
164                 Iblurred,Iblurred_estimated_centre,window_size);
165
166                 % Select object in sharp image
167                 Isharp = imread(fullfile(PathName,SharpFileName));
168                 Isharp = rgb2gray(Isharp);
169                 Isharp = 255 - Isharp;
170                 switch coordinate_for_sharp_target
171                     case 'search'
172                         Isharp_estimated_centre = search_for_target_in_image(
                                Isharp ...
173                         ,Iblurred_user_selected_point+Iblurred_crop_corner);
174                     case 'coordinate'
175                         Isharp_estimated_centre = Iblurred_user_selected_point
                                + Iblurred_crop_corner;
176                     case 'as_blurred'
177                         Isharp_estimated_centre = Iblurred_estimated_centre +
                                Iblurred_crop_corner;
178                     case 'sharp_target_coordinates'
179                         Isharp_estimated_centre = sharp_target_coordinates(
                                point_loop_number,:);
180                 end
```

```
[Isharp, Isharp_crop_corner, Isharp_estimated_centre] =
    RecenterCroppedImage(Isharp, ...
Isharp_estimated_centre,window_size);

%% Run the first thresholding_area_test
disp('Routine081112: thresholding_area_test started')
blur_type = thresholding_area_test(Iblurred,Isharp,
    Iblurred_estimated_centre, ...
Isharp_estimated_centre);
disp(['Routine081112: thresholding_area_test finished   ' upper
    (blur_type)])

%% Load profile parameters

if exist('image_profiles_parameter','var')
    clear image_profiles_parameters
end
if exist(fullfile(PathName,[FileName{image_loop_number}(1:end
    -4) '_data.mat']),'file')
    % Load file specific parameters
    load(fullfile(PathName,[FileName{image_loop_number}(1:end
        -4) '_data.mat']))
    parameters_confirmed = true;
    disp(['File specific parameters used for ' FileName{
        image_loop_number}])
elseif exist(fullfile(PathName,'all_images_data.mat'),'file')
    % Load folder specific parameters
    load(fullfile(PathName,'all_images_data.mat'))
    parameters_confirmed = true;
    disp(['Folder specific parameters used for ' FileName{
        image_loop_number}])
else
    % Load default parameters and save for next time
    image_profiles_parameters = struct( ...
        'NumberOfScanLines', 40, ...
        'MinorAxisExpand', 0.7, ...
        'MajorAxisExpand', 1.3, ...
        'profile_length', 300, ...                  % Number of
            steps in each profile
        'POINT_MARKING_METHOD', 'threshold', ...    % OPTIONS: '
            threshold' 'threshold findpeaks' 'max difference' '
            profile_ransac'
        'include_blur_type_test', false, ...
        'is_simulated_image', false, ...
        'suppress_output', false, ...
        'circle_fitting_method', 'fit_ellipse', ...     %
            OPTIONS: 'standard' 'ransac' 'fit_ellipse'
        'manual_edge_matching', 2, ...
        'assumed_blur_direction', 'horiz', ...        % OPTIONS:
             'horiz' 'vert'
        'force_blur_direction', false, ...
        'overide_threshold_adjustment_at_verify', false, ...
        'ransac_trials', 1000, ... % 1000
        'ransac_dth', 0.1 , ... % 0.1
        'ransac_percent', 10 , ... % 50
```

```
224                     'ransac_rLimits', [1e-12 1e12], ... % [1e-12 1e12]
225                     'first_guess', false);
226                 switch blur_type
227                     case 'internal'
228                         image_profiles_parameters.threshold_adjust = -0.15;
229                         image_profiles_parameters.sensitivity = 0.13;
230                     case 'external'
231                         image_profiles_parameters.threshold_adjust= -0.10;
232                         image_profiles_parameters.sensitivity = 0.10;
233                 end
234                 disp(['Unspecific parameters used for ' FileName{
                        image_loop_number} ' set'])
235                 parameters_confirmed = false;
236             end
237
238             %% Run scanlines_estimate
239             disp('Routine081112: scanlines_estimate started')
240
241             [~, ~, ~, first_profiles_data] = scanlines_estimate(Iblurred,
                    image_profiles_parameters, ...
242             Iblurred_estimated_centre,0,Isharp,Isharp_estimated_centre);
243             first_profiles_data.crop_corner = Iblurred_crop_corner;
244             Iblurred_estimated_centre = first_profiles_data.
                    blob_WeightedCentroid;
245             xc1 = first_profiles_data.xc1yc1xc2yc2(1);
246             yc1 = first_profiles_data.xc1yc1xc2yc2(2);
247             xc2 = first_profiles_data.xc1yc1xc2yc2(3);
248             yc2 = first_profiles_data.xc1yc1xc2yc2(4);
249
250             disp('Routine081112: scanlines_estimate finished')
251             fprintf('\b   Measurement:Row = %1.3f, Col = %1.3f  \n',
                    first_profiles_data.separation_cartesian(1),
                    first_profiles_data.separation_cartesian(2))
252
253             if ~parameters_confirmed && ~AutoAcceptParameters
254                 MenuResponse = menu('The image profiles parameters are not
                        set for this image or folder', ...
255                     'SAVE used parameters for this image and CONTINUE', ...
256                     'CONTINUE without saving parameters', ...
257                     'STOP / bad parameters');
258                 if MenuResponse == 3
259                     return
260                 elseif MenuResponse == 1
261                     save(fullfile(PathName,[FileName{image_loop_number}(1:
                            end-4) '_data.mat']), ...
262                     'image_profiles_parameters')
263                     disp('image_profiles_parameters saved for next time')
264                 end
265                 if MenuResponse == 1 || MenuResponse == 2
266                     minfig(gcf,1)
267                 end
268             end
269
270
271             %% Refine with simulation
```

```
272             window_size = window_size;  Padding = [50 50];
273             % image_profiles_parameters.POINT_MARKING_METHOD = 'threshold';
274             image_profiles_parameters.include_blur_type_test = false;
275             image_profiles_parameters.suppress_output = true;
276             Padded_window_size = window_size + Padding;
277             aa = 0;
278             refinement_iterations = 4;
279
280             % FIRST, RE-CENTRE IMAGES
281             % Sharp: Load again, re-crop to centre
282             disp('Routine081112: Re-centreing SHARP image'),
283             Isharp = imread(fullfile(PathName,SharpFileName));
284             Isharp_estimated_centre = Isharp_estimated_centre +
                    Isharp_crop_corner;
285             [Isharp, Isharp_crop_corner, Isharp_estimated_centre] = ...
286             RecenterCroppedImage(Isharp,Isharp_estimated_centre,
                    Padded_window_size);
287             Isharp = 255 - Isharp;
288
289             % Blurred: Load again, re-crop to centre
290             disp('Routine081112: Re-centreing BLURRED image')
291             Iblurred = imread(fullfile(PathName,FileName{image_loop_number
                    }));
292             Iblurred_estimated_centre = Iblurred_estimated_centre +
                    Iblurred_crop_corner;
293             [Iblurred, Iblurred_crop_corner, Iblurred_estimated_centre] =
                    ...
294             RecenterCroppedImage(Iblurred,Iblurred_estimated_centre,
                    window_size);
295             Iblurred = 255 - Iblurred;
296 %             Iblurred_user_selected_point = Iblurred_estimated_centre;
297             first_profiles_data = RecentreProfilesData(first_profiles_data,
                     Iblurred_crop_corner);
298
299             % Carry out refining
300             % image_profiles_parameters.include_blur_type_test = true;
301             [~, best_match, profiles_data] = refine_with_simulation3
                    (0,0,0,0, window_size, Padding,aa,refinement_iterations,
                    Isharp,Isharp_estimated_centre,Iblurred,0,0, ...
302             image_profiles_parameters,0,first_profiles_data);
303
304             disp('Routine081112: refine_with_simulation finished')
305             fprintf('\b   Measurement:Row = %1.3f, Col = %1.3f  \n',
                    best_match(1),best_match(2))
306
307             xc_av = Iblurred_estimated_centre(2) + Iblurred_crop_corner(2);
308             yc_av = Iblurred_estimated_centre(1) + Iblurred_crop_corner(1);
309             yc1 = yc_av + best_match(1) * sin(best_match(2) *pi()/180) / 2;
310             yc2 = yc_av - best_match(1) * sin(best_match(2) *pi()/180) / 2;
311             xc1 = xc_av + best_match(1) * cos(best_match(2) *pi()/180) / 2;
312             xc2 = xc_av - best_match(1) * cos(best_match(2) *pi()/180) / 2;
313
314             %%% Test with reflection
315             % Test_With_Reflection
316
```

```
317             %% Ask the user what to do
318             if ~exist('BlurDisplacementsPairs','var')
319                 BlurDisplacementsPairs = [];
320             end
321             if AutoResponse == 0
322                 MenuResponse = menu('Routine081112: Where to go next?', ...
323                     'REJECT measurement and REPEAT this target', ...
324                     'ACCEPT measurement and REPEAT this target (may result
                        in duplicates!)', ...
325                     'ACCEPT measurement and CONTINUE to next target', ...
326                     'REJECT measurement and CONTINUE to next target', ...
327                     'STOP where we are');
328             else
329                 MenuResponse = AutoResponse;
330             end
331
332             % Save point
333             if MenuResponse == 2 || MenuResponse == 3
334                 BlurDisplacementsPairs(end+1,:) = [ xc1 yc1 xc2 yc2 ];
335                 tasklist{task_no}.xc1yc1xc2yc2 = [ xc1 yc1 xc2 yc2 ];
336                 tasklist{task_no}.task_status = 'completed';
337                 tasklist{task_no}.datetime = now;
338                 tasklist{task_no}.profiles_data = profiles_data;
339                 disp([num2str(size(BlurDisplacementsPairs,1)) '
                        displacements pairs stored'])
340             end
341             % Repeat
342             if MenuResponse == 3 || MenuResponse == 4 || MenuResponse == 5
343                 PointLoopFinished = true;
344             end
345             if MenuResponse == 5
346                 return;
347             end
348
349         end % End the point finished loop
350         0;
351         %% Ending the task list
352
353     catch ME
354         tasklist{task_no}.task_status = 'error';
355         tasklist{task_no}.error_message = ME.message;
356         tasklist{task_no}.error_identifier = ME.identifier;
357         tasklist{task_no}.error_stack = ME.stack;
358         if ~exist('BlurDisplacementsPairs','var')
359             BlurDisplacementsPairs = [];
360         end
361         BlurDisplacementsPairs(end+1,:) = zeros(1,4);
362     end
363 end % End the task loop of each image
364
365 calculate_circle_fit_variences
366 SaveBlurMeasurementsAsCSV
367
368 waitbar(1,waitbarHandle,'Completed')
```

C.2 'scanlines_estimate'

```
%
% Usage: scanlines_estimate(I,image_profiles_parameters,
    estimated_target_centre,~,Isharp,[Isharp_estimated_centre])
%
% Where     I:                          The grayscale image
%           image_profile_parameters    Is a structure array
%           estimated_target_centre:    After thresolding the image, the blob
%                                       at this position will be examined.
%           Isharp:                     Used to test blur type (Int/Ext)
%           Isharp_estimated_centre:
%
% Outputs:
%    1: [xc1 yc1 xc2 yc2]
%    2: Weighted centroid
%    3: [xc1 yc1 R1 ; xc2 yc2 R2 ] (scanline_circle_data)
%    4: profiles_data structure array

function [varargout] = scanlines_estimate(I,image_profiles_parameters, ...
estimated_target_centre,~, varargin)

SCANMODE = 'auto';                          % OPTIONS: 'auto' 'manual'
auto_accept_auto_threshold_increases = true;

% Unpack variables
NumberOfScanLines = image_profiles_parameters.NumberOfScanLines;
MinorAxisExpand = image_profiles_parameters.MinorAxisExpand;
MajorAxisExpand = image_profiles_parameters.MajorAxisExpand;
threshold_adjust = image_profiles_parameters.threshold_adjust;
sensitivity = image_profiles_parameters.sensitivity;
profile_length = image_profiles_parameters.profile_length;
POINT_MARKING_METHOD = image_profiles_parameters.POINT_MARKING_METHOD;
    % OPTIONS: 'threshold' 'max difference' 'profile_ransac'
suppress_output = image_profiles_parameters.suppress_output;
if strcmp(SCANMODE,'manual'); suppress_output = false; end;

if image_profiles_parameters.include_blur_type_test && nargin < 6
    error('scanlines_estimate was requested a blur type test but did not
        recieve the Isharp image')
elseif image_profiles_parameters.include_blur_type_test
    Isharp = varargin{1};
    Isharp_estimated_centre = varargin{2};
end

if isfield(image_profiles_parameters,'low_threshold')
    low_threshold = image_profiles_parameters.low_threshold;
    high_threshold = image_profiles_parameters.high_threshold;
end

% check we've got the centre of the target
[estimated_target_centre] = search_for_target_in_image(I,
    estimated_target_centre);
% THIS COULD BE MOVED TO PARENT FUNCTION

```

```
50
51 %% Set up the scan lines
52 switch SCANMODE
53     case 'auto'
54         accept_auto_profile_lines = false;
55         while ~accept_auto_profile_lines
56             % This makes some estimates about the shape of the blur using
57             % simple thresholding
58             threshold = graythresh(I) + threshold_adjust;
59             bw = im2bw(I,threshold);
60             blobs = bwconncomp(bw, 4);
61             blobs_labelled =  labelmatrix(blobs);
62
63             estimated_target_centre = round(estimated_target_centre);
64
65             selected_blob_no = blobs_labelled(estimated_target_centre(1)
                   ...
66             ,estimated_target_centre(2));
67             blob_prop = regionprops(struct('Connectivity',4,'ImageSize',
                   blobs.ImageSize, ...
68                 'NumObjects',1, ...
69                 'PixelIdxList', {{ blobs.PixelIdxList{selected_blob_no} }}
                       ) ...
70                 , I ...
71                 , 'Centroid','Orientation','MajorAxisLength','
                       MinorAxisLength','WeightedCentroid','PixelList');
72
73             % Does the blur orientation need correcting?
74             if image_profiles_parameters.force_blur_direction
75                 switch image_profiles_parameters.assumed_blur_direction
76                     case 'horiz'
77                         blob_prop.Orientation = 0;
78                     case 'vert'
79                         blob_prop.Orientation = 90;
80                 end
81             elseif blob_prop.MajorAxisLength/blob_prop.MinorAxisLength <=
                   1.1
82                 % If the blur is almost a circle, sometimes the estimated
83                 % orientation is the opposite to what it really is, so we
                       fix it
84                 % horizontal  !!!!!!!!
85                 disp('This␣is␣quite␣a␣circular␣blob.␣Im␣going␣to␣assume␣the
                       ␣blur␣direction␣to␣be␣')
86                 switch image_profiles_parameters.assumed_blur_direction
87                     case 'horiz'
88                         fprintf('\bHORIZONTAL.\n');
89                         blob_prop.Orientation = 0;
90                     case 'vert'
91                         fprintf('\bVERTICAL.\n');
92                         blob_prop.Orientation = 90;
93                 end
94             end
95
96             % Set up two basic vectors that are used to select coordinates
                   in
```

```
97              % the image
98              BasicMajorVector = [ cos(blob_prop.Orientation*pi()/180) ...
99              -sin(blob_prop.Orientation*pi()/180) ] .* blob_prop.
                    MajorAxisLength/2;
100             BasicMinorVector = [ -sin(blob_prop.Orientation*pi()/180) ...
101             -cos(blob_prop.Orientation*pi()/180) ] .* blob_prop.
                    MinorAxisLength/2;
102             % Create X,Y pairs for the scan lines, saved in ScanLines array
                    .
103             profile_coordinates = zeros(NumberOfScanLines,4);
104             for profile_number = 0:NumberOfScanLines-1
105                 profile_coordinates(profile_number+1,[1 2]) = ...
106                     blob_prop.Centroid + ...
107                     BasicMinorVector*(2*profile_number/(NumberOfScanLines
                            -1)-1)* ...
108                     MinorAxisExpand - BasicMajorVector*MajorAxisExpand ;
109                 profile_coordinates(profile_number+1,[3 4]) = blob_prop.
                        Centroid + ...
110                     BasicMinorVector*(2*profile_number/(NumberOfScanLines
                            -1)-1)* ...
111                     MinorAxisExpand + BasicMajorVector*MajorAxisExpand ;
112             end
113
114             % Check if image profiles exceed image dimensions
115             if ...
116                     sum(sum(profile_coordinates(:,[1 3]) > size(I,2))) +
                            ...
117                     sum(sum(profile_coordinates(:,[1 3]) < 0)) + ...
118                     sum(sum(profile_coordinates(:,[2 4]) > size(I,1))) +
                            ...
119                     sum(sum(profile_coordinates(:,[2 4]) < 0)) ...
120                     ~= 0
121                 warning('scanlines_estimate:␣Profile␣lines␣coordinates␣
                        exceed␣the␣dimensions␣of␣the␣image')
122                 if threshold >= 0.95 % Can't reduce threshold further
123                     figure;
124                     title('Profile␣lines␣exceed␣image␣dimensions')
125                     subplot(1,2,1)
126                     imshow(I);
127                     subplot(1,2,2)
128                     imshow(I);
129                     hold on;
130                     plot(blob_prop.PixelList(:,1),blob_prop.PixelList(:,2),
                            'r.')
131                     drawnow
132                     error('scanlines_estimate:␣Profile␣lines␣coordinates␣
                            exceed␣the␣dimensions␣of␣the␣image,␣and␣threshold␣
                            couldn''t␣be␣increased␣further')
133                 else % Reduce threshold a little more
134                     threshold_adjust = threshold_adjust + 0.05;
135                     if ~auto_accept_auto_threshold_increases
136                         waitfor(msgbox(['threshold␣is␣being␣adjusted␣to␣'
                                num2str(threshold+0.05)]))
137                     end
138                 end
```

```
139             else
140                 accept_auto_profile_lines = true;
141             end
142         end
143
144     case 'manual'
145         % If we're testing in manual mode, just get a pair of coordinates
146         % from the user for a single scan line.
147         figure
148         imshow(I)
149         title('scanlines_estimate: Manual mode. Select two points to take
                improfile between')
150         [inputX,inputY] = ginput(2);
151         profile_coordinates = [inputX(1) inputY(1) inputX(2) inputY(2)];
152         close
153         NumberOfScanLines = 1;
154 end
155
156 %% Check if image profiles exceed image dimensions
157 if ...
158         sum(sum(profile_coordinates(:,[1 3]) > size(I,2))) + ...
159         sum(sum(profile_coordinates(:,[1 3]) < 0)) + ...
160         sum(sum(profile_coordinates(:,[2 4]) > size(I,1))) + ...
161         sum(sum(profile_coordinates(:,[2 4]) < 0)) ...
162         ~= 0
163     warning('scanlines_estimate: Profile lines coordinates exceed the
            dimensions of the image')
164     figure;
165     title('Profile lines exceed image dimensions')
166     subplot(1,2,1)
167     imshow(I);
168     subplot(1,2,2)
169     imshow(I);
170     hold on;
171     plot(blob_prop.PixelList(:,1),blob_prop.PixelList(:,2),'r.')
172     drawnow
173 end
174
175
176 %% Plot the scan lines
177 if suppress_output == false
178     % Original image
179     figure
180     subplot(2,2,1), imshow(I)
181
182     % Image superimposed with profiles
183     subplot(2,2,2)
184     subimage(255-I)
185     colormap('jet')
186     axis off
187     hold on
188     if strcmp(SCANMODE,'auto')
189         % Plot the major and minor axis
190         plot([blob_prop.Centroid(1)-BasicMajorVector(1) blob_prop.Centroid
                (1)+BasicMajorVector(1)], ...
```

```
191             [blob_prop.Centroid(2)-BasicMajorVector(2) blob_prop.Centroid
                    (2)+BasicMajorVector(2)],'r-')
192         plot([blob_prop.Centroid(1)-BasicMinorVector(1) blob_prop.Centroid
                (1)+BasicMinorVector(1)], ...
193             [blob_prop.Centroid(2)-BasicMinorVector(2) blob_prop.Centroid
                    (2)+BasicMinorVector(2)],'b-')
194     end
195     % Plot profile lines
196     for l=1:size(profile_coordinates,1)
197         plot([profile_coordinates(l,1); profile_coordinates(l,3)] ,[
                profile_coordinates(l,2); profile_coordinates(l,4)],'-','color'
                ,[0 0.5 0]);
198     end
199 end
200
201 %% Test for external blur
202 if strcmp(SCANMODE,'manual')
203     image_profiles_parameters.include_blur_type_test = false;
204 end
205 if image_profiles_parameters.include_blur_type_test == true
206     not_user_selected_centre = [blob_prop.Centroid(2), blob_prop.Centroid
            (1)];
207     BlurType = thresholding_area_test(I,Isharp,not_user_selected_centre,
            Isharp_estimated_centre);
208 else
209     BlurType = 'not_requested';
210 end
211
212
213 %% Get image profiles
214 [edge1, edge2, edge3, edge4] = deal(nan(NumberOfScanLines,2));
215
216 for profile_number=1:NumberOfScanLines % FOR EACH SCAN LINE
217
218     inputX = profile_coordinates(profile_number,[1 3]);   % Get the
            coordinates of this scan line
219     inputY = profile_coordinates(profile_number,[2 4]);
220
221     % Get the profile line
222     image_profile_values = improfile(I,inputX,inputY,profile_length,'
            bilinear');
223
224     % Basic filter
225     image_profile_values = smooth(image_profile_values);
226
227     switch POINT_MARKING_METHOD
228         case 'threshold'
229             % IDENTIFY POINTS USING THRESHOLD
230             [~, mid_point] = max(image_profile_values);
231             pixel_range = max(image_profile_values) - min(
                    image_profile_values);
232
233             left_crosssection = image_profile_values(1:mid_point);
234             right_crosssection = image_profile_values(mid_point+1:end);
235             low_left_points  = left_crosssection <= ...
```

```
236             min(left_crosssection)+pixel_range*sensitivity;
237             low_right_points  = right_crosssection <= ...
238             min(right_crosssection)+pixel_range*sensitivity;
239
240             high_points = image_profile_values >= ...
241             max(image_profile_values)-pixel_range*sensitivity;
242
243             point2 = find(high_points,1,'first');
244             point3 = find(high_points,1,'last');
245
246             point1 = find(low_left_points,1,'last');
247             point4 = find(low_right_points,1,'first') + mid_point;
248
249         case 'thresholds_set'
250             % IDENTIFY POINTS USING THRESHOLD
251             [~, mid_point] = max(image_profile_values);
252             pixel_range = max(image_profile_values) - min(
                    image_profile_values);
253
254             if ~exist('low_threshold','var');
255                 low_threshold = min(image_profile_values)+pixel_range*
                        sensitivity;
256                 high_threshold = max(image_profile_values)-pixel_range*
                        sensitivity;
257             end
258
259             left_crosssection = image_profile_values(1:mid_point);
260             right_crosssection = image_profile_values(mid_point+1:end);
261             low_left_points  = left_crosssection <= low_threshold;
262             low_right_points  = right_crosssection <= low_threshold;
263
264             high_points = image_profile_values >= high_threshold;
265
266             point2 = find(high_points,1,'first');
267             point3 = find(high_points,1,'last');
268
269             point1 = find(low_left_points,1,'last');
270             point4 = find(low_right_points,1,'first') + mid_point;
271
272         case 'threshold_findpeaks'
273             % IDENTIFY POINTS USING THRESHOLD
274             [~, mid_point] = max(image_profile_values);
275             pixel_range = max(image_profile_values) - min(
                    image_profile_values);
276
277             left_crosssection = image_profile_values(1:mid_point);
278             right_crosssection = image_profile_values(mid_point+1:end);
279             low_left_points  = left_crosssection <= min(left_crosssection)+
                    pixel_range*sensitivity;
280             low_right_points  = right_crosssection <= min(
                    right_crosssection)+pixel_range*sensitivity;
281
282             point1 = find(low_left_points,1,'last');
283             point4 = find(low_right_points,1,'first') + mid_point;
284
```

```
285             % findpeaks for high points
286             mid_threshold = min(image_profile_values) + round(pixel_range
                    /2);
287             high_points = image_profile_values >= mid_threshold;
288             high_points_left = find(high_points,true,'first');
289             high_points_right = find(high_points,true,'last');
290             mid_values = image_profile_values(high_points_left:
                    high_points_right);
291             [~, peak_locs] = findpeaks(mid_values,'NPEAKS',2,'SORTSTR','
                    descend');
292             if size(peak_locs,1) == 2
293                 if peak_locs(1) > peak_locs(2)
294                     peak_locs = [peak_locs(2) peak_locs(1)];
295                 end
296                 point2 = peak_locs(2) + high_points_left-1;
297                 point3 = peak_locs(1) + high_points_left-1;
298             else
299                 %threshold for high points
300                 high_points = image_profile_values >= ...
301                 max(image_profile_values)-pixel_range*sensitivity;
302                 point2 = find(high_points,1,'first');
303                 point3 = find(high_points,1,'last');
304             end
305
306             0;
307
308         case 'max_difference'
309             % IDENTIFY POINTS USING DIFFERENTIATED PROFILE
310             differentsection = zeros(profile_length,1);
311             for step = 2:profile_length
312                 differentsection(step,1) = image_profile_values(step) -
                        image_profile_values(step-1);
313             end
314
315             % Rudimentary filter
316             differentsection = differentsection.*abs(differentsection)/max(
                    abs(differentsection));
317
318             maxdifferent = max(abs(differentsection)); mindifferent = -
                    maxdifferent;
319
320             positivegradientind = find(differentsection > maxdifferent*
                    sensitivity);
321             negativegradientind = find(differentsection < mindifferent*
                    sensitivity);
322
323             point1 = positivegradientind(1);
324             point2 = positivegradientind(end);
325             point3 = negativegradientind(1);
326             point4 = negativegradientind(end);
327             if sum(isnan([point1 point2 point3 point4])) > 0
328                 warndlg 'Some points have not been located. Try raising
                        threshold'
329             end
330
```

```
331         case 'profile_ransac'
332             % IDENTIFY POINTS USING RANSAC
333             gravity_weighted_centre = ...
334             sum((image_profile_values*1:size(image_profile_values)))/size(
                    image_profile_values,1);
335             left_crosssection = image_profile_values(1:round(
                    gravity_weighted_centre));
336             pts = [ [1:size(left_crosssection)] ; left_crosssection' ;
                    zeros(size(left_crosssection))'];
337             % RANSAC
338             [V, L, inliers] = ransacfitline(pts, thDist)
339 
340 
341             iterNum = 150;
342             thDist = 2;
343             thInlrRatio = .1;
344             [t,r] = ransac(pts,iterNum,thDist,thInlrRatio);
345             k1 = -tan(t);
346             b1 = r/cos(t);
347             figure
348             plot(X,k1*X+b1,'r')
349 
350         case 'type2'
351             [~] = type2_detection(image_profile_values);
352 
353         case 'type3'
354             [~] = type3_detection(image_profile_values);
355 
356         case 'type4'
357             [point1, point2, point3, point4] = type4_detection(
                    image_profile_values,sensitivity);
358     end
359 
360 
361 
362     if ~size(point1,1) || ~size(point2,1) || ~size(point3,1) || ~size(
            point4,1)
363         figure
364         imshow(I)
365         hold on
366         plot(estimated_target_centre(2),estimated_target_centre(1),'r+')
367         0;
368         error('Some points are missing')
369     end
370 
371     % Calculate coordinates and save edge points into an array
372     % Point 1
373     edgeX = inputX(1) + (inputX(2)-inputX(1))/(profile_length-1)*(point1-1)
            ;
374     edgeY = inputY(1) + (inputY(2)-inputY(1))/(profile_length-1)*(point1-1)
            ;
375     edge1(profile_number,[1 2]) = [edgeX edgeY ];
376 
377     % Point 2
```

```
378     edgeX = inputX(1) + (inputX(2)-inputX(1))/(profile_length-1)*(point2-1)
            ;
379     edgeY = inputY(1) + (inputY(2)-inputY(1))/(profile_length-1)*(point2-1)
            ;
380     edge2(profile_number,[1  2]) = [edgeX edgeY];
381
382     % Point 3
383     edgeX = inputX(1) + (inputX(2)-inputX(1))/(profile_length-1)*(point3-1)
            ;
384     edgeY = inputY(1) + (inputY(2)-inputY(1))/(profile_length-1)*(point3-1)
            ;
385     edge3(profile_number,[1  2]) = [edgeX edgeY];
386
387     % Point 4
388     edgeX = inputX(1) + (inputX(2)-inputX(1))/(profile_length-1)*(point4-1)
            ;
389     edgeY = inputY(1) + (inputY(2)-inputY(1))/(profile_length-1)*(point4-1)
            ;
390     edge4(profile_number,[1  2]) = [edgeX edgeY];
391
392     % Halfway though, plot a profile
393     if (profile_number == round(NumberOfScanLines/2))
394         if suppress_output == false
395             subplot(2,2,4);
396             plot(image_profile_values,'-k'); hold on
397             plot([point1 point3],image_profile_values(round([point1 point3
                    ])),'ob');
398             plot([point2 point4],image_profile_values(round([point2 point4
                    ])),'or');
399         end
400     end
401 end
402
403 %% If this was an external blur, correct it
404
405
406 if image_profiles_parameters.manual_edge_matching == 0
407
408     if (strcmp(POINT_MARKING_METHOD,'threshold_findpeaks') || ...
409     strcmp(POINT_MARKING_METHOD,'threshold') ) && strcmp(BlurType,'external
            ')
410         circle_1_edge = [ edge1; edge3 ];
411         circle_2_edge = [ edge2; edge4 ];
412         disp('scanlines_estimate: Switching some co-ords')
413     else
414         circle_1_edge = [edge1; edge2];
415         circle_2_edge = [edge3; edge4];
416     end
417
418
419 elseif image_profiles_parameters.manual_edge_matching == 1
420     circle_1_edge = [edge1; edge2];
421     circle_2_edge = [edge3; edge4];
422 elseif image_profiles_parameters.manual_edge_matching == 2
423     circle_1_edge = [edge1; edge3];
```

```
424     circle_2_edge = [edge2; edge4];
425 else
426     error('scanlines_estimate: incorrect manual_edge_matching parameter')
427 end
428
429
430
431 %% Fit circle to the points
432 switch image_profiles_parameters.circle_fitting_method
433     case 'standard'
434         [xc1, yc1, R1] = circfit(circle_1_edge(:,1),circle_1_edge(:,2));
435         [xc2, yc2, R2] = circfit(circle_2_edge(:,1),circle_2_edge(:,2));
436     case 'ransac'
437         trials = image_profiles_parameters.ransac_trials;
438         dth = image_profiles_parameters.ransac_dth;
439         percent = image_profiles_parameters.ransac_percent;
440         rLimits = image_profiles_parameters.ransac_rLimits;
441
442         [ransac_center, ransac_r] = ransaccircle(circle_1_edge, trials, dth
                , percent, rLimits );
443         [xc1, yc1] = deal(ransac_center(1),ransac_center(2));
444         R1 = ransac_r;
445
446         [ransac_center, ransac_r] = ransaccircle(circle_2_edge, trials, dth
                , percent, rLimits );
447         [xc2, yc2] = deal(ransac_center(1),ransac_center(2));
448         R2 = ransac_r;
449     case 'fit_ellipse'
450         ellipse_t_1 = fit_ellipse(circle_1_edge(:,1),circle_1_edge(:,2));
451         xc1 = ellipse_t_1.X0_in;
452         yc1 = ellipse_t_1.Y0_in;
453         R1 = (ellipse_t_1.a+ellipse_t_1.b)/2;
454         ellipse_t_2 = fit_ellipse(circle_2_edge(:,1),circle_2_edge(:,2));
455         xc2 = ellipse_t_2.X0_in;
456         yc2 = ellipse_t_2.Y0_in;
457         R2 = (ellipse_t_2.a+ellipse_t_2.b)/2;
458 end
459 [circ1_residual] = circfit_residuals(xc1,yc1,R1,circle_1_edge(:,1),
    circle_1_edge(:,2));
460 [circ2_residual] = circfit_residuals(xc2,yc2,R2,circle_2_edge(:,1),
    circle_2_edge(:,2));
461 if circ1_residual > 0.5 || circ2_residual > 0.5
462     fprintf('WARNING: circle fit might not be very good. Mean error: Blue:
        %1.3f   Red: %1.3f \n',circ1_residual,circ2_residual);
463 end
464
465
466 %% Plot the measured edges
467 %  The (last) sampled line profile will also be plotted in the case of
468 %  manual testing mode
469 if suppress_output == false
470     subplot(2,2,3)
471     imshow(255-I) %%%  THIS CHANGES THE INVERSE FOR IMAGE 3
472     hold on,
```

```
473     plot(circle_1_edge(:,1),circle_1_edge(:,2),'ob',circle_2_edge(:,1),
            circle_2_edge(:,2),'or'), caxis auto, %colorbar, colormap(jet)
474     if strcmp(SCANMODE,'manual')
475         figure
476         subplot(1,3,1); % 1: Show the image
477         hold off,imshow(I), hold on, caxis auto,
478         plot(circle_1_edge(:,1),circle_1_edge(:,2),'ob'), caxis auto, %
                colorbar, colormap(jet)
479         plot(circle_2_edge(:,1),circle_2_edge(:,2),'or'), caxis auto, %
                colorbar, colormap(jet)
480
481         subplot(1,3,2); % 2: The line profile
482         %         figure(20)
483         plot(image_profile_values,'-k'); hold on
484         plot([point1 point3],image_profile_values([point1 point3]),'om');
485         plot([point2 point4],image_profile_values([point2 point4]),'om');
486         if strcmp(POINT_MARKING_METHOD,'threshold')
487             plot([0 mid_point],repmat(min(left_crosssection)+pixel_range*
                    sensitivity,1,2),'g-')
488             plot([mid_point profile_length],repmat(min(right_crosssection)+
                    pixel_range*sensitivity,1,2),'g-')
489             plot([0 profile_length],repmat(max(image_profile_values)-
                    pixel_range*sensitivity,1,2),'g-')
490         end
491         hold off;
492
493         % 3: the differentiate profile
494         if strcmp(POINT_MARKING_METHOD,'max_difference')
495             subplot(1,3,3), plot(differentsection);figure(gcf), hold on
496             plot([point1 point2 point3 point4],[maxdifferent*sensitivity
                    maxdifferent*sensitivity mindifferent*sensitivity
                    mindifferent*sensitivity],'or'), hold off
497         end
498     end
499 end
500
501 %% Plot and offer to the user
502 if suppress_output == false && strcmp(SCANMODE,'auto')
503     th = linspace(0,2*pi,20)';
504     % plot1
505     xe1 = R1*cos(th)+xc1; ye1 = R1*sin(th)+yc1;
506     plot([xe1;xe1(1)],[ye1;ye1(1)],'b-',xc1,yc1,'bx')
507     % plot2
508     xe2 = R2*cos(th)+xc2; ye2 = R2*sin(th)+yc2;
509     plot([xe2;xe2(1)],[ye2;ye2(1)],'r-',xc2,yc2,'rx')
510     axis equal
511     set(gcf, 'Position', get(0,'Screensize'));
512     drawnow
513 end
514
515 separation_polar(1) = hypot(yc2-yc1,xc2-xc1);
516 separation_polar(2) = atan2d((yc2-yc1),(xc2-xc1));
517
518 if strcmp(SCANMODE,'auto')
519     varargout{1} = [xc1 yc1 xc2 yc2];
```

```
520     varargout{2} = blob_prop.WeightedCentroid([2 1]);
521     varargout{3} = [xc1 yc1 R1 ; xc2 yc2 R2 ];
522     varargout{4} = struct( ...
523         'circfit_result', [xc1 yc1 R1 ; xc2 yc2 R2 ], ...
524         'blob_WeightedCentroid', blob_prop.WeightedCentroid([2 1]), ...
525         'separation_rc', [yc2-yc1, xc2-xc1], ...
526         'separation_cartesian', [yc2-yc1, xc2-xc1], ...
527         'ecludian_separation', sqrt(sum([yc2-yc1, xc2-xc1].^2)), ...
528         'blur_type', BlurType, ...
529         'point_marking_method', POINT_MARKING_METHOD, ...
530         'scanmode', SCANMODE, ...
531         'circle_1_points', circle_1_edge, ...
532         'circle_2_points', circle_2_edge, ...
533         'separation_polar', separation_polar, ...
534         'xc1yc1xc2yc2', [xc1 yc1 xc2 yc2], ...
535         'separation_distance', hypot( yc2-yc1 , xc2-xc1 ));
536     if strcmp(POINT_MARKING_METHOD,'thresholds_set')
537         varargout{4}.low_threshold = low_threshold;
538         varargout{4}.high_threshold = high_threshold;
539     end
540     if strcmp(image_profiles_parameters.circle_fitting_method,'fit_ellipse'
        )
541         varargout{4}.ellipse_t_1 = ellipse_t_1;
542         varargout{4}.ellipse_t_2 = ellipse_t_2;
543     end
544 else
545     [varargout{1}, varargout{2}, varargout{3}, varargout{4}] = deal(nan);
546     disp('scanlines_estimate:__No_useful_outputs_when_in_manual_scan_mode')
        ;
547 end
```

C.3 'refine_with_simulation3'

```
function [ varargout ] = refine_with_simulation3(~,~,~,~,window_size,
    Padding,aa,iterations_limit, ...
Isharp,Isharp_cropped_estimated_centre,Iobserved,~,~,
    image_profiles_parameters,~,first_profiles_data)

if size(Iobserved,1) == 0, disp('Blurred image is empty'), return, end
if size(Isharp,1) == 0, disp('Sharp image is empty'), return, end

necessary_precision = [ 0.01  5]
iterations_limit = 50
searching_for_zero = false;
iteration = 1;                    % The first iteration will be numbered 1
iteration_level = 1;
necessary_accuracy_reached = false;
necessary_precision_reached_polar = false(2);
image_profiles_parameters,

if isfield(image_profiles_parameters,'first_guess') ...
        && image_profiles_parameters.first_guess
   iterations_limit = 1;
end

% Sets each blur displacement that will be tested in the first iteration
% and sets the target
profiles_polar_target = first_profiles_data.separation_polar;
profiles_polar_target(2) = put_polar_angle_within_range(
    profiles_polar_target(2));
row_th = profiles_polar_target(1) ; % Row = dist
row_th_start = row_th(1); row_th_end = row_th(end);
row_th=0;

% Check if the blur orientation is forced
if image_profiles_parameters.force_blur_direction
    necessary_precision_reached_polar(2) = true;
    switch image_profiles_parameters.assumed_blur_direction
        case 'horiz'
            col_th = 0;
        case 'vert'
            col_th = 90;
    end
else
    col_th = profiles_polar_target(2) ; % Col = angle
end
col_th_start = col_th(1); col_th_end = col_th(end);

0;

row_ind = 1:size(row_th,2);      % Numbers the blur displacements
%%%%%%%%%%%%%%%% row/col_ind variables can
%%%%%%%%%%%%%%%% probably be removed
row_th_span = row_th_end - row_th_start ;
col_ind = 1:size(col_th,2);
col_th_span = col_th_end - col_th_start ;
```

```
51
52
53
54 % Plot first image with scanlines data
55 if ~image_profiles_parameters.suppress_output
56     figh_obs_vs_filtered = figure(10);
57     maxfig(gcf,1);
58     subplot(2,4,[1 2])
59     subimage(Iobserved)
60     caxis auto
61     hold on
62     first_profiles_fit_circles = first_profiles_data.circfit_result;
63     if ~image_profiles_parameters.suppress_output
64         display_image_progress(figh_obs_vs_filtered,Iobserved,
               first_profiles_data,1)
65     end
66
67     hold off
68     title('Blurred observation image')
69 end
70
71
72
73
74 %% THIS IS WHERE ITERATIONS START
75 while ~necessary_accuracy_reached && iteration <= iterations_limit
76     %     c = nan(row_ind(end),col_ind(end));
77     scanline_difference = nan(row_ind(end),col_ind(end));
78     [ polar_dist_difference, polar_ang_difference] = deal(nan(row_ind(end),
          col_ind(end)));
79
80     % First iterate polar angle
81         row = round(row_ind(end)/2);
82   col = 1;
83             fprintf( 'refine_with_simulation:  Polar mode  Iter:%1u  Lev:%
                 lu  Ind:%2.0u,%2.0u  Dist: %5.3f Ang: %5.3f \n', iteration,
                 iteration_level, row, col, row_th(row), col_th(col) );
84             if isnan(col_th(col))
85                 disp('!!!!!!!!!!!!!!! col_th(col is Nan'), end
86             [Isharp_filtered, ~, ~, profiles_data_current] = ...
87                 verify_with_simulation(Iobserved,Isharp, ...
88                 0,[0 0 0 0], window_size, ...
89                 Padding,aa,Isharp_cropped_estimated_centre, ...
90                 image_profiles_parameters, [row_th(row) col_th(col)],
                       searching_for_zero);
91             if ~image_profiles_parameters.suppress_output
92                 display_image_progress(figh_obs_vs_filtered,Isharp_filtered
                       ,profiles_data_current) % Display progress
93             end
94
95             profiles_polar_current = profiles_data_current.separation_polar
                   ;
96             profiles_polar_current(2) = put_polar_angle_within_range(
                   profiles_polar_current(2));
97
```

```
98              polar_dist_difference(row,col) = profiles_polar_current(1) -
                    profiles_polar_target(1);
99              polar_ang_difference(row,col) = profiles_polar_current(2) -
                    profiles_polar_target(2);
100
101             fprintf('\b  Diffs: d: %1.5f a: %1.5f \n',polar_dist_difference
                    (row,col),polar_ang_difference(row,col));
102             disp(['Polar DIST : Target: ' num2str(profiles_polar_target(1))
                     '  Current: ' num2str(profiles_polar_current(1))]);
103             disp(['Polar ANGLE: Target: ' num2str(profiles_polar_target(2))
                     '  Current: ' num2str(profiles_polar_current(2))]);
104
105
106 %           [~, highest_correlation_sub(2)] = min(abs(polar_ang_difference(
    row,:)));
107 %       else
108           highest_correlation_sub(2) = 1;
109 %       end
110
111
112           highest_correlation_sub(1) = 1;
113
114 if ~image_profiles_parameters.suppress_output
115     figure(figh_obs_vs_filtered)
116     jetmap = colormap('jet');
117     %     subplot(1,3,1), imshow(scanline_difference), title('Scanline eclud
        . dist. diff.')
118     subplot(2,4,5), subimage(polar_ang_difference,jetmap), title('Polar.
        ang. diff.')
119     subplot(2,4,6), subimage(polar_dist_difference,jetmap), title('Polar.
        dist. diff.')
120     colormap('jet'), caxis auto
121
122     % Output some handy figures to check on the progress
123     figure(figh_obs_vs_filtered),
124     if ~necessary_precision_reached_polar(2)
125         subplot(2,4,7),
126         plot(col_th,polar_ang_difference(round(row_ind(end)/2),:));
127         axis equal;
128         title('Angular iterations')
129     end
130     if ~necessary_precision_reached_polar(1)
131         subplot(2,4,8),
132         plot(row_th,polar_dist_difference(:,highest_correlation_sub(2)));
133         axis equal;
134         title('Distance iterations')
135     end
136
137 end
138         % Precision check
139         current_precision(1) = abs(polar_dist_difference);
140         current_precision(2) = abs(polar_ang_difference);
141         if (current_precision <= necessary_precision) == [1 1];
142             necessary_accuracy_reached = true;
```

```
143             disp(strcat('Accurecy check :- Current: ',num2str(
                    current_precision),' Limit: ',num2str(necessary_precision),'
                    ACCEPT!'))
144         else
145             disp(strcat('Accurecy check :- Current: ',num2str(
                    current_precision),' Limit: ',num2str(necessary_precision) )
                    )
146         end
147         if current_precision(2) <= necessary_precision(2)
148             necessary_precision_reached_polar(2) = true;
149         end
150         if current_precision(1) <= necessary_precision(1)
151             necessary_precision_reached_polar(1) = true;
152         end
153
154
155         % Columns = Angle
156         if necessary_precision_reached_polar(2)
157 %             [col_th_start, col_th_end] = deal(col_th(
    highest_correlation_sub(2)));
158         else
159             col_th = col_th + polar_ang_difference(1,1);
160         end
161
162         % Rows = Distances
163         if necessary_precision_reached_polar(1)
164 %             [row_th_start, row_th_end] = deal(row_th(
    highest_correlation_sub(1)));
165         else
166             if row_th - polar_dist_difference(1,1) < 0
167                 % Check if looking for zero
168                 row_th = row_th/2
169             else
170                 % Not looking for zero
171                 row_th = row_th - polar_dist_difference(1,1);
172             end
173         end
174         iteration_level = iteration_level +1;
175
176     if ~necessary_accuracy_reached && iteration < iterations_limit  % Check
            if there are more iterations to go
177
178     else   % This was the final iteration - this value
179         % will be passed back to the parent function.
180         best_match_row = row_th;
181         best_match_col = col_th;
182 %         best_match_col = profiles_polar_current(2);
183         best_match = [best_match_row best_match_col];
184     end
185
186     iteration = iteration + 1; % Increase the counter
187 end
188
189 if isfield(image_profiles_parameters,'first_guess') ...
190         && image_profiles_parameters.first_guess
```

```
191     best_match = first_profiles_data.separation_polar -
            profiles_data_current.separation_polar;
192 end
193 0;
194
195 varargout{1} = best_match;
196 varargout{2} = best_match;
197 varargout{3} = profiles_data_current;
198 end
199
200 function [output_angle] =  put_polar_angle_within_range(input_angle)
201
202 if input_angle < 0
203     input_angle = input_angle + 180;
204 end % Output range: 0 ~ 180
205 if input_angle > 105
206     input_angle = input_angle - 180;
207 end % Output range: -45 ~ 105
208
209 output_angle = input_angle;
210 end
211
212 function display_image_progress(fig_handle,Isharp_filtered,
        current_profiles_data, varargin)
213 figure(fig_handle)
214 % Observation image displayed by refine_with_simulation function
215 if nargin == 4
216     subplot(2,4,[1 2])
217 else
218 subplot(2,4,[3 4])
219 end
220 subimage(Isharp_filtered)
221 hold on
222 switch isfield(current_profiles_data,'ellipse_t_1')
223     case false
224         xc1 = current_profiles_data.circfit_result(1,1);
225         yc1 = current_profiles_data.circfit_result(1,2);
226         R1 = current_profiles_data.circfit_result(1,3);
227         xc2 = current_profiles_data.circfit_result(2,1);
228         yc2 = current_profiles_data.circfit_result(2,2);
229         R2 = current_profiles_data.circfit_result(2,3);
230         th = linspace(0,2*pi,20)';
231         xe1 = R1*cos(th)+xc1; ye1 = R1*sin(th)+yc1;      % plot1
232         plot([xe1;xe1(1)],[ye1;ye1(1)],'b-',xc1,yc1,'bx')
233         plot(current_profiles_data.circle_1_points(:,1),
                current_profiles_data.circle_1_points(:,2),'bo')
234         xe2 = R2*cos(th)+xc2; ye2 = R2*sin(th)+yc2;      % plot2
235         plot([xe2;xe2(1)],[ye2;ye2(1)],'r-',xc2,yc2,'rx')
236         plot(current_profiles_data.circle_2_points(:,1),
                current_profiles_data.circle_2_points(:,2),'ro')
237     case true
238         xc1 = current_profiles_data.ellipse_t_1.X0_in;
239         yc1 = current_profiles_data.ellipse_t_1.Y0_in;
240         a1 = current_profiles_data.ellipse_t_1.a;
241         b1 = current_profiles_data.ellipse_t_1.b;
```

```
242         phi1 = current_profiles_data.ellipse_t_1.phi;
243         ellipse(a1,b1,phi1,xc1,yc1,'b')
244         plot(xc1,yc1,'bx')
245 
246         xc2 = current_profiles_data.ellipse_t_2.X0_in;
247         yc2 = current_profiles_data.ellipse_t_2.Y0_in;
248         a2 = current_profiles_data.ellipse_t_2.a;
249         b2 = current_profiles_data.ellipse_t_2.b;
250         phi2 = current_profiles_data.ellipse_t_2.phi;
251         ellipse(a2,b2,phi2,xc2,yc2,'r')
252         plot(xc2,yc2,'rx')
253 
254 end
255 title('Sharp filtered image')
256 hold off
257 axis equal
258 end
```

C.4 'verify_with_simulation'

```
% verify_with_simulation
% D McCarthy Nov 2012
% Takes a blurred and unblurred image, artificially blurs the sharp image,
% and calculates the correlation statistic
%
% Usage: c = verify_with_simulation(Iblurred,Isharp,~, ...
%           BlurDisplacementsPair,window_size,~,aa, ...
%           Isharp_estimated_centre)
%
% where     Iblurred:                   Cropped blurred observations image
%           Isharp:                     Cropped sharp images with padding
%           BlurDisplacementsPair:      [xc1 xc2 yc1 yc2]
%           window_size:                Size of correlation window
%           aa:                         Parameter for the artificial psf
%           Isharp_estimated_centre:    Centre of the sharp image
%

function [varargout] = verify_with_simulation( Iblurred,Isharp,~,
    BlurDisplacementsPair, ...
window_size,~,aa,Isharp_estimated_centre,image_profiles_parameters,
    varargin)


% searching_for_zero = varargin{2};

%% Estimate the blur PSF and filter the sharp image
% kernel_size = [50 50];

% if polar?
if nargin >= 10
    polar_separation = varargin{1};
%     estimated_blur_size = [0 polar_separation(1)];
%     kernel_rotation = polar_separation(2);
else
    xc1 = BlurDisplacementsPair(1);  % Just collecting the input variables
    xc2 = BlurDisplacementsPair(2);
    yc1 = BlurDisplacementsPair(3);
    yc2 = BlurDisplacementsPair(4);
%     estimated_blur_size = [yc2-yc1, xc2-xc1];
%     kernel_rotation = 0;
end

psf = sinusoidal_blur_kernel5(polar_separation(1),polar_separation(2),aa);
Isharp_filtered = imfilter(Isharp,psf, 'replicate');

% Crop away the additional padding added earlier
Isharp_crop_corner2 = round(Isharp_estimated_centre) - window_size./2;
Isharp_filtered = imcrop(Isharp_filtered,[Isharp_crop_corner2(2)
    Isharp_crop_corner2(1) window_size(2)-1 window_size(1)-1]);
% Do the same for unfiltered Isharp
Isharp = imcrop(Isharp,[Isharp_crop_corner2(2) Isharp_crop_corner2(1)
    window_size(2)-1 window_size(1)-1]);
Isharp_estimated_centre = Isharp_estimated_centre - Isharp_crop_corner2;
```

```
50
51 %% Compare to the blurred image
52
53 c = 0;
54
55 % USING PROFILES
56 I_user_selected_point = round(size(Isharp_filtered)/2);
57
58 image_profiles_parameters.is_simulated_image = true;
59 if isfield(image_profiles_parameters, '
       overide_threshold_adjustment_at_verify')
60     if image_profiles_parameters.overide_threshold_adjustment_at_verify
61         image_profiles_parameters.threshold_adjust = 0;
62     end
63 end
64
65 new_Isharp_crop_corner = ((size(Isharp) - size(Iblurred))/2);
66 % Crop the some additional padding?
67 Isharp = Isharp( new_Isharp_crop_corner(1)+1:new_Isharp_crop_corner(1)+size
       (Iblurred,1), ...
68     new_Isharp_crop_corner(2)+1:new_Isharp_crop_corner(2)+size(Iblurred,2)
           );
69
70 [~, ~, ~, current_profiles_data] = scanlines_estimate(Isharp_filtered, ...
71 image_profiles_parameters,I_user_selected_point,0,Isharp,
       Isharp_estimated_centre);
72
73 scanline_current_magnitude = current_profiles_data.separation_polar(1);
74 scanline_current_rotation = current_profiles_data.separation_polar(2);
75 current_profiles_data.separation_polar;
76
77 %% Figures
78
79 % FULLSCREEN
80 % set(gcf, 'Position', get(0,'Screensize'));
81 if ~image_profiles_parameters.suppress_output
82     caxis auto
83     drawnow
84 end
85
86 varargout{1} = Isharp_filtered;
87 varargout{2} = 0; %scanline_current; % UNUSED
88 varargout{3} = current_profiles_data.separation_polar; % UNUSED
89 varargout{4} = current_profiles_data;
```

C.5 'sinusoidal_blur_kernel5'

```
function psf = sinusoidal_blur_kernel5(psf_magnitude,psf_rotation,aa)

kernel_size = [1 ceil(psf_magnitude/2)*2+5];

bb = 1 - aa;

psf = nan(kernel_size);       % Create an array for the blur kernel
centre_of_psf = kernel_size/2;

kernel_col_min = centre_of_psf(2)-psf_magnitude/2+0.5;
kernel_col_max = centre_of_psf(2)+psf_magnitude/2+0.5;

% Check for special cases
if psf_magnitude == 1
    psf = [0 1 1 0];
elseif psf_magnitude < 1
    psf = fspecial('motion',abs(psf_magnitude)+1);
elseif psf_magnitude < 2 && psf_magnitude > 1
    psf = [ 0,  psf_magnitude/2, 2-psf_magnitude, psf_magnitude/2, 0];
else
    % Not a special case
    row = round(kernel_size(1)/2);
    for col = 1:kernel_size(2)
        % pixel is on the minimum edge of the blur function
        if col == floor(kernel_col_min)
%             % Linear interpolation
            left = kernel_col_min-col;
            right = 1-left;
            left_part = 0;
            right_part = ( 1/2*cos( (( right/2  )) *2*pi()/(psf_magnitude)
                )+1/2 )*bb+aa;
            psf(row,col) = left * left_part + right * right_part ;
            continue
        end

        % pixel is inside the blur function
        if (col >= floor(kernel_col_min)) && (col < ceil(kernel_col_max))
            psf(row,col) = ...
                (1/2*cos( ((col-kernel_col_min)) *2*pi()/psf_magnitude  )
                    +1/2 )*bb+aa;
            continue
        end

        % pixel is on the maximum edge of the blur function
        if col == ceil(kernel_col_max)
            psf(row,col) = left * left_part + right * right_part ;
        end
    end
end

psf(isnan(psf)) = 0;

% Rotate kernel
```

```
52 psf = imrotate(psf,psf_rotation,'bilinear');
53
54 psf = psf./sum(sum(psf));
55
56 % plot(psf)
```

Appendix D

Accuracy Regression Analysis Results

The full output of the MS Excel regression analysis for the accuracy assessment described in section 3.4 follows.

Summary Output

Regression	Statistics
Multiple R	0.999688
R Square	0.999376
Adjusted R Square	0.999370
Standard Error	0.095532
Observations	115

ANOVA

	df	SS	MS	F	Significance F
Regression	1	1653	1653	181105	6.096E-183
Residual	113	1.0313	0.009127		
Total	114	1653			

	Coefficients	Standard Error	t Stat	P-value
Intercept	-0.3369	0.0181	-18.600	3.501E-36
X Variable 1	1.035	0.002432396	425.6	6.0964E-183

	Lower 95%	Upper 95%	Lower 95.0%	Upper 95.0%
Intercept	-0.3727	-0.3010	-0.3728	-0.3010
X Variable 1	1.030	1.040	1.030	1.040

Residual Output

Observation	Predicted Y	Residuals	Observation	Predicted Y	Residuals
1	0.145	-0.053	41	4.540	-0.052
2	0.145	-0.072	42	4.540	0.114
3	0.145	-0.031	43	4.540	0.084
4	0.145	0.033	44	4.540	0.112
5	0.587	0.070	45	5.020	-0.059
6	0.587	0.019	46	5.020	0.126
7	0.587	0.152	47	5.020	0.048
8	0.587	0.191	48	5.020	0.112
9	1.058	-0.083	49	5.427	-0.029
10	1.058	-0.064	50	5.427	0.146
11	1.058	-0.038	51	5.427	0.130
12	1.058	-0.021	52	5.427	0.082
13	1.498	0.076	53	5.927	-0.118
14	1.498	0.060	54	5.927	0.130
15	1.498	0.072	55	5.927	0.115
16	1.498	0.091	56	5.927	0.141
17	1.878	-0.123	57	6.419	-0.138
18	1.878	-0.103	58	6.419	0.023
19	1.878	-0.119	59	6.419	0.026
20	1.878	-0.104	60	6.419	0.007
21	2.324	-0.004	61	6.875	-0.234
22	2.324	-0.020	62	6.875	-0.041
23	2.324	-0.008	63	6.875	-0.022
24	2.324	0.031	64	6.875	-0.038
25	2.745	-0.125	65	7.301	0.049
26	2.745	-0.021	66	7.301	0.066
27	2.745	-0.012	67	7.301	0.223
28	2.745	-0.028	68	7.301	0.121
29	3.191	-0.083	69	7.728	0.037
30	3.191	-0.041	70	7.728	0.074
31	3.191	-0.056	71	7.728	0.202
32	3.191	0.009	72	7.728	0.105
33	3.696	-0.174	73	8.189	-0.178
34	3.696	-0.016	74	8.189	-0.116
35	3.696	-0.016	75	8.189	-0.009
36	3.696	0.021	76	8.189	-0.130
37	4.152	-0.139	77	8.598	-0.039
38	4.152	-0.043	78	8.598	0.000
39	4.152	-0.078	79	8.598	0.135
40	4.152	-0.024	80	8.598	0.005

Observation	Predicted Y	Residuals
81	9.092	-0.187
82	9.092	-0.151
83	9.092	0.020
84	9.092	-0.135
85	9.528	-0.144
86	9.528	-0.119
87	9.528	0.035
88	9.528	-0.102
89	9.997	0.067
90	9.997	0.026
91	9.997	0.198
92	9.997	0.021
93	10.443	0.023
94	10.443	0.014
95	10.443	0.215
96	10.443	0.106
97	10.918	0.009
98	10.918	0.016
99	10.918	0.113
100	10.918	0.065
101	11.381	-0.069
102	11.381	-0.042
103	11.381	-0.024
104	11.825	-0.063
105	11.825	-0.015
106	11.825	-0.041
107	12.261	-0.081
108	12.261	0.018
109	12.261	0.014
110	12.676	-0.009
111	12.676	0.086
112	12.676	0.093
113	13.189	-0.144
114	13.189	-0.073
115	13.189	-0.076

Appendix E

Camera Settings for LEMBI Measurement

Consumer grade DSLR cameras are typically supplied with the automatic setting of many parameters activated. The LEMBI measurement tests required some of these settings which are listed below to be manually enforced.

As is common in photogrammetry, focus was fixed when the camera was calibrated to preserve interior orientation. Throughout this project flash was never used. The settings listed below were used to optimise images of motion-blurred targets for measurement with the developed algorithm. These also provided enhanced control over the short interval between shutter button activation (manual or automated) and the start of the image capture, for when the double external trigger was used.

The enforced settings were:

- Manual shooting mode
- Exposure set with regard to expected vibration frequency (see section 5.2.4)
- Sensitivity set to the lowest ISO100
- Aperture was set through trial and error so that targets were appropriately exposed, which for the Nikon D80 camera was between f/11 & f/22.
- When outdoors, it was necessary to use ND filters, and a combination of ND2, ND4 & ND8 filters were used, selected by trial whilst checking image exposure.